Precise measurements of cosmic ray spectra at ground level

Taylor, Frank E.

Precise Measurements of Cosmic Ray Spectra at Ground Level

by Frank E. Taylor, M.Sc.

A thesis submitted to the University of Durham in support of an application for the degree of Doctor of Philosophy.

September, 1961.

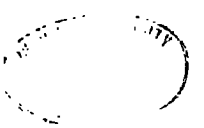

CONTENTS

	Page
Abstract	1
Preface	3
Chapter 1. Introduction	4
1.1. General	4
1.2. Present Work	6
Chapter 2. Previous Measurements of the Muon Spectrum at Sea-Level	8
2.1. Principles	8
2.2. Previous Magnetic Measurements at Sea-Level	9
2.3. Comparison of the Previous Measurements.	12
Chapter 3. The Durham Spectrograph	14
3.1. General Features	14
3.2. The Electromagnet	15
3.3. The Detecting System	15
3.4. The Recording System and Mode of Momentum Measurement	16
3.5. Alignment	19
3.6. The Nature of Particles accepted by the Instrument	20
3.7. The Flash Tube Spectrograph	20
3.8. Magnetic Bias - the Acceptance Function.	22
3.9. Other Instrumental Corrections	28

Page

Chapter 4. Analysis of Single Event Data 29

4.1. Experimental Data and General Scheme ... 29

4.2. Consistency of Basic Data 30

4.3. Correction for Superimposed Events 30

4.4. Conversion of Deflection Spectrum to a Momentum Spectrum 31

4.5. Correction for Magnetic Bias 34

4.6. Correction for the Proton Component of Cosmic Rays at Sea-Level 35

4.7. Correction for Coulomb Scattering 36

4.8. Correction for Momentum Loss in the Material above the Magnet 43

4.9. Normalisation 45

4.10 Combination of Events and Final Differential Momentum Spectrum 47

4.11 Relaxation of Spectrum to "Best-Fit" Line 47

4.12 The Sea-Level Energy Spectrum 48

4.13 The Integral Momentum Spectrum 49

Chapter 5. Bias Effects on the Spectrum 51

5.1. Multiple Events and Associated Phenomena 51

5.2. Observations 52

5.3. Analysis of Results 53

5.4. Double Muon Events 54

5.5. Knock-on Electron Events 56

Page

5.6. Events Producing High Density Records ... 57

5.7. Conclusions With Regard to Spectrum Bias. 58

Chapter 6. Comparison with Other Workers 59

6.1. Procedure 59

6.2. Spectra Normalised to Rossi 59

6.3. Spectra not Normalised to Rossi 60

6.4. Spectra Re-normalised to Rossi 61

6.5. Possible Latitude Effects 61

Chapter 7. Derivation of the Pion Generation Spectrum 62

7.1. A Simple Propagation Model - Unique Generation Height 62

7.2. Extended Generation Model 65

(i) Previous Attempts 65

(ii) The Author's Computations 66

(iii) Stage 1 Computations 68

(iv) Stage 2 Computations 71

(v) Incremental Production of Muons 74

(vi) The Pion Generation Spectrum 74

(vii) Mean and Median Depths and Heights of Production 75

(viii) The Effect of Change in Absorption Length 76

(ix) Comparison with the Direct Measurement of the Pion Generation Spectrum 76

Page

7.3. The Sea-Level Pion Spectrum 78
(i) General 78
(ii) Details of Computation 78
(iii) Final Sea-Level Pion Spectrum 80
(iv) Determination of Absorption Length 80
(v) Incremental Production of Pions 81
(vi) Accuracy of Pion Generation Spectrum ... 81
Chapter 8. The Positive-Negative Ratio 83
8.1. Experimental Observations 83
(i) General 83
(ii) Previous measurements 84
(iii) The Positive-Negative ratio from the Present Work 85
(iv) Correction for Proton Component 85
(v) Final Experimental Results 86
8.2. Interpretation of the Positive-Negative Ratio 86
(i) Terminology 86
(ii) General 87
(iii) Computation of Theoretical Positive-Negative Ratio 88
(iv) Comparison Between Experiment and Theory 93
Chapter 9. Correlation with Underground Measurements 96
9.1. Nature of Correlation 96

Page

9.2. The Range-Momentum relationship for Muons in Rock 96

9.3. The Integral Range Spectrum and the Depth-Intensity Curve 99

Chapter 10. Conclusions 102

10.1. Present Work 102

Acknowledgments 105

References 106

Appendices 113

ABSTRACT

This work describes a series of experiments performed to make an accurate determination of the differential momentum spectrum of cosmic ray muons at ground level in the momentum range $0.3<p<10$ GeV/c. The results of measurements on 192,090 single particles passing through the Durham Cosmic Ray Spectrograph are given. The bias resulting from rejection of multiple events has been investigated from 5988 such events recorded and a corrected spectrum derived.

The spectrum is used to derive information about nuclear processes at high energy. In particular, an accurate determination is made of the generation spectrum of cosmic ray pions in the atmosphere. It is found that the intensity of pions, $I(p_\pi)$, of momentum p_π may be represented by an equation of the form:-

$$I(p_\pi)dp_\pi = A\, p_\pi^{-\gamma}\, dp_\pi$$

where $\gamma = 2.64$, and A is constant for p_π above 4 GeV/c, and is given by the expression

$$A = 1.82.10^{-4} \left(p_\pi/4 \right)^{0.712}$$

for p_π less than 4 GeV/c.

The ratio of positive to negative muons is used to examine the multiplicity of generation of charged pions.

The sea-level spectrum has also been used to derive the expected underground depth-intensity relation - this is found to be in good agreement with that directly measured, indicating that the assumed form of energy loss of muons is correct.

PREFACE

This thesis describes the accurate measurement and interpretation of the momentum spectrum of cosmic ray muons at Durham, 198 feet above sea level.

The work described was performed between October, 1958 and July, 1961 under the direction of Dr. A.W. Wolfendale. Some of the initial data for the muon spectrum were collected by previous members of the Magnet Group: acknowledgment is made to their work, where appropriate, in the text. The remainder of the data, all the analysis and interpretation, and the study of bias effects on the spectrum were the sole responsibility of the author.

Part of the work has been published by the author and his colleagues (Ashton et al, 1960) and another part was presented by the author at the Glasgow Conference on Nuclear Physics, (1960).

Chapter 1.

Introduction

1.1. General

The cosmic radiation reaching ground level consists of two main types of particle - electrons, from interaction of high energy photons (produced by decay of neutral pions), termed the 'soft' component; and mesons, together with a small fraction of nucleons, termed the 'hard' component. This work deals solely with the latter, the main interest being measurement and interpretation of the ground level muon flux at Durham, 198 feet above sea-level. This is to all practical purposes and intents sea-level so far as intensity and propagation theory are concerned, and the term 'sea-level' will be used in the following text.

Many previous experiments investigating the number and momenta of cosmic ray muons at sea-level have yielded a number of differential muon spectra - see, for example, Wilson (1946); Rossi (1948); Glaser et al (1950); Caro et al (1951); Owen and Wilson (1955); Pine et al (1959); Allkofer (1960). With the exception of the work of Pine et al, the number of events measured has been limited by the time taken for analysis of each event. In the present work, and that of Pine et al, semi-automatic or fully-automatic electronic reduction of data has enabled a

greater number of events to be measured in a reasonable time. A detailed review of previous work is given in Chapter 2.

The life history of the muons reaching ground level may be briefly summarised. The origin of cosmic rays is still not clearly defined, but theories put forward by Fermi (1949 and 1954), Morrison et al (1954), Fan (1955) and Morrison(1957), would appear to explain the acceleration to high energies, within the universe, of nuclear particles, usually protons. It is likely that these are released from hot stars under certain circumstances and a study of shock waves in stars and their effect has been made by Hazelhurst and Sargent (1958). Work supporting this theory and that of the diffusion of such particles through space has been given by Powell (1960). A comparison between the composition of the primary cosmic radiation and that of the general matter of the universe is reproduced in Fig. 1.1.1. The similarity is clear.

Also supporting these theories is the fact that when sunspots connected with solar emissions occur, a decrease in the intensity of low energy cosmic rays is observed. (Parker, 1957, 1958).

Upon reaching the top of the earth's atmosphere, the energetic primary cosmic rays interact with one or other constituent nucleons of an air molecule to produce

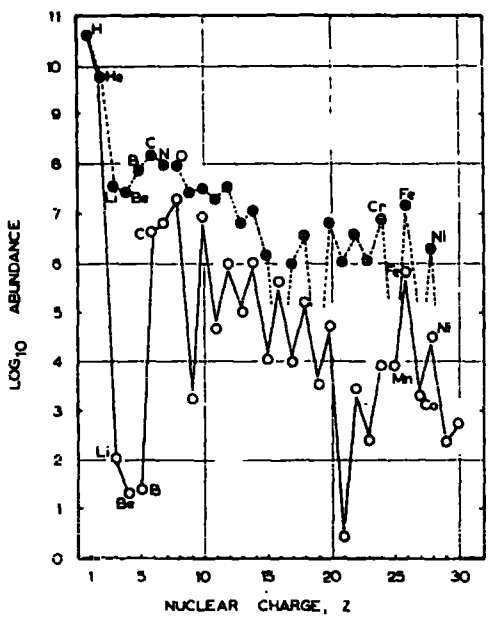

Relative abundances of different elements in the primary cosmic radiation and in the general matter of the universe.

Results for cosmic radiation are shown by full circles: for the general matter of the universe, open circles, the two distributions being normalized to hydrogen and helium. The crucial points of difference are the appreciable abundance of lithium, beryllium and boron, and the over-abundance of nickel, iron and other neighbouring elements, in cosmic radiation.

FIG. 1.1.1. Composition of the Primary cosmic Radiation relative to general matter of the Universe. After POWELL, 1960.

pions. These in turn decay (or interact and decay in the case of those of higher energies) to muons, which are observed at ground level. The whole process is shown schematically in Fig. 1.1.2.

1.2. Present Work

In the momentum range chosen for detailed study, competition between interaction and decay of the secondary pions giving rise to the sea-level spectrum is greatly biassed towards decay, interaction only becoming important at momenta above 20 GeV/c. It is therefore possible to evaluate accurately the pion spectrum from considerations of muon survival probability, momentum loss, and other (minor) factors. This has been done. Further, it is possible, from a knowledge of the primary spectrum, to investigate the multiplicity of the primary interactions. This is described in the later section of this thesis (Chapter 8).

Measurements were performed on 192,090 single events, (i.e. events where only one counter at each of the measuring levels was discharged) using a technique of semi-automatic analysis, and an accurate differential momentum spectrum has been derived for muons at sea-level.

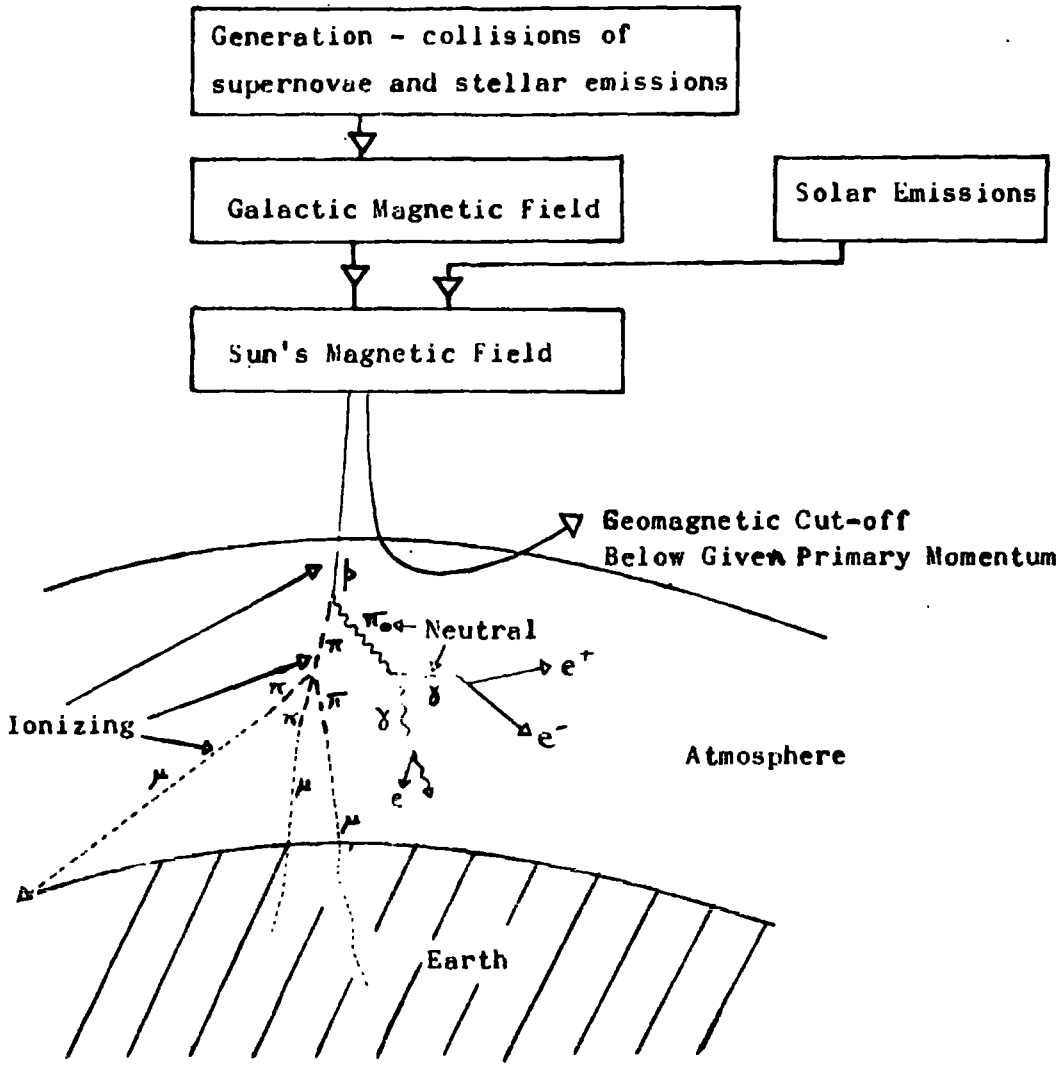

FIG. 1.1.2. Schematic Flowsheet of the Life History of Cosmic Rays

Possible bias effects have been examined from observation of a large number of multiple events, (i.e. events where two or more particles were recorded simultaneously by at least one of the counter measuring levels of the Durham instrument) and measurement of some of these has given an estimate of the inaccuracy of spectra from which such multiple events have been excluded. It has not proved possible to study the bias due to showers of high density where many particles traverse the instrument.

The particles initiating these events will have momenta well above 20 GeV/c and thus it seems likely that many of the secondary particles will have momenta outside the range of the present work.

The differential muon spectrum obtained has been used to give an integral momentum spectrum and a range spectrum. Conclusions are drawn about the rate of energy loss of muons from a comparison of the range spectrum with the underground depth-intensity curve.

Finally, the present results and those obtained by other workers using other techniques, in particular the emulsion technique, are compared and conclusions drawn.

Chapter 2.

Previous Measurements of the Muon Spectrum at Sea Level

2.1. Principles

From the time when it became evident that cosmic rays have energies large compared with previously known particles, three modes of momentum or energy measurement have been used.

The first is that of observation of absorption after traversal of a large mass of material, such as rock or water. The counting rate of a detector is measured as a function of depth, and the energy spectrum is determined from a knowledge of the relation between energy and range (This will be described at greater length in Chapter 9).

The second method is that of scattering arising from close encounters between particles and nuclei. The quantity determined is the product of momentum and velocity ($p\beta$) which reduces to momentum at the high velocities ($\beta \sim 1$) under discussion. The scattering can be measured using either a multiplate cloud chamber or nuclear emulsion. In practice this method is limited to measurement of low momenta ($\lesssim 5$ GeV/c) due to the presence of various noise effects. See, for example, Nash and Pointon, 1956, for details of an approximate measurement of the underground momentum spectrum using this principle.

A much more reliable method of measuring the momentum of single charged particles is to measure the deflection from a straight line trajectory undergone on passing through a region of magnetic field. Instruments using this principle are termed 'magnetic spectrographs' - this work describes the application of such an instrument.

2.2. Previous Magnetic Measurements at Sea Level

Previous work using magnetic spectrographs has been performed by Caro et al (1951); Glaser et al (1950); Owen and Wilson (1955); Pine et al (1959); and Allkofer (1959, 1960). A review of the methods used and the results obtained by these workers follows. A table of the important properties of these instruments and their use is given in Table 2-2-1.

Caro et al (1951) used the instrument shown in Fig. 2.2.1, detection being by means of geiger counters at a series of 'measuring levels'. Recording of the tracks was semi-automatic by means of a punched card system. Analysis of the punched cards was somewhat slow, as electronic computers were not then available The accepted flux was also low, hence the rate of collection of data was necessarily low. The results are reproduced in Fig. 2.2.2. - all multiple events, (i.e. events where two or more counters in any one measuring layer were

Worker(s)	Date	Collecting Power (sterad cm^2)	M.d.m. GeV/c (Probable error)	No. of events	Material above Instrument	Measuring Detector
Caro et al	1950	0.69*	90*	6,023	$<1 g.cm^{-2}$	G.M.
Glaser et al	1950	0.082	50*	1,547	NIL	G.M.; C.C.
Owen & Wilson	1955	0.93	31	60,000	NIL	G.M.
Rogers	1957	0.93	356	4,566	NIL	G.M.; C.C.
Pine et al	1959	7.9	260	1,089/	NIL	G.M.; C.C.
Allkofer	1960	-	12*	2,324	NIL	S.C.
Durham group (counters)	1960	8.0	26.5	192,090	0/2/5.5 cm of Pb	G.M.
(flash-tubes)	1960	8.0	700	3,489	5.5 cm of Pb	F.T.

Abbreviations:-

G.M. - Geiger-Müller counters

C.C. - Cloud Chambers

S.C. - Spark Counters

F.T. - Flash Tubes

* Value estimated by the author

/ This is the number of high energy particles only, measured with the cloud chamber technique.

Table 2-2-1.

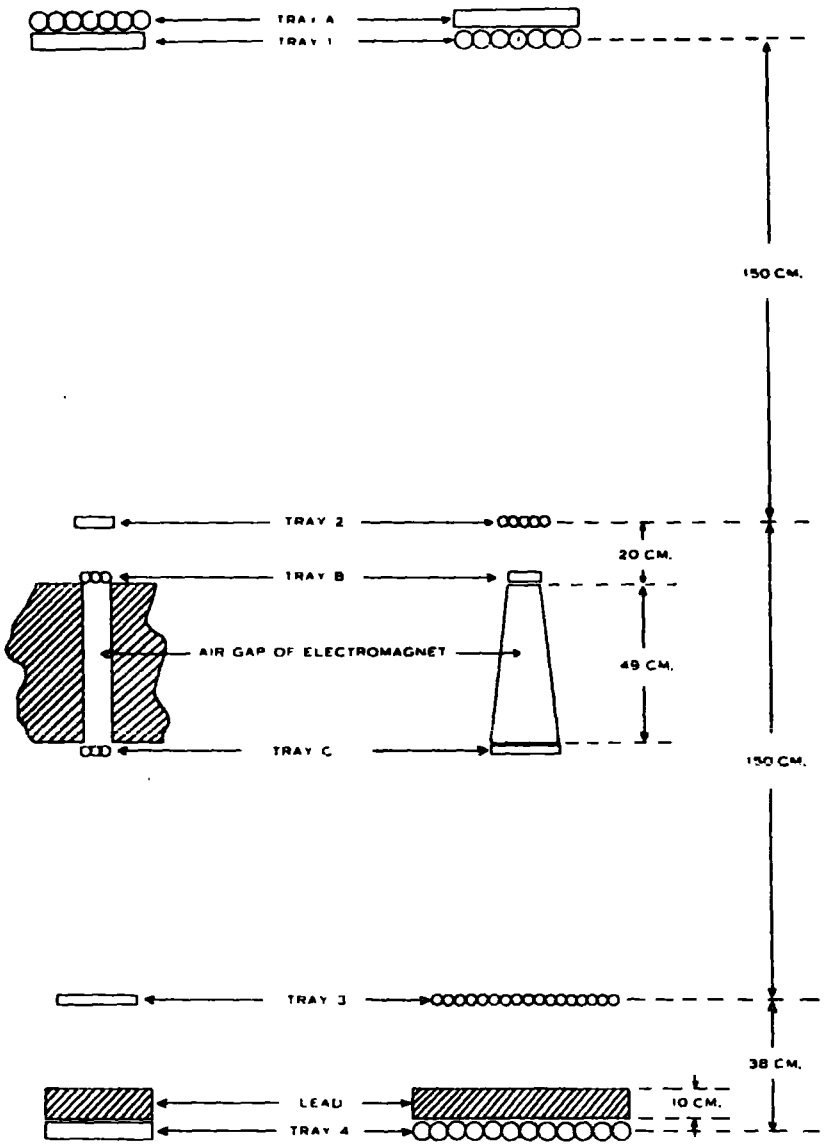

FIG. 2.2.1. The Spectrograph of CARO et al, 1950.- (the Melbourne spectrograph).

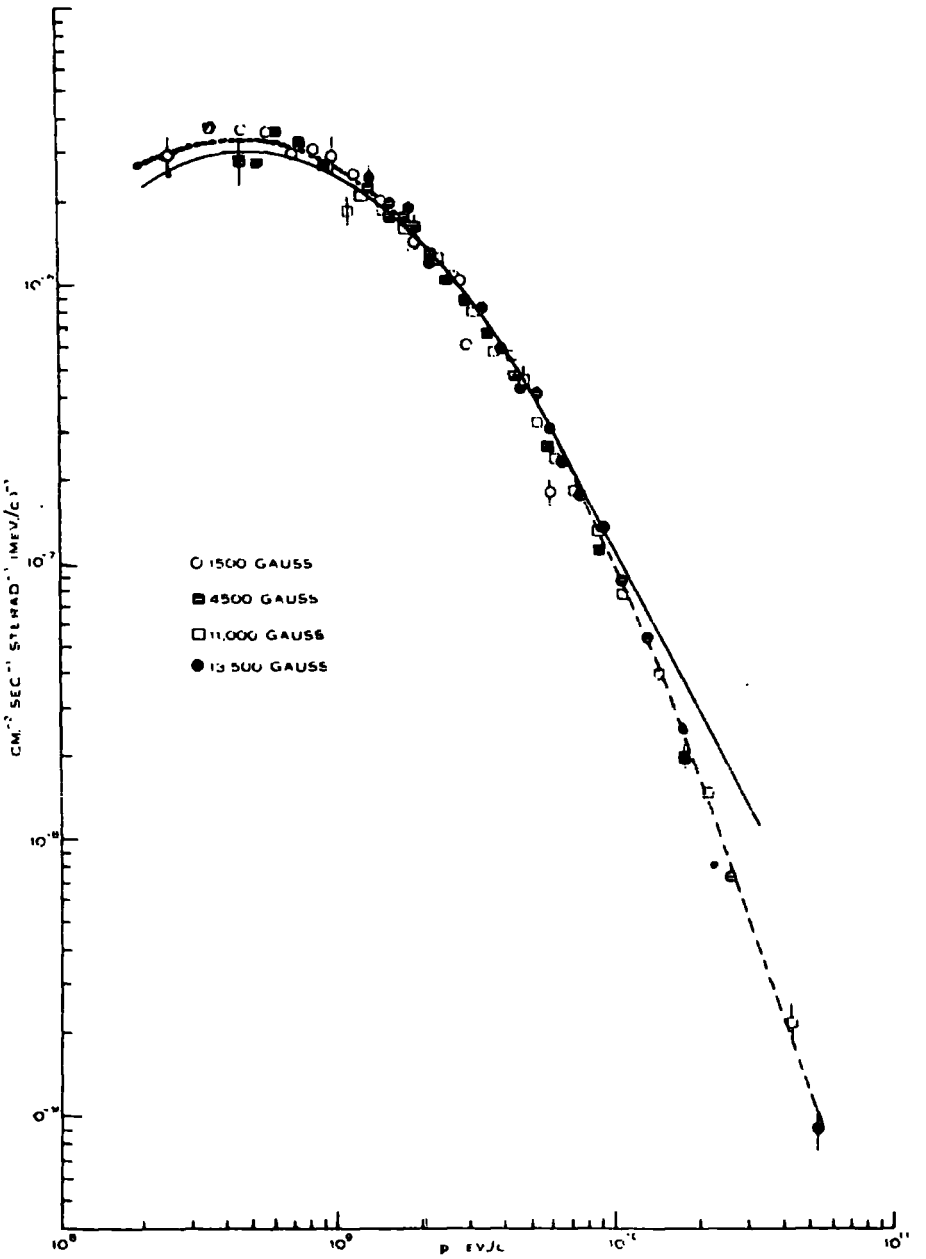

FIG. 2.2.2. The Spectrum of CARO et al, 1950, (dashed line), with that of ROSSI, 1948 (full line) for comparison.

discharged) were rejected (Rathgeber, 1960).

Glaser et al used cloud chambers as an alternative to geiger counters at the measuring levels. This reduced the uncertainty in location of the particle track from the diameter of a geiger counter to the effective diameter of the column of condensation drops after drift and mobility have been considered - e.g. as discussed by Lloyd and Wolfendale, (1955). A disadvantage of this instrument was the long dead-time after each observation (approximately 4 minutes) due to re-cycling and clearing of the cloud chambers. (Recent developments in the overcompression technique have reduced this time - French, 1959). The spectrograph is shown in Fig. 2.2.3 and results in Fig. 2.2.4. Rodgers (1957) and the latter section of the paper by Pine et al (1959) describe variations on this technique.

Owen and Wilson (1955) used a magnetic spectrograph with a much larger accepted flux (Fig. 2.2.5.). Each counter was connected to a hodoscope circuit and a photographic record made when a particle traversed all measuring levels. The mode of deflection measurement is shown in Fig. 2.2.6. Only single events were fully analysed, and the spectrum of these is shown in Fig. 2.2.7.

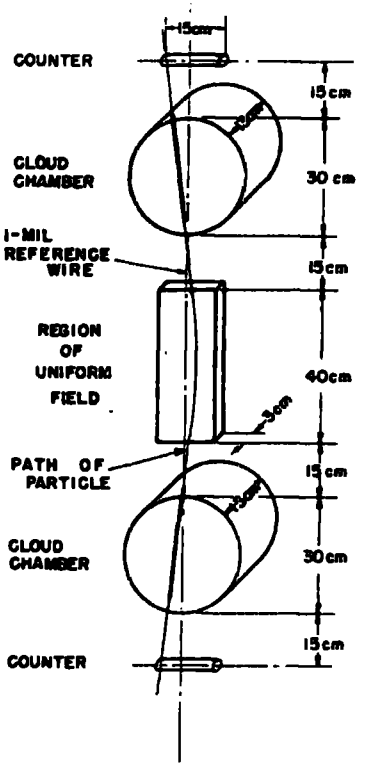

Arrangement of apparatus showing the path of a typical particle which passes through the two counters, two cloud chambers, and the region of uniform magnetic field. The 1-mil tungsten wire furnishes a reference direction for measuring angles in the photographs.

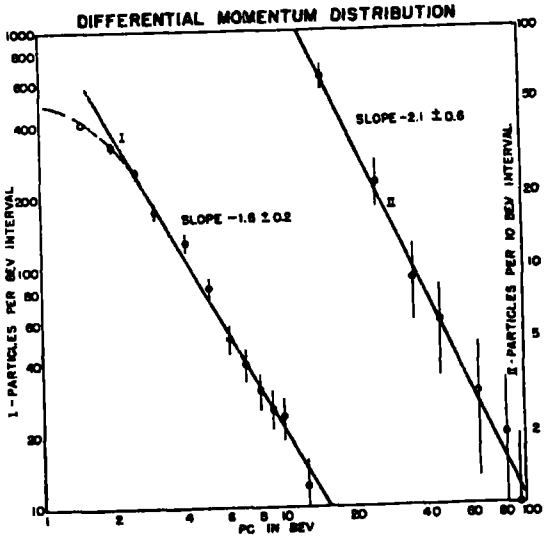

Logarithmic plot of total differential momentum distribution.

FIGS. 2.2.3. (left) and 2.2.4. (right). The spectrograph and Spectrum of GLASER, HAMERMESH and SAFONOV, 1950.

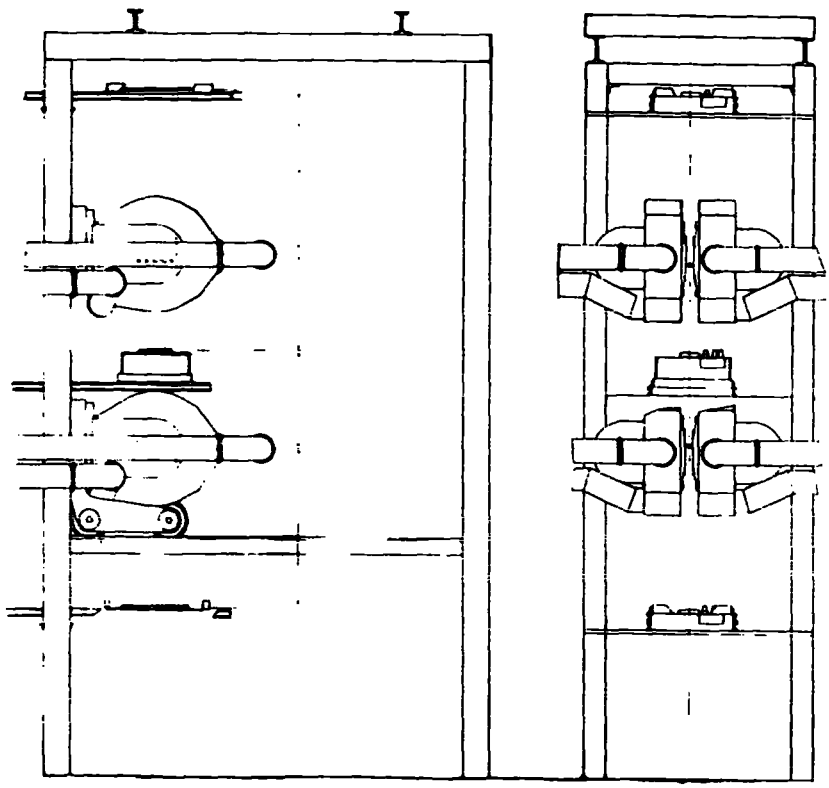

FIG. 2.2.5. The Manchester Spectrograph, as used by OWEN and WILSON. RODGERS et al (1957) added three flat cloud chambers adjacent to each counter tray.

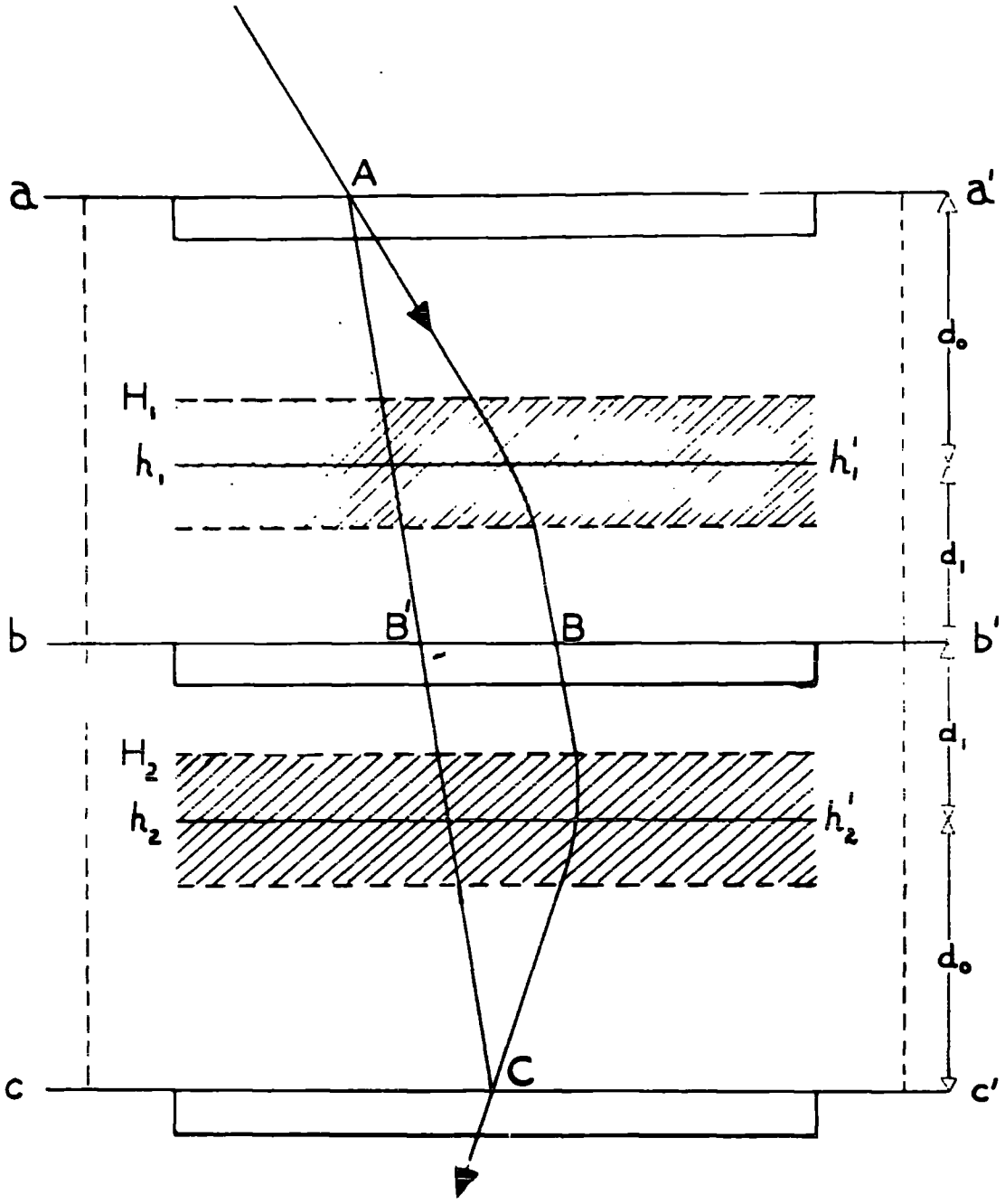

FIG. 2.2.6. The Principle of Particle Deflection Measurement of the Manchester Spectrograph.

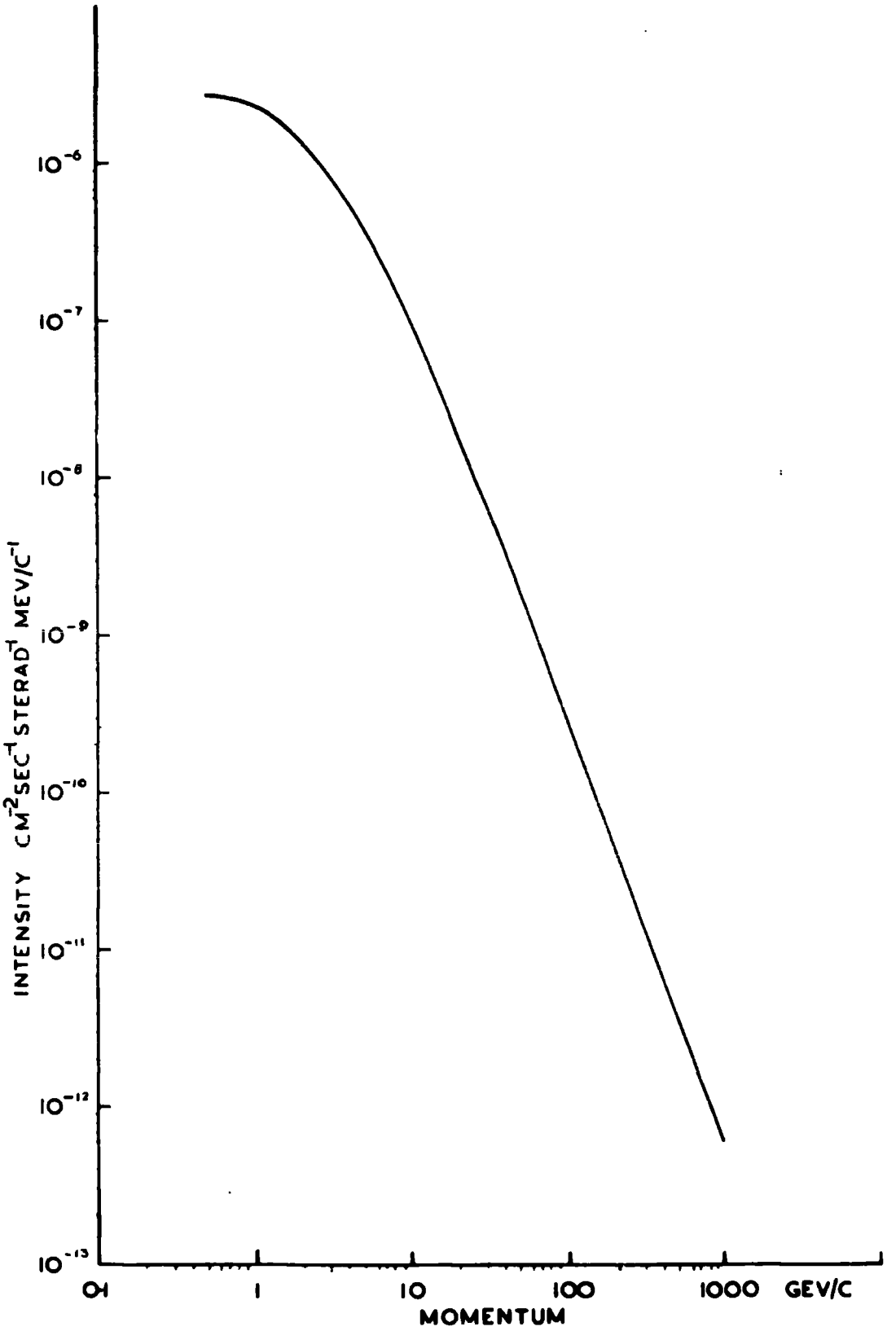

FIG. 2.2.7. The sea-level spectrum of Muons measured at Manchester by OWEN and WILSON (1955) and extended by RODGERS (1957).

One great drawback of this instrument was the tedium of reducing hodoscope results. The maximum detectable momentum was less than with Caro's instrument since only one layer of geiger counters was used at each measuring level.

The instruments of Pine et al (Figs. 2.2.8., 2.2.9.) and the Durham group are somewhat similar to that of Owen and Wilson, except that only one electromagnet is used. The latter mentioned instrument will be described in the next Chapter.

The most recent work is that of Allkofer (1959 and 1960) (Figs. 2.2.10 and 2.2.11.). This is not particularly accurate since the statistical accuracy is low, but is unique in that spark counters were used for particle detection and measurement.

2.3. Comparison of the Previous Measurements

The measurements of Caro et al and Owen and Wilson do not agree - Ashton (1959) has shown their probability of being consistent is less than 1%. One of the purposes of the present work was to resolve this difference, since an accurate measurement of the sea level flux is needed as initial data in other cosmic-ray investigations. The spectra of Caro and Owen and Wilson are plotted on the same scale in Fig. 2.2.12, and a comparison, due to

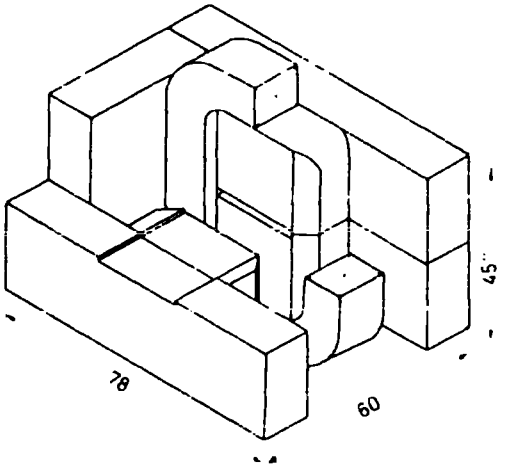

Cut away view of magnet and coil assembly. For clarity, one of the two symmetrically placed coils is not shown in the Figure. Also removed are half of one side and pole-face, and one return leg of the magnet. The slot leading to the center of the magnetic field is used for illumination and photography of the central cloud chamber.

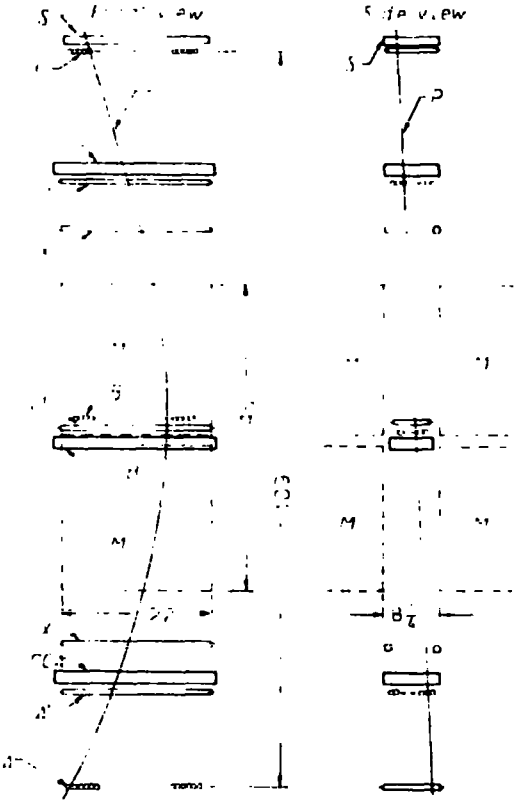

Arrangement of Geiger counters and cloud chambers, with illustrative particle trajectory.

FIG. 2.2.8 The Spectrograph of Pine et al, 1959.

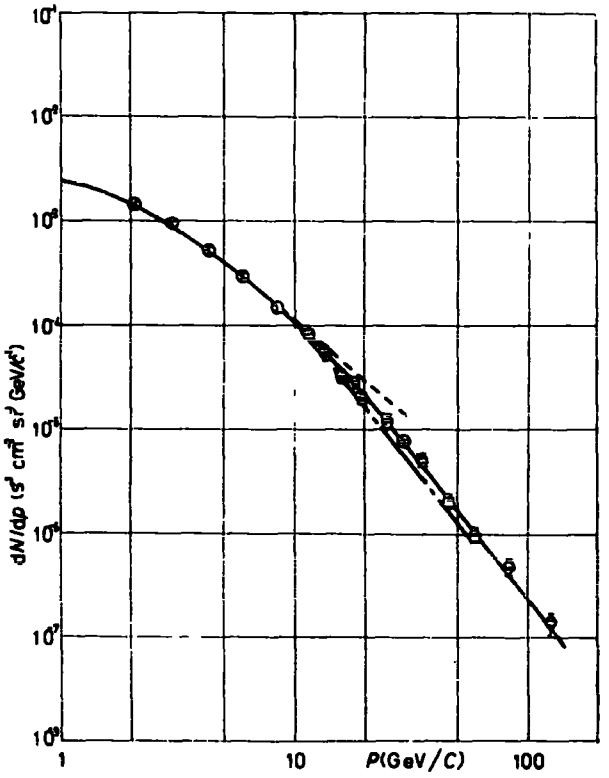

The differential μ-meson momentum spectrum. Key: ● This experiment, cloud chambers; O This experiment, Geiger counters; ---- Rossi (5); —— Owen and Wilson (1); – – – Caro *et al.* (2).

FIG. 2.2.9 . The Differential Muon Spectrum of Pine et al, 1959.

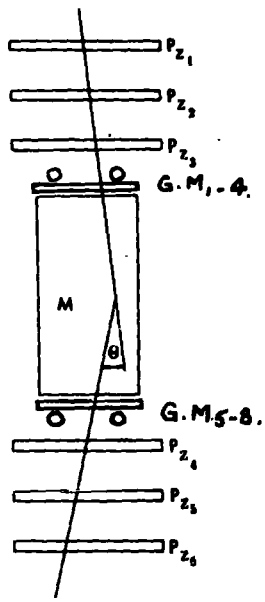

FIG. 2.2.16. Alikofer's Spectrograph (1959).

P_{Z1} etc. are spark counters used both to detect and to record particles. G.M$_{1-4}$ etc. are geiger counters, collectively hodoscoped to signify tracks not passing through the homogeneous region of magnetic field. Such records are rejected.

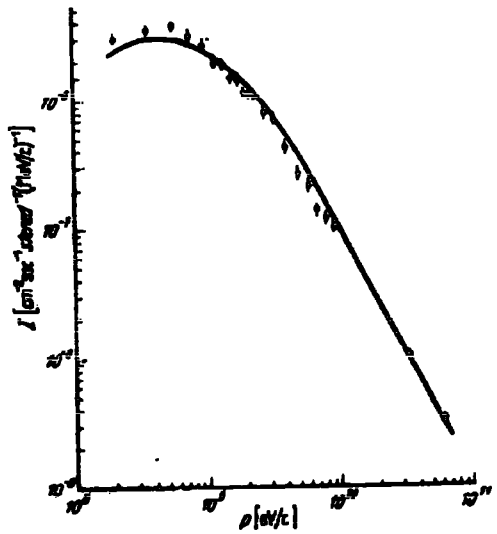

FIG. 2.2.11. Co-ordinates of the Spectrum of ALLKOFER, 1960, measured using Spark Counters, with the curve of OWEN and WILSON.

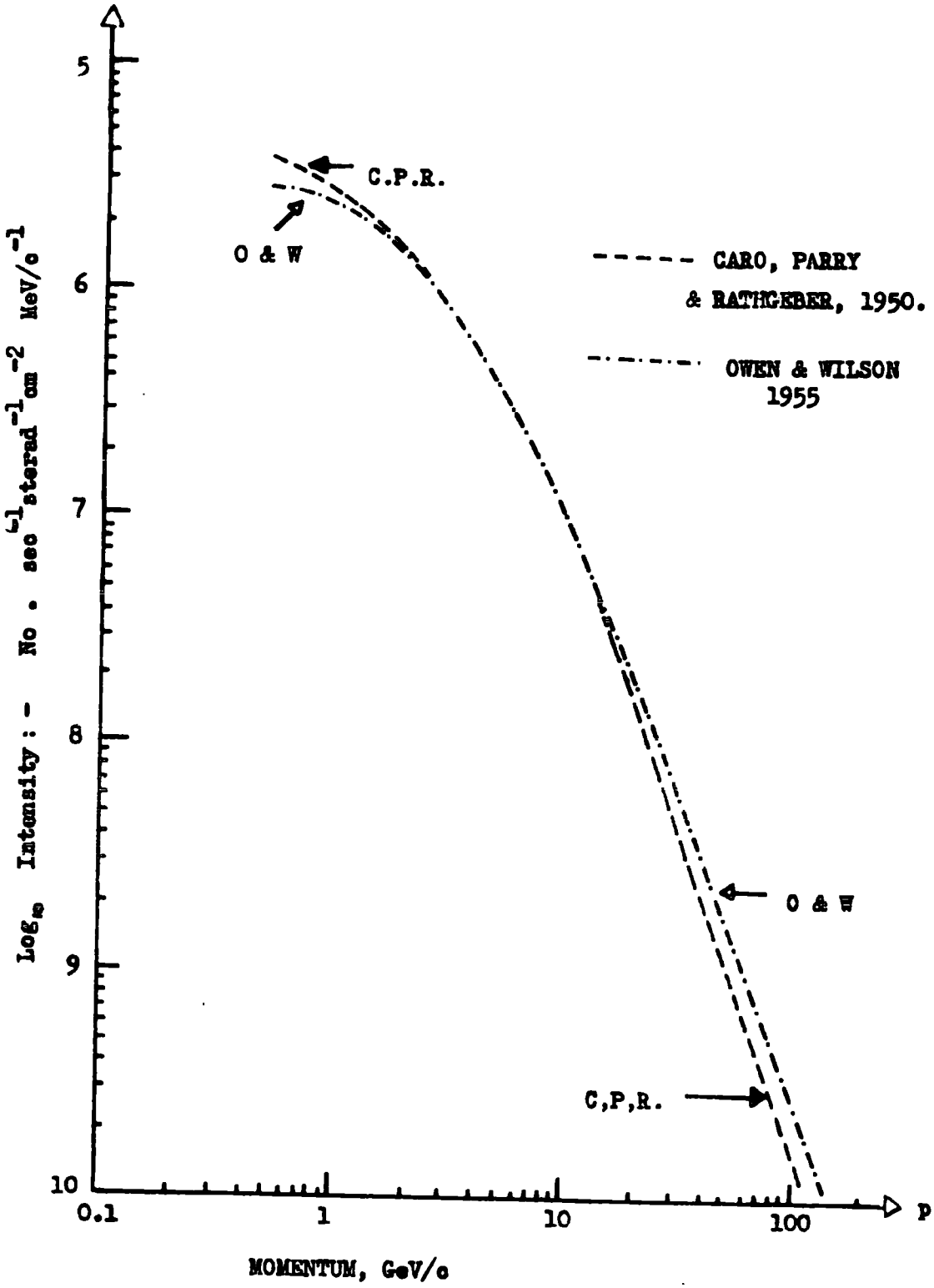

FIG. 2.2.12 Plot of the Spectra of CARO et al and OWEN and WILSON, showing differences.

Rodgers, who extended Owen and Wilson's work, in Fig. 2.2.13. It is believed that this comparison may be based on other than the published points of Caro et al.

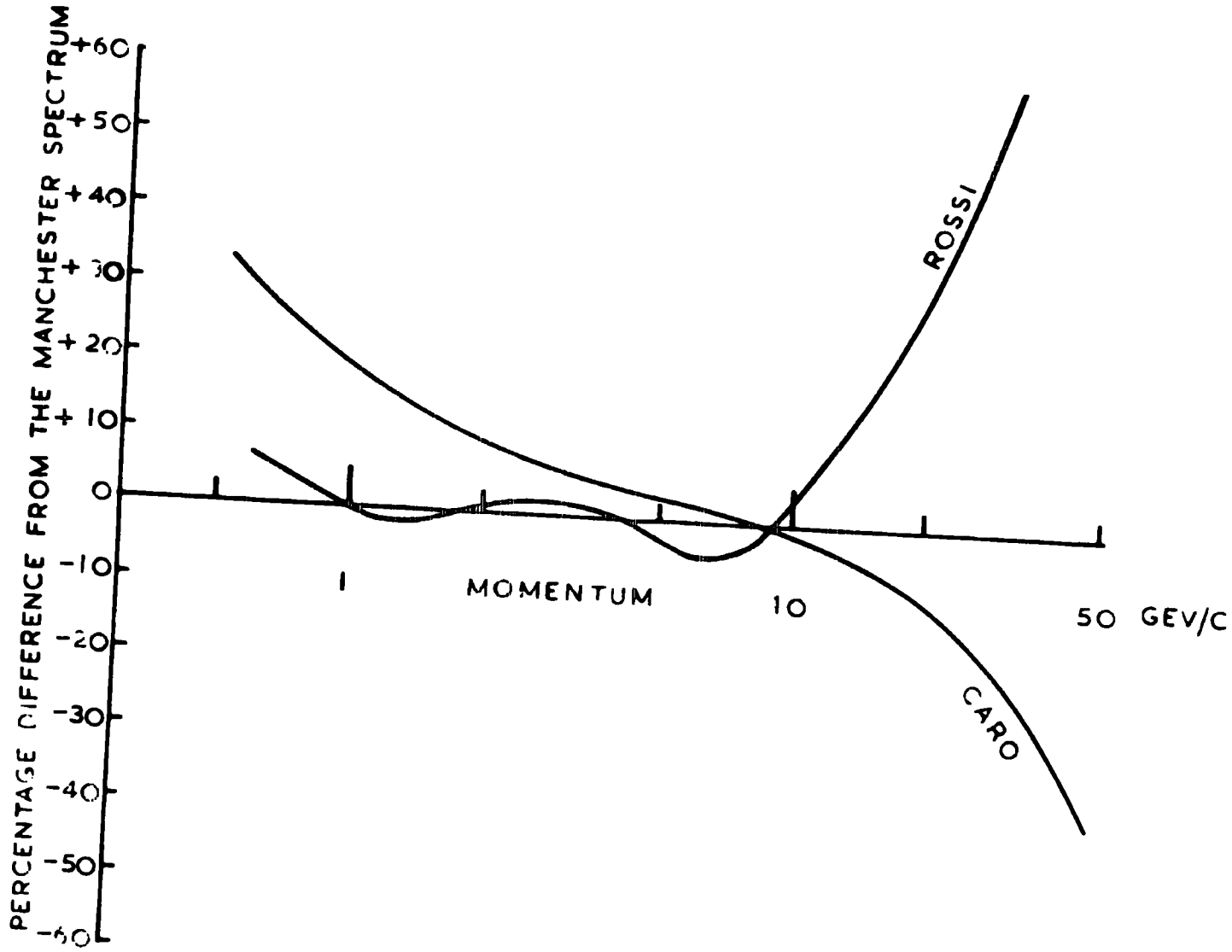

FIG. 2.2.13. Comparison of the Manchester Spectrum with other workers. Anomalies are clearly shown.

Chapter 3.

The Durham Spectrograph

3.1. General Features

This instrument uses one of the two electromagnets of the Manchester Spectrograph (Hyams et al, 1950) arranged to collect a high cosmic ray flux and to have a high resolution (Fig. 3.1.1). The resolution of the geiger counter trays A,B,G,C,D (termed the 'G-M system') may be increased by a factor of approximately 40 by use of stacks of neon flash-tubes, 0.72 cm in diameter, each stack containing 8 layers (Ashton, 1959). These are 'triggered' only when selected events have been recorded by the G-M system. Levels A,B,C,D of both types of detector form 'measuring levels', and a measurement of the particle momentum is obtained from them. (Sections 3.4 and 3.7).

Tray G forms a 'location level' and simply eliminates any scattered trajectories passing through any part of the pole pieces. The greater part of this work deals with experiments with the G-M system to measure the momentum spectrum, and corresponding analysis.

The flash-tube section of the instrument was used only to resolve more fully events recorded by the G-M system as being multiple, i.e. two or more different counters were discharged at any one of the measuring

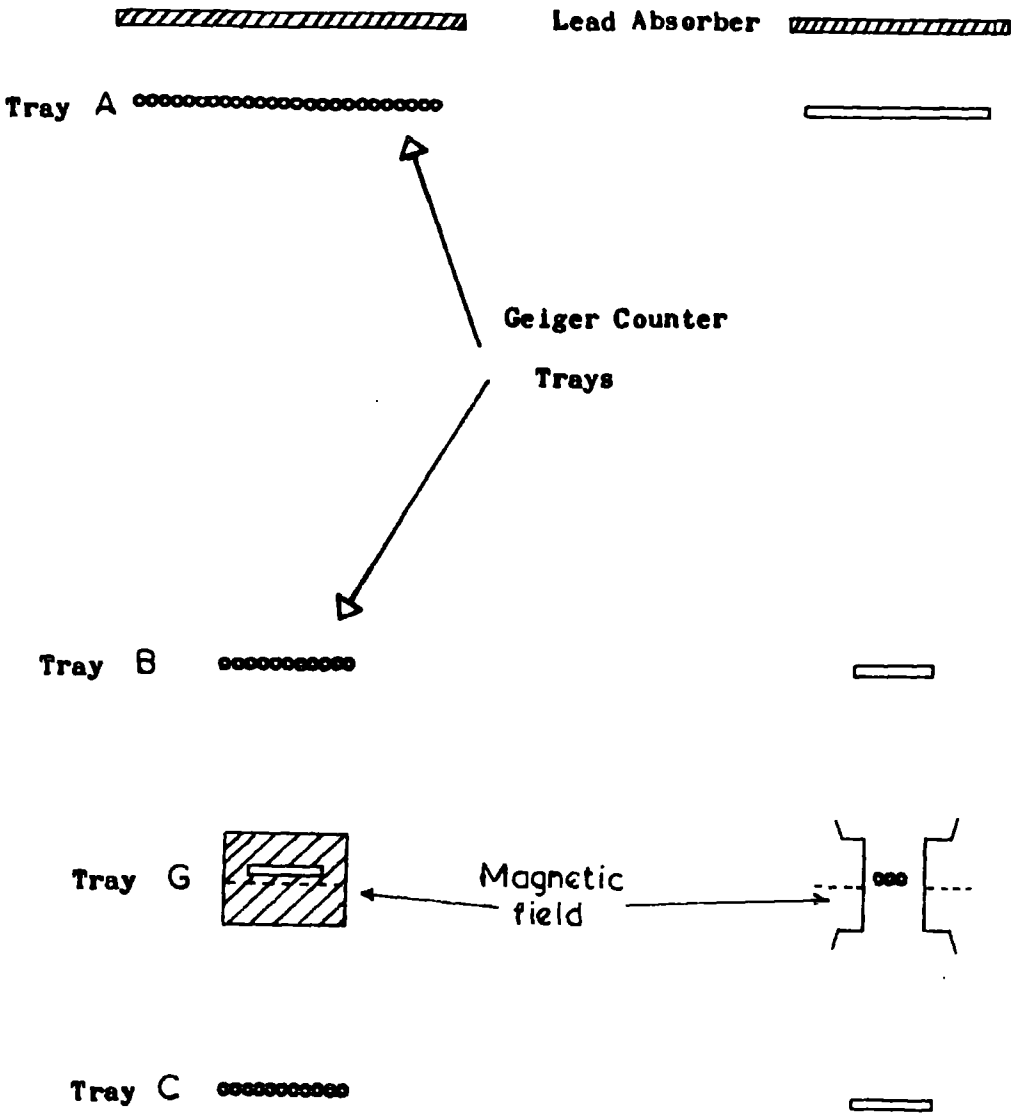

FIG. 3.1.1. Scale Drawing
of the Durham Spectrograph

levels. The instrument has the properties already detailed in Table 2-2-1.

3.2. The Electromagnet

The electromagnet has already been described by Hyams et al, 1950, and will not be described in detail here. The line integral of flux over distance, $\int_{\ell} H.dl$, active upon a charged particle traversing the gap, was determined by two independent methods, one using hanging wires, performed by Mr. M. Gardener, the other using a search coil, performed by Dr. J.L. Lloyd. The two agree closely - the resultant plot of $\int H.dl$ versus current due to Lloyd (adopted here) being shown in Fig. 3.2.1.

3.3. The Detecting System

The geiger counters are commercially manufactured types (20th Century Electronics) arranged as shown (Fig. 3.1.1.). They consist of glass tubing, 3.6 cm in diameter, with a carbon coating inside forming the cathode, and a wire anode. The gas filling is of the self-quenching type, though to reduce the dead time of the instrument the discharge is quenched by means of electronic quenching units attached to each counter. The counter spacing within the trays is 3.82 cm. A fifth layer of Geiger counters, tray G, located between the magnet pole pieces ensured that only particles were accepted which traversed the air between the magnet pole pieces and were not scattered by the magnet structure.

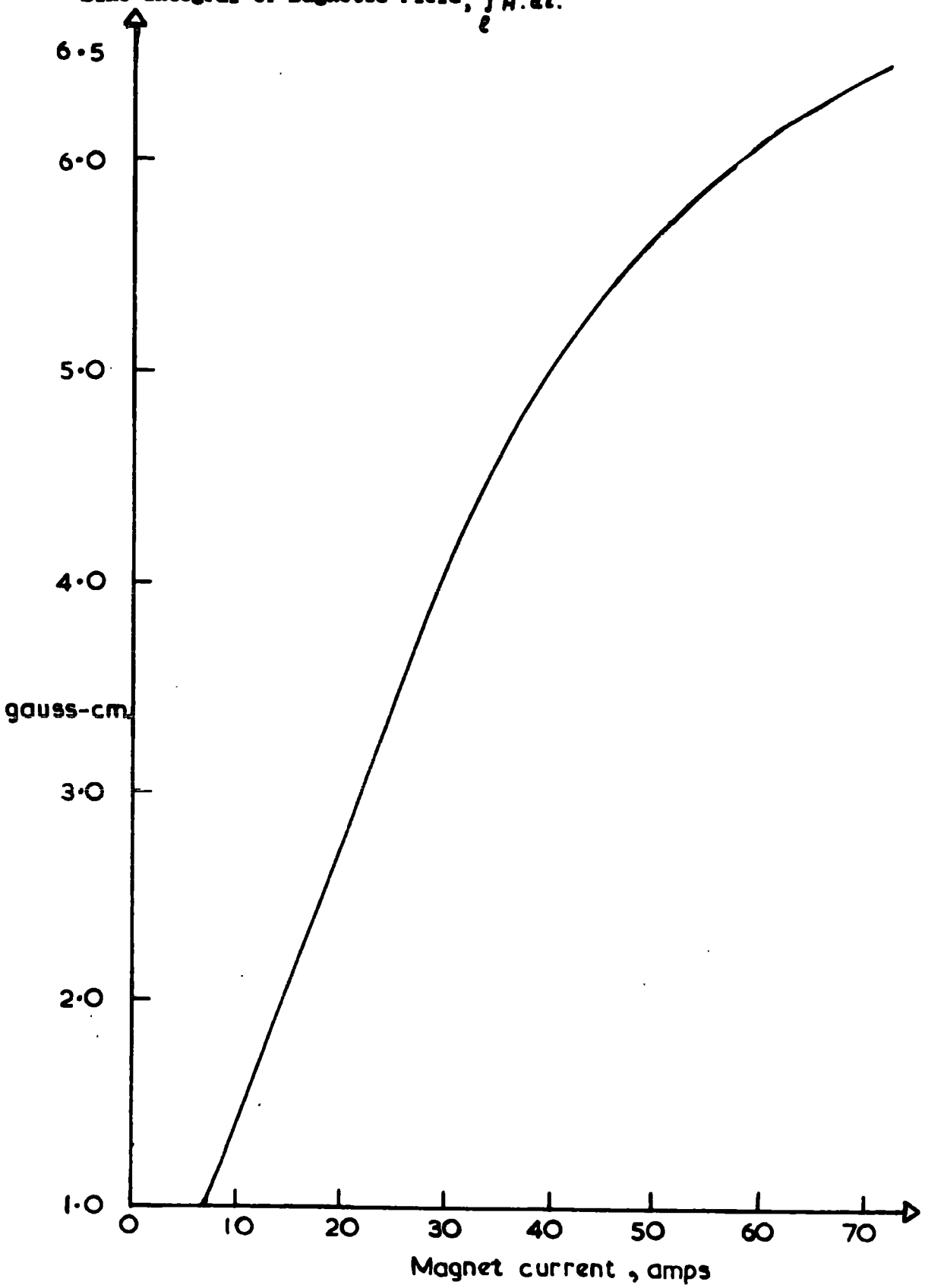

FIG. 3.2.1. Variation of the Line Integral of Magnetic field with magnet current

3.4. The Recording System and Mode of Momentum Measurement

Each quenching unit is connected to one input of the electronic equipment - described in detail elsewhere (Jones, 1961) - only briefly described here.

When a coincidence (detected by a standard Rossi type circuit) occurs between any one (or more) counters in each of the measuring levels, a 'categorised' output pulse is produced, proportional in amplitude to the inverse of the particle momentum, by a small analogue computer. This is termed a 'category pulse', and has one of a series of allowed values of amplitude corresponding to different configurations of counters triggered. In effect, each geiger counter is assigned a number corresponding to the distance, in counter spacing units, from a line 1.6 cm to the left of the extreme left-hand counters in trays A and D. Such numbers are shown in Fig. 3.4.1. When any counter is triggered, the electronic circuits produce a pulse proportional to its number plus 6 (the addition of '6' being necessary for design reasons) of appropriate polarity-trays A and D give positive output, trays B and C negative output. Addition of such pulses gives a final category pulse N, which corresponds to the combination:-

$$N = n_A + n_D - n_B - n_C.$$

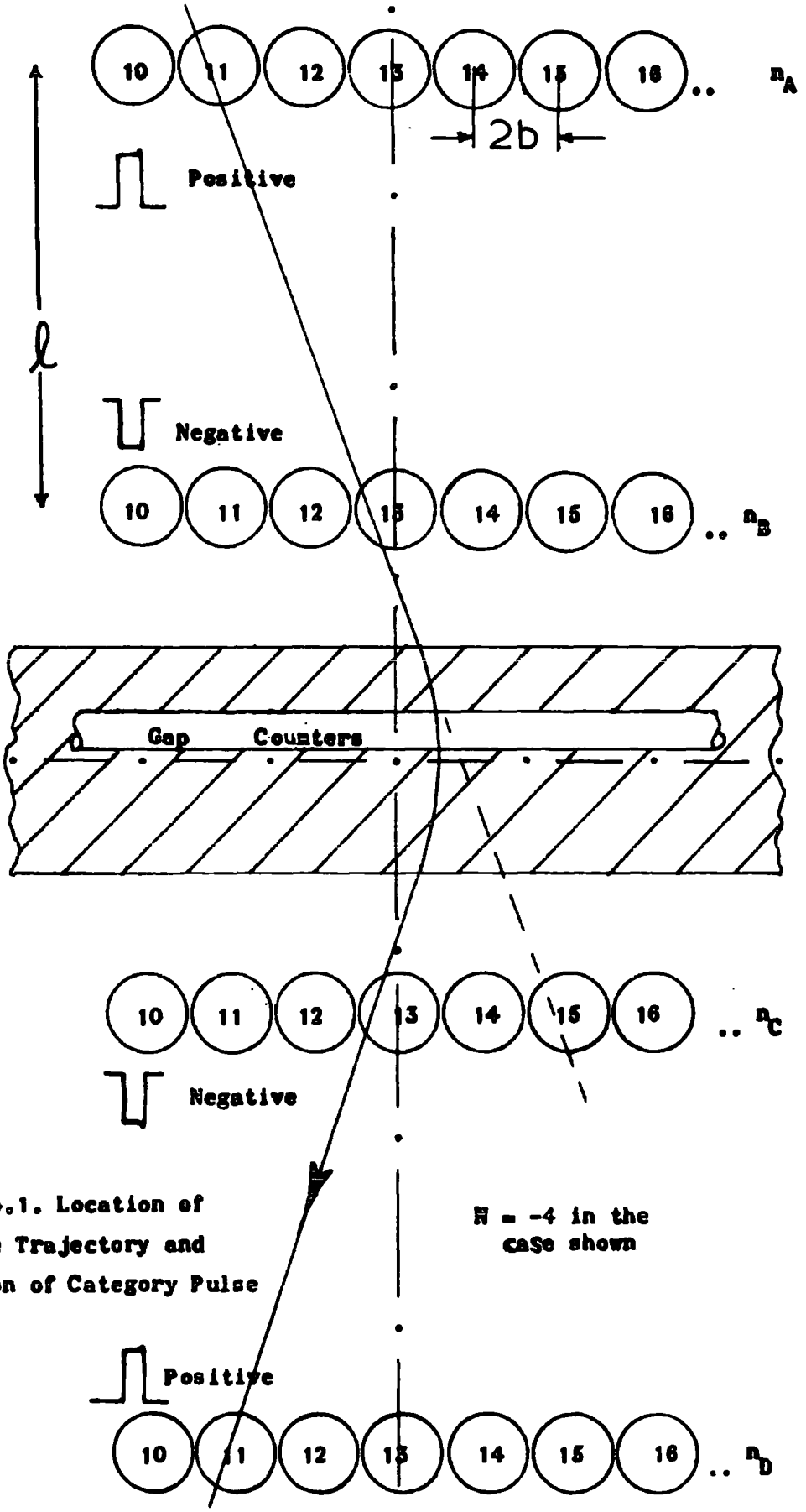

FIG. 3.4.1. Location of Particle Trajectory and formation of Category Pulse

N = -4 in the case shown

By simple geometry N may be shown to be the displacement in counter spacing units over the arm l, i.e. AB or CD (equal for all practical purposes), in counter spacing units.

Such category pulses were recorded in the present work using a commercial (Furzehill) oscilloscope, and photographed. Exposure of each frame of H.P.S. film was for two minutes, and the face of the cathode ray tube, which carried a watch and a scale marked in category numbers, was recorded on each frame. Timing was by means of an electromechanical timing system and standard clock. The films were analysed by projection and visual analysis, the number of each category in which events had occurred being recorded. Typical records are shown in Fig. 3.4.2. A spread of events about the actual divisions on the scale was observed - however, this rarely amounted to more than one-third of a category, and it was possible to assign events to their correct categories. Events of category greater than 15, if visible, were ignored. A correction factor for possible superposition of events of given category during the exposure time of any frame was applied and is detailed in Chapter 4. The instrument was checked at 24-hour intervals during the collection of data, E.H.T. and H.T. voltages and total counting rates for individual counter trays were checked

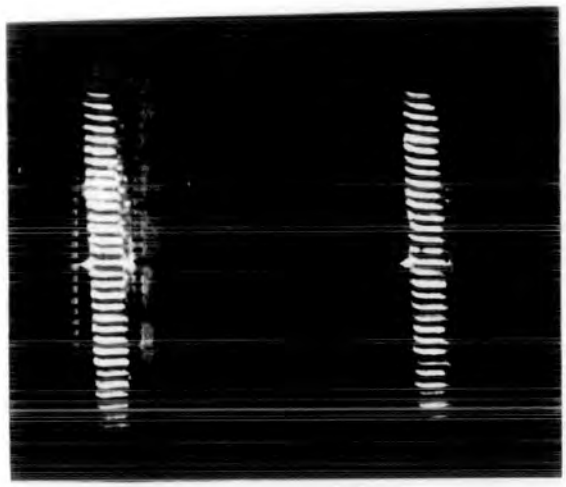

2-fold coincidences (Used to check alignment between pulses and scale)

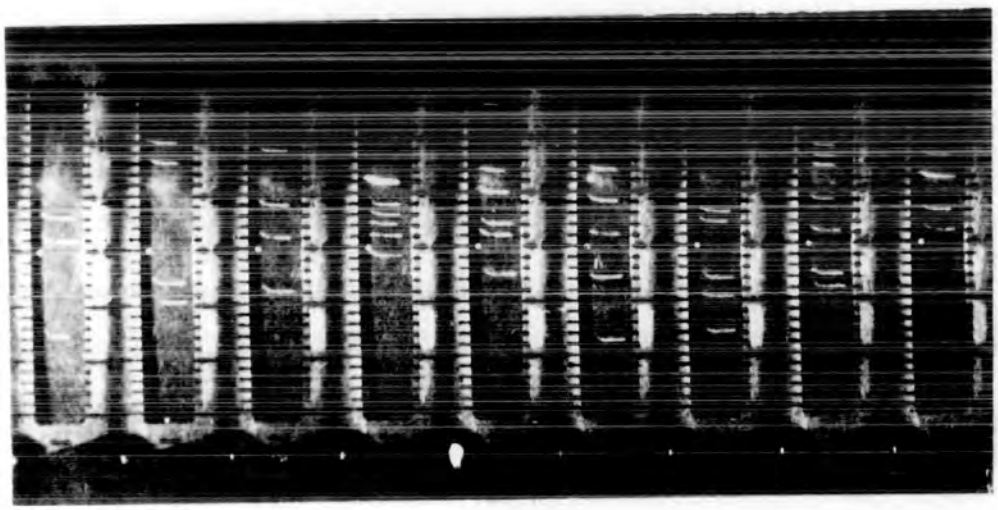

5-fold coincidences

FIG. 3.4.2. Typical Momentum Analyser Records

and maintained within tight limits.

The recording system has one further important characteristic - a discriminator separates 'multiple event' pulses and they are eliminated when a single event spectrum is required by modulating the oscilloscope electron beam. The effect of excluding such events was investigated and will be discussed in Chapter 5.

Category numbers may be converted into corresponding momenta as follows:-

It is well known that:-

$$pc_{(eV)} = 300\ H\rho_{(gauss-cm)}$$

where p is the momentum of a charged particle, H is the magnetic field, ρ is the radius of curvature of its trajectory, and c is the velocity of light.

Thus, over any incremental length dl, and corresponding angular deflection $d\phi$,

$$pc = 300\ \frac{H_{l}.dl}{d\phi}$$

$$\text{or}\quad pc = \frac{300\int H_{l}\,dl}{\phi}$$

If now Δ,N correspond to the displacement over arm ℓ in cms, and counter spacing units, respectively, then:-

$$pc = \frac{300\ell\int Hdl}{\Delta},$$

since $\phi = \frac{\Delta}{\ell}$, and

$$pc = \frac{300\ 1 \times 3.8 \int Hdl}{N} = \frac{K'}{N}$$

or $$p_{(GeV/c)} = \frac{K'}{N} \qquad (i)$$

where K' is constant, equal to 300 l x 3.8 $\int$Hdl, for given exciting current, i.e. given $\int$H.dl.

Thus observed values of N may easily be transformed into corresponding values of momentum, with consideration of small correction factors in certain cases, which will be considered in Chapter 4.

3.5. Alignment

The counter trays have been aligned by a straightforward method using a plumbline, lateral location of the counter trays being by means of suitable slots in metal strips arranged to form locating jigs. The vertical alignment was checked by Mr. M. Gardener by placing an artificial scatterer in the centre of the Magnet gap, below the gap counters, with no field, and observing the number of particles with positive and negative deflection (from corresponding sign of category number). These were plotted to form a histogram, and it was found that the mean occurring was very close to zero deflection, showing that the alignment was correct.

3.6. The Nature of Particles Accepted by the Instrument

It has already been pointed out that cosmic rays consist of a soft electronic component and a hard mesonic and nucleonic component (Section 1.1).

In the experiments to be described the instrument has been operated with varying thicknesses of lead above tray A. This filters out the soft component, and also affects the hard component. From a knowledge of the relative interaction lengths of muons, pions and protons it can be seen that some of the pion and proton fluxes will be filtered out before reaching the instrument (even with no lead absorber) due to the thickness of absorbing matter above the magnet, whereas the muon flux is virtually unaffected. Also, since the intensity of pions at momenta lessthan 20 GeV/c is small (see Section 7.3) only muons and protons will in general be recorded. The correction of the intensities of each for the absorbing material, and the subtraction of the proton component from the muon component will be dealt with in Chapter 4.

3.7. The Flash-Tube Spectrograph

It has already been mentioned in Section 3.1. that the limited resolution of the geiger counters was extended by addition of flash-tubes. The characteristics of these have already been described fully. (Gardener et al, 1957,

Kisdnasamy, 1958, Ashton et al, 1958, Ashton, 1959, Coxell, 1961). In the present work the flash tube instrument has been used to investigate the nature of multiple events. Pulses corresponding to such events were fed to the flash-tube trigger circuits and an 8 KV/cm. pulse applied across each layer of flash-tubes. Those containing electrons flashed, such flashes being photographed on Ilford HPS film. A dead time of 2 seconds was imposed electronically after passage of a particle to allow de-ionisation to take place, and cycling of the recording equipment.

The films were analysed by projection onto a full size diagram of the flash tube assembly and the position of the best line through the observed flashes recorded. Measurement was made on a scale marked along the horizontal central axis of each tray (Fig. 3.7.1.) - the zero of each scale corresponded to the extreme left hand edge of the flash tube stack and was the line from which the deflections Δ, etc., were measured. The displacement measured over an arm l_1 was obtained by combination of the four known positions of the particle track, taking into account an arbitrary constant Δ_0, allowing for the fact that the arbitrary zeros of each tray are not vertically aligned. Δ_0 is equal to 65.01 tube spacing

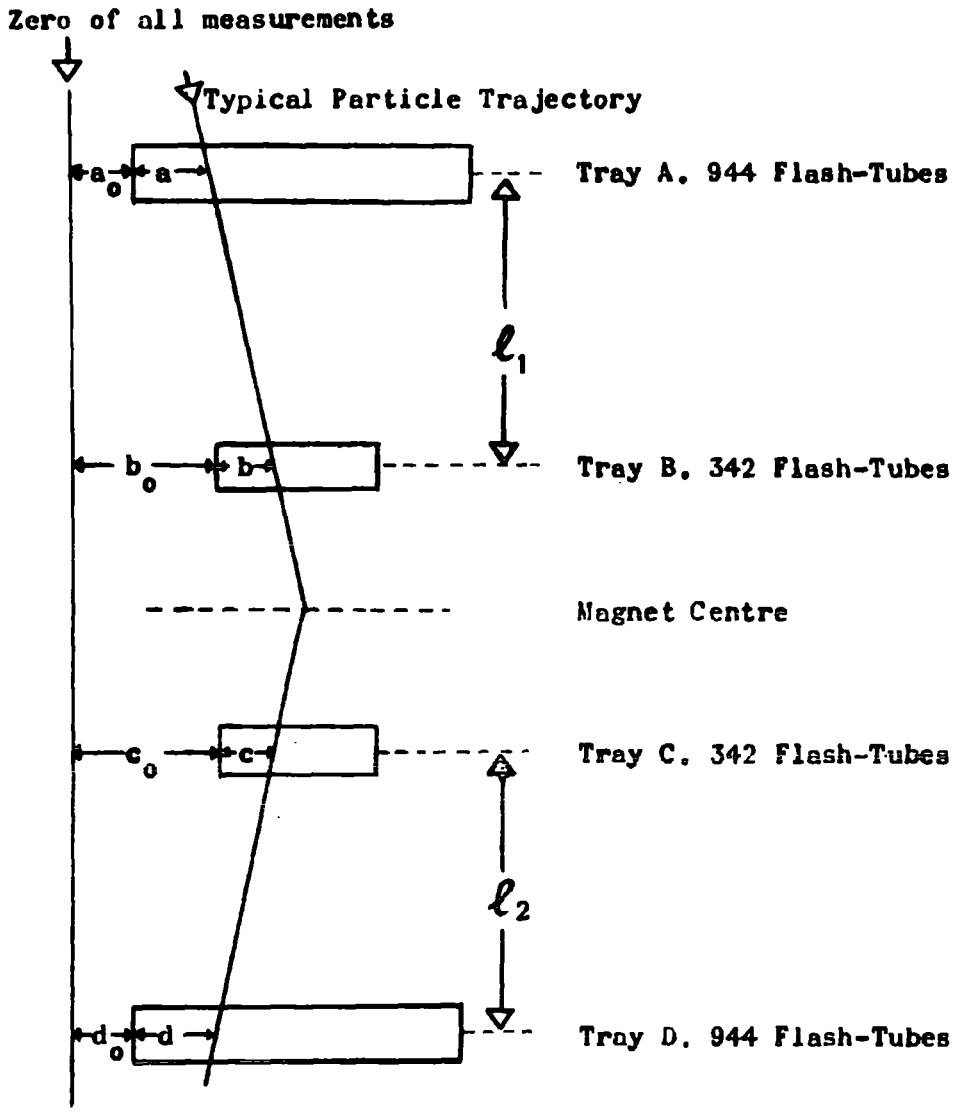

FIG. 3.7.1. The Flash-Tube Spectrograph,

Simplified, showing Mode of Deflection Measurement.

units (0.80 cm) and has been found by direct measurement from the aligning plumblines.

Δ is given by the equation

$$\Delta = (a-b) - \ell_1/\ell_2 (c-d) - \Delta_o,$$

over the arm l_1. (In the case of the flash-tube spectrograph, the arms l_1, l_2 are sufficiently different to make correction necessary).

The momentum, p, is calculated exactly as in the case of the geiger counter data, except that the constant K' has a different value. (Equation 3.4(i)).

3.8. Magnetic Bias - The Acceptance Function

It has already been mentioned in section 3.4. that particles recorded by the instrument within a given momentum range (corresponding to categories 1 to 15) are recorded as a pulse of amplitude proportional to 1/p. It may be seen from Fig. 3.8.1. that the accepted flux for each category varies according to the value of the particular category, N, falling as N increases. It is therefore necessary to evaluate the relative acceptance of those categories which will be used in later investigations and to formulate a series of 'acceptance factors', by which the number of events observed in any category may be multiplied to give an effective acceptance equal to that of the full aperture of the instru-

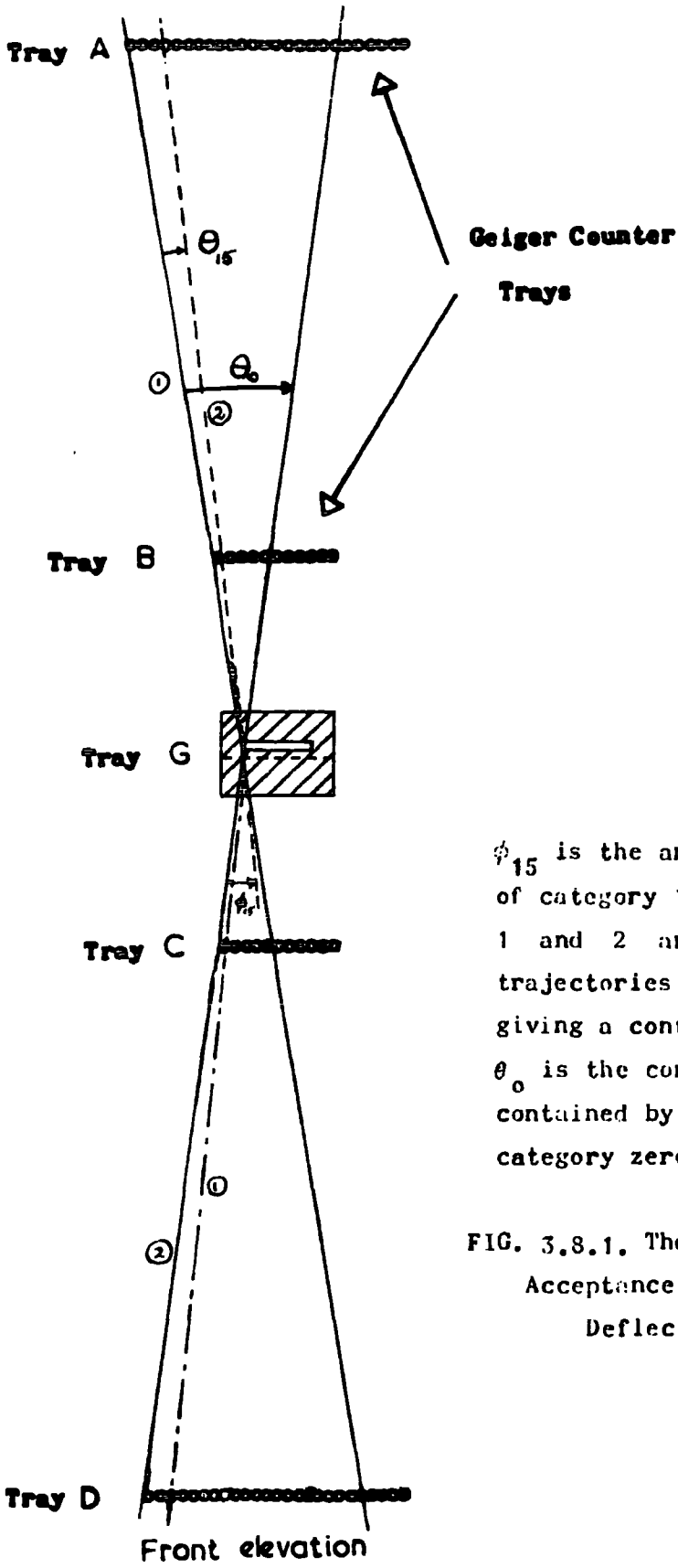

ϕ_{15} is the angular deflection of category 15, trajectories, 1 and 2 are the limiting trajectories for this deflection, giving a contained angle θ_{15}. θ_0 is the corresponding angle contained by particles of category zero.

FIG. 3.8.1. The Variation of Acceptance with Angular Deflection, ϕ.

ment.

Investigation of the required function connecting accepted flux and category number was undertaken by two methods - firstly using a geometric scale drawing (in two dimensions) of the instrument, and secondly by analytical considerations involving certain approximations. The former involves experimental errors, the latter errors of approximation. The former method of investigation performed by the author is described here, details of the latter methods, investigated by other workers, are given in a paper in preparation. In effect, the problem reduces to that of finding the total solid angle subtended to the cosmic ray flux, as a function of angular deflection. Further, the variation of acceptance with small change in angular deflection within a given category or configuration of counters is also required.

Firstly, the spectrograph dimensions were obtained by direct measurement. The sensitive length of the gap counters was determined by a radioactive probe method of investigating counter efficiency as a function of position on the counter (Fig. 3.8.2.). The sensitive length of the counter was taken to be the width of the rate/position curve at half height. Each of the three gap counters was investigated separately, and a mean effective length obtained ($25.04 \pm .10$ cm).

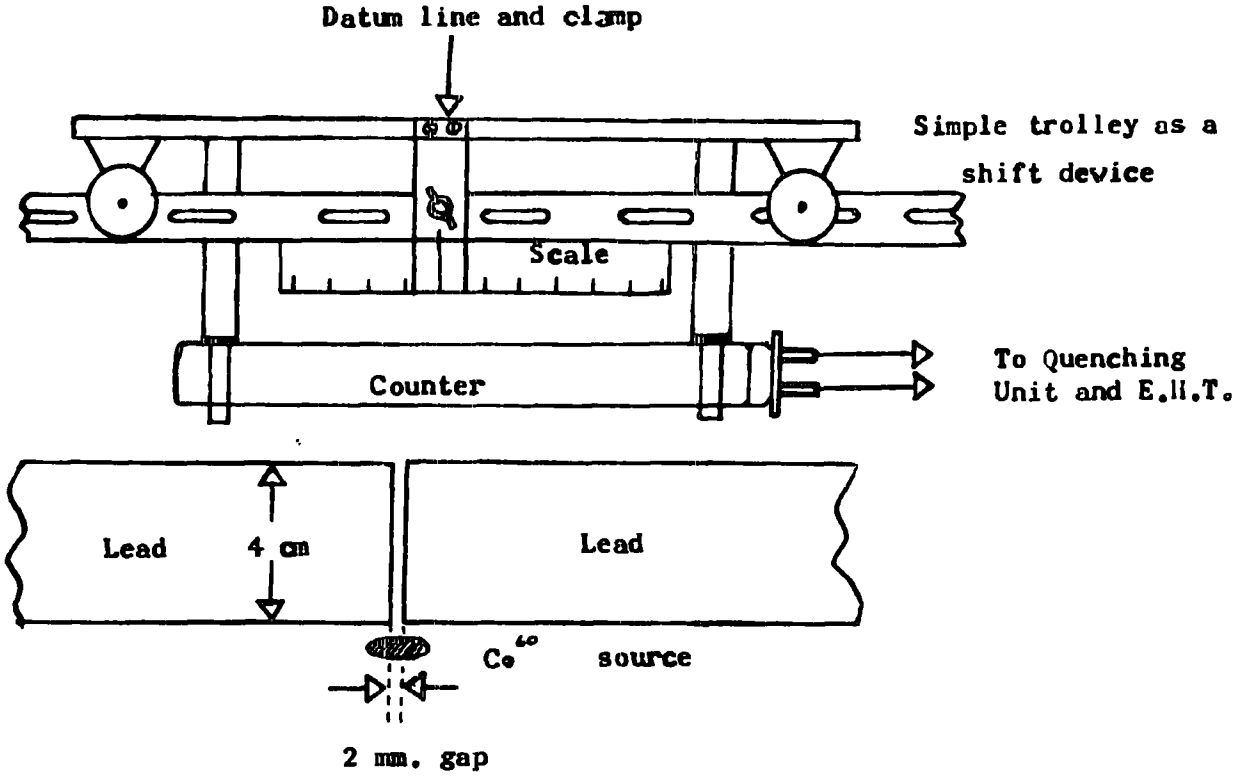

FIG. 3.8.2. Radioactive probe method of Determining the Sensitive Length of the Gap Counters

From the dimensions an accurate scale drawing was made of the instrument in the east-west plane. Two perspex arms, with fine datum lines ruled along their centres, were mounted in such a way as:-

(a) to enable the angle between them to be fixed at any given value up to approximately $16\frac{1}{2}^{o}$ (Category 15)

(b) to enable the assembly to be pivoted above the scale drawing, in the same plane.

The angle swept through by the top arm is measured on a linear scale. The whole assembly is shown in Fig. 3.8.3.

The procedure adopted to determine the accepted flux for any angular deflection ϕ was:-

(a) ϕ was set on the two perspex arms.

(b) For a given position along a scale marked along the gap counter axis (the arms pivoting about the magnet axis), the integral 'sensitive length' recorded on the linear scale was found. 'Sensitive length' is defined as that section of the scale corresponding to a simulated particle trajectory passing through sensitive sections of one counter in each of the four measuring trays. 'Sensitive' and 'insensitive' angles, θ, and corresponding scale readings were obtained by direct observation. This was repeated for several positions along the 'G' counter axis and a graph plotted of acceptance angle versus position on G. This was integrated numerically to give

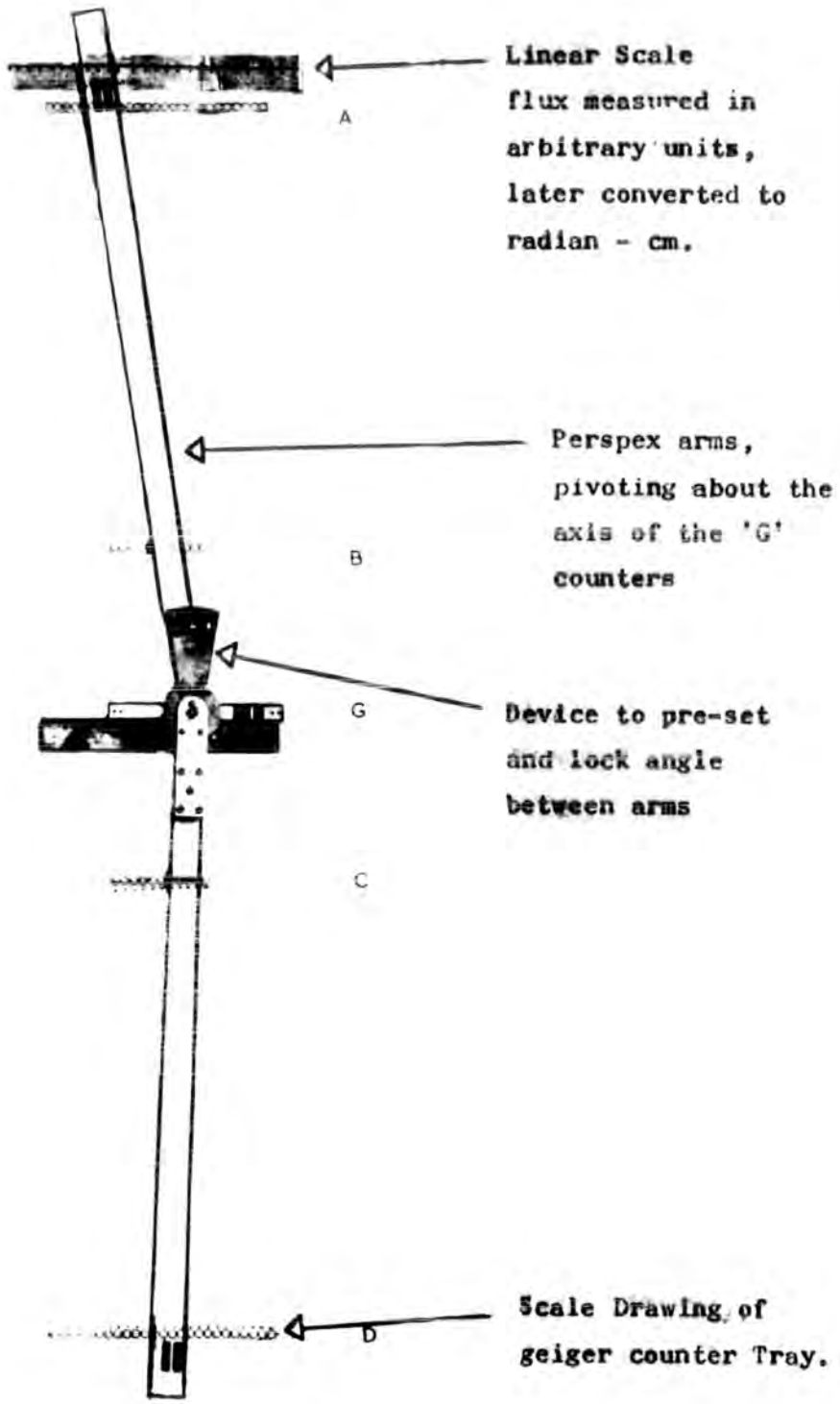

FIG. 3.8.3. Equipment used for Graphical Determination of the Acceptance Function.

the acceptance of the particular category considered. (c). Procedure (b) was repeated for a series of different values of ϕ. The units were (on the full scale instrument) cm. radian units. By multiplying the accepted flux in the E-W plane by the constant acceptance (flux) in the N-S plane (only a function of counter length and counter diameter) the three-dimensional accepted flux was obtained.

From a series of investigations in the range $-.0198 < \phi < .0198$ radians an 'elementary function' curve, relating ϕ and accepted flux within any category, was obtained - this is shown in Fig. 3.8.4.

The median acceptance angle with regard to flux was determined from this 'elementary function' curve by numerical integration, and was found to be 0.0073 radians. This is a measure of the uncertainty in angular deflection measurements within any category - in the case of category 0 the corresponding momentum is defined as the 'maximum detectable momentum'. See Table 2-2-1.

Determination of Total Accepted Flux.

The variation with deflection angle of flux accepted by any given series of four counters is given by the function described above. However, the acceptance of different configurations of four counters detecting

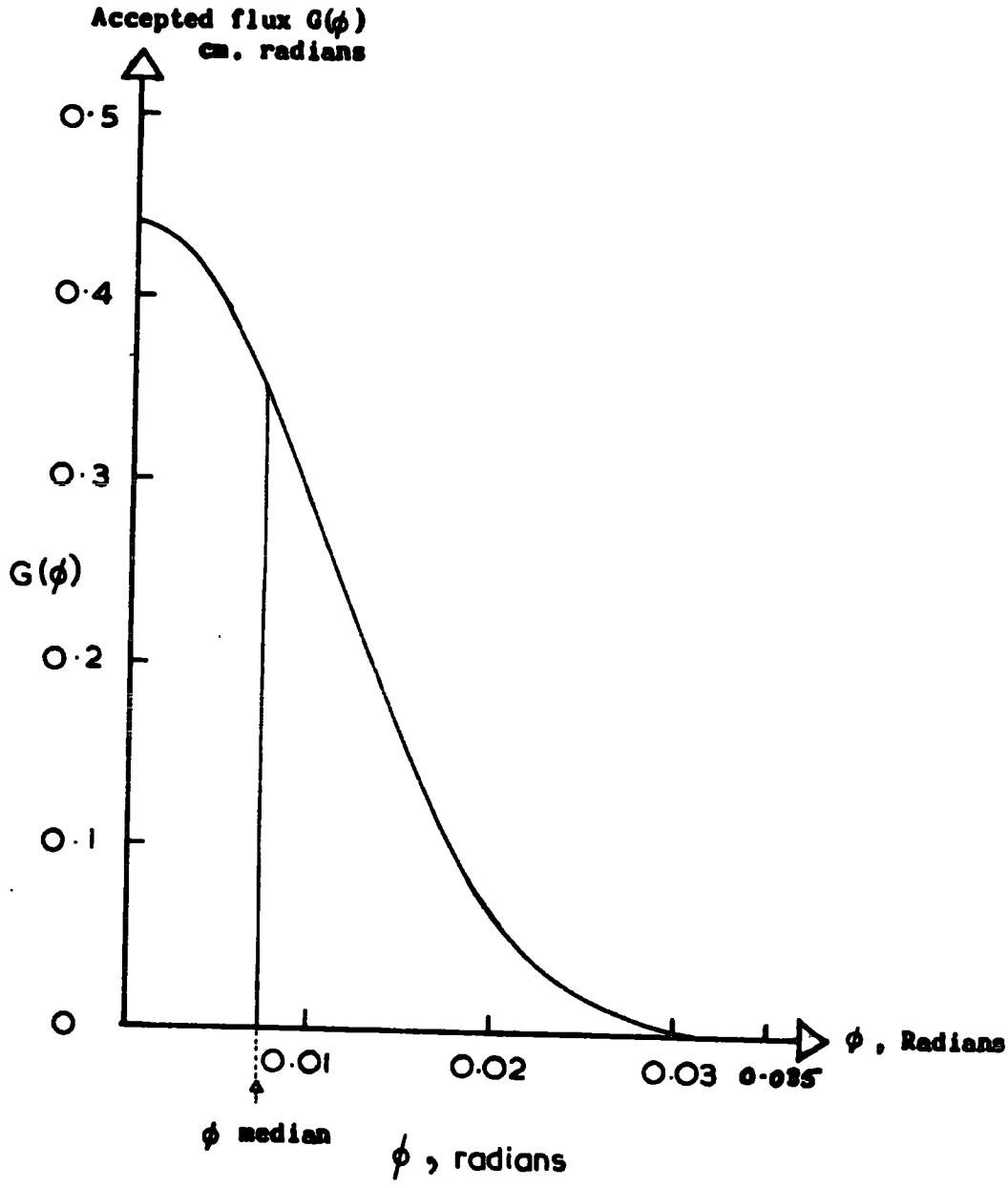

FIG. 3.8.4. The Acceptance Function - the 'Elementary Function' Curve

particles of differing category is not constant. Variation in the accepted flux with ϕ was investigated by Lloyd using the method shown in Fig. 3.8.5. Referring back to Fig. 3.8.1. it can be seen that when $x = \pm L$, $\theta_2 = 0$, i.e. the accepted flux is zero. This fact has been used to superimpose the acceptance characteristics for trays A, D and B, C taken together, taking into account any relative shift for a given angular deflection, after which the common area was found by computation. The actual equations for the acceptance characteristic lines are given in Fig. 3.8.5., and the result for total acceptance as a function of angular deflection is shown in Fig. 3.8.6.

Corrections to Theoretical Values of Accepted Flux

A correction to the analytical theory for the effect of asymmetry about the magnet axis was made by Lloyd, who showed that the correction to accepted flux for this is of the order of 0.075% and thus may be neglected.

Throughout the present work the small angle approximations were assumed to hold. For angles larger than 'small' (approximately greater than 10°) Lloyd has shown that a factor $\cos\theta$ enters into the expression for the accepted flux, due to the effective change of 'dead-space' between counters. In the case of the model an

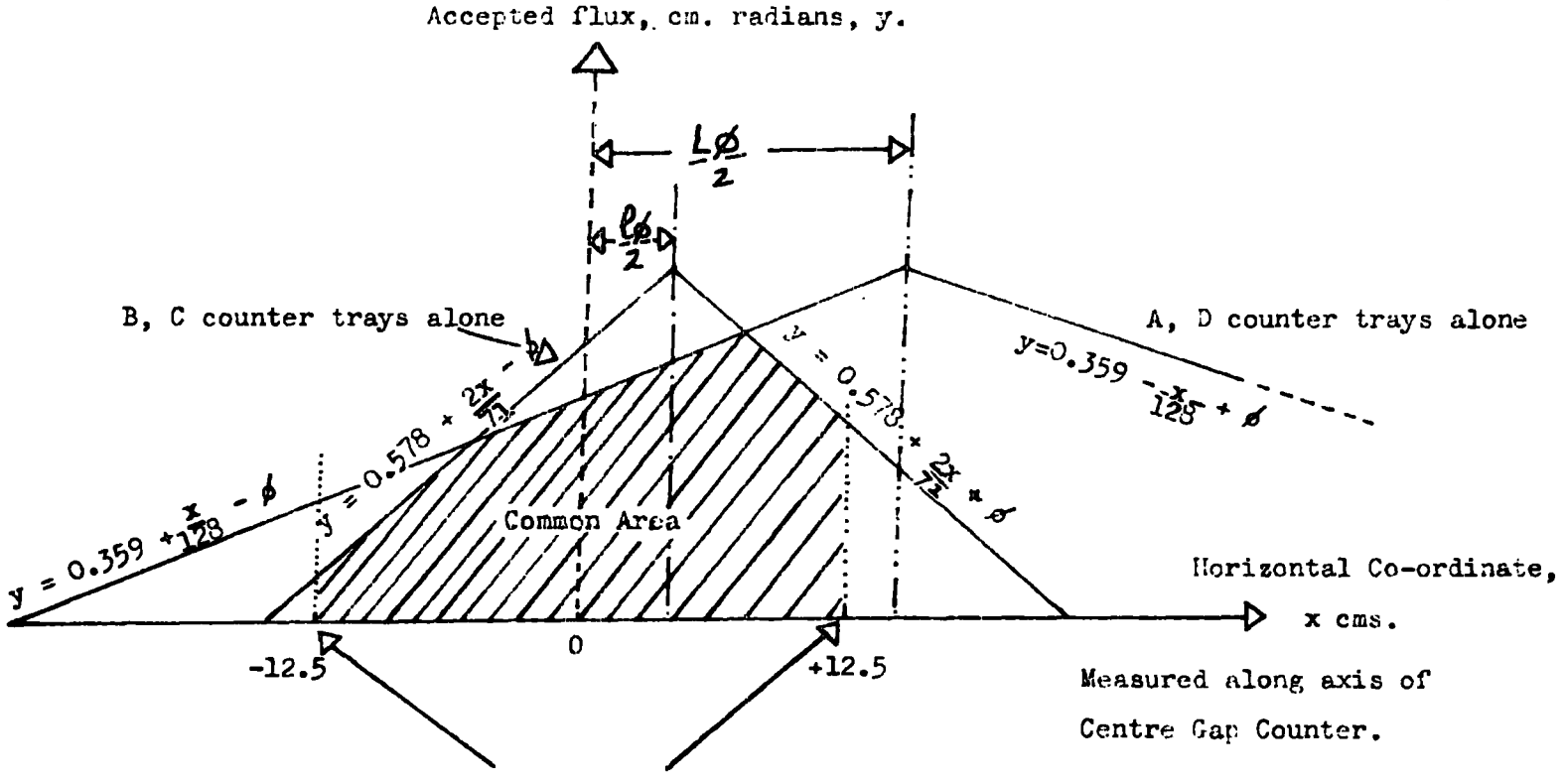

FIG. 3.8.5. Determination of Total Accepted Flux - the 'Envelope Curve'.

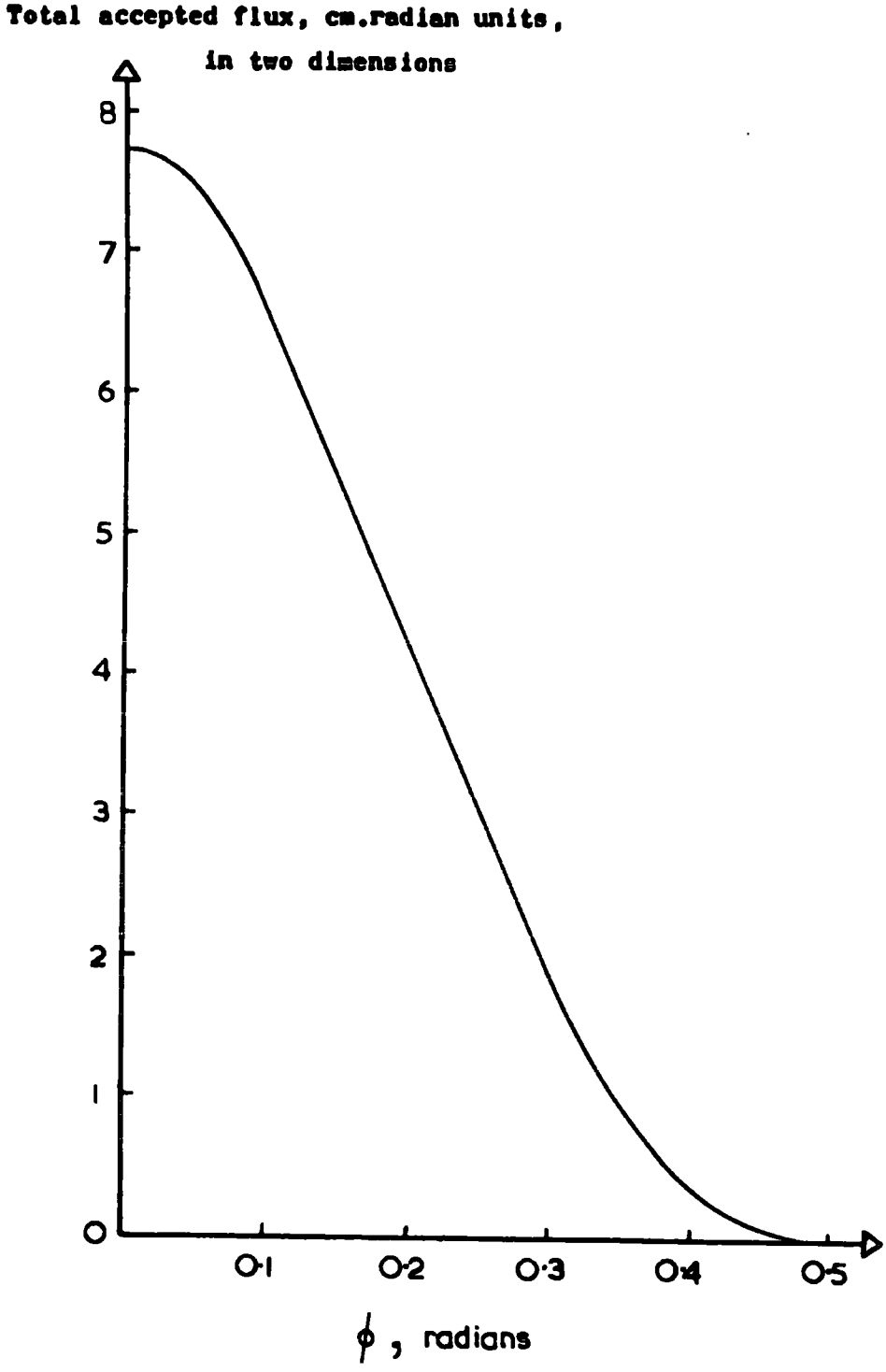

FIG. 3.8.6. The Acceptance Function - total Acceptance - The 'Envelope Curve'

effective 'expansion of flux' occurs due to the linear scale - a further factor of $\cos\theta$. (See Fig. 3.8.7.).

A correction for zenith angle variation in incident intensity was made, following the investigations of Moroney and Parry (1954). It is assumed that the variation is given by:-

$$I_\theta = I_0 \cos^m \theta.$$

where m has a mean value of approximately 1.8. (See Fig. 3.8.8.). These small corrections were incorporated into the acceptance curve, and are included in the curve shown in Fig. 3.8.6.

A small correction to the accepted flux also arises due to curvature of the trajectories within the region of magnetic field. The effective height of the field region is taken to be 53 cm. Reference to Fig. 3.8.9. shows that a particle going along trajectory JRKSL will just be recorded if K is the actual end of the gap counter, whereas the trajectory RMS, assuming one unique plane of deflection, would not be recorded in G. The effective lengthening of the gap counter is given by KM and may be shown to be:-

$$\begin{aligned} KM &= OM - OK \\ &= R(1/\cos \phi/2 - 1) \\ &= \frac{l_A}{\sin \phi/2} \cdot \frac{\phi^2}{8} \quad \text{i.e.} \simeq \frac{l_A \phi}{4} \end{aligned}$$

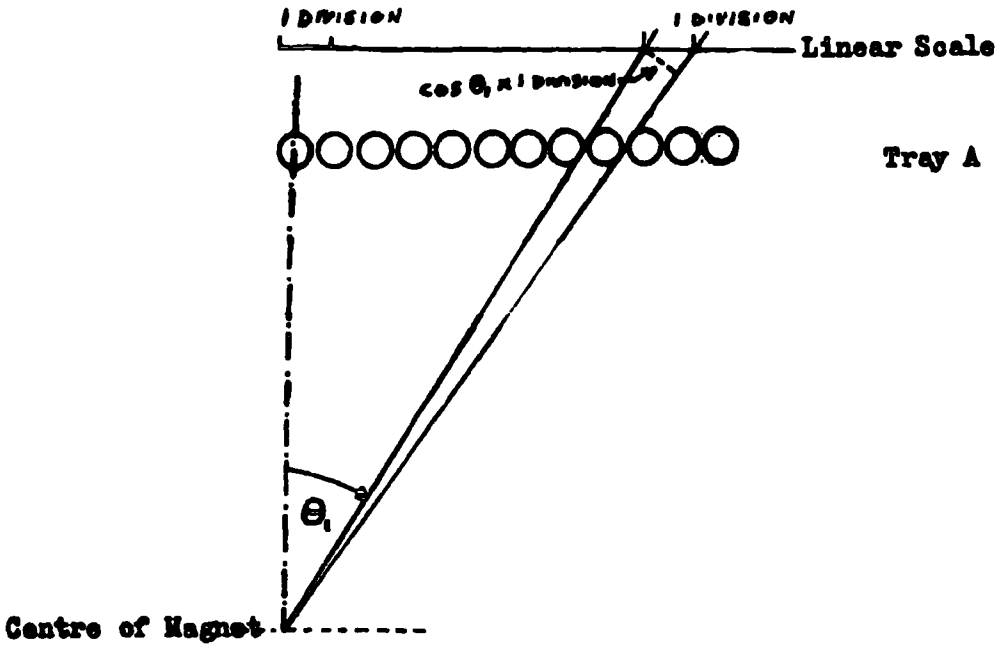

FIG. 3. 8. 7. Expansion of Flux - Model

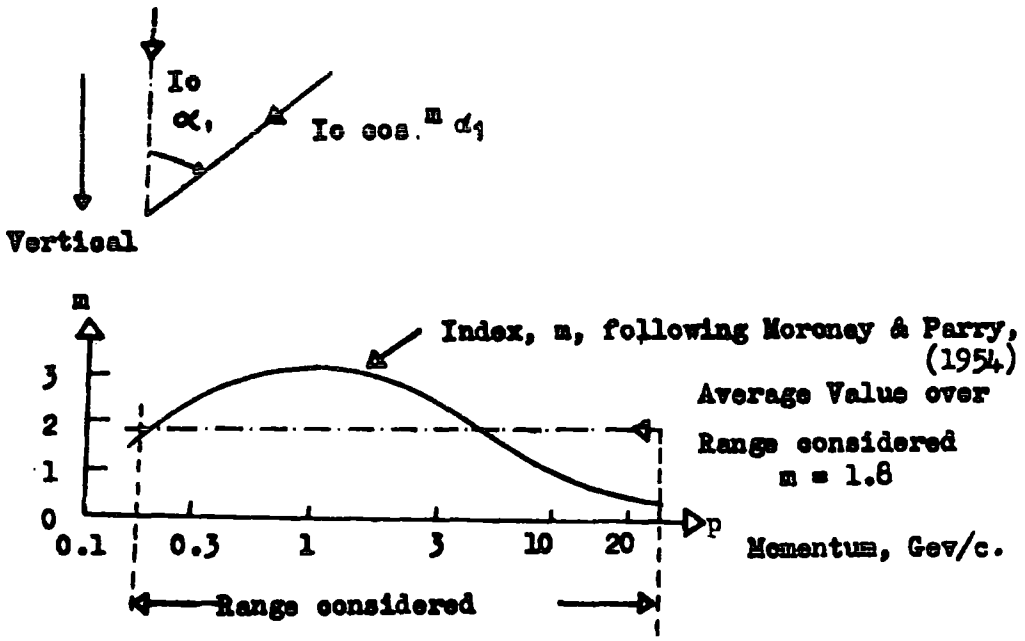

FIG. 3.8.8. Zenith Angle Correction.

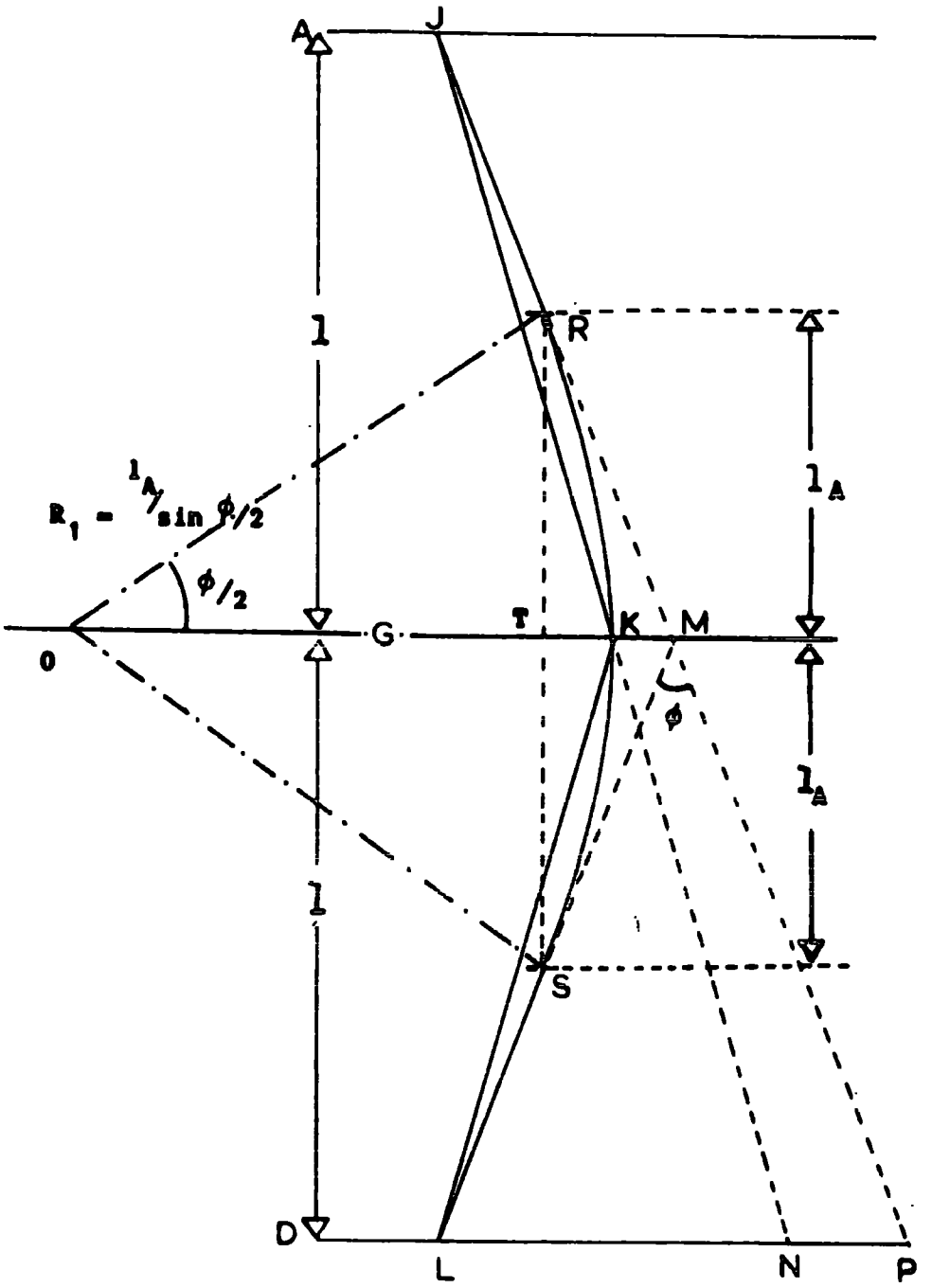

FIG. 3.8.9. Correction of Effective length of Gap Counters for curved particle trajectory.

This correction was also included in the curve given in Fig. 3.8.6. A further small correction for the difference between RKS, an arc of a circle and RTS, a straight line, has been shown in Appendix A 3.7.1 to be negligible.

3.9. Other Instrumental Corrections

Other factors modifying the incident muon spectrum before observation are:-

(i) Momentum loss in the material of the instrument itself.

(ii) the fact that protons are observed as well as muons.

(iii) Scattering in the material of the instrument.

The nature of these factors and associated corrections are dealt with fully in Chapter 4, describing treatment of the experimental results.

Chapter 4.

Analysis of Single Event Data

4.1. Experimental Data and General Scheme

The way in which single events are recorded using the counter spectrograph has been described in the preceding chapter. A schematic diagram of the processes involved in experiments to obtain both single and multiple event data (Chapter 5) is given in Fig. 4.1.1. Five different sets of data were obtained - referred to as Series H, M_1, M_2, L I, L II, respectively. The first three sets were obtained by Messrs. M. Gardener and D.G. Jones - the last two by the author. All the data were reduced by the author and at a later stage of the analysis the different series were combined to give a complete spectrum. For each series (corresponding to a given value of field strength), data were collected together and the assembled deflection spectra are shown in Fig. 4.1.2.

Conversion of such results to a differential momentum spectrum is straightforward, but in order to obtain the precise spectrum required, corrections must be applied. Part of the calculations were performed by hand, the remainder using an electronic computer. A block diagram of the operations and their sequence is given in Fig. 4.1.3.

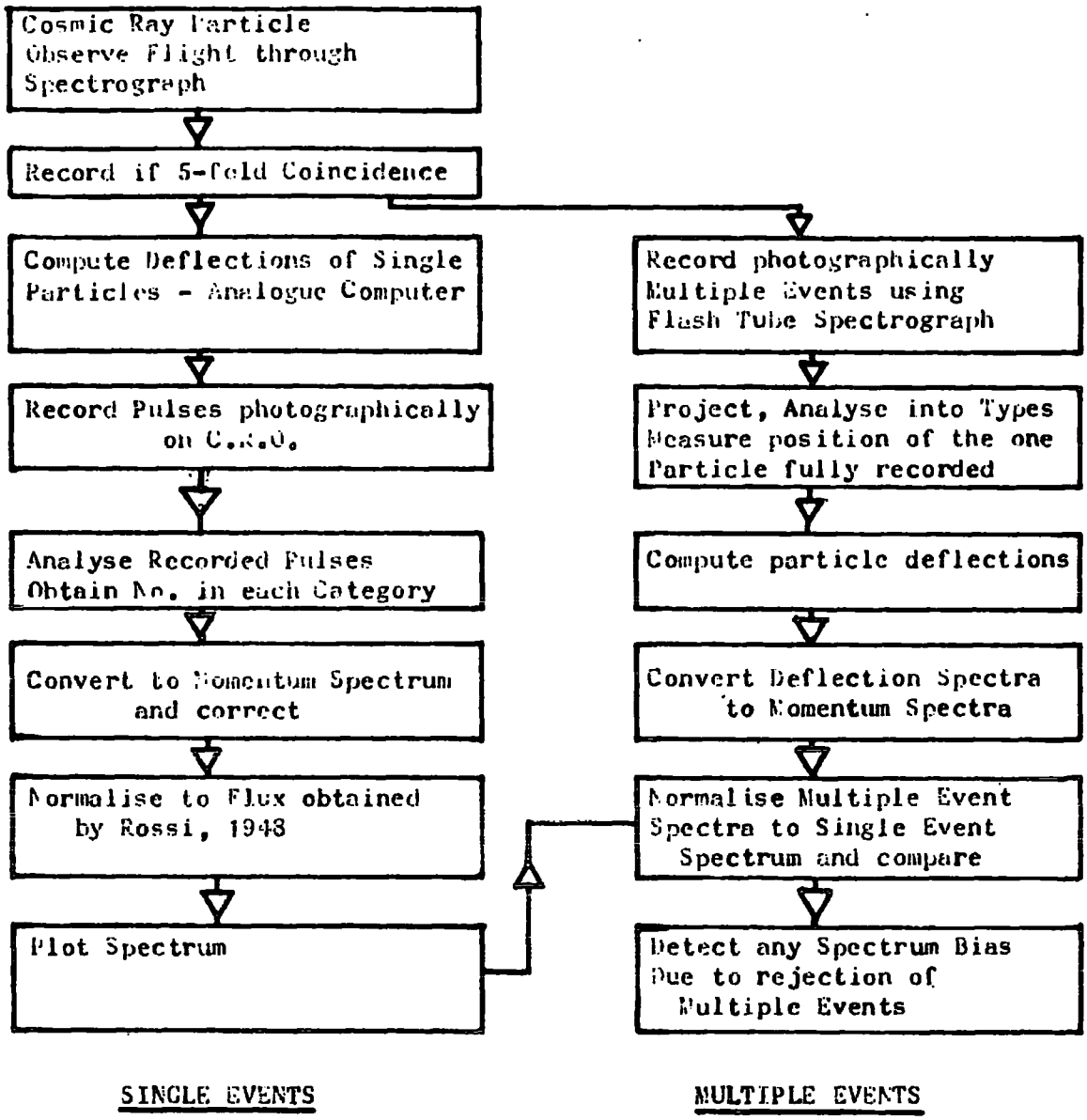

Fig. 4.1.1. SCHEMATIC DIAGRAM OF SPECTRUM DETERMINATION

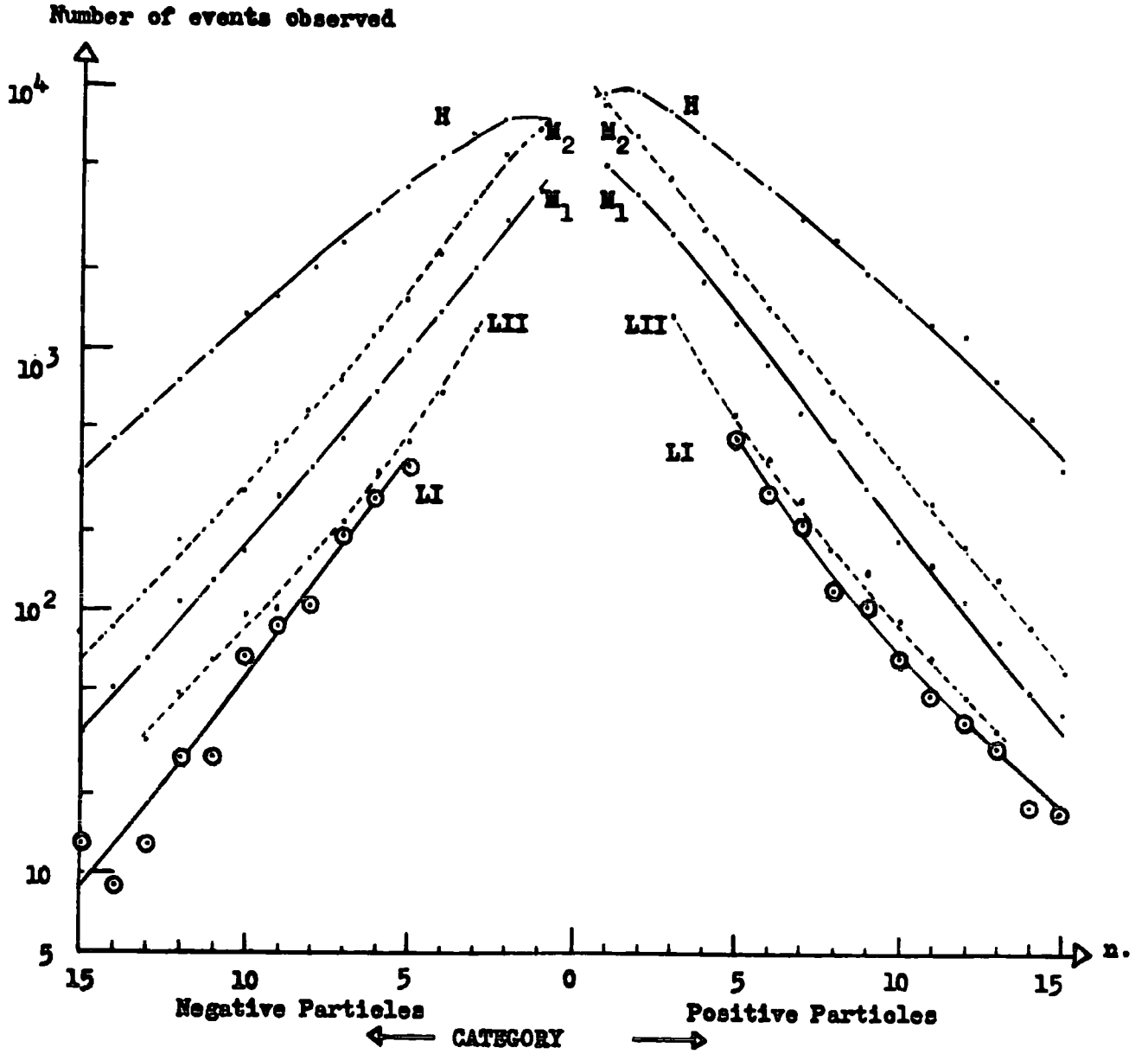

FIG. 4.1.2. Basic Data - the observed deflection spectra for particles of different charge

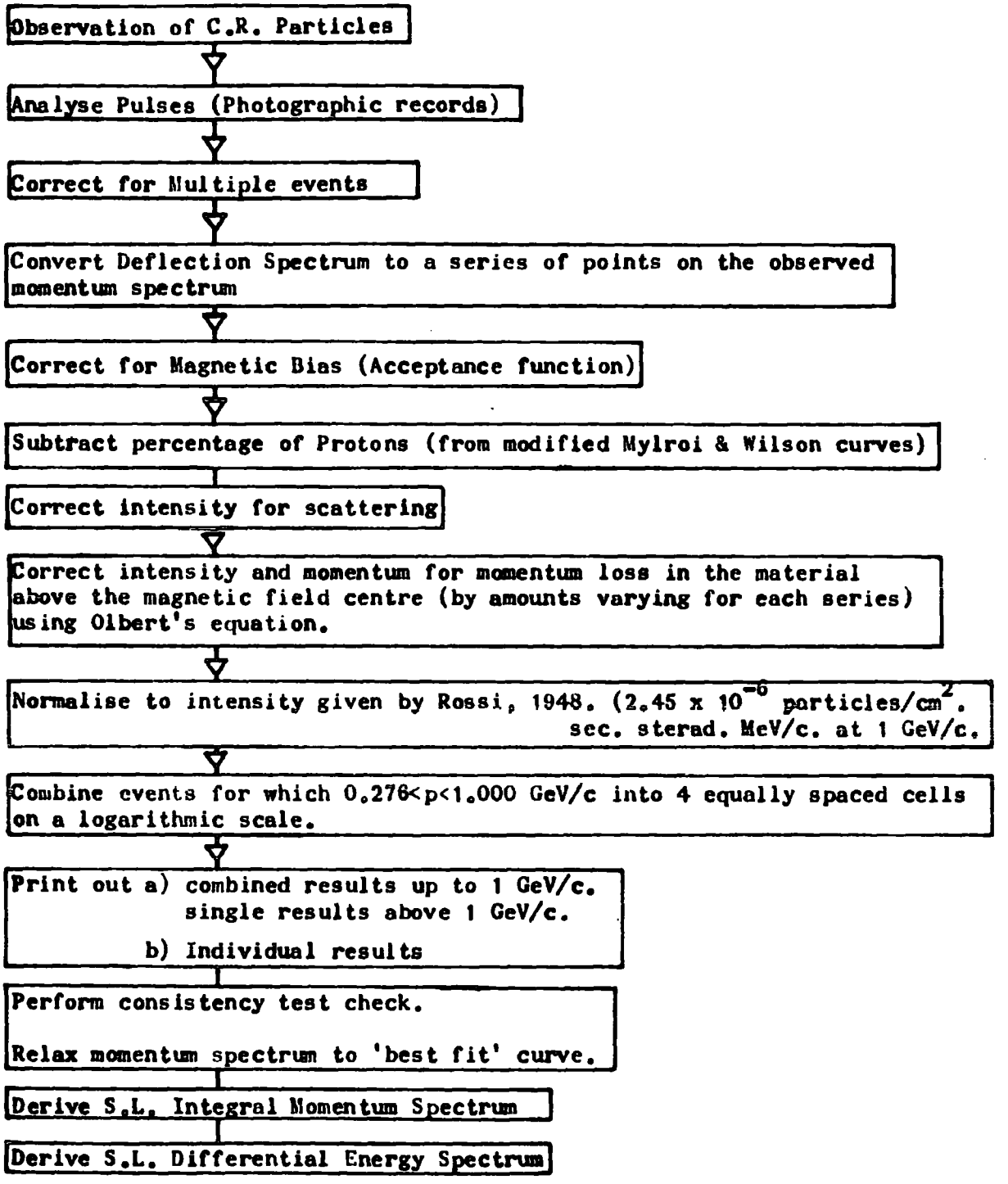

FIG. 4.1.3. STEPS IN TREATMENT OF SINGLE EVENT RESULTS.

4.2. Consistency of Basic Data

The consistency of the basic data was checked by plotting the results film by film separately, (each film being approximately 23 hours running time), as an observed deflection spectrum at the gap of the instrument. A typical curve(for Series LI) is given in Fig. 4.2.1. It can be seen that the lines corresponding to the deflection spectrum for each film are superimposed (to within the statistical accuracy expected) showing the instrument to have performed consistently during operation to obtain results forming the series concerned. The results for each series were found to be consistent.

4.3. Correction for Superimposed Events

The method of recording events has already been described in Chapter 3, and mention was made of the possibility of records of more than one event of the same category being superimposed during the recording interval of (usually) 2 minutes. Records where events were possibly superimposed were recorded as one event and a statistical correction applied to the total observed number to give the actual number traversing the instrument. The relation between the true rate R, and the observed rate r, both per frame, is given by:

$$R = \ln\left(\frac{1}{1-r}\right) \qquad \text{(i)}$$

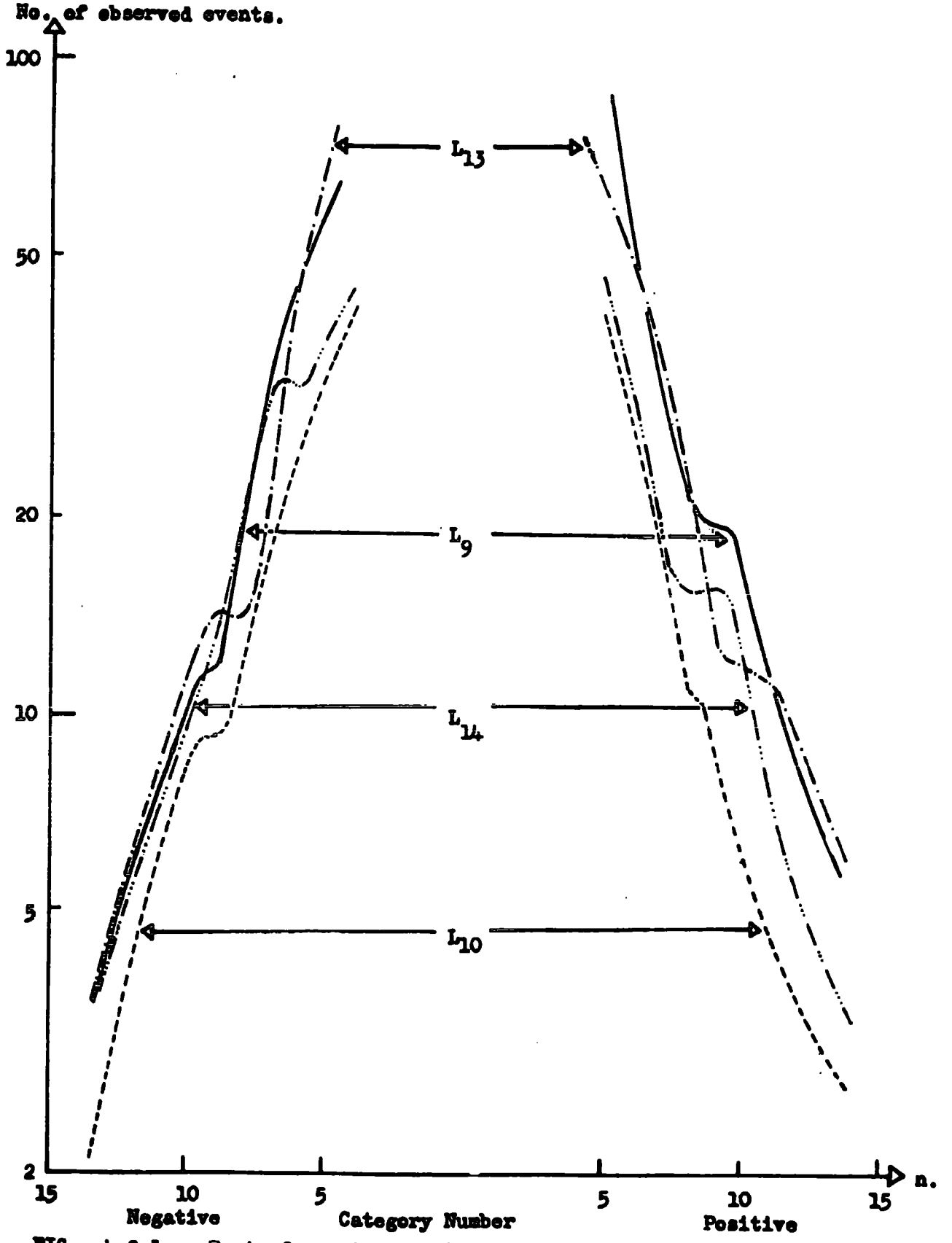

FIG. 4.2.1. Test of consistency between four typical films of Series L.I.

where R, r are both much less than 1, and the number of events considered is large.

This equation is originally due to Gardener, and is verified in Appendix A.4.3.1. Correction of results was performed by manual computation using data record sheets designed for systematic application of this correction.

4.4. Conversion of Deflection Spectrum to a Momentum Spectrum

It has already been shown (Equation 3.5(i)) that the momentum corresponding to a given category N is

$$p(\text{GeV/c}) = K'/N \qquad \text{(i)}$$

If one now considers a small cell of momentum width δp and corresponding width δN, then:-

No. in cell $= I(p).\delta p = I(N).\delta N$

where I(p), I(N) denote corresponding points on the momentum and deflection spectra respectively.

Thus:- $I(p) = I(N)\ \delta N/\delta p$,

or $I(p) = I(N)\ dN/dp$ (ii)

as the cells become infinitesimally small.

Now, dN/dp may be obtained by differentiation of 4.3.(i), and is given by:

$$dN/dp = -N^2/K'$$

Hence $I(p) = I(N) \times (-N^2/K')$ (iii)

In this way, each point on the deflection spectrum may be converted to a corresponding point on the momentum spectrum. Values of K' are given by the equation

$$K' = 1.51492. \int Hdl. \text{ GeV/c} \qquad \text{(iv)}$$

(See Chapter 3)

and those used here tabulated below, together with other important parameters used in later calculations.

A weighted mean value for the magnet current was obtained by summing the product of number of events and current for each run, then dividing by the total number of events.

The treatment above for conversion of the deflection spectrum to a momentum spectrum assumes that all particles of a given category have unique deflection corresponding to the nominal deflection of that category. The median ordinate of the elementary acceptance function corresponding to any category is the nominal deflection for that category if the incident deflection spectrum is flat. However, this is not so:- in practice the actual deflection spectrum rises steeply, then falls off exponentially. For large category numbers, ≥ 3, the deflection spectrum is sufficiently flat for the difference between the median and the nominal momenta to be negligible. For categories 1 and 2, this difference is not sufficiently small to be neglected and a correction

ACTUAL OBSERVED DATA

Series	Thickness of Lead	Mean Magnet Current	$\int H.dl \times 10^5$ gauss.cm	Range of categories used	Range of nominal momenta	No. of particles accepted	K, in equation $p=K/\Delta$	K', in equation $p=K'/n$
L I	5.5	12.200	1.720	5-15	0.174 to 0.531	2,332	4.977	2.606
L II	5.5	16.939	2.346	3-13	.273 " 1.185	6,309	6.788	3.554
M_1	0.0	19.097	2.650	1-14	0.289 " 4.052	30,941	7.670	4.015
M_2	2.0	19.097	2.650	1-14	0.289 " 4.052	52,420	7.670	4.015
H	0.0	67.30	6.30	1-14	0.681 " 9.684	99,378	18.390	9.544

TABLE 4-4-1.

factor has been computed and applied by West (1961).

4.5. Correction for Magnetic Bias

The way in which corrections for magnetic bias arise has been detailed in Section 3.7. For ease of application the corrections were converted to a form which, when applied to the observed momentum spectrum, gave that flux which would have been observed if the instrument had a constant acceptance - that for particles of infinite momentum. Such a correction is always greater than unity, increasing with decreasing momentum. The corrections derived from the acceptance function results are given in Fig. 4.5.1.

In the case of Series L.I, two of the geiger counters in Tray C were inoperative. The change in geometrical correction factor for such circumstances was obtained by finding the sum over G of the allowed angles traversed, using a scale drawing and paper jig representing a trajectory, in exactly the same way as in the determination of the acceptance function. This was done with and without the two counters in question, and the ratio of summed fluxes found for five given acceptance angles. These ratios were applied to the magnetic bias correction factors previously obtained. The final curve for Series L.I is also shown in Fig. 4.5.1.

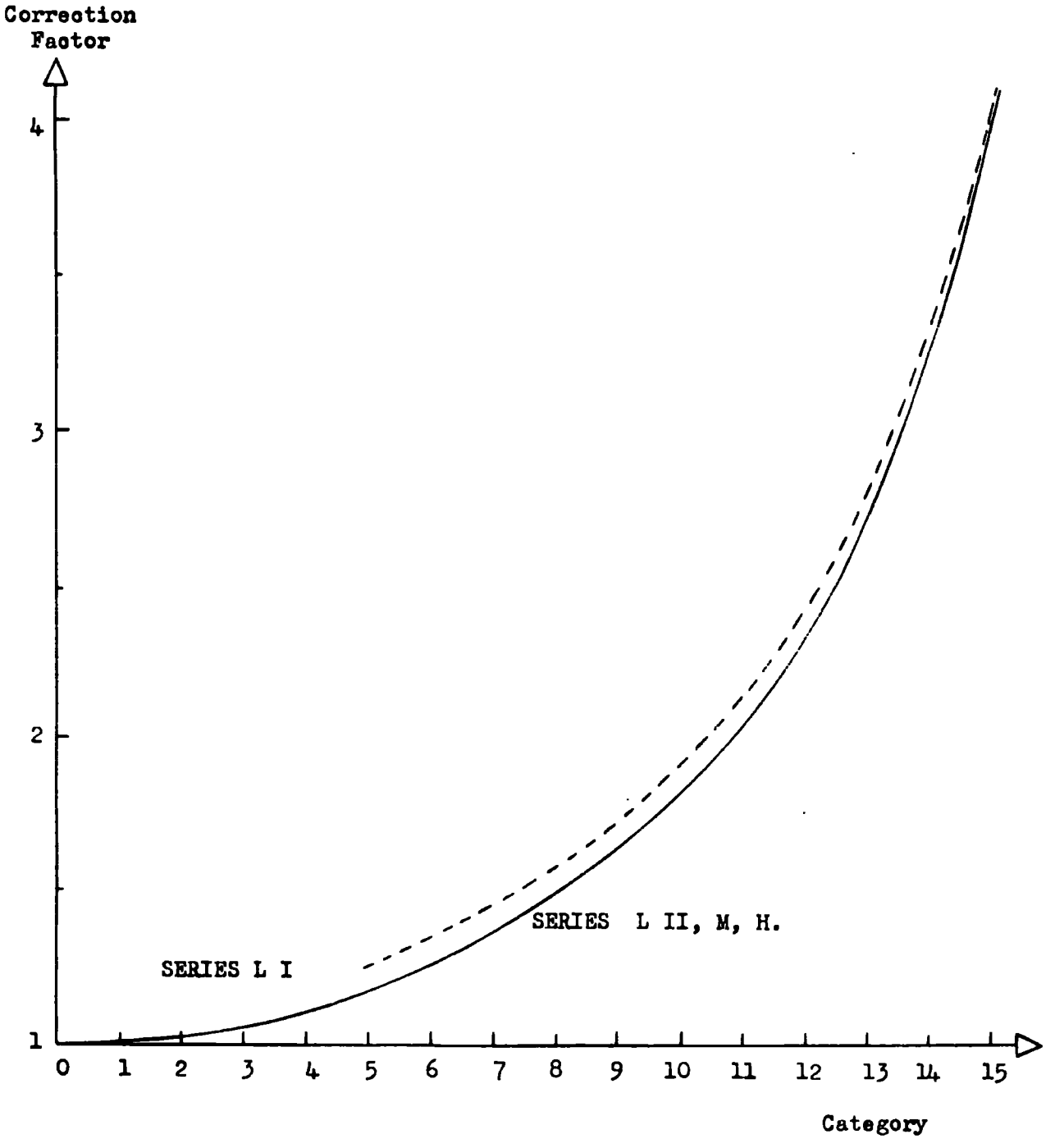

FIG. 45.1 Correction Factor for Magnetic Bias.

4.6. Correction for Proton Component of Cosmic Rays at Sea-Level.

An investigation of the magnitude of the proton component as a fraction of the total hard component of cosmic rays at sea level was published by Mylroi and Wilson (1951).

In the present experiments, certain runs were performed with an absorbing layer of lead above the spectrograph, (Table 4-4-1) and Mylroi and Wilson's results were modified to give the proton spectrum which would be observed under the layers of lead actually used. This modification was performed using values for the range-momentum relationship given by Sternheimer (1959), Fig. 4.6.1. For a given thickness of lead (one of the two values required) corresponding momenta of particles above (p_a) and below (p_b) the lead were obtained from the range-momentum curve. From this dp_a/dp_b was also obtained (Fig. 4.6.2.). This is the cell width correction to the proton intensity, as can be seen by considering a small cell. Let I_a, I_b denote proton intensities at corresponding momenta p_a, p_b above and below the lead. Then, no. in cell

$$= I_a . dp_a = I_b . dp_b$$

$$\text{or} \quad I_b = I_a . \frac{dp_a}{dp_b} \qquad (i)$$

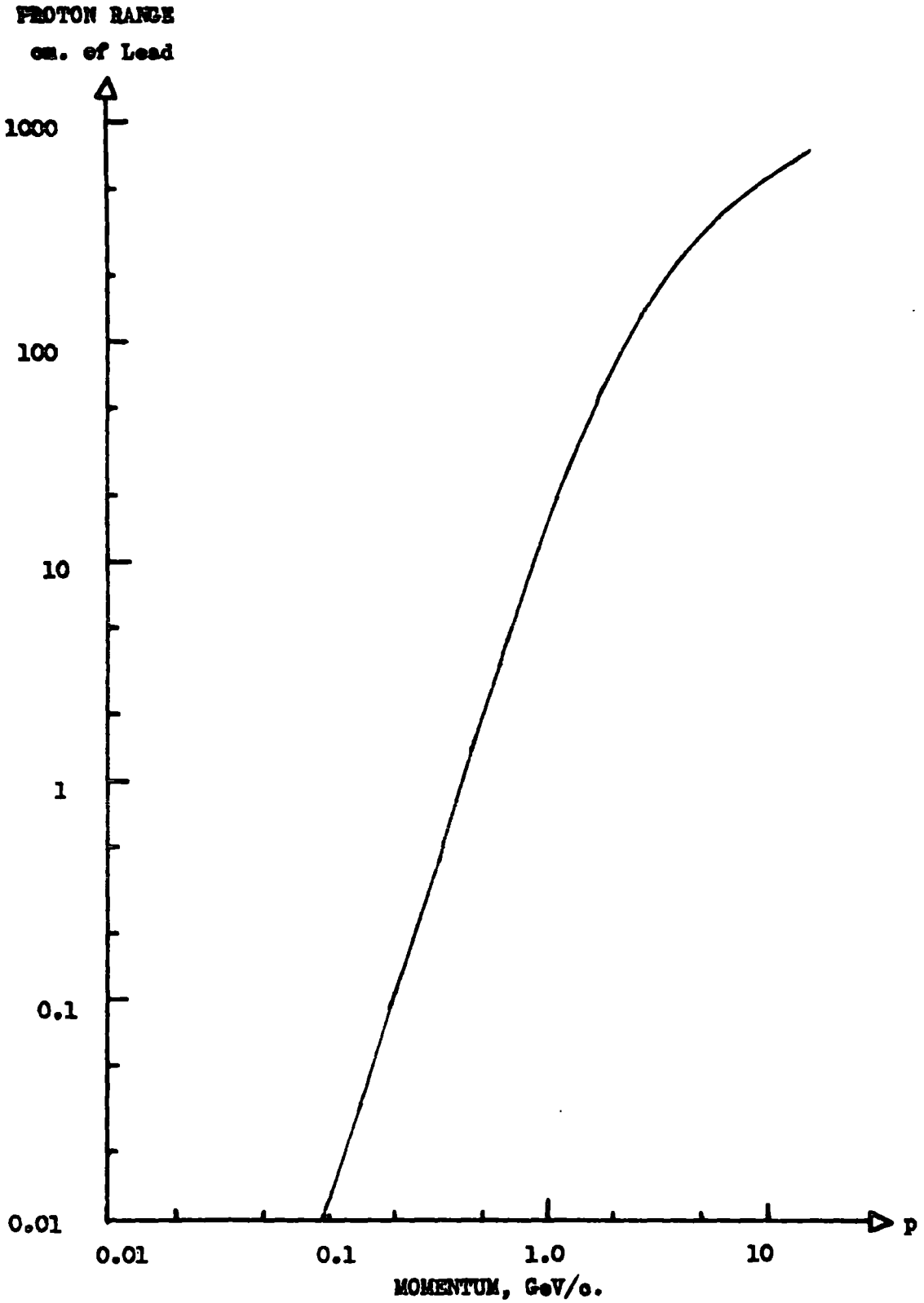

FIG. 4.6.1. Range momentum relationship for Protons in Lead, from the work of STERNHEIMER, 1959.

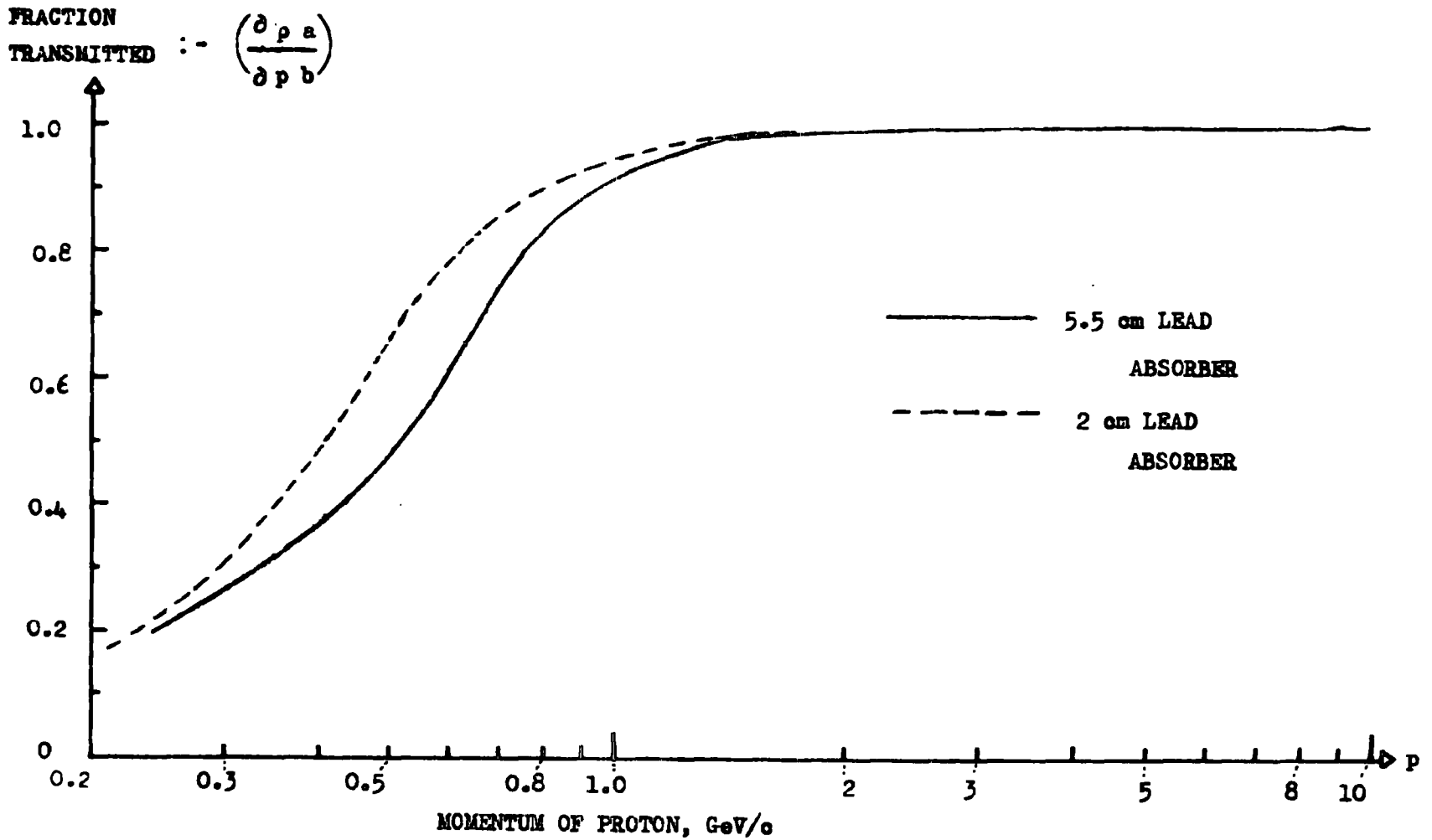

FIG. 4.6.2. Fraction of Proton Intensity transmitted after ionisation loss in lead absorber above Spectrograph

This factor (dp_a/dp_b) only accounts for ionisation loss, and further correction is due to the fact that, on average, only a fraction of the protons are transmitted through the lead without absorption, (0.67 through 5.5 cm), (0.87 through 2 cm).

These corrections, and the appropriate momentum loss due to the lead were applied to Mylroi and Wilson's results, and the resulting percentage proton spectra are shown in Fig. 4.6.3.

Appropriate percentages were subtracted from the momentum spectrum for each momentum value, to give a momentum spectrum of mesons only.

4.7. Correction for Coulomb Scattering

Measurement of particle deflection is only made in two dimensions, in a plane mid-way between the magnet pole-pieces, and transverse to the axis of the geiger counters. This is commonly termed the 'front plane'. The plane parallel to both the axis of the magnet pole pieces (passing through their centre) and the axis of the geiger counters is termed the 'back plane'. Scattering of incident mesons occurs in random directions, these may be resolved into components - only that in the front plane has any effect on the accuracy of measurement. The large number of scatters in random

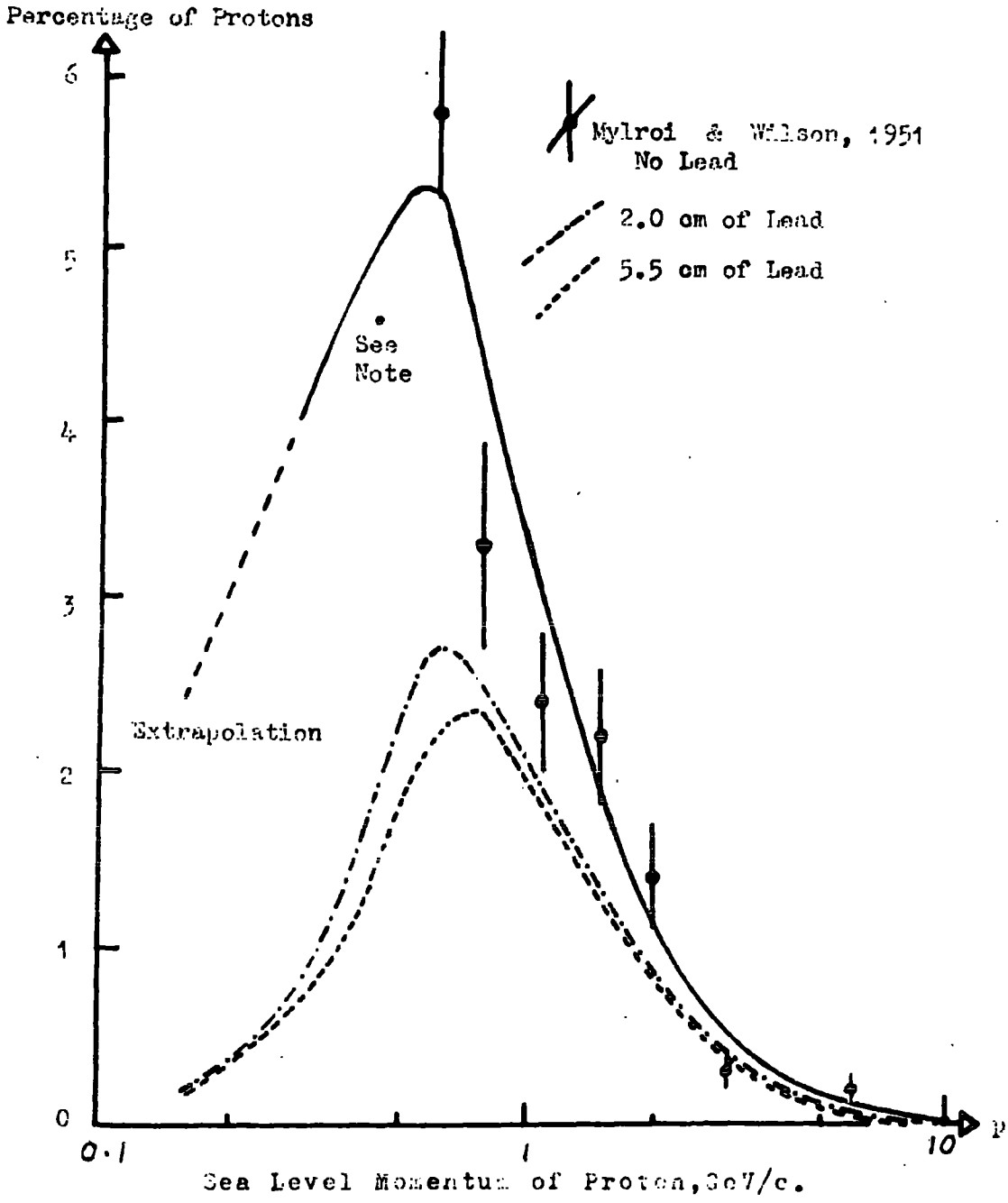

FIG.4.6.3. The Proton Spectrum of Mylroi and Wilson (1951) used in correcting for proton intensity. Modified after Sternheimer, (1959). Note : this point is originally due to Rochester and Bound, 1940, but is plotted as corrected by York, 1952.

directions are projected by multiplying by a mean projection factor of $1/\sqrt{2}$ (sin 45°) to obtain the r.m.s. scatter angle in the front plane. (Following Rossi 1952a).

The effect of scattering in the front plane is to convert any infinitesimally small cell of the incident deflection spectrum to a Gaussian distribution. The width of such a distribution increases as ϕ_M, the magnetic angular deflection increases, hence when in any small cell the incremental scattering into such a cell is integrated to obtain the observed number after scattering, it is found that more particles are in principle scattered into any given cell than are scattered out. After correction the scattered curve is normalised to have the same area as the unscattered curve, so as to represent the same number of events. (See Fig. 4.7.1. for a diagram of the procedure). The scattering correction to convert observed intensity to actual incident intensity is thus less than unity - this was calculated and applied as follows.

Rossi (1952b) gives as the r.m.s. projected angle, $\langle\phi_s\rangle$ through which a particle is scattered when passing through a material whose thickness in terms of radiation lengths is t, as:-

$$\langle\phi_s\rangle = \frac{1}{\sqrt{2}} \sum \frac{K' t^{\frac{1}{2}}}{p\beta} \qquad (i)$$

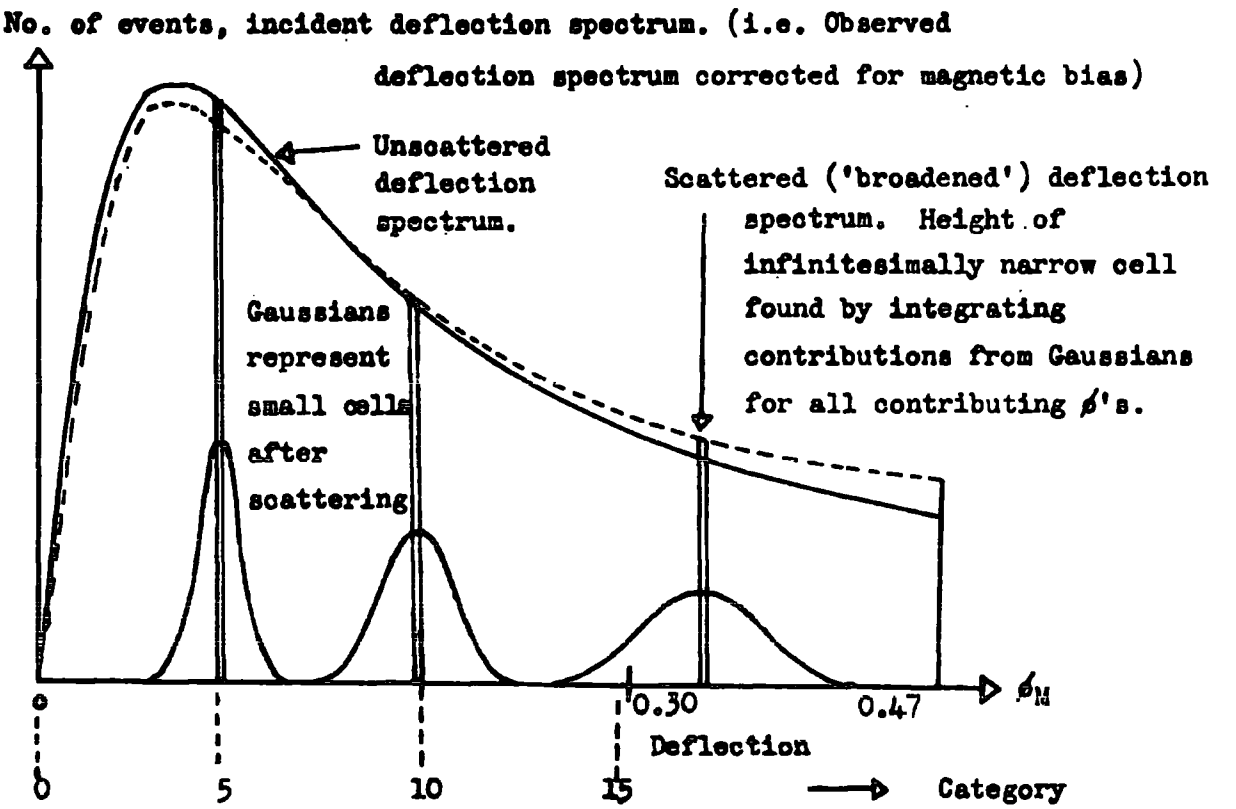

The scattered deflection spectrum is re-normalised after scattering so as to represent the same number of events.

FIG. 4.7.1. The effect of noise scattering on the deflection spectrum.

where K' is a constant equal to 21 MeV/c.

hence $$\langle \phi_s \rangle = \frac{0.1482}{p\beta} \sum t^{\frac{1}{2}} \qquad \text{(ii)}$$

where p is measured in GeV/c, for scattering in layers of material of known t.

Now, $$pc_{(GeV/c)} = \frac{300. \int Hdl}{\phi_M} \times 10^{-9}$$ (Section 3.4)

Hence $$\frac{\langle \phi_s \rangle}{\phi_M} = \frac{0.1482}{300 \int H.dl} \sum t^{\frac{1}{2}} \qquad \text{(iii)}$$

$\frac{\langle \phi_s \rangle}{\phi_M}$ is thus a constant, termed k.

In consideration of scattering, only geiger counter trays B, G, C, and flash tube trays A, B, C, D are important. Scattering at tray A is not important since only relative position to the located position and not angle of incidence, is of importance, hence variations in effective angle of incidence caused by scatter have no effect. In the case of tray D, only the incident position of the particle is measured, the emergent angle being of no importance. The type and mass of material in the beam of the particle is detailed in Table 4-7-1.

For the geiger trays, with 1.008 $g.cm^{-2}$ of pyrex glass of radiation length 32.34 $g.cm^{-2}$ in the beam,

$$t^{\frac{1}{2}} = (0.031)^{\frac{1}{2}} = 0.176$$

Using equation 4.7 (ii) above one sees that:

Item	Thickness, cm.	Density, $g.cm^{-3}$	Series L	Series M_2	Series M_1,H.
Roof	0.5	2	1	1	1
Lead	0/2/5.5	11.3	62.15	22.6	-
Wood Floor for lead	3	2	6	6	6
Tray A G.M.	-	-	1.008	1.008	1.008
Tray A F.T.	-	-	4.67	4.67	4.67
Air, upper Half	192	.001293	0.25	0.25	0.25
Tray B G.M.	-	-	1.008	1.008	1.008
Tray B F.T.	-	-	4.67	4.67	4.67
Tray G G.M.	-	-	1.008	1.008	1.008
Tray C F.T.	-	-	4.67	4.67	4.67
Tray C G.M.	-	-	1.008	1.008	1.008
Air, Lower Half	192	.001293	0.25	0.25	0.25
Tray D F.T.	-	-	4.67	4.67	4.67
Tray D G.M.	-	-	1.008	1.008	1.008
			Matter in the particle beam, in $g.cm^{-2}$		

Only this section involved in momentum loss before measurement.

Only this section relevant to scatter considerations

Table 4-7-1. Absorbing and Scattering Material in the Particle Beam.

$$\langle \phi_s \rangle = \frac{0.1482}{p\beta} \times 0.1762 \text{ radians}$$

$$\text{i.e. } \frac{2.608}{p\beta} \times 10^{-3} \text{ radians} \qquad \text{(iv)}$$

For the Conversi flash tube stacks, with aluminium electrodes, two components arise which add in quadrature. The first of these is due to the glass, 4.50 $g.cm^{-2}$ of radiation length 28.86 $g.cm^{-2}$ i.e.

$$t^{\frac{1}{2}} = (0.156)^{\frac{1}{2}} = 0.395$$

Hence $$\langle \phi_s \rangle = \frac{5.85}{p\beta} \times 10^{-3} \text{ radians} \qquad \text{(v)}$$

and for the aluminium foil, 0.17 $g.cm^{-2}$ of radiation length 26.3 $g.cm^{-2}$,

$$t^{\frac{1}{2}} = (0.00646)^{\frac{1}{2}} = 0.0804$$

$$\text{i.e. } \langle \phi_s \rangle = \frac{1.191}{p\beta} \times 10^{-3} \text{ radians} \qquad \text{(vi)}$$

adding 4.7 (v) and (vi) in quadrature one obtains:

$$\langle \phi_s \rangle \text{(Conversi stacks)} = \frac{5.96}{p\beta} \times 10^{-3} \text{ radians} \qquad \text{(vii)}$$

For the air between the trays A, B and C, D, of the spectrograph there is a 192 cm column, i.e. 0.24 $g.cm^{-2}$ of radiation length 43 $g.cm^{-2}$.

$$\text{hence} \qquad t^{\frac{1}{2}} = (0.00557)^{\frac{1}{2}} = 0.0236$$

$$\text{and} \qquad \langle \phi_s \rangle = \frac{0.350}{p\beta} \times 10^{-3} \text{ radians} \qquad \text{(viii)}$$

Three geiger trays, 4 Conversi stacks and the air are involved in scattering, thus equations 4.7 (v), (vii) and (viii), multiplied by the appropriate number of units, are added in quadrature, giving:-

$$\langle \phi_s \rangle_{total} = \frac{10.36 \times 10^{-3}}{p\beta} \text{ radians} \qquad \text{(ix)}$$

Hence, from equation 4.7 (iii),

$$K = \frac{\langle \phi_s \rangle}{\phi_M} = \frac{10.36 \times 10^{6}}{300\beta \int H dl} \qquad \text{(x)}$$

when the Conversi stacks are in the beam. For Series M, H, when the Conversi stacks were not in place in the instrument,

$$\langle \phi_s \rangle = \frac{4.53 \times 10^{-3}}{p\beta} \text{ radians}$$

$$\text{and } K = \frac{\langle \phi_s \rangle}{\phi_M} = \frac{4.53 \times 10^{6}}{300\beta \int H dl} \qquad \text{(xi)}$$

K is hence a function of β and thus of p. Values of the constant $(K\beta)$ for the various series are given in table 4-7-2 below.

Series	$\langle \phi_s \rangle / \phi_M = (K\beta)$.	b, in equation $N_{\phi_M} = Ae^{-b\phi_M}$
L I	0.201	12.596
L II	0.147	11.658
M	0.057	9.374
H	0.240.	5.539

Table 4-7-2.

The width of the Gaussian distribution, $\langle \phi_s \rangle$, at any given magnetic angular deflection ϕ_M is thus given by:

$$\langle \phi_s \rangle = \left(\frac{K\beta}{\beta}\right).\phi_m. \qquad \text{(xii)}$$

Other errors in ϕ_M should be combined with $(K\beta)$ at this stage, and an investigation of the significance of current variations, giving corresponding variation in $\int H.dl$, was made. The standard deviation of these, giving a parameter σ (expressed as a percentage) adding to K in quadrature, was found to be less than 5% of K, giving no effective charge in K when added in quadrature. Current variations were thus shown to be insignificant.

An analytical integration for any deflection ϕ_M was performed, assuming the deflection spectrum to have the form:-

$$N(\phi_M) = Ae^{-b\phi_M} \qquad \text{(xiii)}$$

This was verified by plotting the observed deflection spectrum corrected for magnetic bias, giving the incident deflection spectrum, on log/linear scales, and obtaining b from the slope of the straight section of the plot.

The regions outside the exponential section of the incident deflection spectrum, i.e. at those values of ϕ_M either nearly 0, where $\langle\phi_s\rangle$ is very small, or approaching magnetic cut-off ($\phi_M \approx 0.47$ radians) are not of interest. Values of the exponential slope, b for the various series are also given in Table 4-7-2. The value of b used is that giving the best fit at the larger values of ϕ_M used. As mentioned, the correction to intensity, R, for such 'noise-scattering' is less than unity, and is given by:-

$$R = \left(\frac{\text{unscattered no.}}{\text{scattered no.}}\right) \text{ at any } \phi_M, \phi_i \text{ (say)}$$

$$= \exp -\left(\frac{K^2 b^2 \phi_i^2}{2}\right) \qquad \text{(xiv)}$$

This may be verified using a method similar to that used by Lloyd and Wolfendale, (1955).

Correction has been made by computer to the data, after correction for the factors previously detailed, the procedure being:-

(i) From p (at the magnet gap) find β, and hence K from $(K\beta)$.

(ii) From K, now known, calculate R, the correction factor to intensity. Modify the intensity accordingly, and record p, R, and the modified and unmodified intensities.

The relation between p and R for the various series is given in Fig. 4.7.2. It can be clearly seen that scattering becomes more significant the higher the category number, and the corrections are more significant at the lower values of $\int H.dl$ used.

4.8. Correction for Momentum Loss in the Material Above the Magnet

Two corrections must be applied to the observed magnitude of momentum and intensity at the magnet gap, in order to obtain the incident spectrum. One is for momentum loss of the incident particles, assumed to be muons, in the material of the upper half of the spectrograph, as

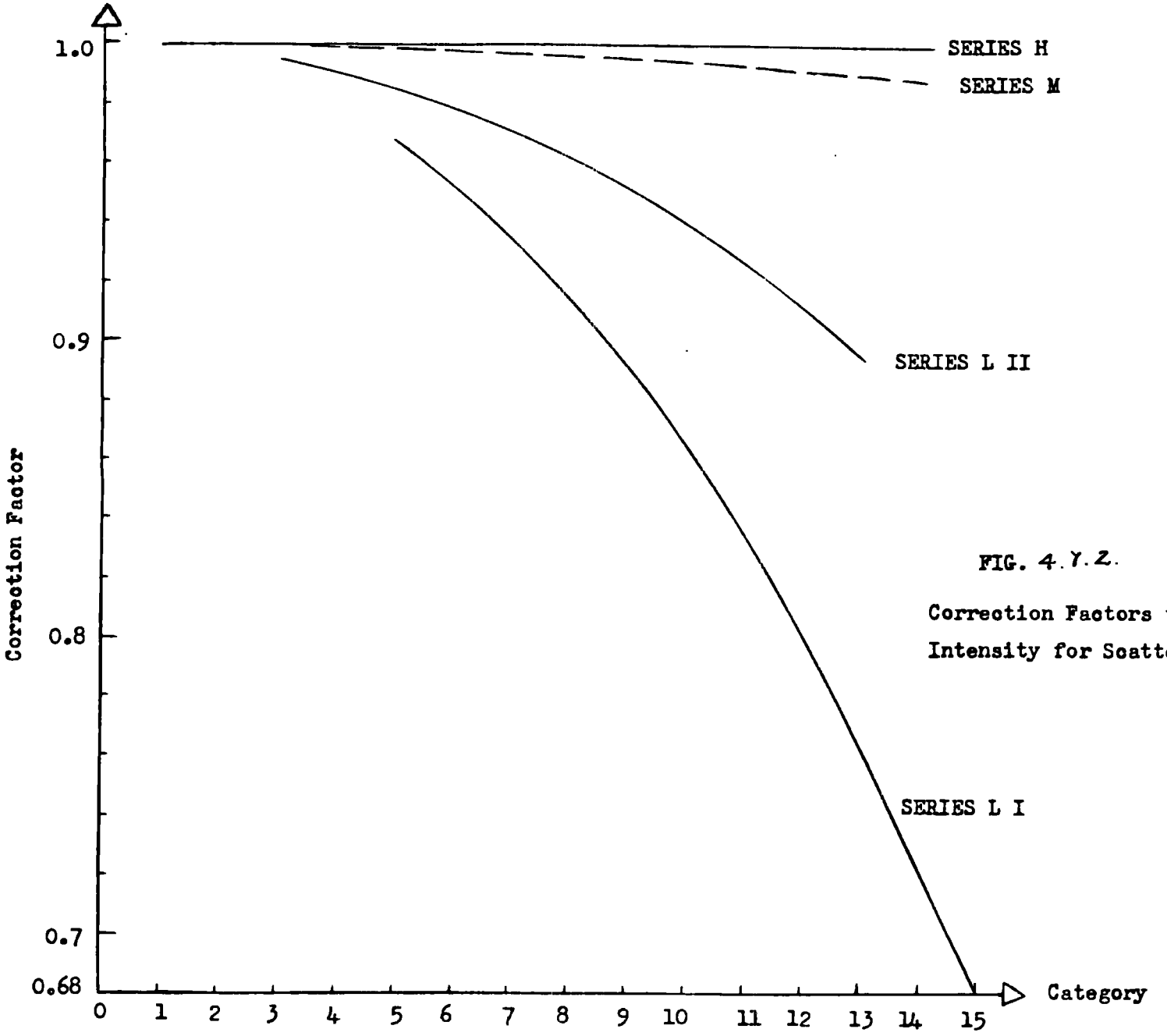

FIG. 4.Y.Z.

Correction Factors to Intensity for Scattering

detailed in Table 4-7-1. The other is a change in apparent intensity due to a cell width correction. As before:-

$$I_a = \frac{dp_a}{dp_b} \cdot I_b$$

where suffix 'a' refers to above, and 'b' to below.

Both corrections have been applied using an analytical range-momentum relationship first given by Olbert, (1954), for muons in air, i.e.

$$\frac{m_\mu c}{p} = \frac{B}{(b+R)} - u \qquad (i)$$

where $m_\mu c$ = rest mass of muon

p = momentum of muon

and R = range of muon in $g.cm^{-2}$,

B, b, u are constants - revised values of these were evaluated for lead, and were found to be:-

B = 91.44, b = 93.12, u = 0.00275.

The range-momentum relationship given by this equation was checked against that of Sternheimer (1959), for muons in lead, and found to be correct to better than 1%. The range momentum relationship for muons in lead, used in these calculations, is shown in Fig. 4.8.1.

Correction for momentum loss was made by:-
(i) Converting momentum to range, adding the effective range loss in lead (in $g.cm^{-2}$), then

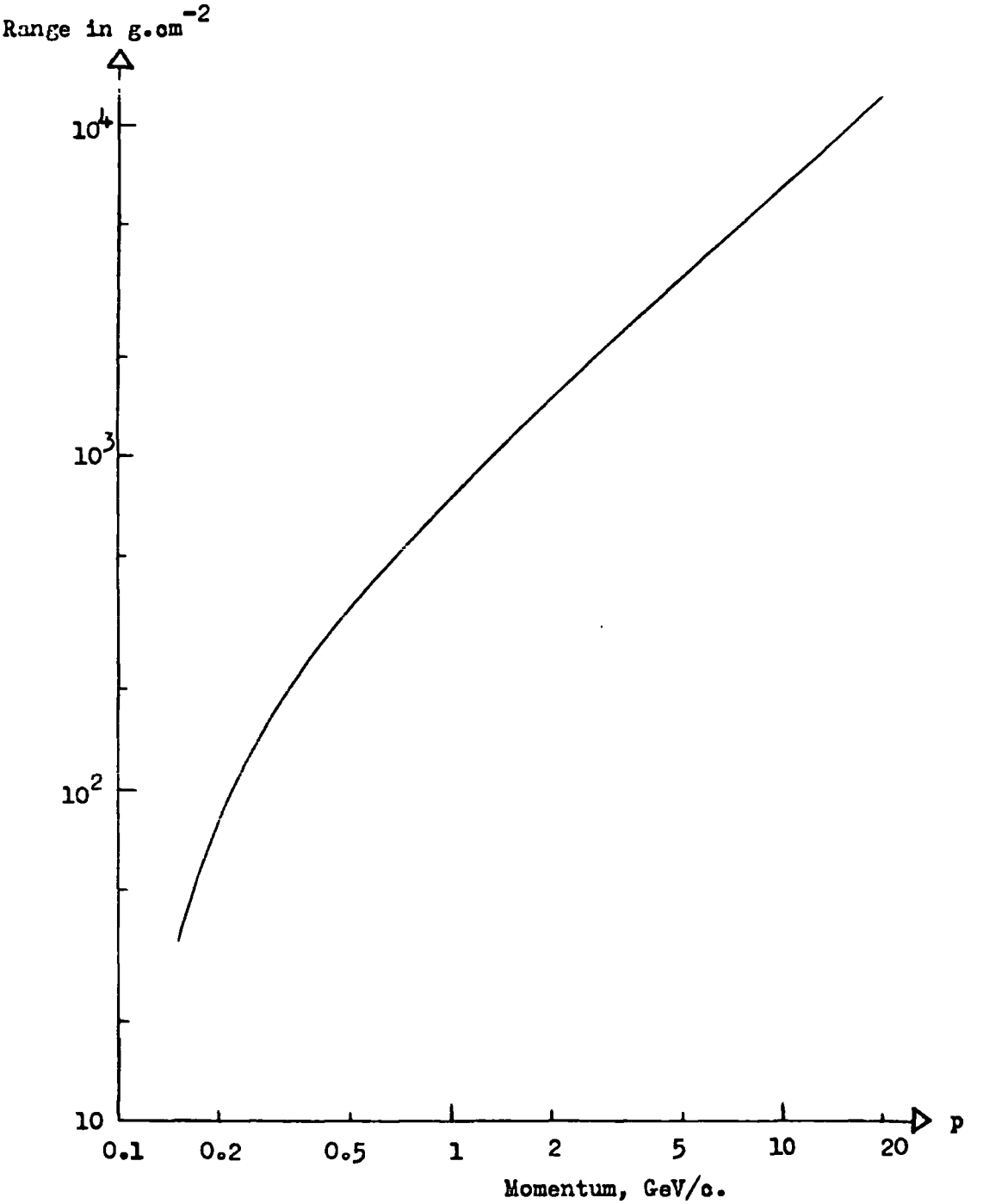

FIG. 4.8.1. Range-Momentum Curve for muons in lead.

(Used in Correction for Momentum Loss).

After Sternheimer, 1959.

(ii) Converting the corrected range back to momentum, using Olbert's equation ((i) above).

Olbert's equation with terms transposed was used for operation (i), i.e.:

$$R = \frac{B}{\left\{\frac{m_\mu c}{p} + a\right\}} - b \qquad \text{(ii)}$$

Correction for cell width change was made by using the differential form of equation (i), i.e.

$$dp_a = \frac{B}{(b+R_a)^2} \cdot \frac{p_a^2}{(m_\mu c)} \cdot dR_a$$

and $$dp_b = \frac{B}{(b+R_b)^2} \cdot \frac{(p_b)^2}{(m_\mu c)} \cdot dR_b$$

Now, since $R_a - R_b < R_a$ or R_b, $dR_a \approx dR_b$ (very closely) hence:-

$$\frac{dp_a}{dp_b} = \frac{(b+R_b)^2}{(b+R_a)^2} \cdot \frac{(p_a)^2}{(p_b)^2} \qquad \text{(iii)}$$

This is the correction which has been applied to the intensity for the cell width change due to momentum loss.

4.9. Normalisation

After application of appropriate momentum loss corrections by computer to each series, each series was normalised separately to Rossi's figure (1948) for the intensity of muons at 1 GeV/c, i.e. 2.45×10^{-6} particles/cm^2 sec. steradian (MeV/c), with the exception

Sea-Level Momentum, p	Intensity, $\times 10^{-6}$ particles.cm^{-2}sec^{-1}sterad^{-1}(MeV/c)$^{-1}$			Percentage error, %	No. of results combined to give cell	No. of events in combined cell
	ACTUAL	MAXIMUM	MINIMUM			
0.334	1.814	1.936	1.691	6.74	5	220
0.420	2.640	2.679	2.602	1.45	14	4725
0.588	2.863	2.892	2.833	1.05	8	9130
0.808	2.647	2.667	2.626	0.77	7	17023
0.993	2.576	2.624	2.528	1.87	1	2860
1.012	2.402	2.464	2.340	2.57		
1.055	2.395	2.421	2.369	1.10		
1.101	2.298	2.337	2.259	1.70		
1.310	2.184	2.227	2.141	1.98		
1.236	2.223	2.256	2.190	1.48		
1.393	2.055	2.073	2.036	0.88		
1.408	1.980	2.008	1.953	1.39		
1.640	1.774	1.795	1.753	1.16		
1.963	1.490	1.505	1.474	1.04		
2.071	1.378	1.388	1.368	0.73		
2.448	1.159	1.170	1.149	0.92		
3.256	0.778	0.785	0.772	0.83		
4.010	0.513	0.517	0.510	0.64		
4.854	0.421	0.424	0.418	0.76		
9.721	0.110	0.111	0.110	0.78		

Total number of events 192090.0

Table 4-10-1. Final Results for Sea-Level Muon Differential Spectrum.

that Series L I was normalised to series L II at 0.45 GeV/c, since L I has no momentum values near or above 1 GeV/c.

4.10. Combination of Events, and Final Differential Momentum Spectrum

Immediately after correction for momentum loss, events for which the momentum is less than 1 GeV/c, were combined into four cells, equally spaced as a logarithmic scale, between the values $0.276 < p < 1.000$ GeV/c. This reduced the 35 points below 1 GeV/c of relatively poor statistical accuracy to four points of good statistical accuracy. The results for the final spectrum after correction for the factors detailed above, are given in Table 4-10-1. The error in any point has been taken to be the statistical error, $\pm 100\ N^{-\frac{1}{2}}\%$, in the corrected number of events, N, represented by that point.

4.11. Relaxation of Spectrum to "Best-Fit" Line

The points on the differential deflection spectrum obtained in the manner described were plotted and the best smooth curve drawn by eye through them. Intensity values were then compared with the corresponding ordinate from this curve, and a plot made of the ratio of the intensity for each result of each series to the ordinate from the smooth curve. Statistical errors were included,

then a 'trend' line drawn for each series. Where all series showed an unbalanced trend from the 'p' axis representing the smooth curve, the smooth curve was shifted by an appropriate percentage till the trend either way (plus or minus) was balanced. The original smooth curve was thus relaxes until a 'best-fit' line based on trends differing from the initial line shown by the individual series, was obtained. This 'best-fit' spectrum is shown in Fig. 4.11.1.

4.12. The Sea-Level Energy Spectrum

The curve of Fig. 4.11.1. has been converted to a sea-level energy spectrum. Corresponding values of momentum, p, were converted to energy, E using the usual relativistic formula, viz:-

$$E = \sqrt{p^2c^2 + m^2c^4} \qquad \text{(i)}$$

By differentiation, the cell width correction arising may be shown to be:

$$\frac{dp}{dE} = 1 + \tfrac{1}{2}.\frac{(mc^2)^2}{E^2} \qquad \text{(ii)}$$

$$= 1 + \frac{.005586}{E^2} \qquad \text{(iii)}$$

taking the rest energy of the muon as 0.1057 GeV (Barkas et al, (1959)). The resulting converted spectrum is shown in Fig. 4.12.1.

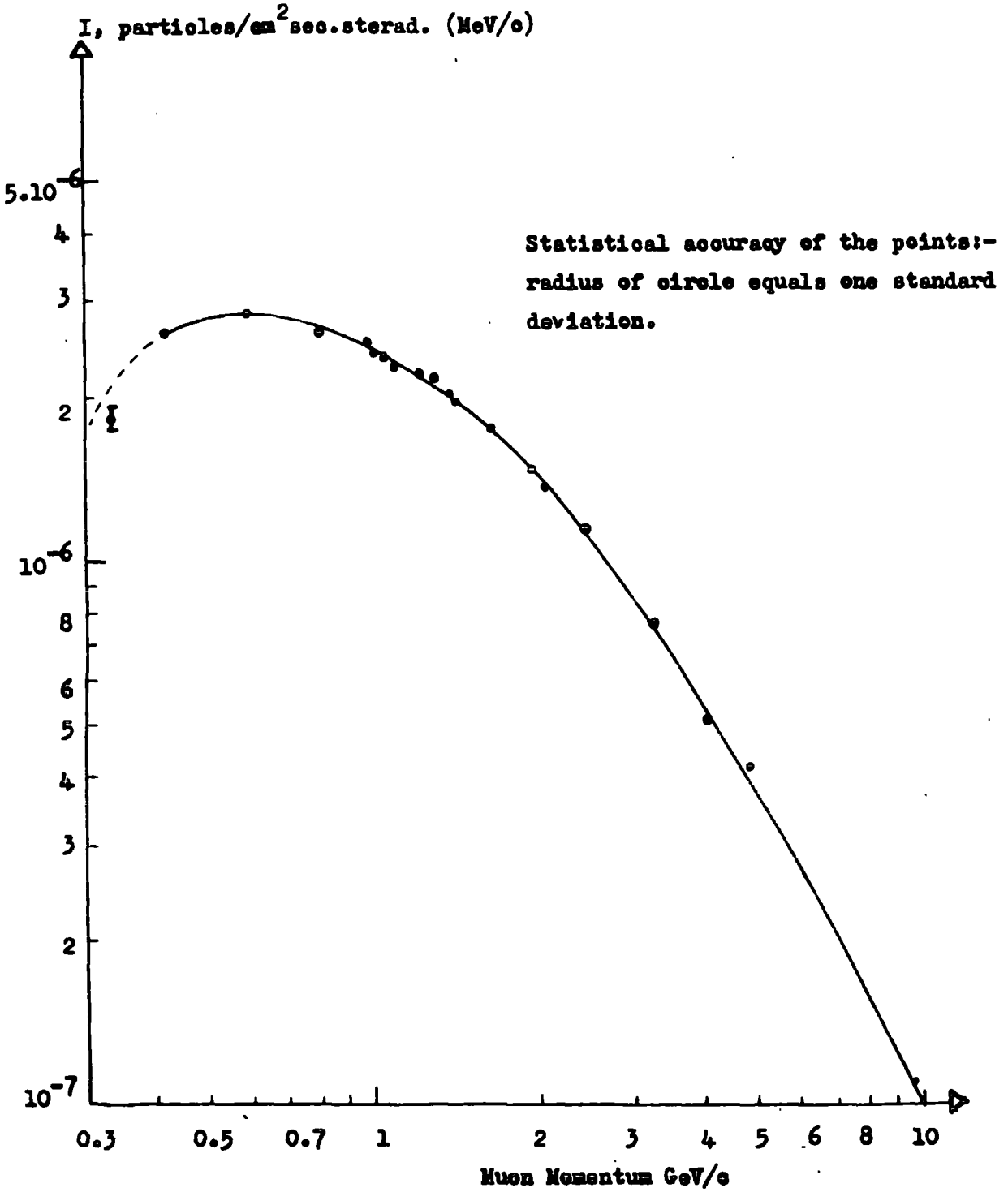

FIG. 4 . II . 1 Differential Momentum Spectrum of Muons at Sea-Level. Best curve fitted by a Relaxation Method.

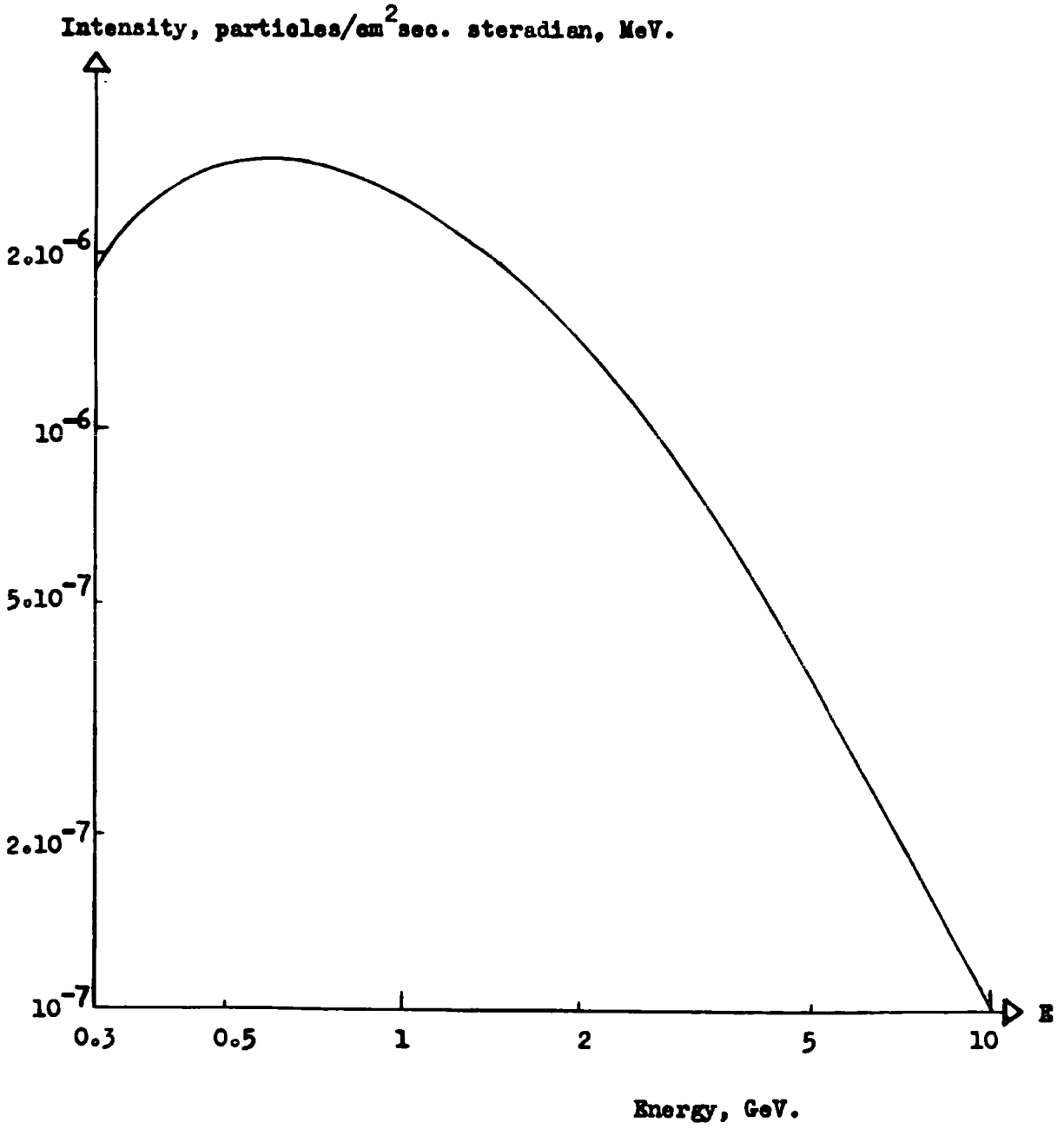

FIG. 4.12.1. The Sea-Level Energy Spectrum of Muons.

4.13. The Integral Momentum Spectrum

The integral momentum spectrum of muons at sea-level was obtained by integrating numerically the differential spectrum of Fig. 4.11.1., extended by addition of points from Ashton et al, (1960) (See Fig. 10.1.1.). The first mentioned curve covers the region from 0.4 to 10 GeV/c, the second from 10 to 1000 GeV/c. A total of 226 points (pairs of p, I values) were integrated using the trapezoidal rule, accurate since the cell width is small. The initial integral intensity at 1000 GeV/c was found as follows:-

If the differential spectrum above a certain momentum is represented by a power law of constant slope, , i.e.

$$I(p).dp_{(p>p')} = K.p^{-\gamma} \qquad \text{(i)}$$

which is the case at high momentum - (here p' was taken to be 1000 GeV/c) then the integral intensity at p' is:

$$\int_{p'}^{\infty} I(p).dp = \frac{K}{\gamma-1} \cdot p'^{-(\gamma-1)} \qquad \text{(ii)}$$

Substituting p' = 1000 GeV/c, γ = 3.24, K = 0.968 (observed values) one has:-

$$\int_{1000}^{\infty} I(p).dp = 8.2589.10^{-8} \text{ particles.cm}^{-2}\text{sec}^{-1}\text{sterad}^{-1}. \qquad \text{(iii)}$$

To obtain the integral intensity at any momentum p, below 1000 GeV/c it is only necessary to add $\sum_{p}^{1000} I(p).dp$ to the known integral intensity at 1000 GeV/c.

This was performed numerically using known values of p, I(p), from the differential spectrum, and corresponding small increments in p.

The result of such numerical integration (performed using the computer) is shown in Figs. 4.13.1. and 4.13.2. The last mentioned figure shows intensity as a percentage of that at 0.400 GeV/c as a function of p.

The intensity at p = 0.400 GeV/c is, for most practical purposes, that at zero momentum, the cell neglected, of width 0.4 GeV/c, contributing little to the total intensity since the spectrum is falling rapidly in the region 0.4 to 0 GeV/c. The spectra presented can therefore be taken to be, for most purposes, the integral muon spectra in the range 0 to 1000 GeV/c.

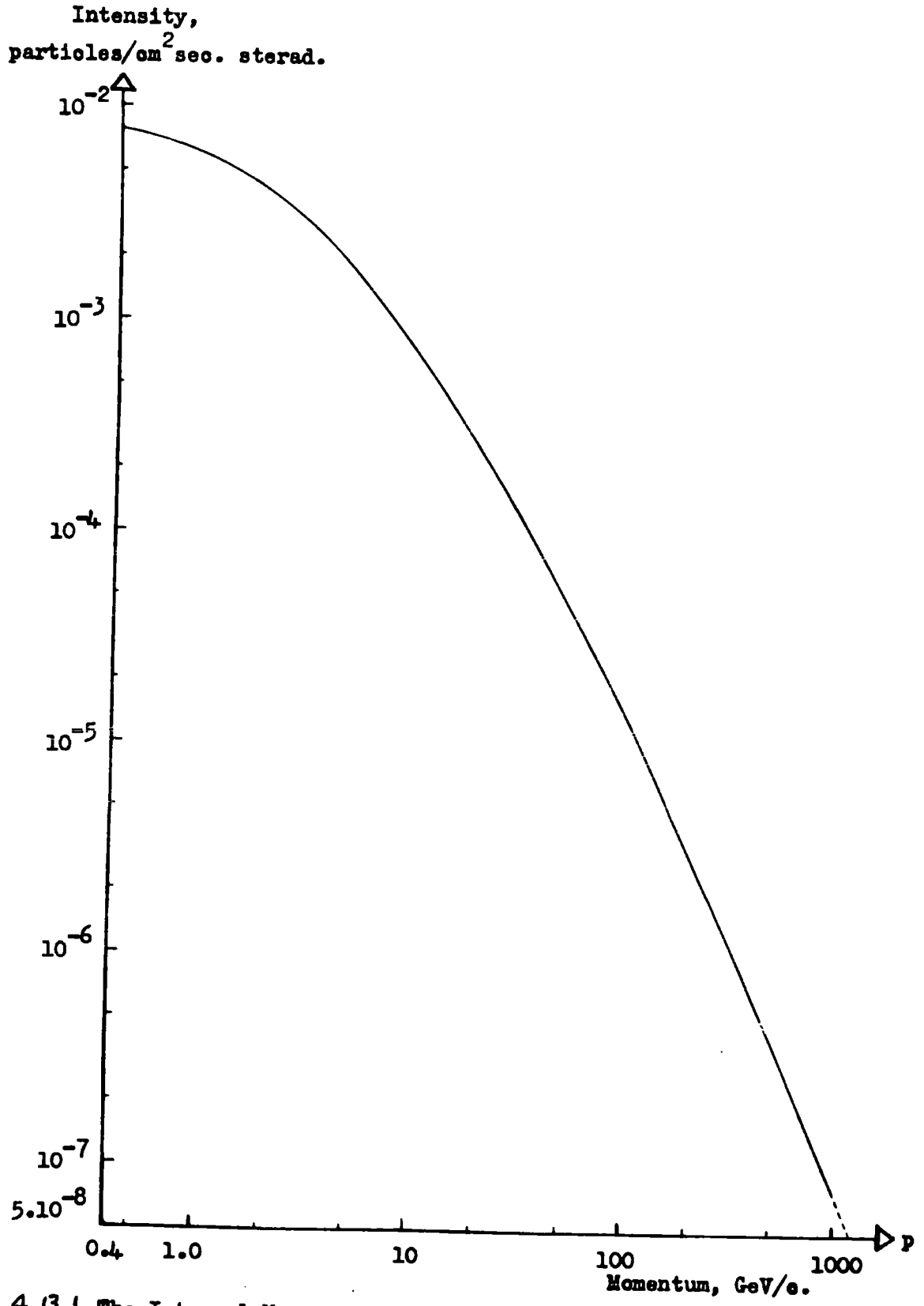

FIG. 4.13.1. The Integral Momentum Spectrum of Muons at Sea-Level.

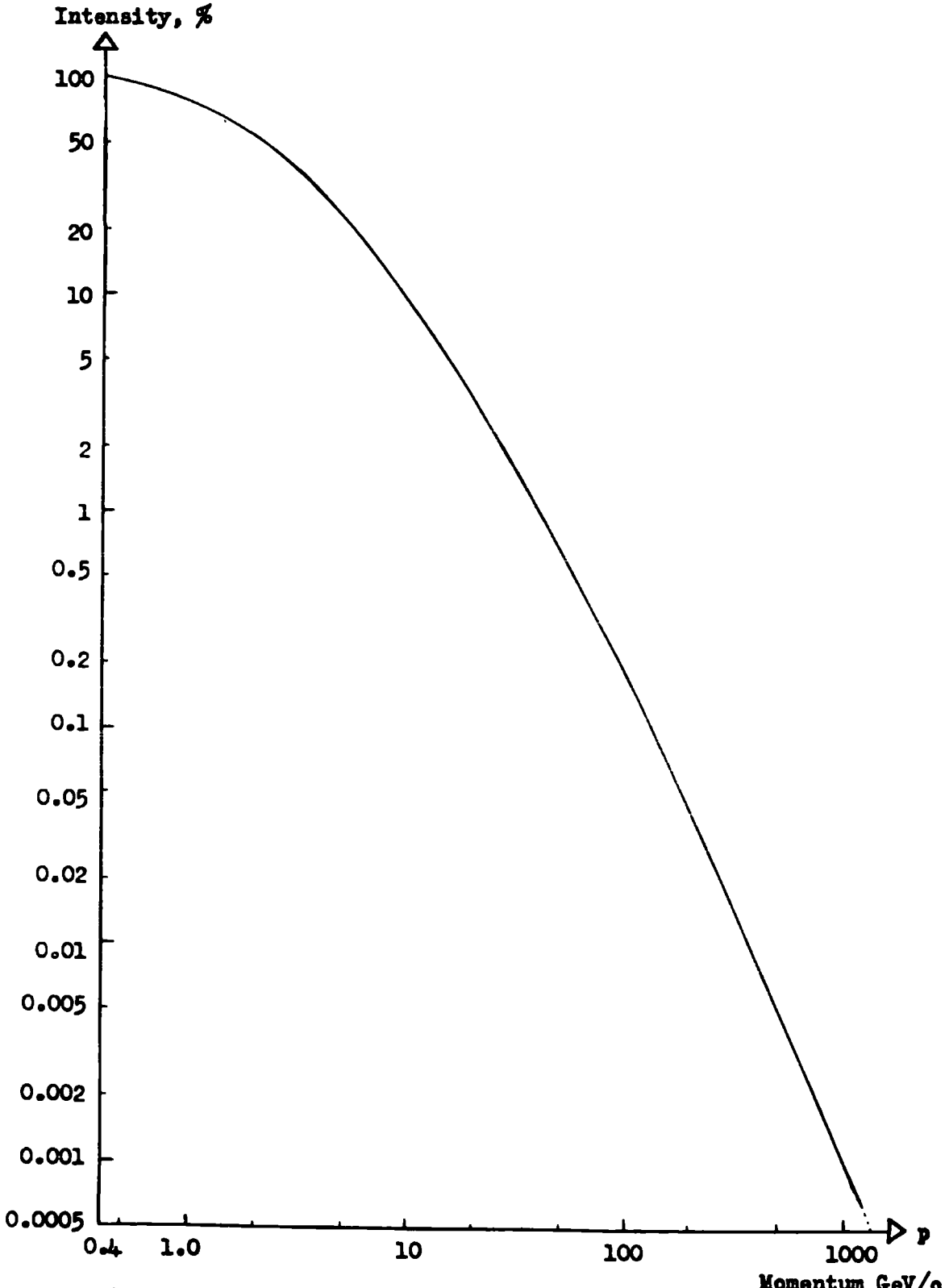

FIG. 4.13.2. Integral Intensity of Muons at Sea-Level
Expressed as a percentage of the Intensity above 0.4 GeV/c.

Chapter 5.

Bias Effects on the Spectrum

5.1. Multiple Events and Associated Phenomena.

Mention has already been made in Chapter 3 of the fact that only events triggering a single counter in each tray were recorded by the momentum analyser. Events in which two or more counters at any level were triggered were rejected. To estimate the effect of the rejection of such events on the final spectrum, an experiment was performed to measure the spectra of these events - the flash-tube spectrograph being used to record these. This involved adding an electronic unit, to feed a suitable triggering pulse to the flash-tubes when the multiple pulse discriminator circuit was triggered. The added circuit is detailed in Appendix A.5.1.1.

The nature of phenomena associated with multiple events may be briefly considered as follows - a very high energy primary cosmic ray ($>10^{15}$eV) will, in general, produce many particles on interaction - these in turn will interact producing a cascade of charged and neutral particles. The resulting particles at sea-level are termed a shower, this consisting mainly of electrons from the $\pi_0 \rightarrow 2\gamma, \gamma \rightarrow e^+ + e^-$ sequence, together with a few percent of mesons and nucleons. The electrons are mainly confined to an area about the 'core' or axis of

the shower, in the case of a large shower covering a radius of some few hundred metres at sea level. The density of muons falls off much less rapidly with distance from the core centre, and one of the two investigations made was in this region of low density of muons.

A second phenomenon leading to two or more particles being observed in any tray is the production of secondary electrons. The probability of a muon producing a knock-on electron in a given thickness of material is a slowly varying function of the muon momentum and is, for example, approximately 6% in a 1 cm lead plate, for muons of momenta greater than 10 GeV/c. (Lloyd and Wolfendale, 1959).

5.2. Observations

Operation of the spectrograph to obtain data for a single event spectrum yielded information that 20% of all hard particles traversing the instrument were recorded as 'multiple events'. Using the flash tube spectrograph in the way already outlined, 5988 multiple events were recorded in a total running time of 233 hours. These were analysed and classified into various types as will be outlined below.

Firstly the possibility of chance coincidences within the resolving time of the Rossi circuit, ($6\mu s$),

must be mentioned. It is possible for two consecutive single events to pass through different parts of the instrument within this time - the probability of the 5-fold coincidence required occurring may be shown to be negligibly small (.05%).

5.3. Analysis of Results

It was found on inspection that the events could be classified into 3 main types. These were:-

1) Events where one trajectory was seen passing through all 5 trays, and a second through tray A, which did not intersect in the layer of lead or the material of the counter trays. Such events were classed as 'double-muons'.

2) 'Knock-on' events, where a secondary electron was produced in the lead absorber above the instrument or in the material of the counter trays and two diverging tracks were seen in tray A.

3) Local showers or parts of dense extensive air showers where a large number of particles had traversed the instrument and no definite single particle paths could be defined. These events were not considered further on account of their complexity.

The film records of the flash tubes were analysed in the way already outlined in Chapter 3. The direction of the track was recorded by drawing directly onto a

reduced scale diagram of the instrument. This procedure was performed in turn for all 4 measuring trays, after which the particle paths were completed on each scale diagram. It was then possible to separate the accompanied muon events from the knock-on electron events. In the case of double muon events, since both particles come from well above the instrument both incident directions are parallel or nearly so. In contrast, the two tracks corresponding to a knock-on event intersect within the matter where the knock-on collision had occurred. Typical records of the two types of event are given in Figs. 5.3.1. and 5.3.2. respectively.

From the measurements made, the momentum, p, was found in the usual way. In each case a corresponding momentum spectrum was obtained. A check on accuracy was made by finding the distance separating the intersecting upper and lower parts of the trajectory of the fully recorded event at the axis of the magnet- those separated by more than 1.0 cm in this plane were rejected.

5.4. Double Muon Events

Only those events giving two tracks in tray A were analysed - since any event parallel to a fully recorded event must, if recorded, pass through this tray. The average density of the double events observed correspon-

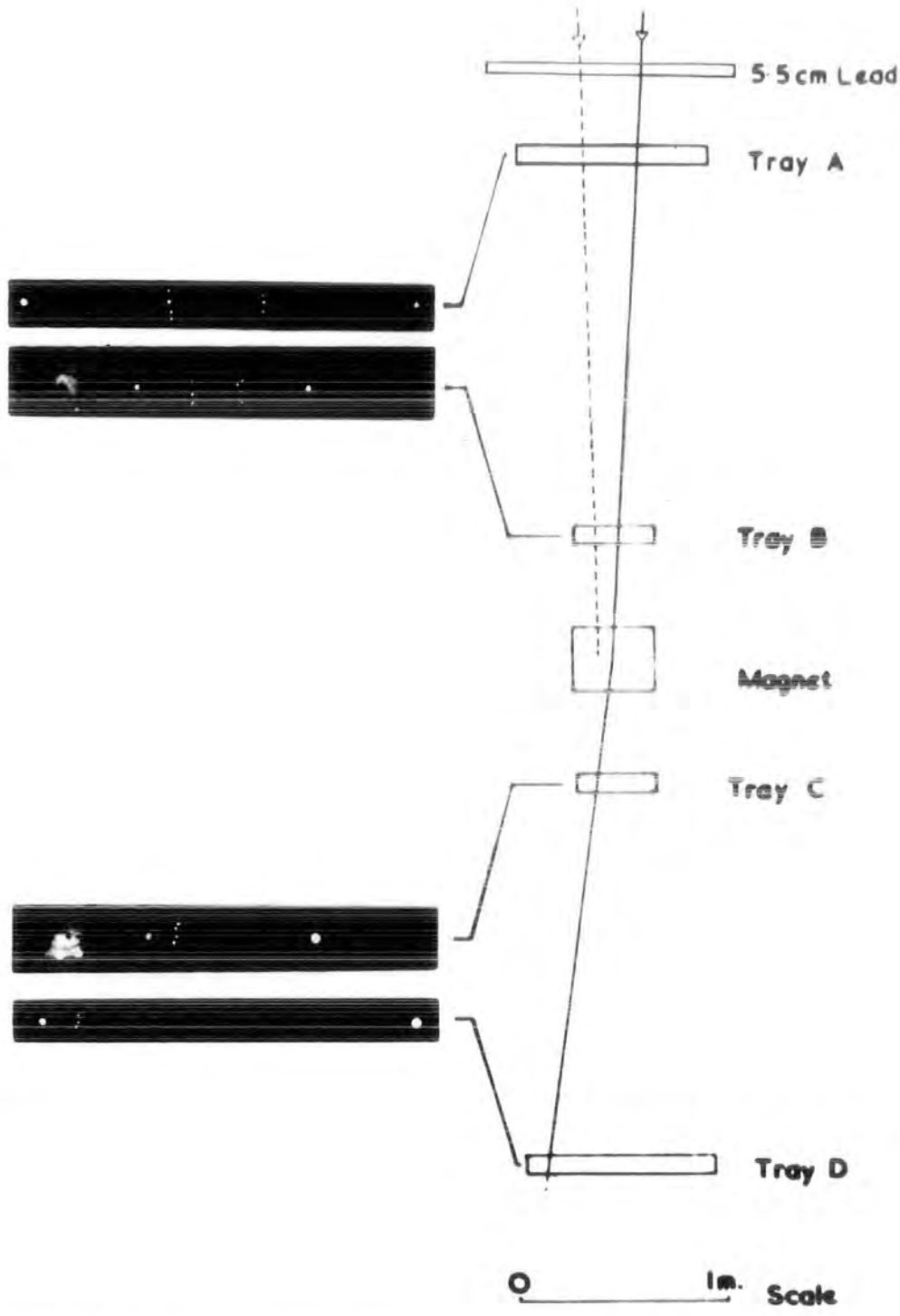

FIG. 5.3.1. Typical muon event accompanied by a second muon.

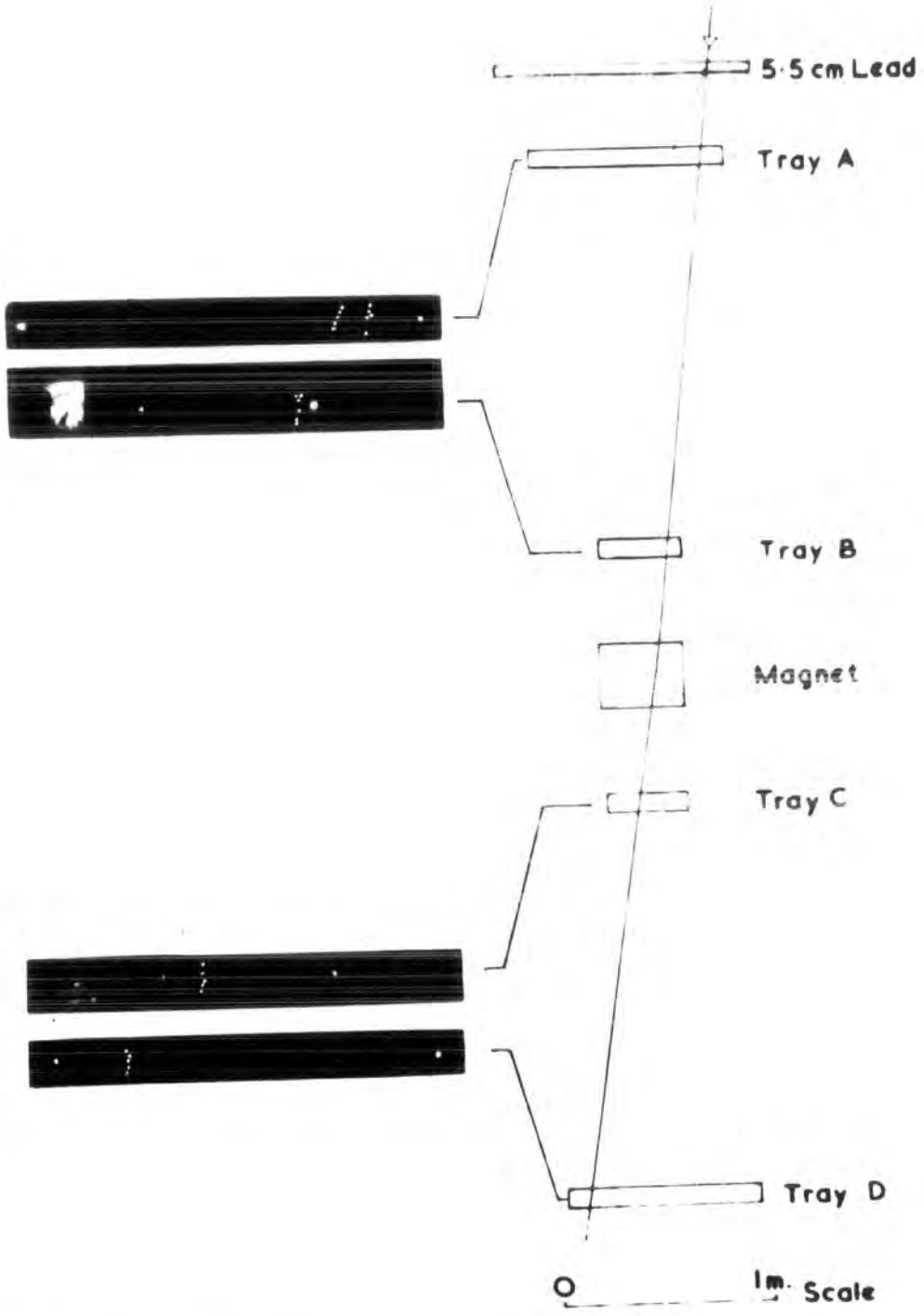

FIG. 5.3.2. Typical muon event accompanied by a knock-on electron produced in the lead absorber.

ded to a particle density of 2 particles within the area of tray A, or 3.7 particles.m^{-2}.

The first aim of the work was to search for these simultaneous muon events, and to define their rate, since if relatively frequent they would affect a spectrum based on single events, presented as the complete spectrum of muons. 112 such events were found in 5988 multiple events, giving a relative ratio to single muon events of 0.0047:1. The bias is hence very small, but to determine any differential effects a momentum spectrum for these events was found from the measured deflection spectrum, and is given, together with the single event spectrum normalised at a momentum of 1 GeV/c, in Fig. 5.4.1.

It can be seen that the differential bias (change in relative intensity of the two curves) with momentum is negligible, presence of double meson events of the density considered only affecting the normalisation factor of the spectrum by approximately 0.4%.

Two independent checks were made upon the nature of the accompanying particles which support the assumption that these are muons.

A first check was obtained by investigating the distribution of the angular separation of the particles by direct measurement from a drawing of each event. The observed distribution of separation angle versus frequency

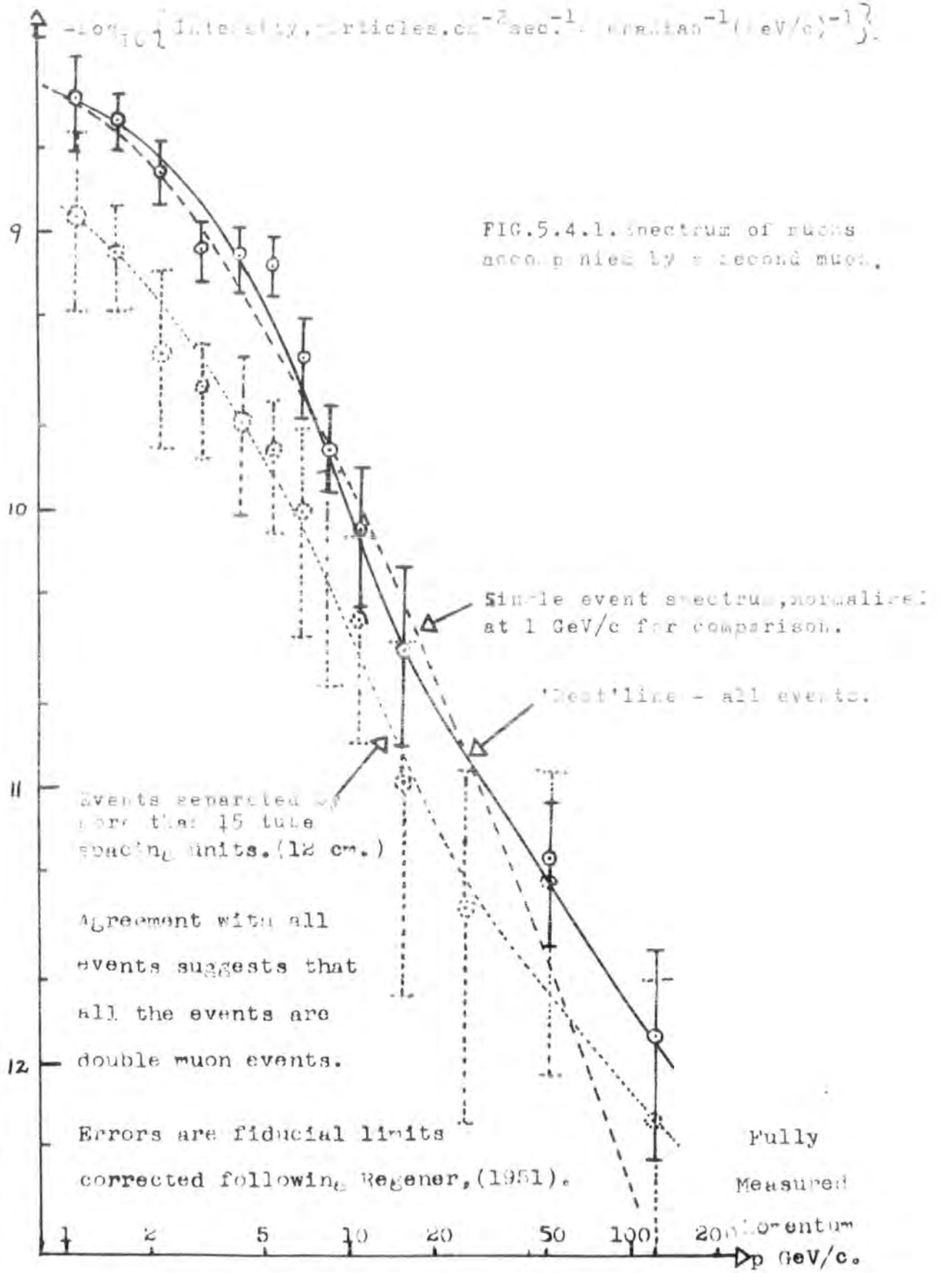

FIG.5.4.1. Spectrum of muons accompanied by a second muon.

is shown in Fig. 5.4.2., together with a $\cos^2$ distribution for comparison. If the events were independent, a $\cos^2$ distribution for angular separation would be expected from zenith angle intensity variations. (As mentioned in Chapter 3). The observed distribution was found to fall off much more rapidly than a $\cos^2$ distribution, verifying that the events were low density shower particles, the small angular separation showing that the shower apex is high in the atmosphere.

The second check was that the overall positive to negative ratio for the fully observed particles was $(1.21 \pm .12)$, this being in good agreement with that for single muons.

5.5. Knock-on Electron Events

Events of this type have been readily identified since the knock-on electron almost always comes from condensed matter (Fig. 5.3.2.). The two trajectories obtained on the scale drawing intersect either in tray A or in the lead.

Only those knock-on electrons produced in the lower few mm. of the lead emerge, since only primary muon momenta of less than 10 GeV/c are considered. Comparison with previous work using lead plates thicker than this 'maximum range' may be made, and the bias at low momentum ($\leq$10 GeV/c) is hence independent of the amount

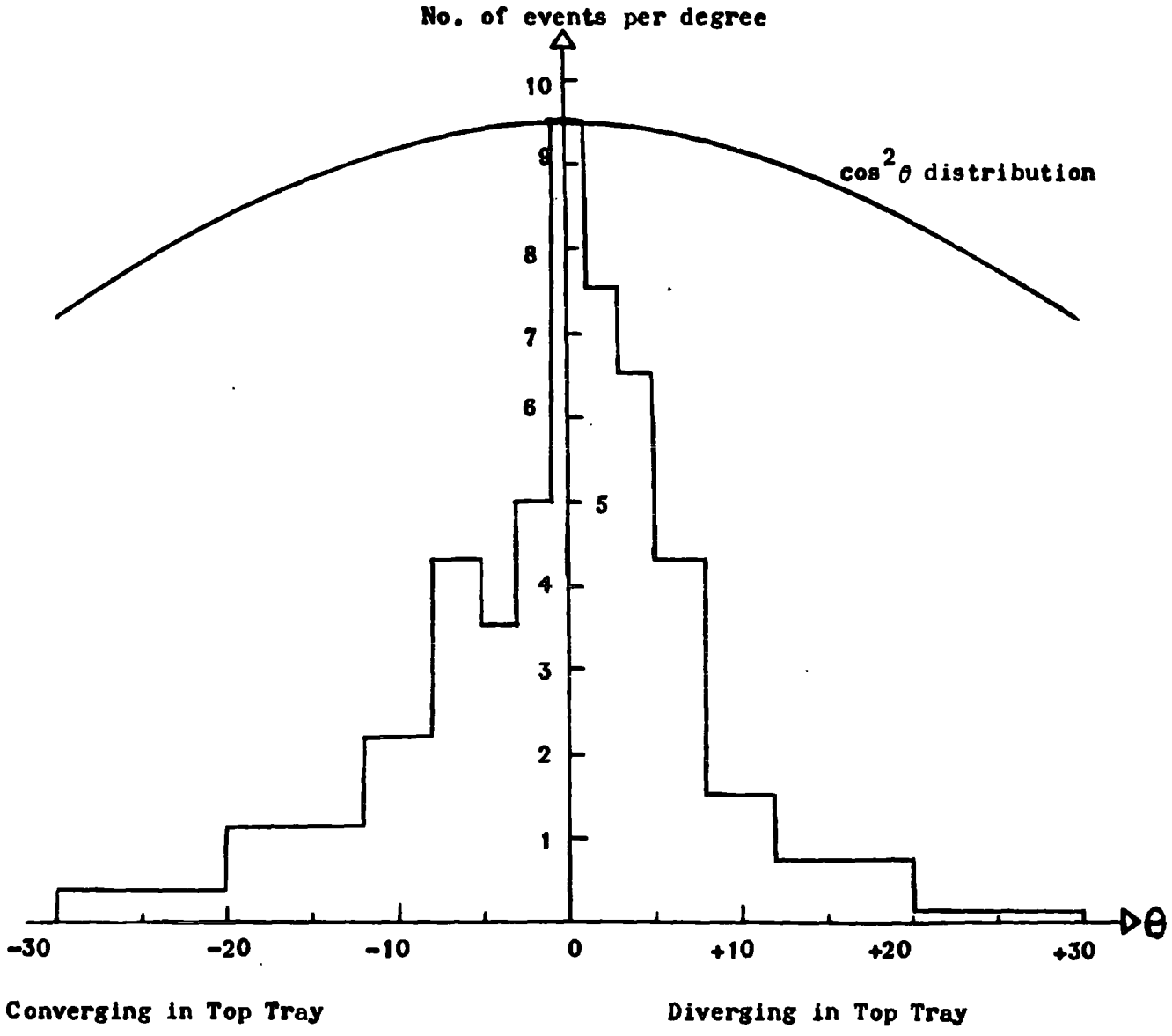

FIG. 5.4.2. Distribution of Angles Between Double Muon Events, Compared with a $\cos^2\theta$ distribution.

of condensed matter above the instrument, over and above a few mm. (7 mm. from the range of 10 MeV/c electrons, the most probable momentum from the highest primary momentum considered).

One hundred and six such events were measured fully, and their momentum spectrum is shown in Fig. 5.5.1. The relative intensity of accompanied events to single events can be seen to increase with momentum as would be expected from the work of Lloyd and Wolfendale. The relative bias would appear to increase from 1 at 1 GeV/c to an approximately constant value of 2.8 above 4 GeV/c. Since this bias is known to be approximately 4.5% above 4 GeV/c (from Lloyd and Wolfendale) the bias at 1 GeV/c is thus of the order of 1.6%.

5.6. Events Producing High Density Records.

No measurements were made on events producing a high density of particles, i.e. more than four or five tracks in any tray, often many tracks being observed. However, from a knowledge of momentum of particles as a function of distance from the shower core (Coxell, 1961), it would appear that such particles have a momentum around or above 10 GeV/c in or near the instrument. This leads one to conclude that no significant bias arises from such events within the momentum range considered here.

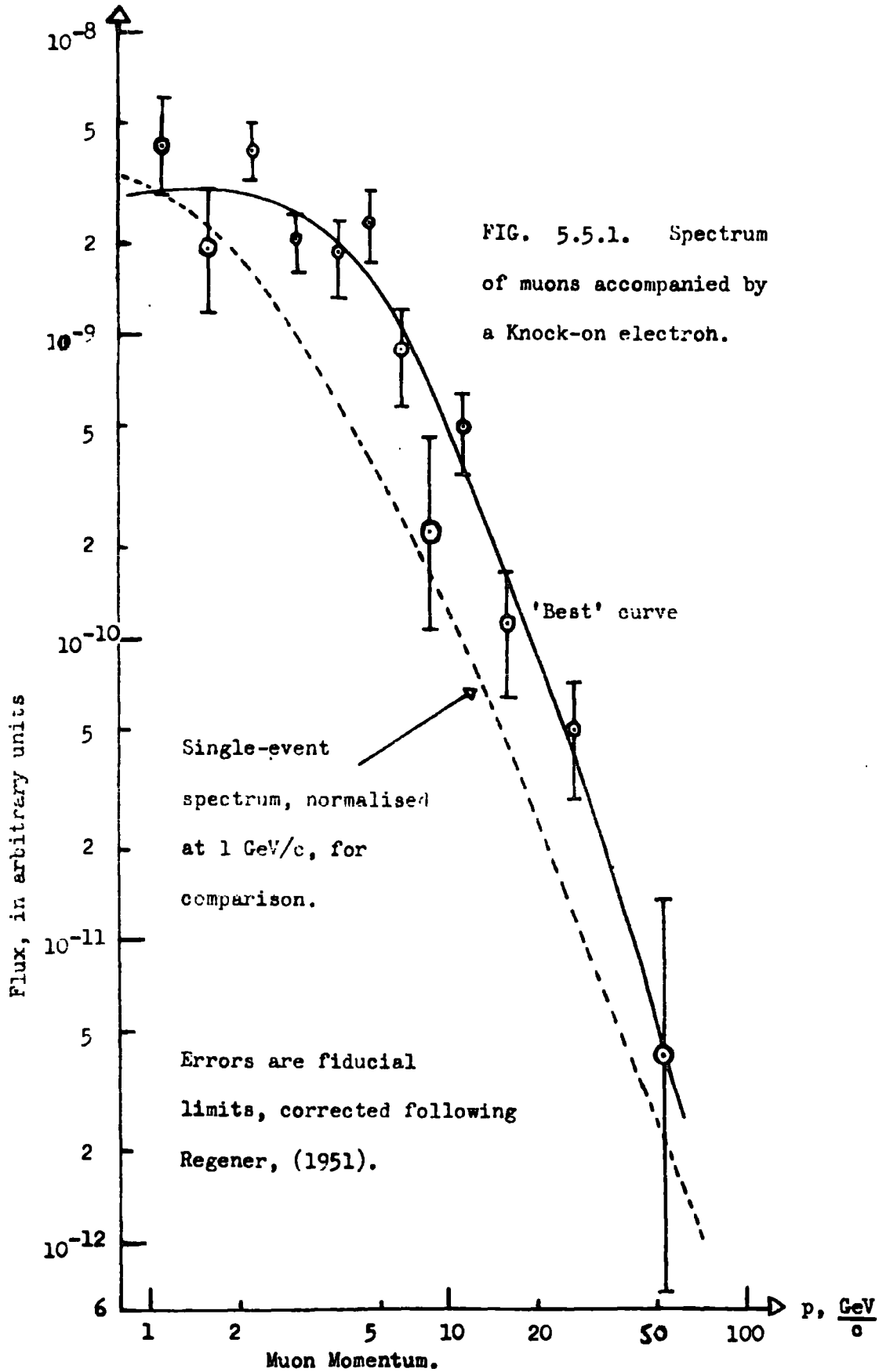
FIG. 5.5.1. Spectrum of muons accompanied by a Knock-on electron.
'Best' curve
Single-event spectrum, normalised at 1 GeV/c, for comparison.
Errors are fiducial limits, corrected following Regener, (1951).
Flux, in arbitrary units
Muon Momentum.
p, GeV/c
10^-8
5
2
10^-9
5
2
10^-10
5
2
10^-11
5
2
10^-12
6
1
2
5
10
20
50
100

5.7. Conclusions with Regard to Spectrum Bias

The possible bias due to low density double muon events has been shown to be negligibly small and that due to high density showers may be neglected for the reasons stated above. The bias due to knock-on electrons is shown to vary from approximately 1.6% at 1 GeV/c i.e. of the order of the statistical accuracy of the present work at that momentum, to approximately 4.5% above 4 GeV/c. The greater majority of the multiple events are of this type.

A final curve for the sea level muon spectrum, being the smooth curve of Fig. 4.11.1. corrected for knock-on electron bias, is presented in Fig. 5.7.1. This is the most accurate sea-level muon spectrum from the present observations.

A similar bias to that in the Durham case exists in the other work, and the spectrum as presented before correction for bias was used for comparison, so as to make comparisons under similar conditions.

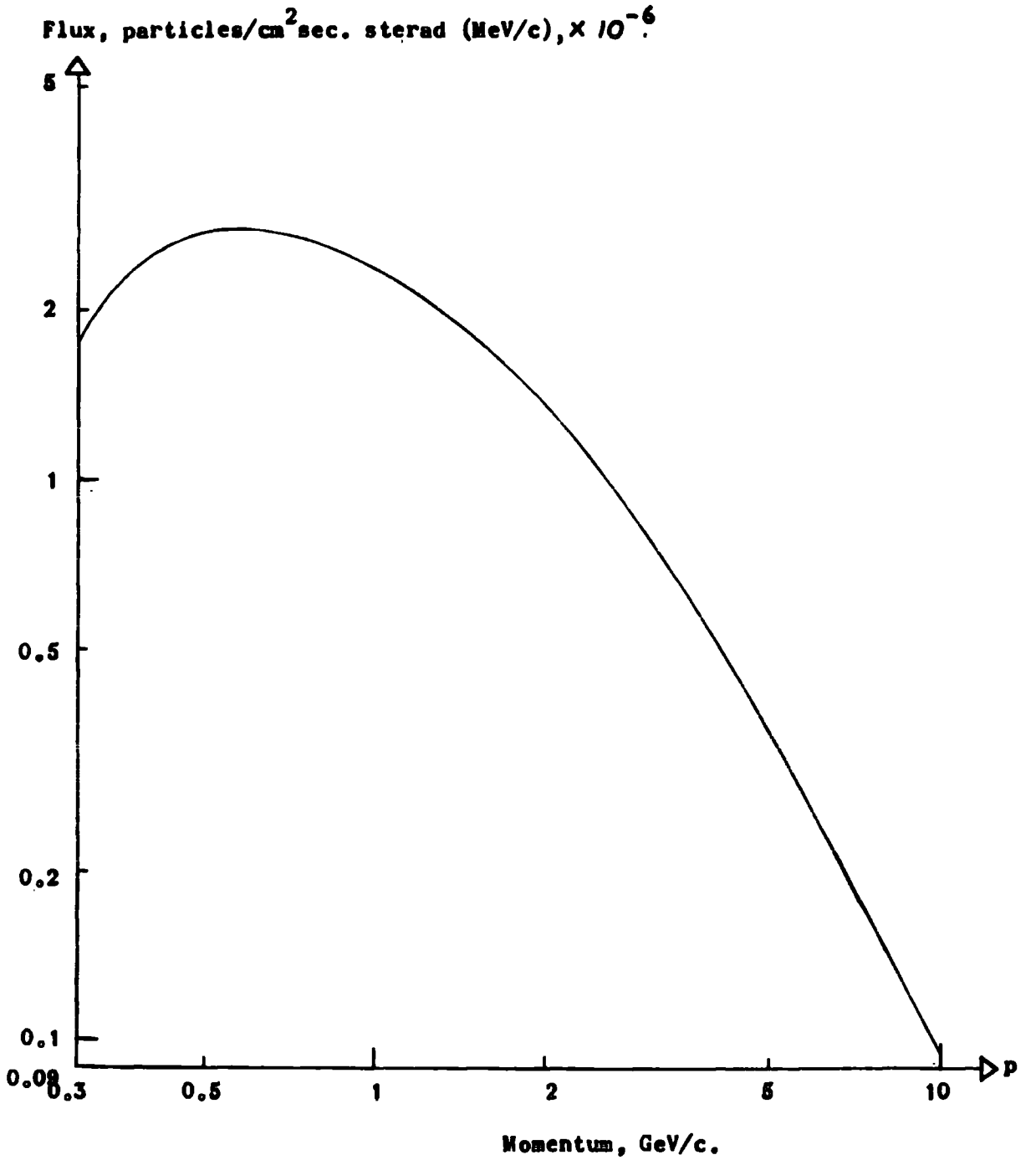

FIG. 5.7.1. Final Differential Sea Level Spectrum of Muons, being the Curve of Fig. 4. II. 1. corrected for Bias Effects

Chapter 6.

Comparison with Other Workers

6.1. Procedure

A comparison has been made between the spectrum presented in Fig. 4.11.1. and those obtained by other workers, already detailed in Chapter 2. In Chapter 5 it has been shown that bias effects are small in the range covered by this work (0.4 to 10 GeV/c) - a comparison was made with other single event spectra for reasons already mentioned (Section 5.7).

6.2. Spectra normalised to that of Rossi

Three plots have been made of sets of comparison curves. Fig. 6.2.1. shows those spectra which have been normalised to the Rossi spectrum (1948) at 1 GeV/c. With the exception of Allkofer's work, which is relatively inaccurate statistically compared to that of Owen and Wilson, and Rossi (based on the results of several workers), agreement is obtained to approximately (+10 to -5)%. Considering the fact that most spectra are presented with a logarithmic plot of intensity, from which it is difficult to read to better than $\pm 3\%$, this is considered satisfactory. Variations from the Durham spectrum are random, hence it is believed that the Durham spectrum resolves the small discrepancies in previous work.

The work of Pine et al (1959) is a recent signifi-

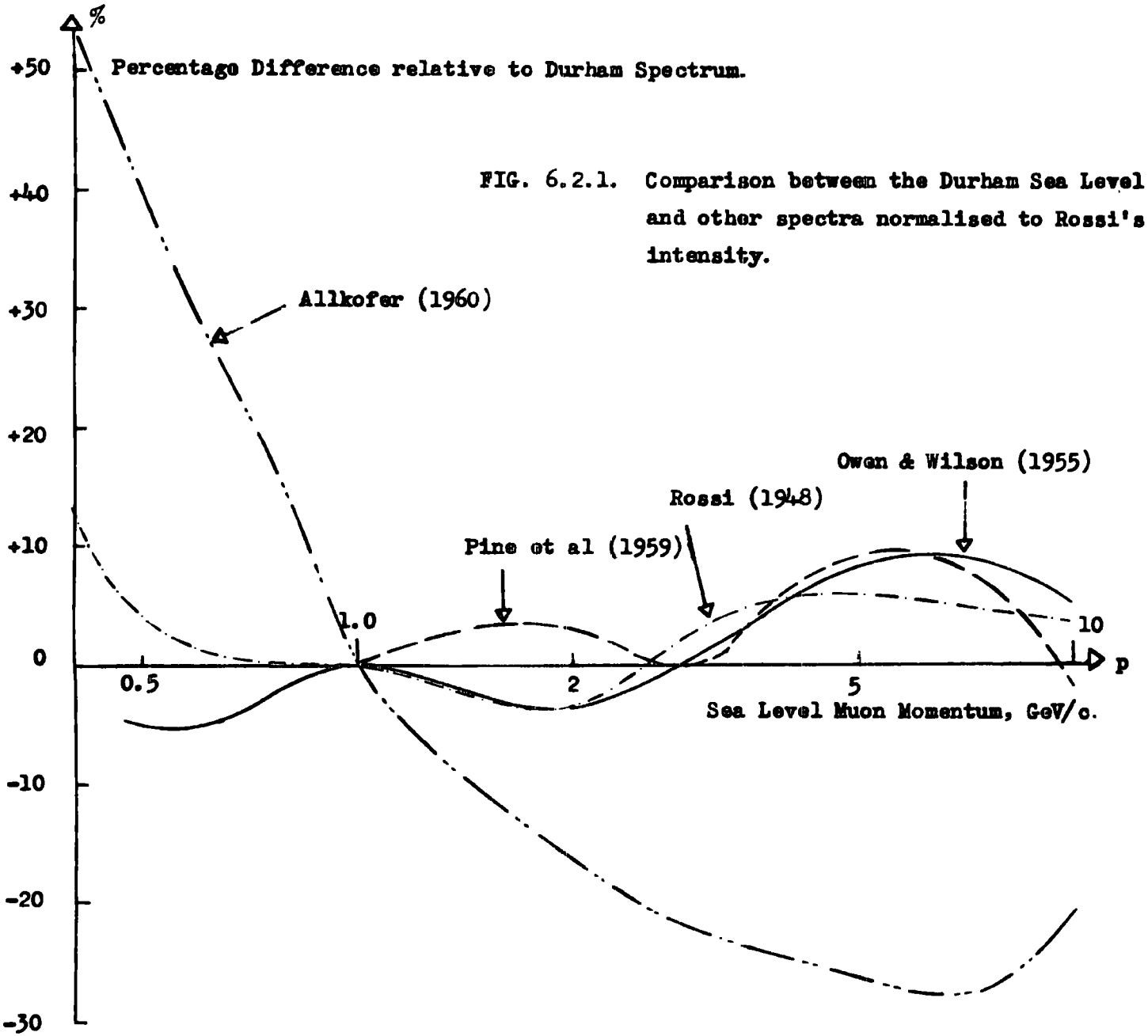

FIG. 6.2.1. Comparison between the Durham Sea Level Spectrum and other spectra normalised to Rossi's 1 GeV/c intensity.

cant measurement - intensities were calculated from the known acceptance and efficiency of their instrument. However, no corrections would appear to have been made for scattering or momentum loss within the apparatus, no mention of these factors being given. In view of the cloud chambers within the geiger counter measuring levels, these factors will be applicable, and the factor of differential knock-on bias may become important. Insufficient data on the mass of material in the beam is available for correction to be made by the present author. The spectrum intensities given by Pine will be reduced by correction for scattering (i.e. 'noise' scattering, as discussed in Chapter 4) and increased very slightly if a small differential bias due to knock-on events applies. These factors would bring this work into closer agreement with the present and previous work.

6.3. Spectra not Normalised to Rossi

The second plot (Fig. 6.3.1.) shows those spectra not normalised to Rossi's spectrum at 1 GeV/c. Here, since there is no unique point of agreement the variations are greater and more random. The work of Caro et al (1950) and Moroney and Parry (1954), found to differ from previous accurate work, has again been found to differ from the present work. No reason is immediately obvious - it has been stated by these workers that there was little absorbing and scattering material in the

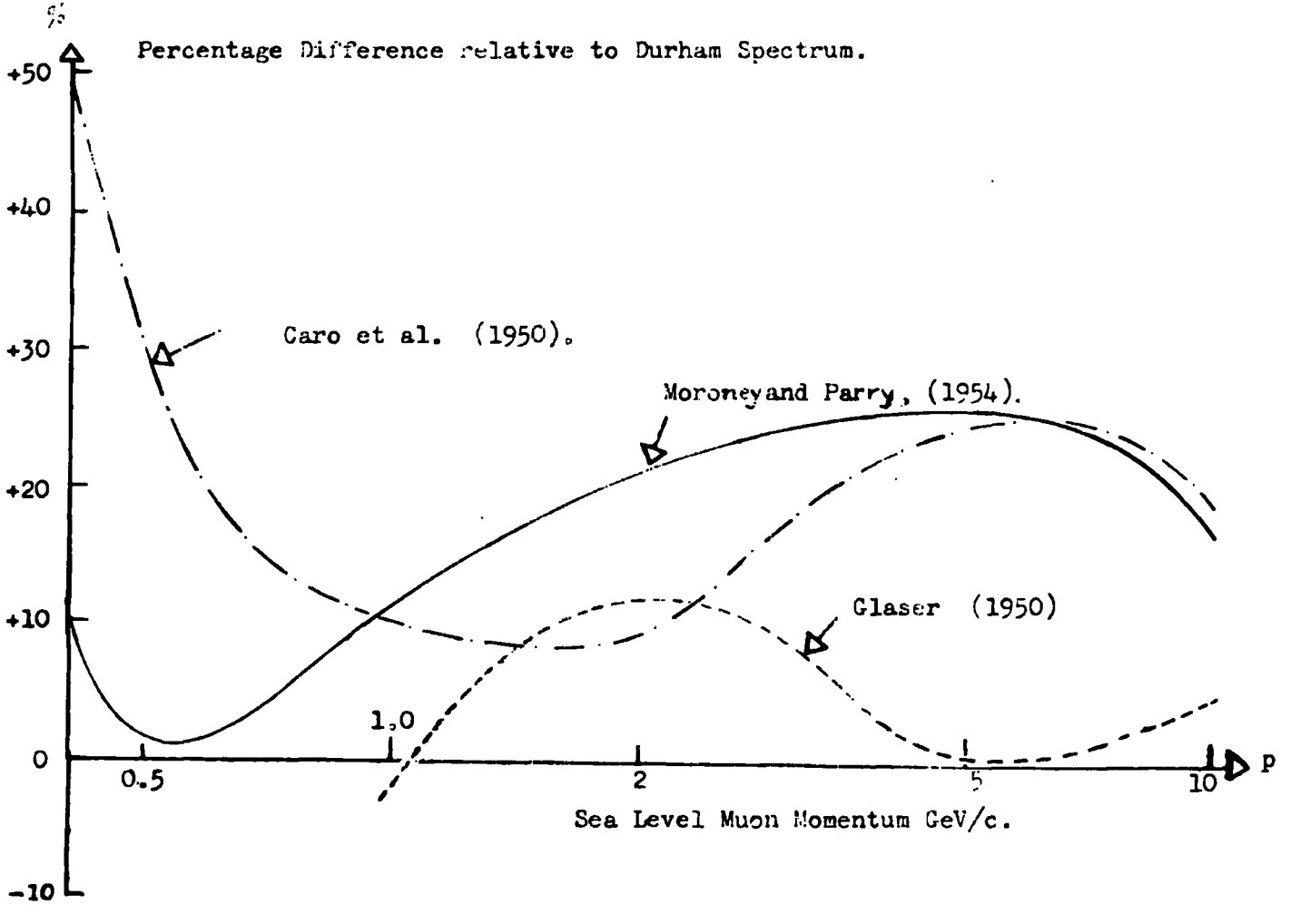

FIG. 6.3.1. Comparison between the Durham Sea Level Spectrum and other spectra not normalised to Rossi's 1 GeV/c intensity.

beam of the particles, hence it would not be expected that the discrepancy is due to a bias effect. The work of Glaser, (1950) of relatively low statistical accuracy, is regarded as being within the agreement expected.

6.4. Spectra Re-normalised to Rossi

In Fig. 6.4.1. the work described in Section 6.3. is shown after re-normalisation of each curve to Rossi's intensity at 1 GeV/c. Much closer agreement is now obtained with the present work, agreement being generally within the range (+10 to -5)%.

6.5. Possible Latitude Effects

The effect of variations in latitude of places of measurement of the 'hard' cosmic ray spectrum has been computed by Olbert (1954). Curves for variation versus range are presented - using Sternheimer's (1959) range-momentum relationship for muons in air (see Fig. 7.1.2.). The results given were converted to a momentum-intensity variation with latitude (Fig. 6.5.1.). It can be seen that above 1 GeV/c, differences of less than 1.8% per 10° change in latitude are to be expected, the difference increasing with decreasing momentum. Though possibly accounting for part of the discrepancy between the work of Caro et al and Moroney and Parry (47°S) and the present work (54°N), this does not fully explain the observed difference.

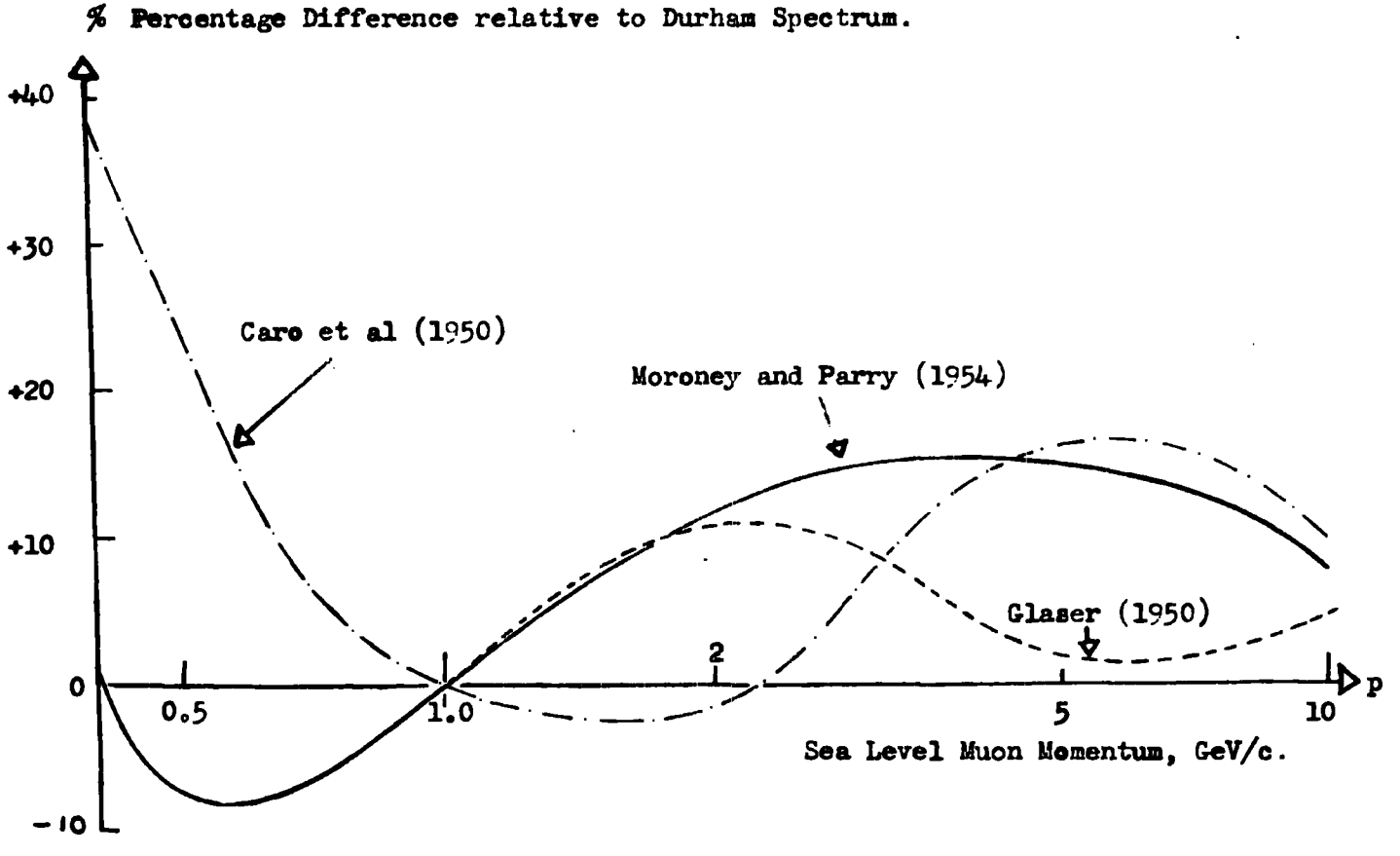

FIG. 6.4.1. Comparison between the Durham Sea Level Spectrum and the curves of FIG. 6.3.1. Normalised to Rossi's 1 GeV/c intensity.

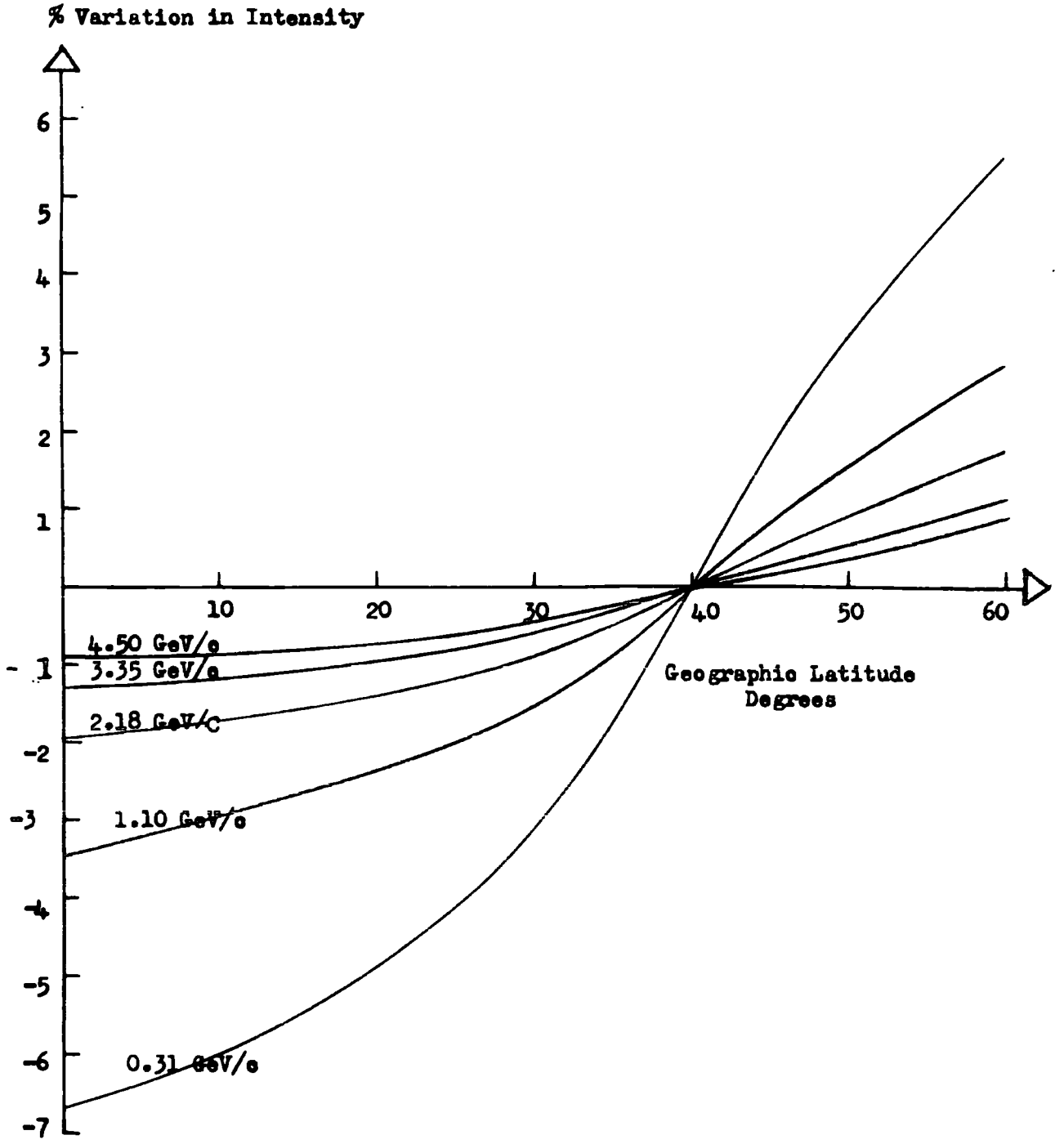

FIG. 6.5.1. Variation in Sea-Level Muon Intensity with Latitude, and a Function of Momentum.
(Calculated from Data of Olbert, 1954).

Chapter 7.

Derivation of the Pion Generation Spectrum

7.1. A Simple Propagation Model - Unique Generation Height

The muons observed at sea level are now known to come almost certainly from the decay of pions, generated in turn by the interaction of primary cosmic rays with the atmosphere. An alternative process, other than the primary-pion-muon sequence is the sequence primary-kaon-muon. The second process has been shown to yield a negligible intensity of muons at sea level with momentum below 15 GeV/c compared with that due to the first process. This follows from the work of Kocharyan et al, (1960) in which polarisation of the muons was measured. Kaon generation would yield different polarisation to pion generation, and the latter was shown to predominate.

Many early workers (e.g. Owen and Wilson 1955) followed Duperier, (1951) who assumed a unique depth of generation of pions by the primaries (100 $g.cm^{-2}$) and then showed that such an assumption would only result in a few percent error compared with distributed production. It has generally been assumed that the path length of pions before decay is negligible. For the momenta considered in the present work this assumption is correct - the mean range of a pion of momentum p_π GeV/c is $\bar{S} = 772\left\{\frac{p_\pi}{m_\pi c} - \frac{m_\pi c}{2p_\pi}\right\}$ cm. (See Appendix A. 7.1.1.).

Thus a pion of momentum 10 GeV/c will have a mean range of 0.55 Km which at the 100 $g.cm^{-2}$ layer is a mean depth of 7.86 gm. cm^{-2}.

The effective unique height of formation of muons is thus known, so that by multiplying the intensity at sea-level by the inverse probability of survival and a correction for momentum loss causing effective cell width change, also adding an appropriate momentum loss to the momentum at sea level, a production spectrum of muons may be obtained.

The cell width correction is a simple correction, as follows:- if the I_s particles in a cell of width δp_s at sea level occupy a cell of width δp_t at depth t in the atmosphere, then the number I_t in the corresponding cell must be the same

Hence:- $$I_s.\delta p_s = I_t.\delta p_t$$

$$\text{or} \quad I_t = \frac{\delta p_s}{\delta p_t} \times I_s$$

Allowing δp_s and δp_t to become infinitesimally small, then:-

$$I_t = \frac{dp_s}{dp_t} \times I_s \qquad (i)$$

The survival probability, P, is given by an expression due to Owen and Wilson (1955), verified in Appendix A.7.1.2.

$$\ln P = \frac{-h_o}{\tau_o} \cdot \frac{\mu}{p+p_o} \ln\left\{\frac{t_o}{t} \cdot \left[1+\frac{p_o}{p}\left(1-\frac{t}{t_o}\right)\right]\right\} \quad \text{(ii)}$$

where h_o is the scale height of the atmosphere, taken to be a mean value of 7.02 Km. for this purpose (See Rossi, 1952c), τ_o is the mean lifetime of a muon, 2.22 x 10^{-6} sec; μ its rest energy, 105.7 MeV. (Barkas et al, 1958); p its sea-level momentum, p_o the momentum loss it would undergo in traversing the whole atmosphere of depth t_o (1033 g. cm^{-2}) and t is its production height. A series of values of P for t = 50, 100 and 150 g.cm^{-2} are given in Fig. 7.1.1.

Rearranging the equation, evaluating the first (constant) terms and letting Δp be the momentum loss from the depth t to sea-level, it can be seen that:-

$$\ln P = -\frac{1.174}{p+p_o} \ln\left[\frac{t_o}{t}\left(\frac{1+\Delta p}{p}\right)\right] \quad \text{(iii)}$$

This is a form convenient for computation.

The generated differential muon spectrum may then be seen to be:-

$$(I_\mu)_t \cdot dp_t = I_s \times \frac{dp_s}{dp_t} \times \frac{1}{P}$$

Assuming a median angle of emission of the muons from pion decay, it can be shown that (Appendix A.7.1.3.):-

$$p_\pi = \frac{1}{r} \cdot p_\mu \quad \text{(iv)}$$

and correspondingly a cell width correction of r must be applied to the muon intensity to transform it to the corresponding pion intensity. Thus, at height t, p_π is

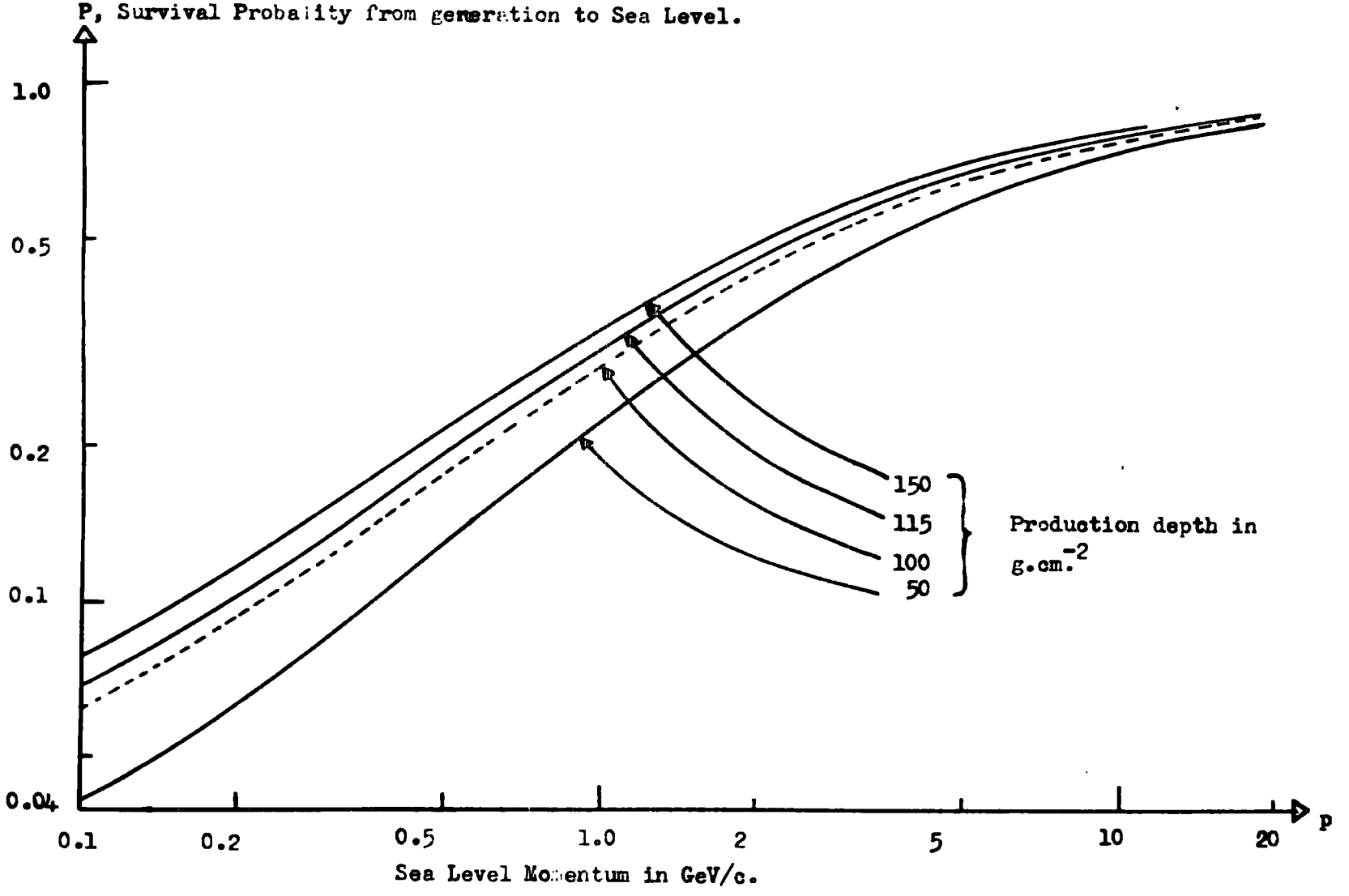

FIG.7.1.1. Survival Probability as a function of Sea Level Momentum, for a series of production depths.

given by (iv) above, and:-

$$(I_\pi)_t = r.\ (I_\mu)_t \qquad \text{(v)}$$

hence

$$I_\pi = I_s \times \frac{dp_s}{dp_t} \times \frac{1}{p} \times r \qquad \text{(vi)}$$

Pine et al (1959) showed that a small modification for the number of pions interacting may be obtained from the diffusion equation of the pions:-

Fractional loss of pions by interaction

$$= \frac{1}{1+\frac{p_\mu}{B'}} \qquad \text{(vii)}$$

where B' is a constant equal to 91 GeV/c and r (Pine's value) is equal to 0.76.

The final equation for the single height differential pion generation spectrum is thus:-

$$(I_\pi)_t = I_s \times \frac{dp_s}{dp_t} \times \frac{1}{p} \times r \left(\frac{1+p_\mu}{91} \right) \qquad \text{(viii)}$$

This was evaluated for the Durham sea level muon spectrum by the author for a unique production depth of 115 $g.cm^{-2}$ (suggested by Olbert, 1954), with momentum loss following the momentum-range relation of Sternheimer 1959 (Fig. 7.1.2.). The schematic process is shown in Fig. 7.1.3. and the result in Fig. 7.1.4.

7.2. Extended Generation Model

7.2.(i) Previous Attempts

The model already described is only correct to within a few percent due to the nature of the assumptions

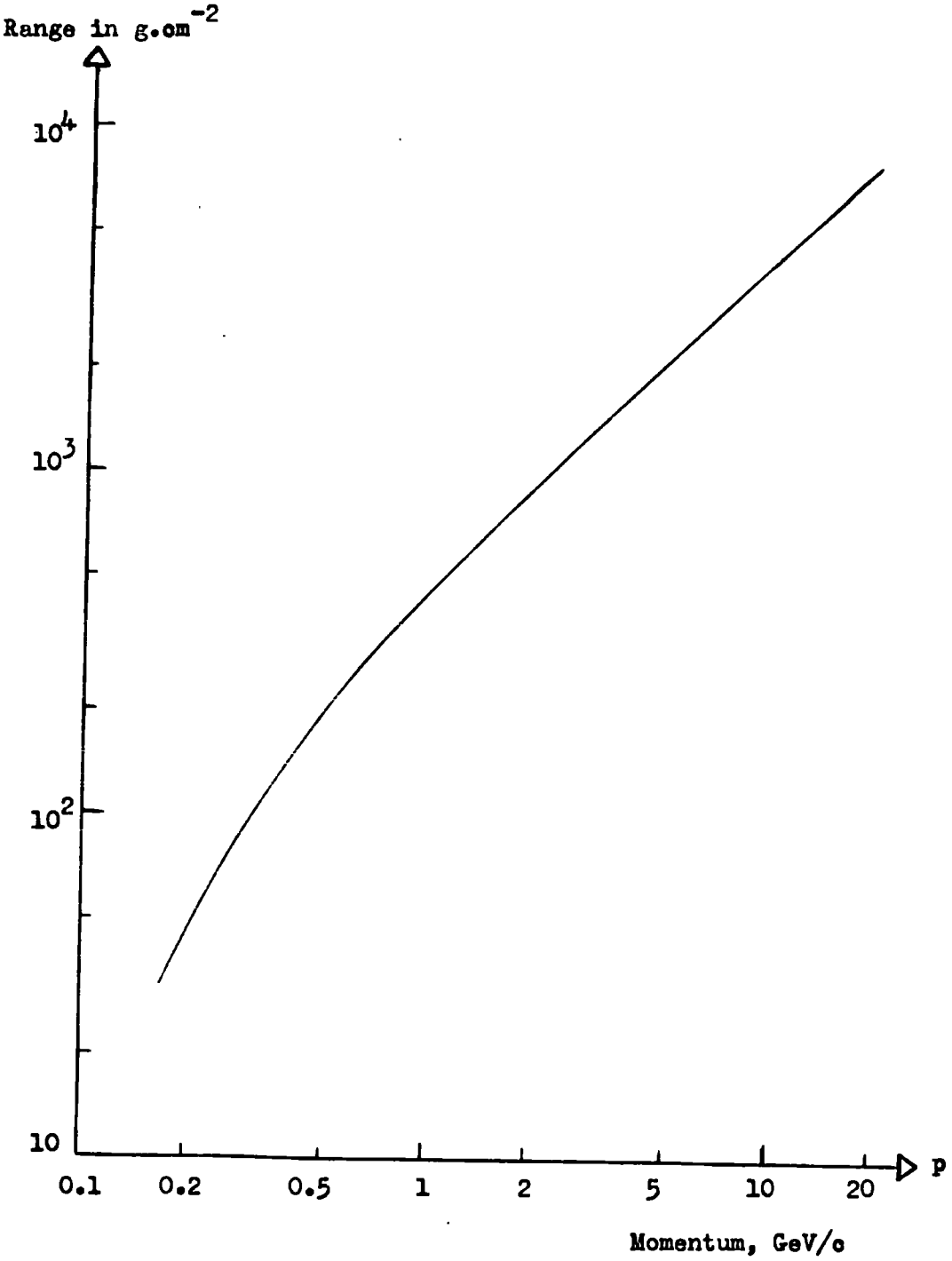

FIG. 7.1.2. Range Momentum Curve for Muons in Air

(After Sternheimer, 1959).

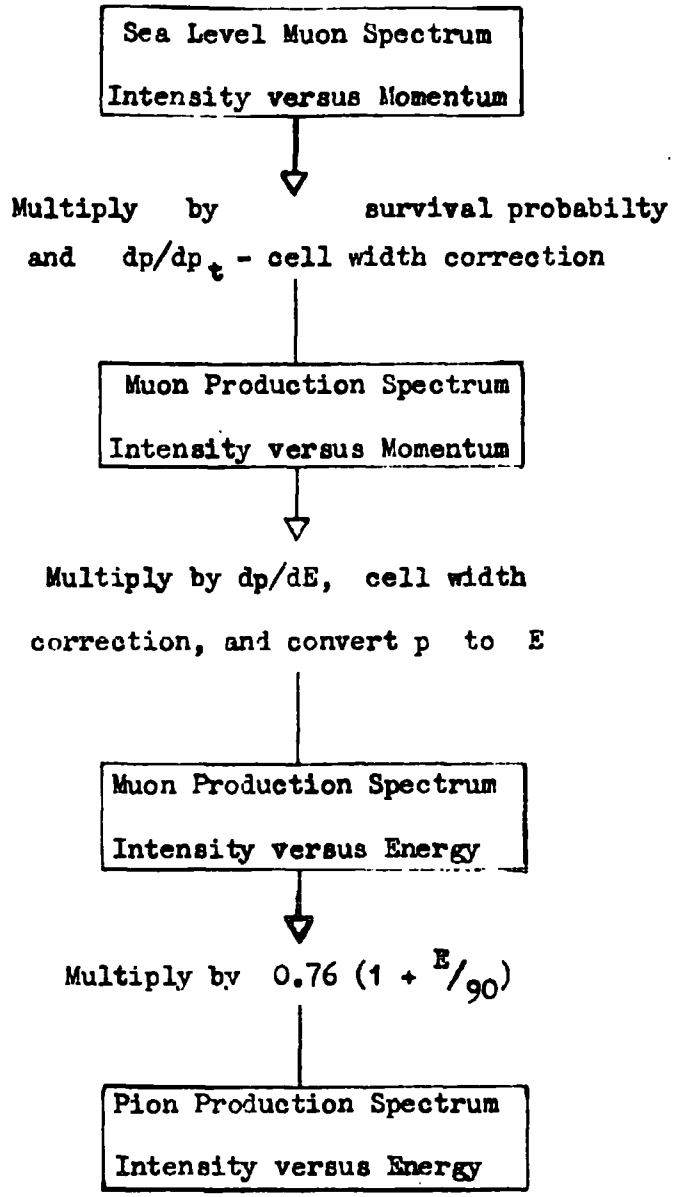

FIG. 7 .1.3. Schematic diagram of derivation of the Pion Generation Spectrum from the Sea-level Muon Spectrum assuming Unique height of Muon production and varying momentum loss.

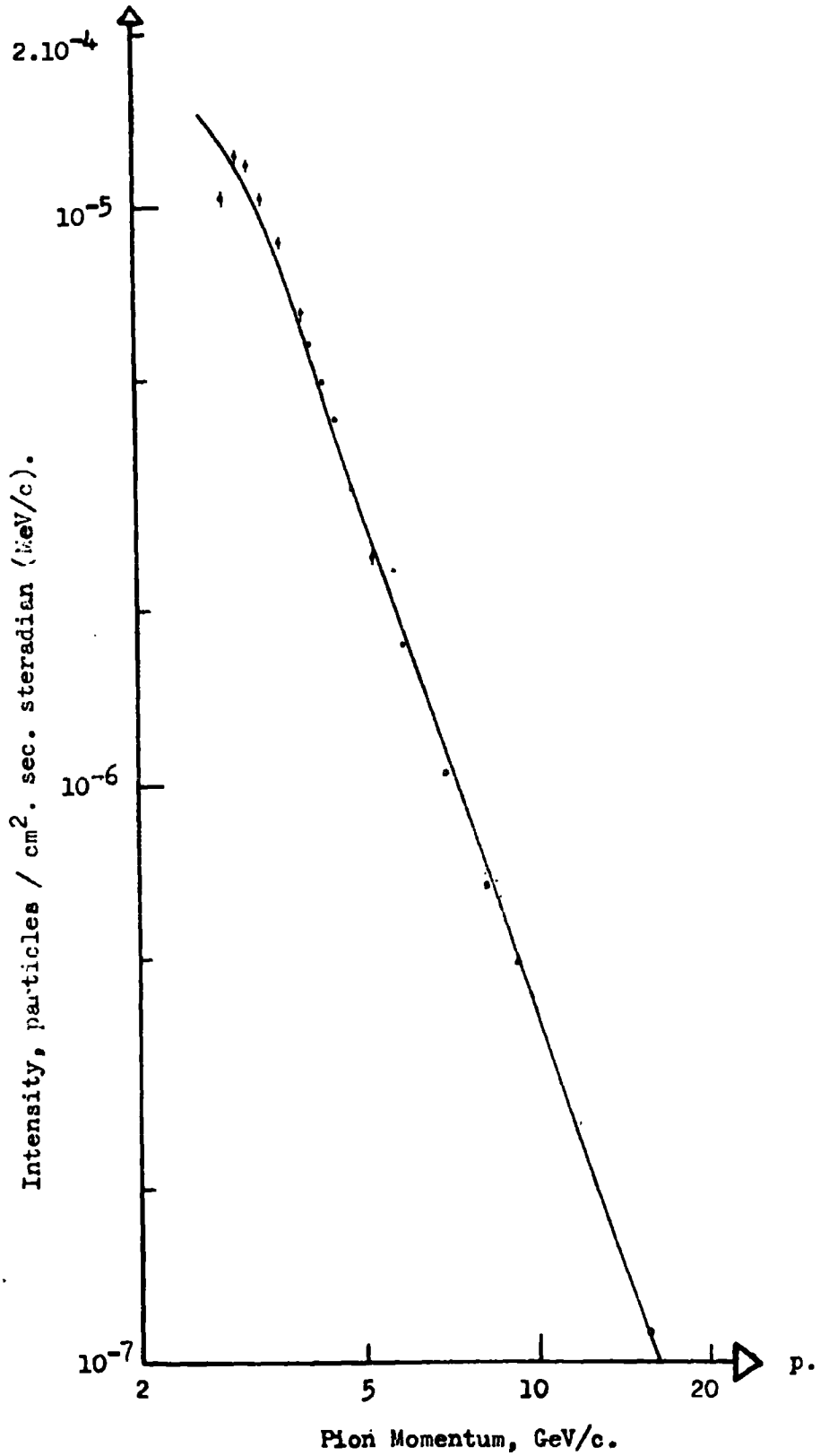

FIG. 7.1.4. The Pion Generation Spectrum, assuming Unique Height of Muon Production (115 g.cm^{-2}) and varying momentum loss.

made, the accuracy decreasing with decreasing momentum. Muons of increasing momentum at sea level may be seen to come mainly from decreasing depths in the atmosphere as the survival probability from such small depths increases with increasing momentum.

Several workers have attempted analytical solution of the propagation problem allowing for production decreasing exponentially with increasing depth, first suggested by Barrett et al (1952), outstanding examples being those of Haber-Schaim and Yekutieli (1954) who used their considerations to define the absorbtion length more accurately, Puppi (1956) who states that his solution is not accurate below 5 GeV/c, and Maeda (1960) who based his work on the muon generation spectrum of Sands (1950), shown by Owen and Wilson to be unsatisfactory in many respects.

7.2.(ii) The Author's Computations

Numerical solution has been performed above a sea level muon energy of 5 GeV by Apostolakis and Allen (1961), and a similar solution over the sea level momentum range relevant here by the author. The model is a logical extension of the single unique height generation model. At each depth in the atmosphere the incremental production in a 1 $g.cm^{-2}$ layer is considered, assuming a law for the pion production spectrum, and an exponential

law for absorption of the primaries. An absorption length of 120 $g.cm^{-2}$ was initially assumed. The incremental production of pions in any 1 $g.cm^{-2}$ layer is thus:-

$$(\delta I_\pi).dp_\pi = (I_p).dp_p \times \frac{e^{-t/120}}{120} \qquad (i)$$

Experimental evidence for this assumption was found by Duthie (1961) who plotted the intensity of neutral pions with p>550 GeV as a function of depth and found good agreement with a law of the form:-

$$I_{\pi_0} = Ke^{-\alpha t}$$

K, α being constants, $\alpha \simeq \frac{1}{120}$, referring to absorption of the primaries.

For a series of values of momentum at sea level for which the intensity is known, corresponding values of p_π, and attenuation constant, K, modifying the differential pion intensity $(I_\pi)_t$, p_π to give the incremental contribution to I_μ at sea level and hence an incremental intensity from a small cell, ΔI_μ, were obtained, for a series of 't' values covering the whole atmosphere. These were integrated numerically to obtain the total sea-level intensity, I_μ. Increments in t were chosen to be conveniently large (100 $g.cm^{-2}$) in the lower regions of the atmosphere where there is less production, and small (50, decreasing to 20 $g.cm^{-2}$) in the upper regions of the atmosphere. The process was programmed and com-

puted in 2 stages:-

Stage 1 consisted of evaluating t, p_π and the attenuation constant K for the series of convenient depths in the atmosphere just mentioned.

Stage 2 consisted of assuming a law relating the pion generation spectrum intensity and p_π, then integrating the incremental contributions (ΔI_μ) to I_μ at sea level, from the known increments in t (and corresponding values of p_π) over the whole atmosphere.

7.2. (iii) Stage 1 Computation

A flow-diagram is given in Fig. 7.2.1.

The figures given by Sternheimer (1959) were taken for momentum loss of muons by ionisation below 10 GeV, (Fig. 7.2.2.), other losses were neglected. Equations were fitted to the curve obtained from this data, and these give the momentum loss of a muon of momentum p, in air, as:-

for p<1 GeV/c,

$$\frac{dp}{dx} = 2.0.10^{-3} + 1.79.10^{-4} \ln p + 8.9.10^{-5} (\ln p)^2 \quad \text{GeV/g.cm}^{-2}$$

for p>1 GeV/c,

$$\frac{dp}{dx} = 2.10^{-3} + 2.85.10^{-4} \ln p \quad \text{GeV/g.cm}^{-2} \qquad \text{(ii)}$$

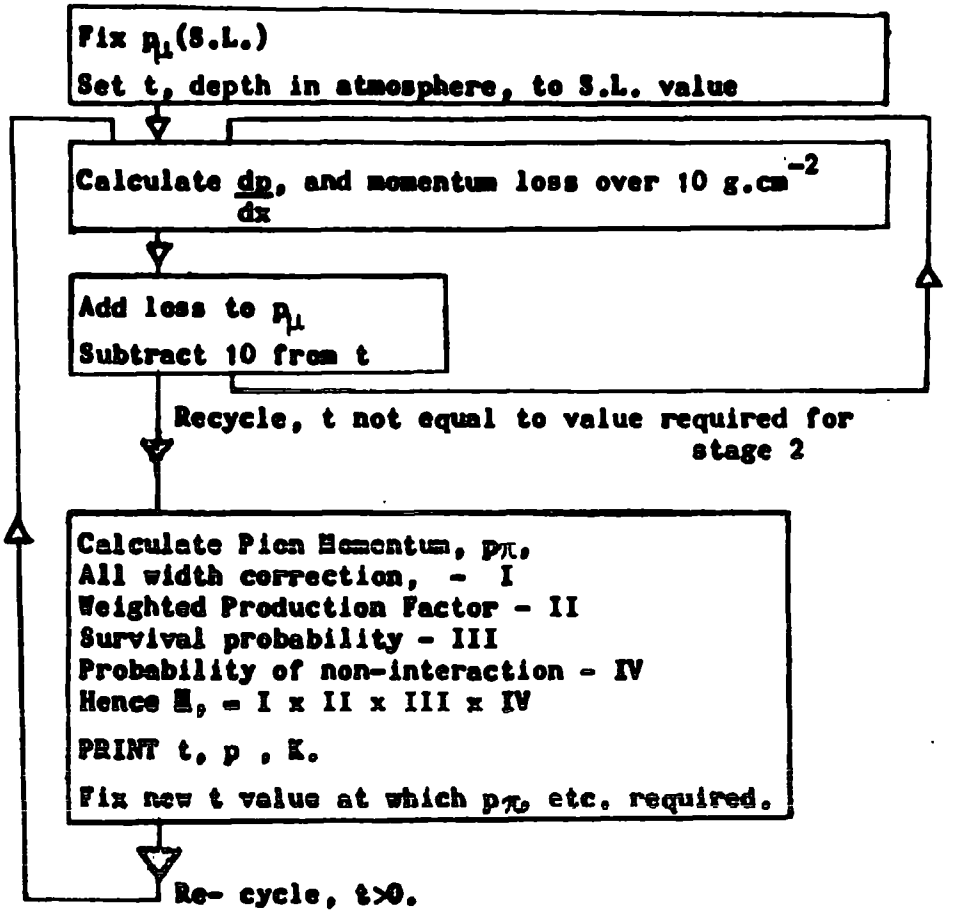

FIG. 7.2.1.

Flow Diagram for Stage 1 - Computation, Extended Production Pion Generation Spectrum.

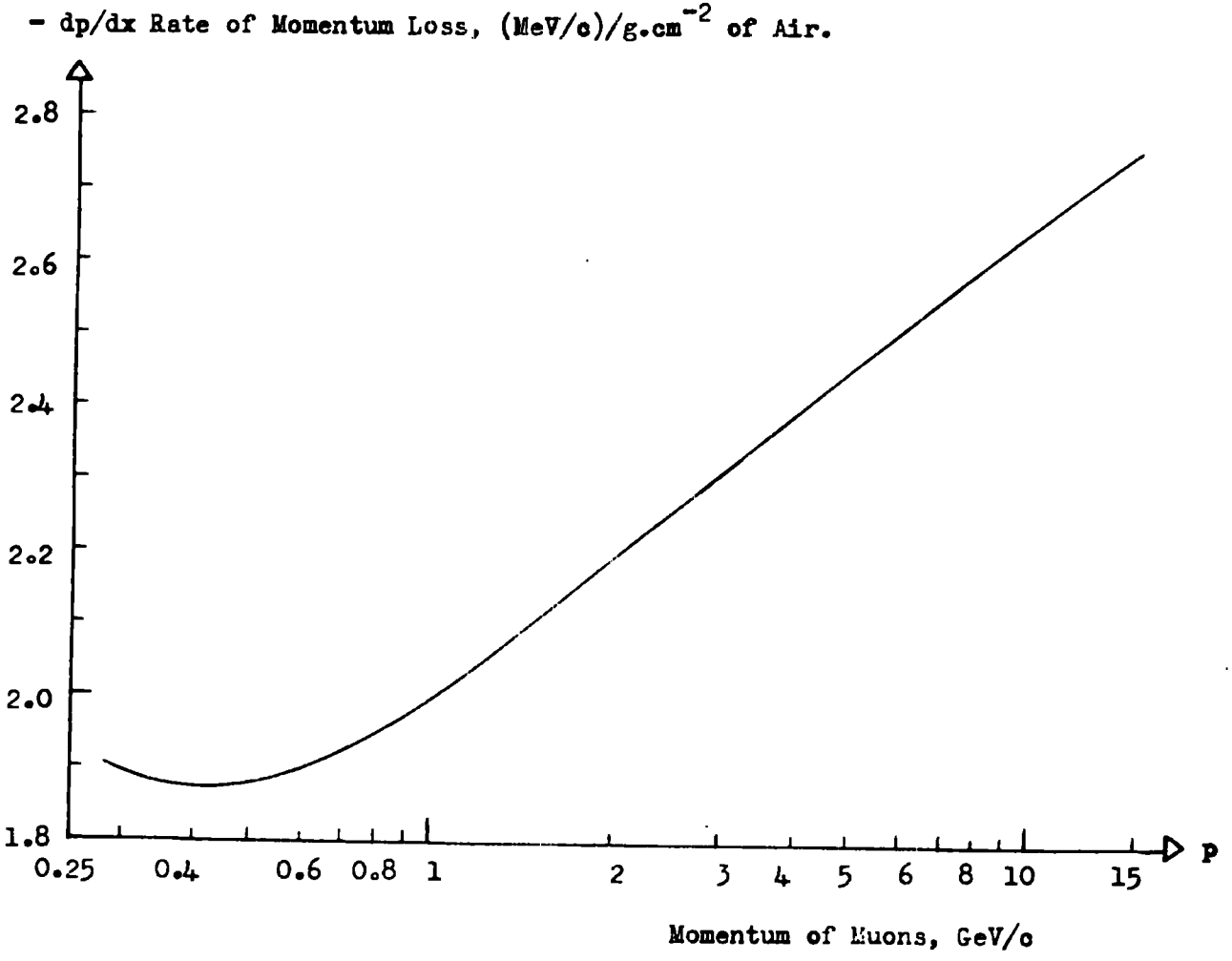

FIG. 7.2.2. Rate of Momentum Loss of Muons in Air.
(After Sternheimer, 1959).

Using the above laws for dp/dx for a series of values of p at sea level, actually 0.4, 0.7, 1.0, 2.5, 5.0 and 10.0 GeV/c, p_μ at decreasing depth, t, was computed by taking 10 $g.cm^{-2}$ increments in t, finding the momentum loss in each layer and adding it to the initial momentum at the bottom of the layer. The new momentum is then used to find the loss in the next 10 $g.cm^{-2}$ layer and so on. At certain depths, (Fig. 7.2.3.) the muon momentum at that depth, p_t, is converted to p_π using equation 7.1(iv) and r = 0.787. The usually adopted value of r (the factor connecting mean muon and pion momenta) is 0.76, but it is shown in Appendix 7.2.1. that r = 0.787 is a more accurate value, by considering the kinematics of $\pi \rightarrow \mu$ decay. This value was used throughout the present computations.

Values of (i) Δp and (ii) p_o, required in the calculation of survival probabilities, are calculated when required by evaluating:

(i) the difference between $p_{S.L}$ and p_t, and

(ii) multiplying Δp by $(1-t/t_o)$ to obtain the momentum loss the muon would incur in traversing the whole atmosphere at the same average rate of momentum loss. The attenuation constant at the chosen depths was evaluated from the following:-

(i) cell width correction. Following equation 7.1(i) inverted since it is now necessary to convert I_π to AI_μ and not vice-versa,

$$I_s = \frac{dp_t}{dp_s} \times I_t \qquad \text{for muons.}$$

The factor $\frac{dp_t}{dp_s}$ may be replaced by:-

$$\left(\frac{dp_t}{dx} \times \frac{dx}{dp_s} \right) \qquad \text{I}$$

The appropriate values of momentum loss were obtained from the momentum loss equations (7.2.ii) and divided. It is assumed, as in Section 7.1, that the pions decay almost instantaneously to muons.

(ii) Weighted Production - already given in equation 7.2(i). as:

$$\frac{1}{120} \cdot e^{-t/120} \text{ per 1 g.cm}^{-2} \text{ layer} \qquad \text{II}$$

iii) Survival Probability - calculated from Owen and Wilson's equation (Equation 7.1.(iii)). Values of Δp and p_o are already known at any given t. III

(iv) Nuclear Interaction. Following Pine et al and equations 7.1.(iv) and 7.1.(vii):-

$$I_\mu = f\, I_\pi \text{ where}$$

$$f = \frac{1}{r\left(\frac{1+p_\pi}{B'}\right)} \qquad \text{IV}$$

where B' is the momentum corresponding to an energy B, given by:-

$$B = \frac{m_\pi . c^2 . r . h_o}{c \tau_o}$$

(m_π, τ_o refer to the mass and lifetime respectively of the pion, c is the velocity of light, and r = 0.787).

In this equation h_o, the scale height of the atmosphere (h_o) was assumed to be 6.46 Km. This is a value relevant to the upper atmosphere, which is where the greater proportion of production takes place, and differs from the mean value of h_o used in the survival probability computation (7.02 Km).

The attenuation constant, K, for any given sea level momentum p, for height t, is then given by the product:-

$$K = I \times II \times III \times IV$$

Values of K were computed at intervals of 20 $g.cm^{-2}$ in t down to 200 $g.cm^{-2}$, 50 $g.cm^{-2}$ down to 400 $g.cm^{-2}$, and 100 $g.cm^{-2}$ down to 1000 $g.cm^{-2}$. An allowance for the lowest layer of 33 $g.cm^{-2}$ was made in the integration (Stage 2). The values of t (upper limit of layer considered) p_π (mean value) and $K_{(t,p)}$ were used as data for stage 2 of the computation in which a law was obtained for the pion generation spectrum fitting the sea level muon spectrum observed, making the assumptions stated.

7.2 (iv) Stage 2 Computation

Muons arriving at sea-level with any given momentum come from a steadily increasing series of values of p_π with decreasing depth in the atmosphere. By assuming a law

connecting I_{π} and p_{π}, and integrating I_{μ} from the known values over the whole depth of the atmosphere (Section 7.2.(ii)) $(I_{\mu})_{S.L}$ was found for any given $(p_{\mu})_{S.L}$. This was repeated for the values of $(p_{\mu})_{S.L}$ available (See Section 7.2.(iii)).

The integration was performed by approximating a histogram to the smooth curve corresponding to incremental muon production. The cell widths already mentioned, or rather depths chosen for calculation of p_{π}, K, etc. were chosen from a knowledge of the form of the curve from preliminary calculations. The integration was computed and a triangle approximated to the first cell. (See Fig. 7.2.3.).

By plotting the sea level muon spectrum for a known pion spectrum law a test of fit was made between the predicted and actual sea level muon intensity curves. By relaxing the pion spectrum by the ratio of the observed to predicted sea level intensities at an appropriate mean p_{π}, corresponding to a given $(p_{\mu})_{S.L}$ a pion spectrum giving a closer fit was obtained. This, a method of successive approximation, was applied.

The first power laws tried for the pion spectrum followed approximately Puppi (1956) and were:-

$$I_{\pi} = Ap_{\pi}^{-\gamma}$$

where γ has values between 2.6 and 2.7 and $A = 1.88.10^{-4}$.

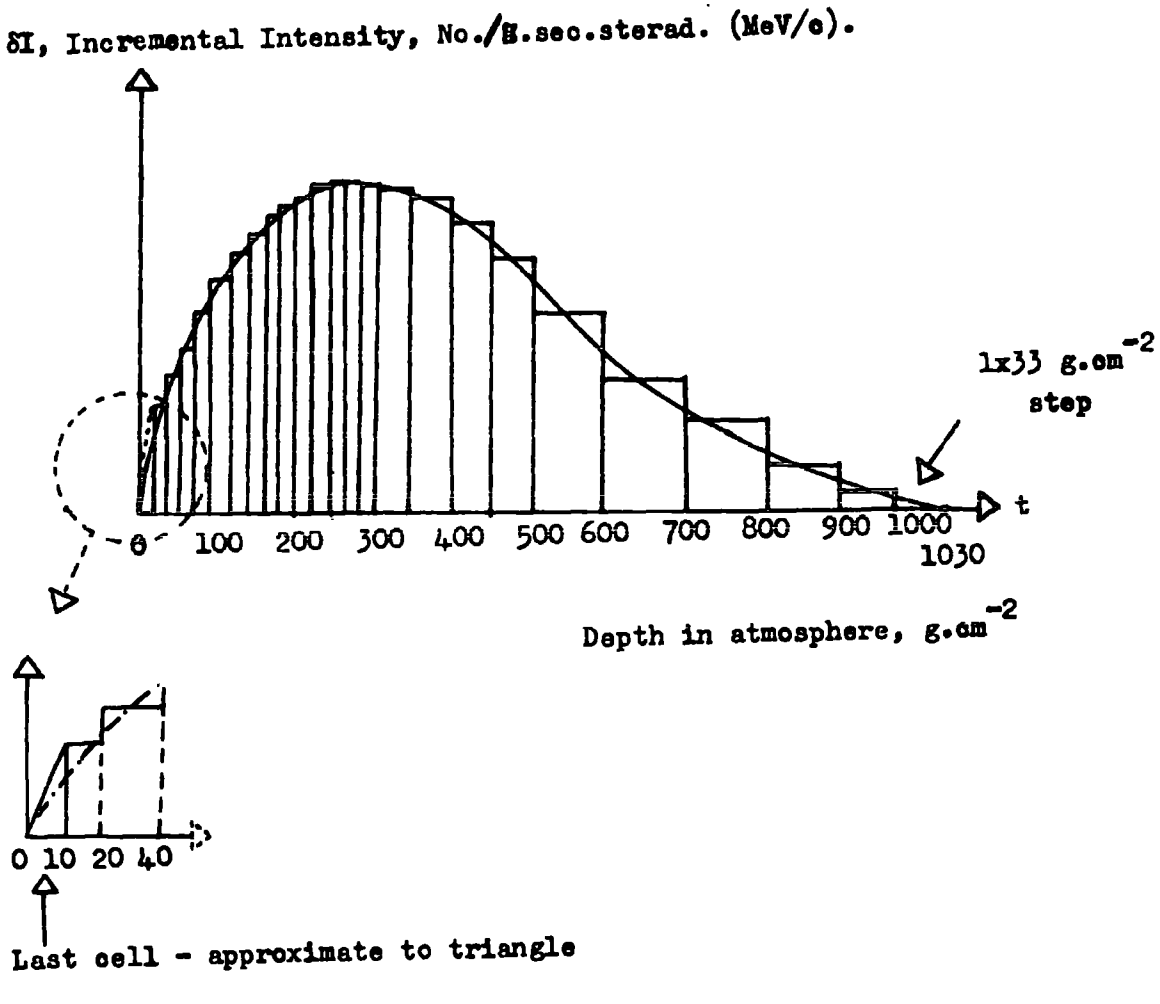

FIG. 7.2.3. Mode of Numerical Integration of Incremental Intensity

(units of intensity). An interpolated value of $\gamma = 2.64$ was found to give a good fit for $(p_\mu)_{S.L} > 5.0$ GeV/c. For $(p_\mu)_{S.L} < 3$ GeV/c no unique values of A and γ were found to fit. Correspondingly functions complex in p_π for A and γ were taken, appropriate functions being obtained from the graphically relaxed pion spectrum, for each approximation. (A = intercept at $p_\pi = 1$ GeV/c, γ = slope, for any point. A and γ were plotted vs. p_π).

The forms of A and γ found to give the best fit are:-

$$A = 1.82.10^{-4} \left(\frac{p_\pi}{4}\right)^{0.712} \quad \text{for } 0.6 < p_\pi < 4.0 \text{ GeV/c}$$

$$A = 1.82.10^{-4} \quad \text{for } p_\pi > 4.0 \text{ GeV/c}$$

and $\gamma = 2.64$ (constant),

where $I_\pi = Ap_\pi^{-\gamma}$ with A, γ as above. A table of values for p_π, A, γ and I for these parameters are given in Table 7-2-1.

p	A	γ	$I_{(p_\pi)}$
1.00	$7.01.10^{-5}$		$7.01.10^{-5}$
2.00	$1.15.10^{-4}$		$1.84.10^{-5}$
3.00	$1.53.10^{-4}$		$8.43.10^{-6}$
4.00			$4.839.10^{-6}$
5.00			$2.685.10^{-6}$
6.00		2.64	$1.659.10^{-6}$
7.00	$1.82.10^{-4}$		$1.104.10^{-6}$
8.00			$7.762.10^{-7}$
9.00			$5.688.10^{-7}$
10.00			$4.307.10^{-7}$
12.00			$2.661.10^{-7}$

Table 7-2-1.

7.2.(v) Incremental Production of Muons

Concurrently with summation of the incremental intensities of muons at sea level produced from pions at depth t, the actual incremental intensities of muons at such depth t was printed and is shown in Fig. 7.2.4a. Specimen curves given by Maeda (those for momenta of 1 and 10 GeV/c) and those of the author are shown plotted on the same scale (normalised at their peaks) in Fig. 7.2.4b. Little importance, however is attached to the deviations occurring, since Maeda's work was based on the production spectrum of Sands.

7.2.(vi) The Pion Generation Spectrum

The 'best-fit' spectrum was plotted and relaxed graphically by very small amounts to fit the sea level spectrum. The final relaxed generation spectrum of pions is shown in Fig. 7.2.5; together with the spectra of Puppi and Olbert for comparison. A pion generation spectrum published by Jakeman (1956) is shown in Fig. 7.2.6. These are in reasonable agreement with the present work. Excellent agreement is also obtained with the work of Pine et al. Table 7-2-2 shows summarised results for the exponent of the pion generation spectrum.

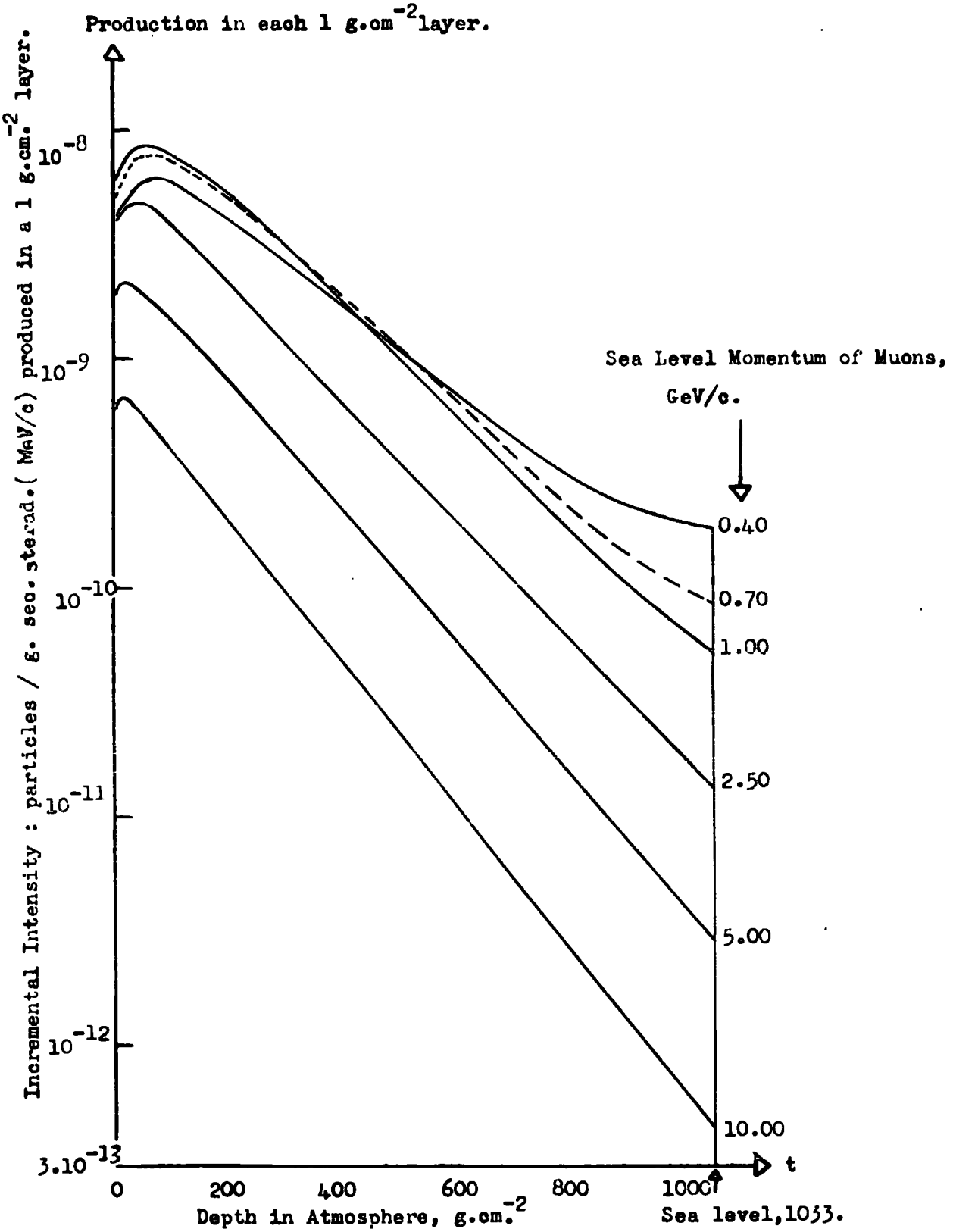

FIG.7.2.4.a. Incremental Production in the Atmosphere of Muons Reaching Sea Level as a function of Sea Level Momentum.

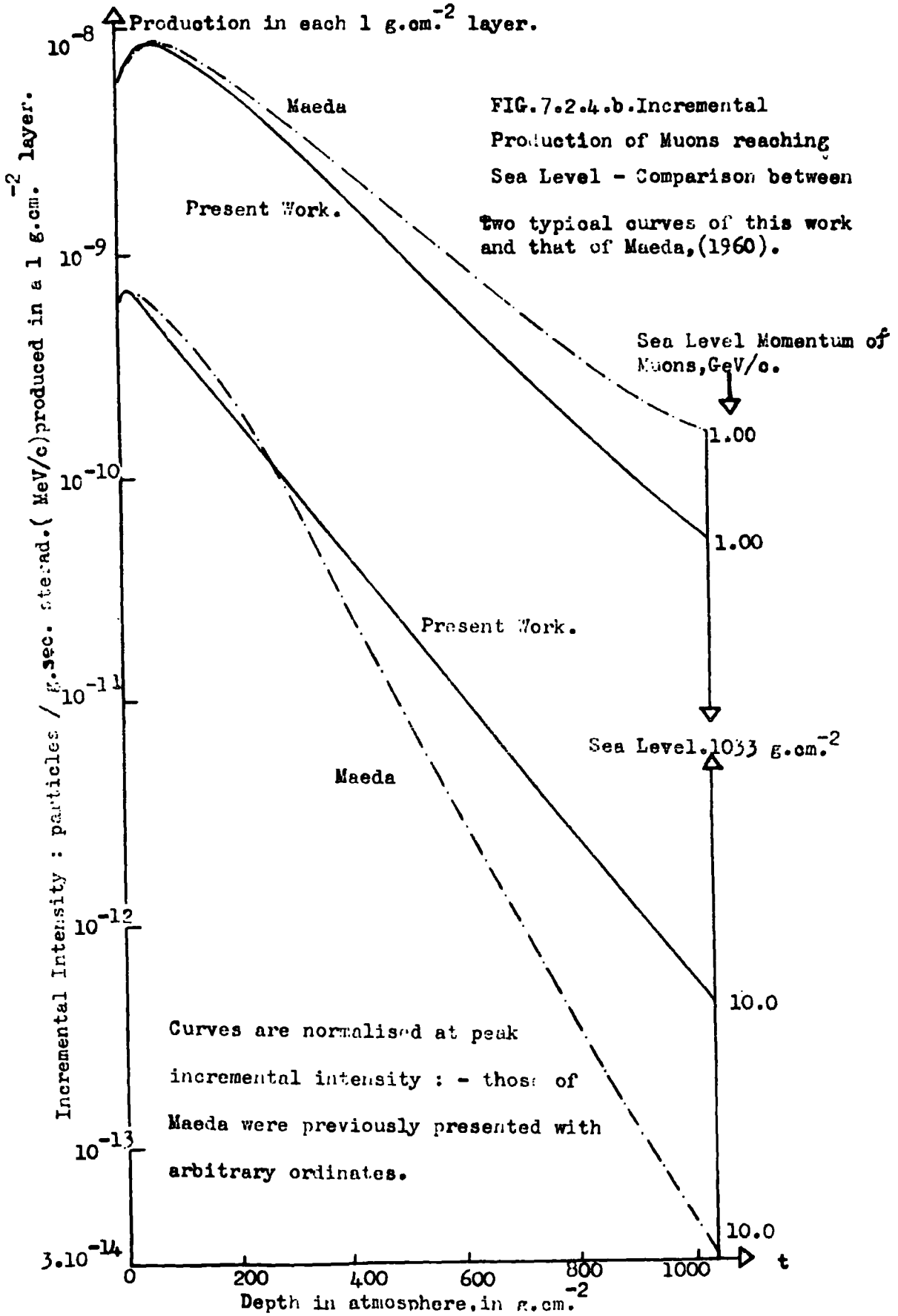

FIG.7.2.4.b.Incremental Production of Muons reaching Sea Level - Comparison between two typical curves of this work and that of Maeda,(1960).

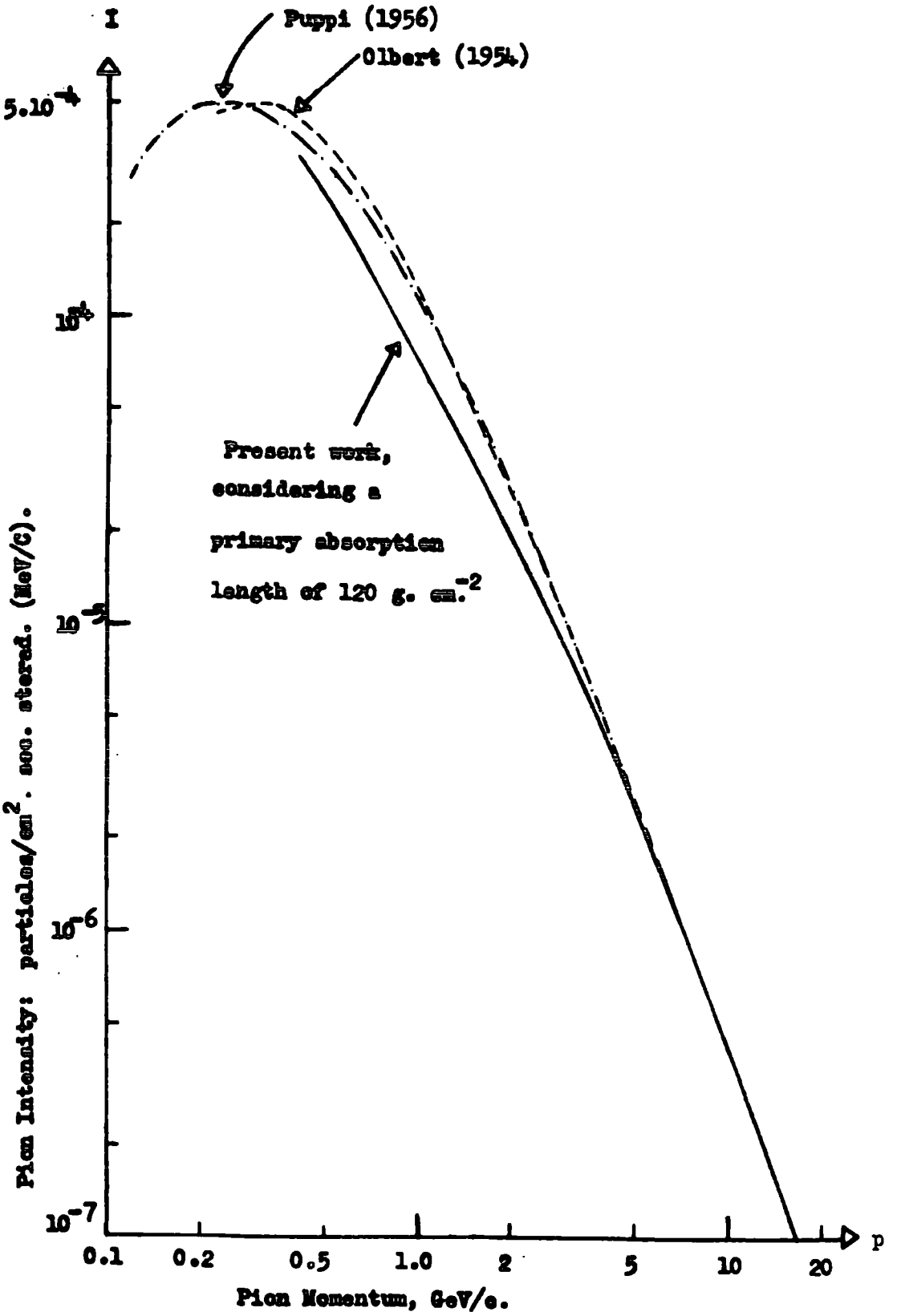

FIG. 7.2.5. The Generation Spectra of Pions in the Atmosphere, considering extended production of muons.

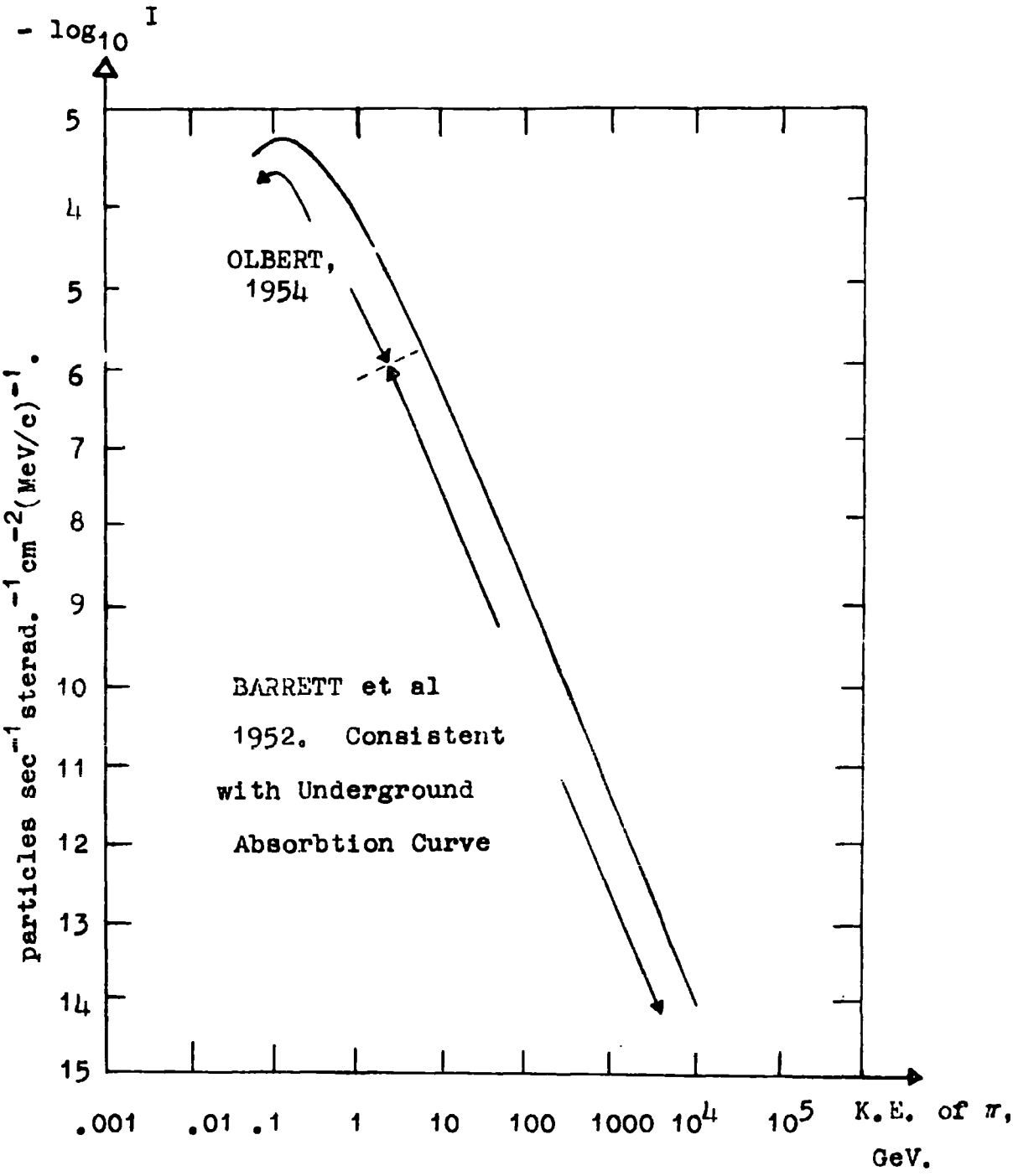

FIG. 7.2.6. The Generation spectrum of Pions in the range $0.01 < T_\pi < 10^4$ GeV, assembled from previous work by JAKEMAN, 1956.

Workers	Momentum range in GeV/c	Exponent of π-meson spectrum
Durham	2-12	-2.64 *
	10-1000	-2.64 /
Owen et al, 1955	3-22	-2.85
Puppi, 1956	3-22	-2.75
Rodgers, 1957	3-30	-2.70
	30-1000	-2.80
Pine et al, 1959	4-175	-2.64

* Present work, complex A as described in text.

/ Work of Hayman (1961)

Table 7-2-2.

7.2.(vii) Mean and Median Depths and Heights of Production

From the curves for the incremental production of muons shown in Fig. 7.2.4., a median depth of production of muons was obtained by numerical integration and a mean depth of production by computation (Fig. 7.2.7.). By means of the curve connecting height and depth given by Rossi (1952c) these were converted to mean and median height of production - Fig. 7.2.8. The inadequacy of assuming a unique production depth is clearly shown by these curves.

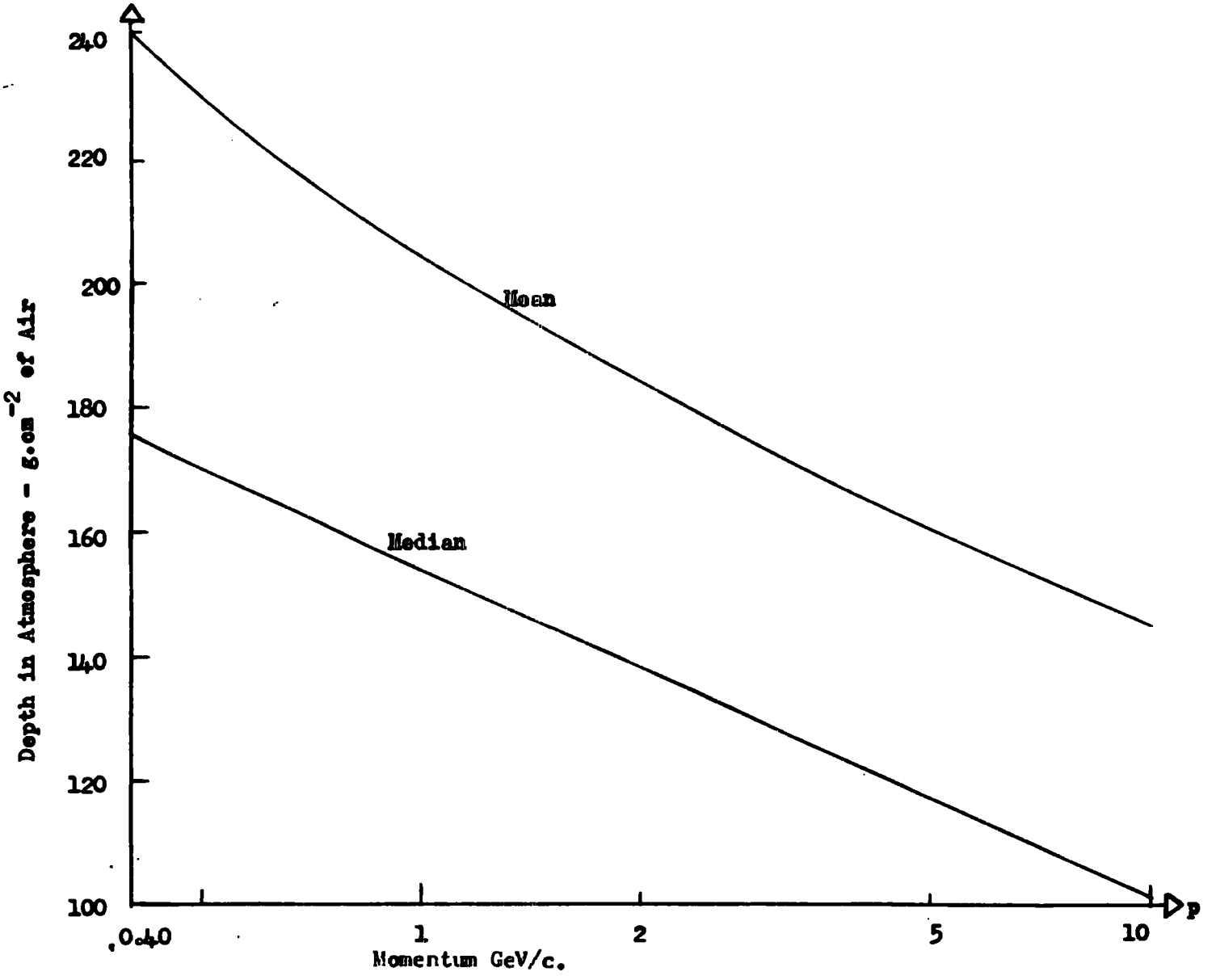

FIG. 7.2.7. Mean and Median Production Depths of Muons, as a function of Sea Level Momentum

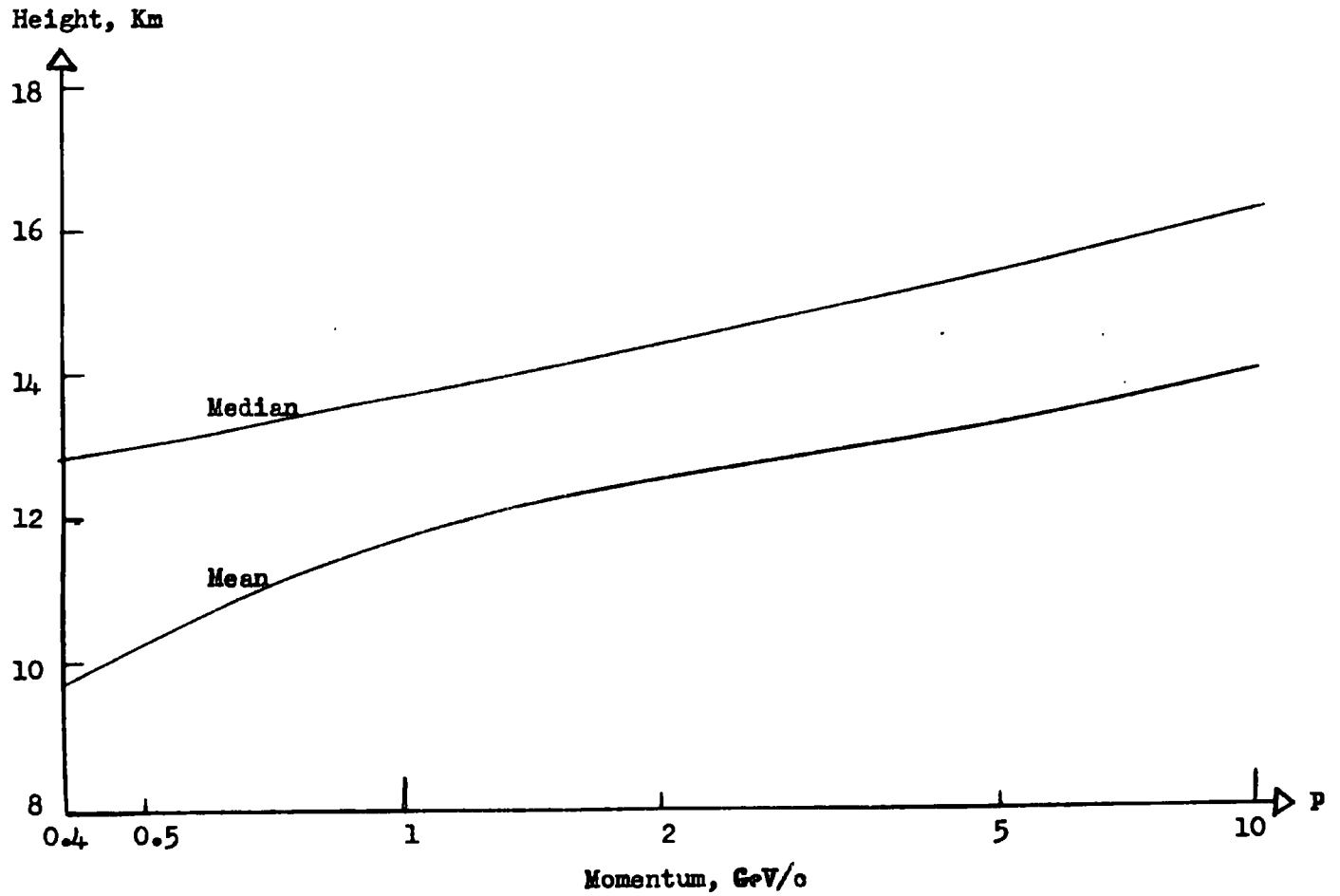

FIG. 7.2.8. Variation in Height of Production with Sea-Level Momentum

7.2(viii) Effect of Change in Absorption Length.

The numerical computations were repeated for absorption lengths of 110 and 130 $g.cm^{-2}$ using the known pion generation spectrum. From the effect of such changes on the sea level muon spectrum alternative implied changes to the pion generation spectrum were evaluated. (To give the known observed sea level muon spectrum). The effects are shown graphically in Fig. 7.2.9., the change in pion generation intensity being shown. Since the greater part of the muon flux is produced in the upper atmosphere where the factor $\frac{t}{\lambda}$ in $e^{-t/\lambda}$ is less than 1, the sea level flux is not sensitive to small changes in the absorption length of the primary component, as would be expected. The effects decrease with increasing $(p_\mu)_{S.L}$ since production at lower depths becomes less significant with increasing sea level momentum.

7.2(ix) Comparison with the Direct Measurement of the Pion Generation Spectrum

Observations of pairs of γ-ray tracks by means of decay electrons resulting from decay of neutral pions, have been observed in emulsions by the Bristol group. (Duthie, et al, 1960). From such observations an energy spectrum of the initial neutral pions was obtained. If

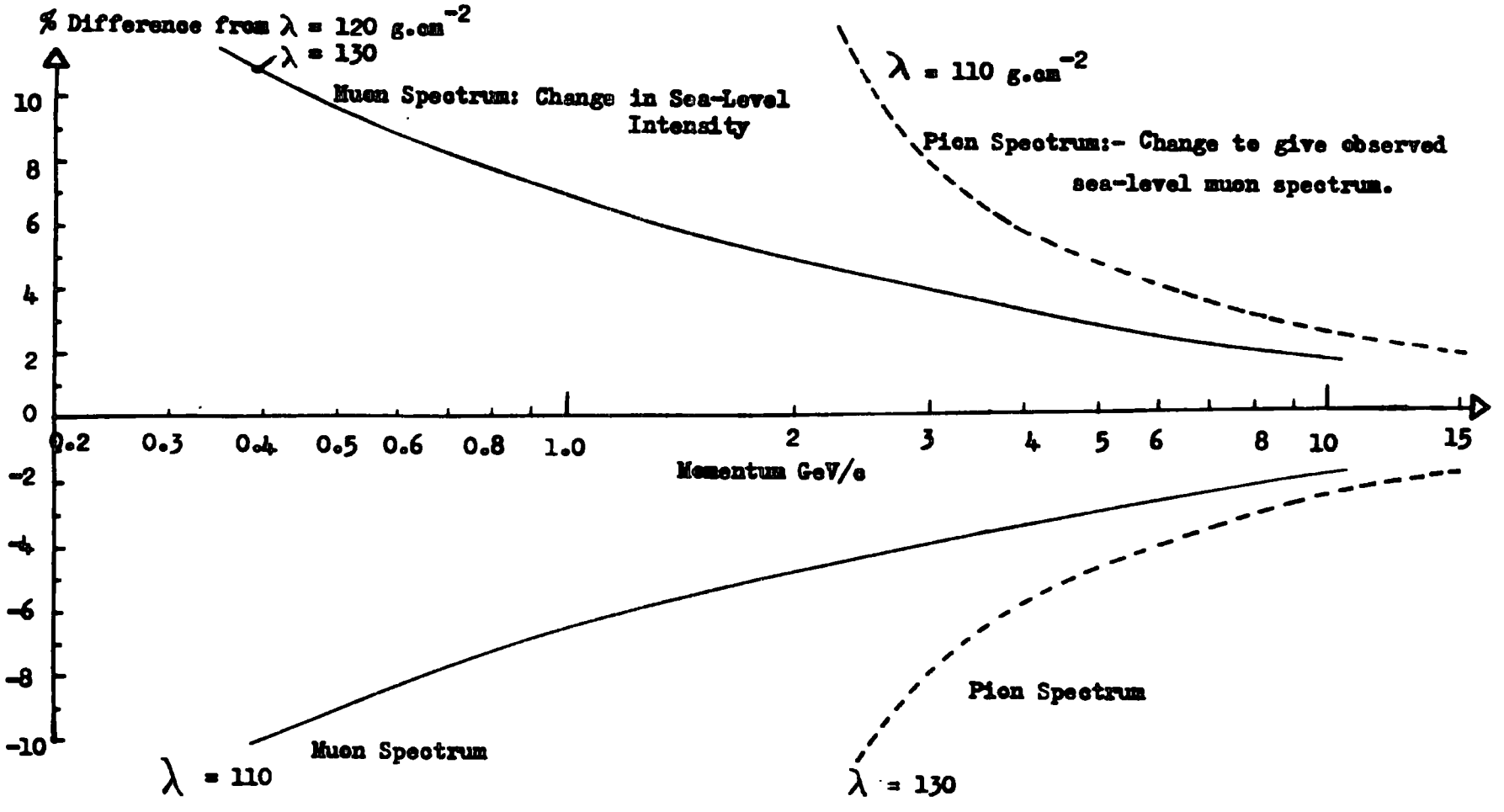

FIG. 7.2.9. Effect on Sea Level Muon and Pion Generation Spectra of Varying the Absorption Length of the Primary Particles.

it is assumed that the partition of the energy of the primary particles between the processes giving rise to neutral and charged pions is constant, then the slope of the neutral pion spectrum is a measure of that of the charged pion spectrum. The value of the negative exponent found by the Bristol group was (3.5 ± 0.3) compared with the charged pion spectrum value of $(2.64 \pm .04)$ described in the present work and in agreement with Pine et al. This originally suggested that the intensity of neutral pions at low momentum is a factor of approximately 5 times that which would be expected. Powell (1960) has suggested that processes other than inelastic collision of primary cosmic rays may give rise to neutral pions. Other possibilities which may account for this phenomenon are direct muon production by the primary cosmic rays (which would relatively increase the sea-level spectrum intensity) or non-constant equipartition of energy between production of chargedand uncharged pions in inelastic collisions. At least one contemporary theory of such collisions, the isobaric model, cannot account for such a difference.

Though the situation is not at present clear the differences have been partly resolved:- the emulsion work refers to primary cosmic rays with $10^3 < E < 10^4$ GeV.

Balloon flight and high altitude work (e.g. Fujimoto et al, 1960) in the range $500 < E < 1000$ GeV tends to show a negative exponent of (3.4 ± 0.3) and the most recent counter work in this region, above the range of the author's work, would tend to show an exponent of approximately 3.0.

7.3. The Sea Level Pion Spectrum

7.3.(i) General

It was assumed previously that all pions decay to muons which are observed at sea-level. However, a very small number of pions survive as such down to sea-level. A computation of the pion spectrum at sea-level was made and compared with the directly observed spectrum of Brooke et al (1961). From this a more accurate value of the absorption length was obtained. The direct measurement just referred to was made by observing those negative strongly interacting particles, of known momentum, which interacted in a neutron monitoring pile. Events due to pions were separated from those due to protons by observing the polarity of the initial particle.

7.3.(ii) Details of Computation

This follows very closely the numerical solution of the diffusion equation for cosmic ray muons in the atmosphere already described in Sections 7.2.(iii) and 7.2.(iv), with necessary modifications to the terms accounting

for momentum loss, survival probability and probability of not being lost by nuclear interaction. The process is shown schematically in Fig. 7.3.1.

Momentum Loss: this follows the work of Sternheimer (1959), being the rate of momentum loss of protons multiplied by an appropriate mass-ratio factor, and is given in Fig. 7.3.2. Within the range considered here (0.5 to 100 GeV/c) the rate of momentum loss is given by the following equations:-

for $0.5 < p_\pi < 1.321$ GeV/c:

$$dp_\pi/dx = 2.10^{-3} + 1.79.10^{-4}(\ln p - 0.2784) + 8.9.10^{-5}(\ln p - 0.2784)^2 \text{ GeV/g.cm}^{-2}.$$

for $1.321 < p_\pi < 100$ GeV/c:

$$dp_\pi/dx = 2.08.10^{-3} + 2.85.10^{-4}.\ \ln p\ .\ \text{GeV/g.cm}^{-2}.$$

Survival Probability - Owen and Wilson's equation is again used with the following constants modified:-

h_o = 7.40 Km. (a value more correct at the lower levels of the atmosphere where production of the pions reaching sea-level occurs.)

$\tau = 2.56 \times 10^{-8}$ sec. and $m_\pi c = 139.63$ MeV/c } (Barkas et al, 1958).

giving for the modified equation:-

$$\ln(P) = \frac{-134.63}{p_t} \ln \left\{ \frac{t_o}{t} \cdot \left(1 + \frac{\Delta p}{p_{S.L}}\right) \right\}$$

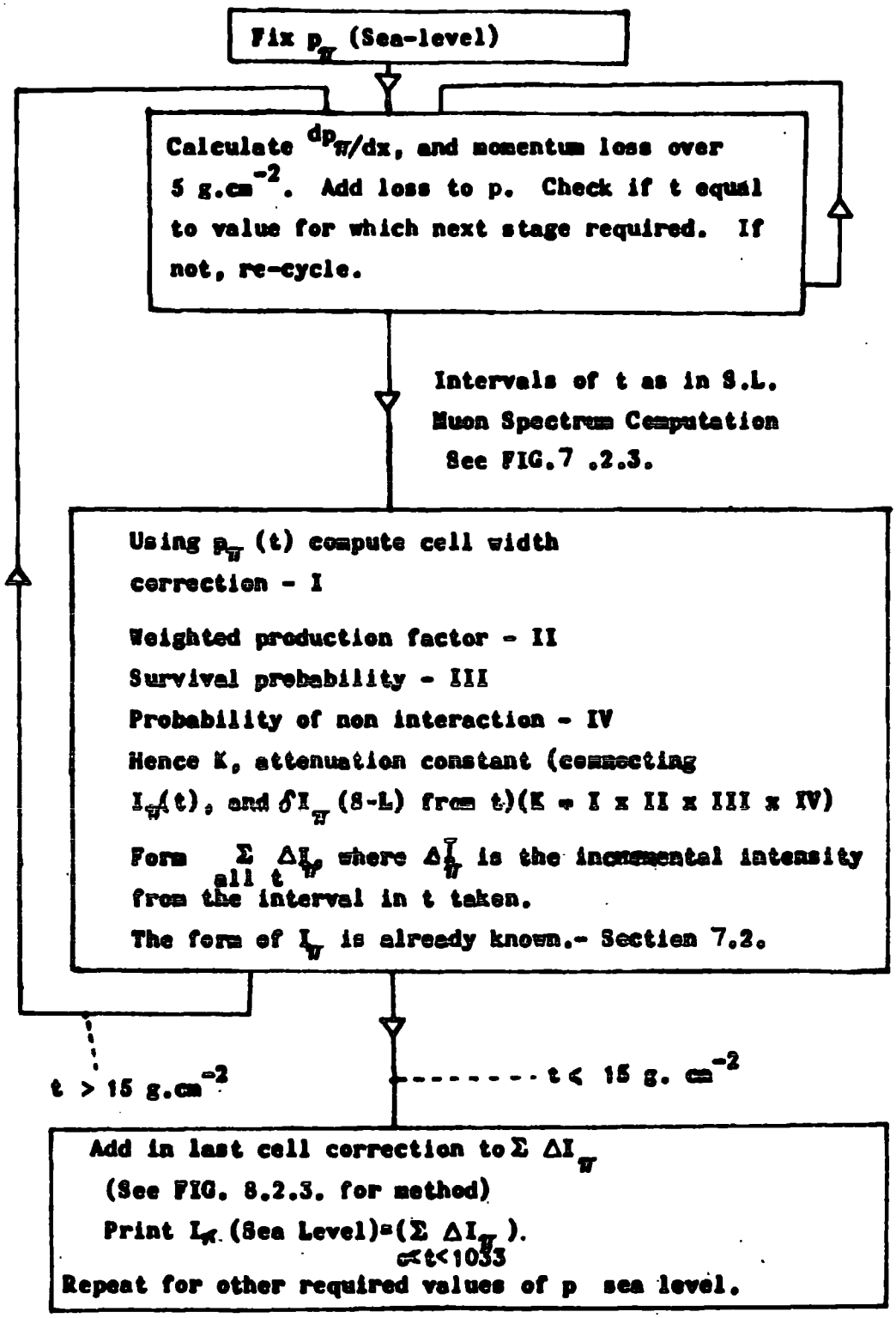

FIG. 7.3.1. Flowsheet for Computation of Sea Level Pion Spectrum from Pion Generation Spectrum.

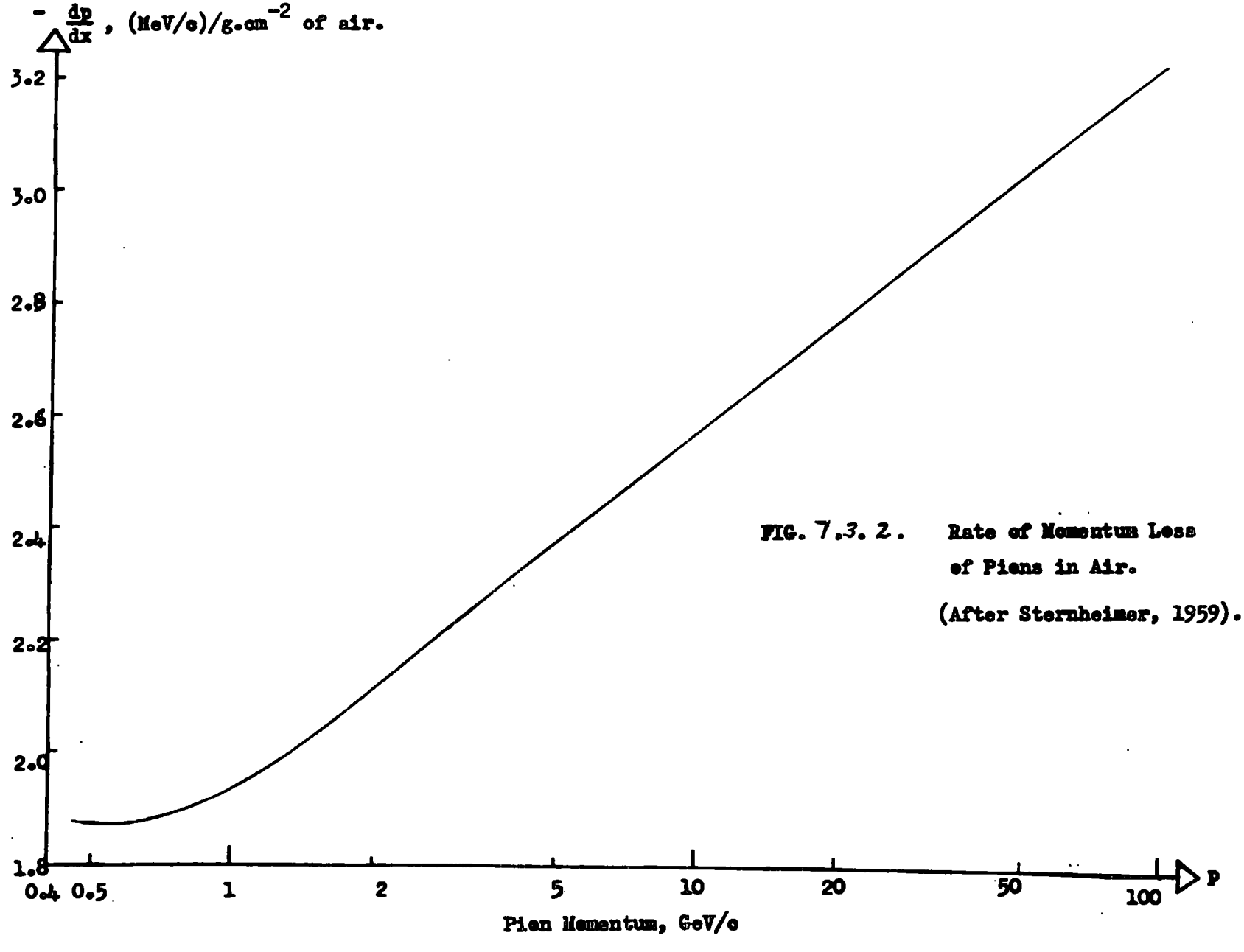

FIG. 7.3.2. Rate of Momentum Loss of Pions in Air.

(After Sternheimer, 1959).

Probability of non-interaction:- pions interacting between formation and sea-level are lost to the sea-level flux. The number not interacting between t and sea-level t_o, may be shown to be:-

$$I_{S.L} = I_t \, e^{-\left(\frac{t_o - t}{\lambda}\right)}.$$

by simple absorption considerations.

7.3.(iii) Final Sea-Level Pion Spectrum

The pion spectrum was computed, as described, from the pion generation spectrum given in Section 7.2.(vi). This is shown in Fig. 7.3.3., the measured pion spectrum also being shown. The fact that the sea level pion intensity was disregarded in computation of the generation spectrum is seen to be of little consequence, since the ratio of pion to muon intensities is in the range $5.10^{-4} < \left(I_\pi / I_\mu\right)_{S.L.} < 2.10^{-3}$ within the momentum range considered.

7.3.(iv) Determination of Absorption Length

The ratio $\left(I_\pi / I_\mu\right)_{S.L.}$ was plotted versus $p_{S.L.}$ for the absorption length $\lambda = 120$ g.cm^{-2} and for the measured pion spectrum and found not to agree (Fig. 7.3.4.). The computation was repeated for $\lambda = 130$ g.cm^{-2} and by extrapolation from the two theoretical curves it was clear that the absorption length of the primary component in the atmosphere giving the best fit to the measured $\left(I_\pi / I_\mu\right)$ ratio was:

$$\lambda = (135 \pm 3) \text{ g.cm}^{-2}$$

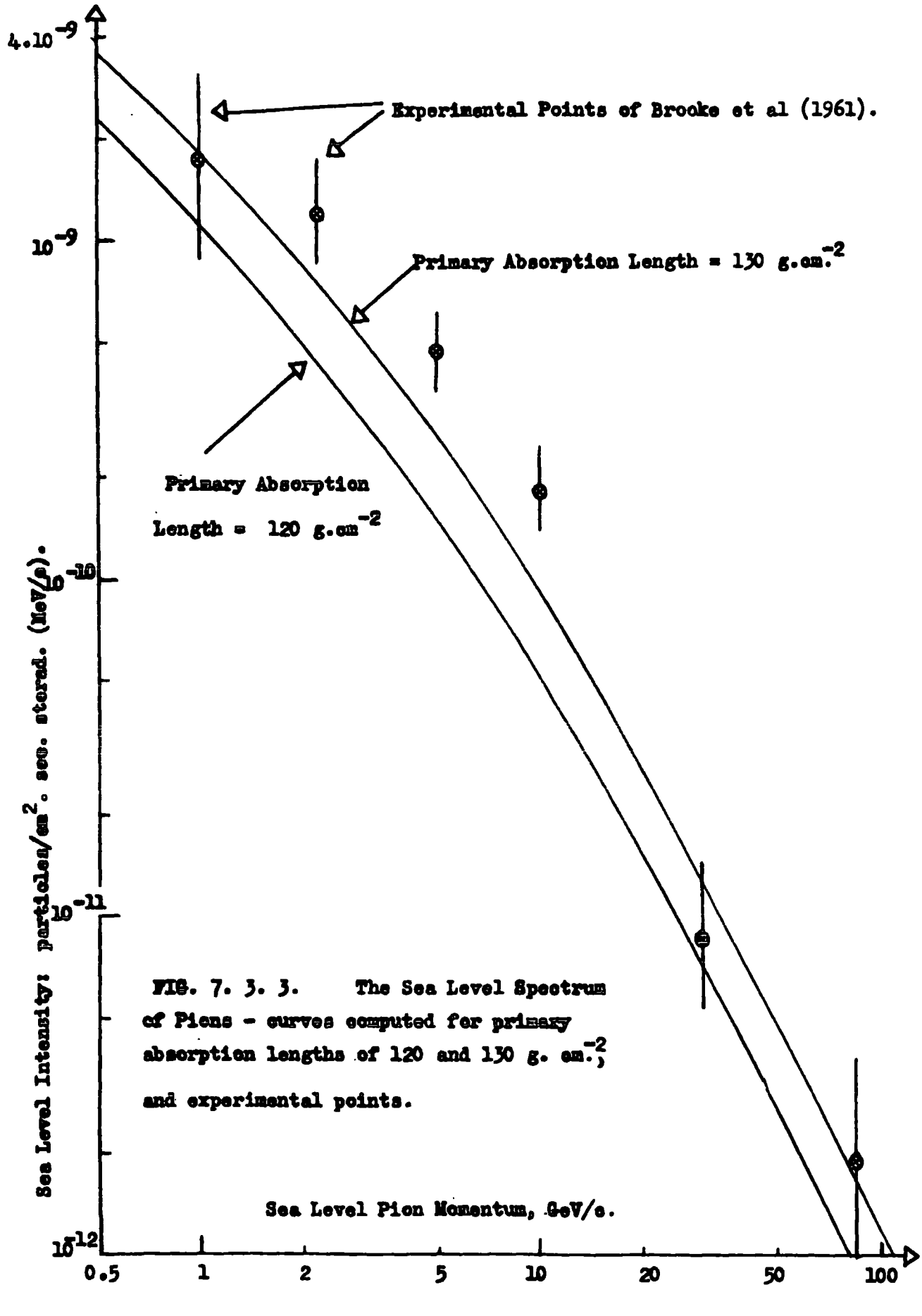

FIG. 7. 3. 3. The Sea Level Spectrum of Pions - curves computed for primary absorption lengths of 120 and 130 g. cm.$^{-2}$; and experimental points.

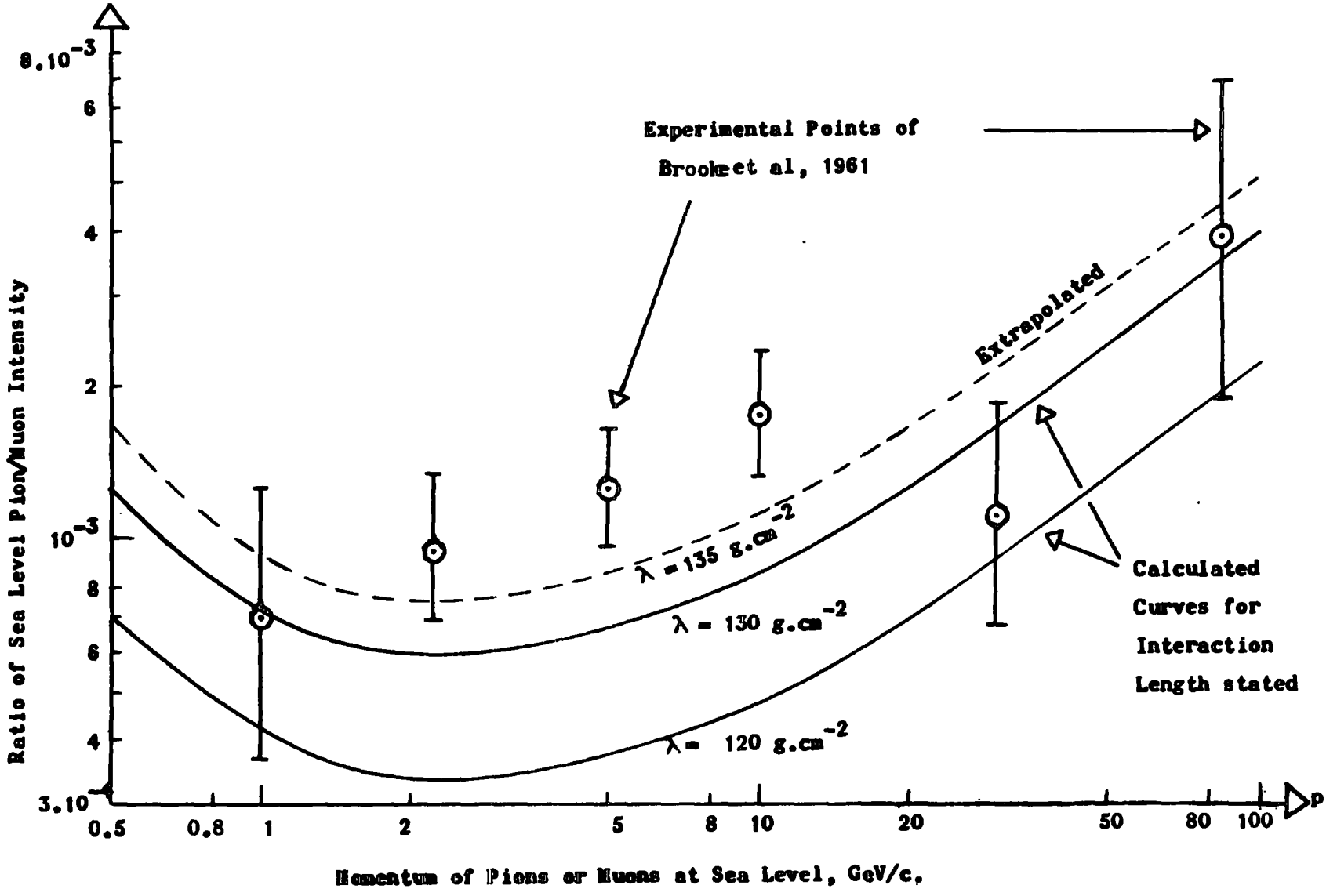

FIG. 7.3.4. Ratio of Sea Level Intensity of Pions to that of Muons as a function of Primary Absorption Length, λ.

7.3.(v) Incremental Production of Pions

As in the computation of the pion generation spectrum, incremental intensities of pions at various depths were obtained and typical curves are shown in Fig. 7.3.5. It can be seen that pions of low momentum observed at sea-level are predominantly produced in the lower levels of the atmosphere due to their high rate of decay. Since the 'weighted production factor', $e^{-t/\lambda}$, is much more sensitive to change in λ when $t/\lambda \gg 1$, the pion spectrum is very sensitive to changes in λ as may be seen from the results for the two different values of λ used in computation of Fig. 7.3.4.

7.3.(vi) Accuracy of Pion Generation Spectrum

The pion generation spectrum described in section 7.2.(vi) would appear to be changed by the more accurate value of absorption length now determined. However, as already shown, the 'average' median depth of production within the range of momenta considered here is approximately 140 $g.cm^{-2}$. The mean value of $e^{-t/\lambda}$ is hence changed from $e^{-140/120}$ to $e^{-140/135}$, a ratio of $e^{-0.1}$ or approximately 10%. Accurate changes to be applied to the pion generation spectrum (a function of momentum) were obtained from Fig. 7.2.8., and a final pion generation spectrum for a mean primary absorption length of 135 $g.cm^{-2}$ is shown in Fig. 7.3.6. This is the most

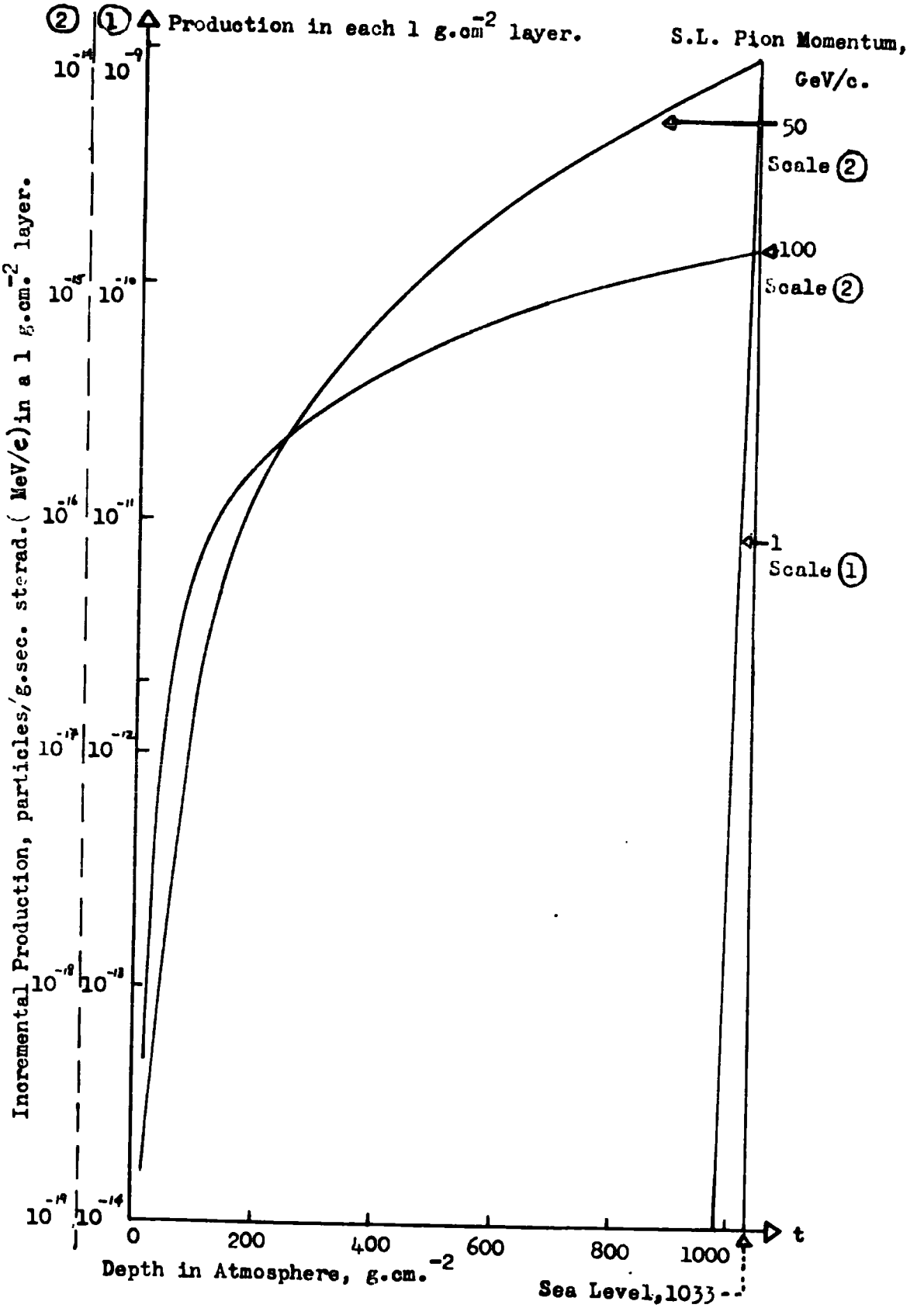

FIG. 7. 3. 5. Incremental Production in the Atmosphere of Pions reaching Sea Level, as a Function of Momentum.

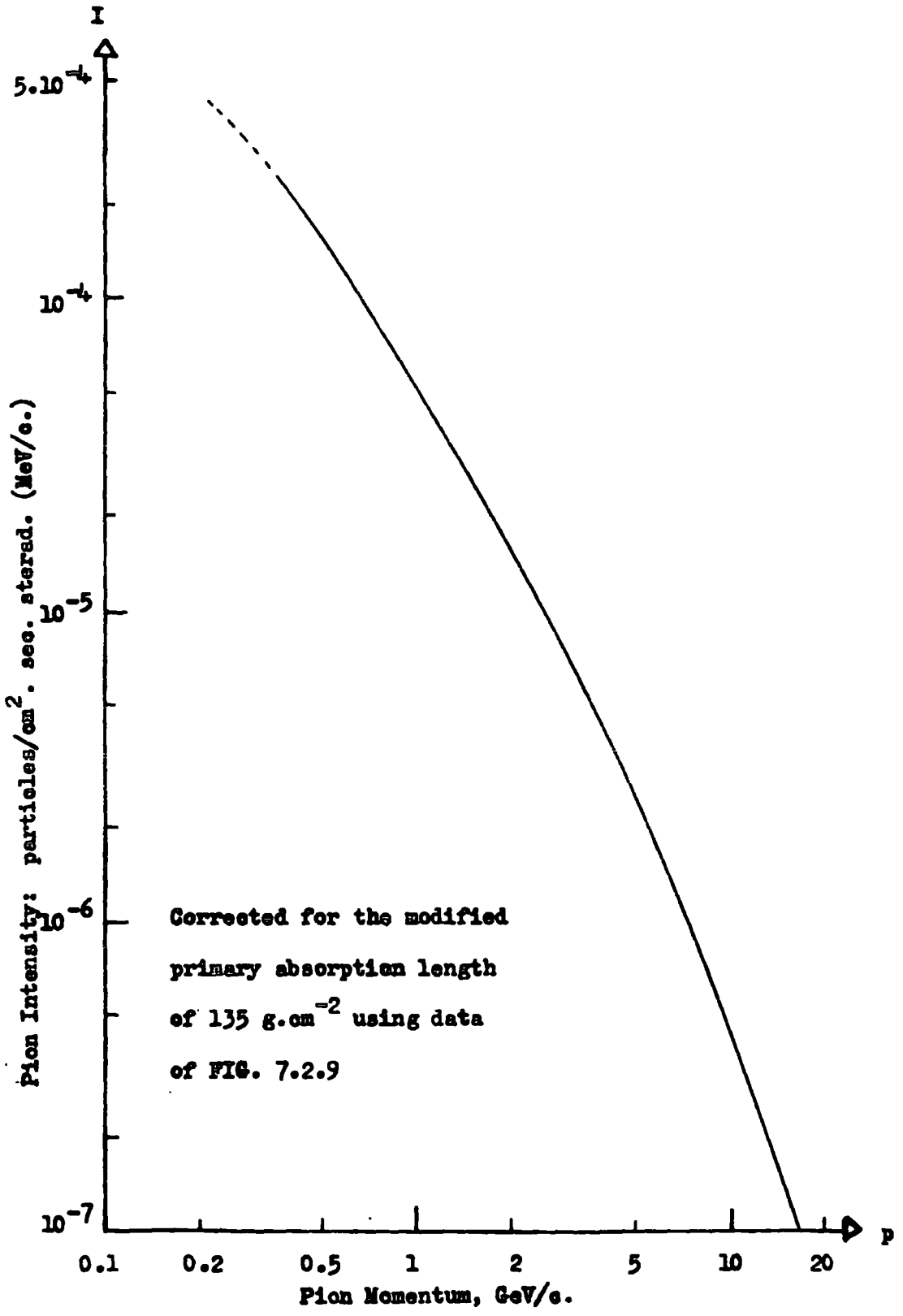

FIG. 7.3.6. The Durham Pion Generation Spectrum (FIG. 7.2.5) corrected for the modified absorption length.

accurate pion generation spectrum from the present work.

Chapter 8

The Positive-Negative Ratio

8.1. Experimental Observations

8.1.(i) General

The positive-negative ratio of muons is one of the easiest cosmic ray properties which may be measured with a magnetic spectrograph. The number of positive particles and the number of negative particles, of known momentum, are observed by virtue of different signs of deflection in such an instrument and the ratio of positive to negative numbers in any small cell gives the positive-negative ratio. The positive-negative ratio is always greater than one- because the primary cosmic radiation consists predominantly of protons (Chapter 1) and the positive charge, or a part of it, of the initial protons, is passed on to secondary particles produced by collisions of such primaries. After correction for the number of protons reaching sea-level it is found that the positive-negative ratio rises from a value of nearly 1 at low momentum to a maximum of approximately 1.25 at about 5 GeV/c, then falls with increasing momentum. This is qualitatively explained by the fact that, at low momentum, the muons come predominantly from primaries which, with their corresponding secondaries, have made more than one collision before reaching sea-level. This is due to geomagnetic cut-off of low energy primaries.

The fall at higher momenta is explained by the fact that the multiplicity in collisions of the primaries increases with momentum, decreasing the net excess positive charge per particle carried off after each collision. Both these processes will be considered quantitatively in the numerical treatment of propagation considered in section 8.2.

8.1.(ii) Previous Measurements

Previous measurements of the positive-negative ratio, σ, are shown in Fig. 8.1.1. The points presented have been compiled from those given by Owen and Wilson (1951) and Pine et al (1959). The latter present the 'positive excess', η, as a function of momentum. The relation between σ and η is as follows - if one lets n_+ be the number of positive particles represented by a single point and n_- the number of negative, then η is defined as:-

$$\eta = \frac{n_+ - n_-}{n_+ + n_-} \qquad \text{(i)}$$

and $$\sigma = \frac{n_+}{n_-}$$

hence $$\eta = \frac{\sigma - 1}{\sigma + 1} \quad \text{or} \qquad \text{(ii)}$$

$$\sigma = \frac{1 + \eta}{1 - \eta} \qquad \text{(iii)}$$

Equation (iii) above was used to transform 'positive

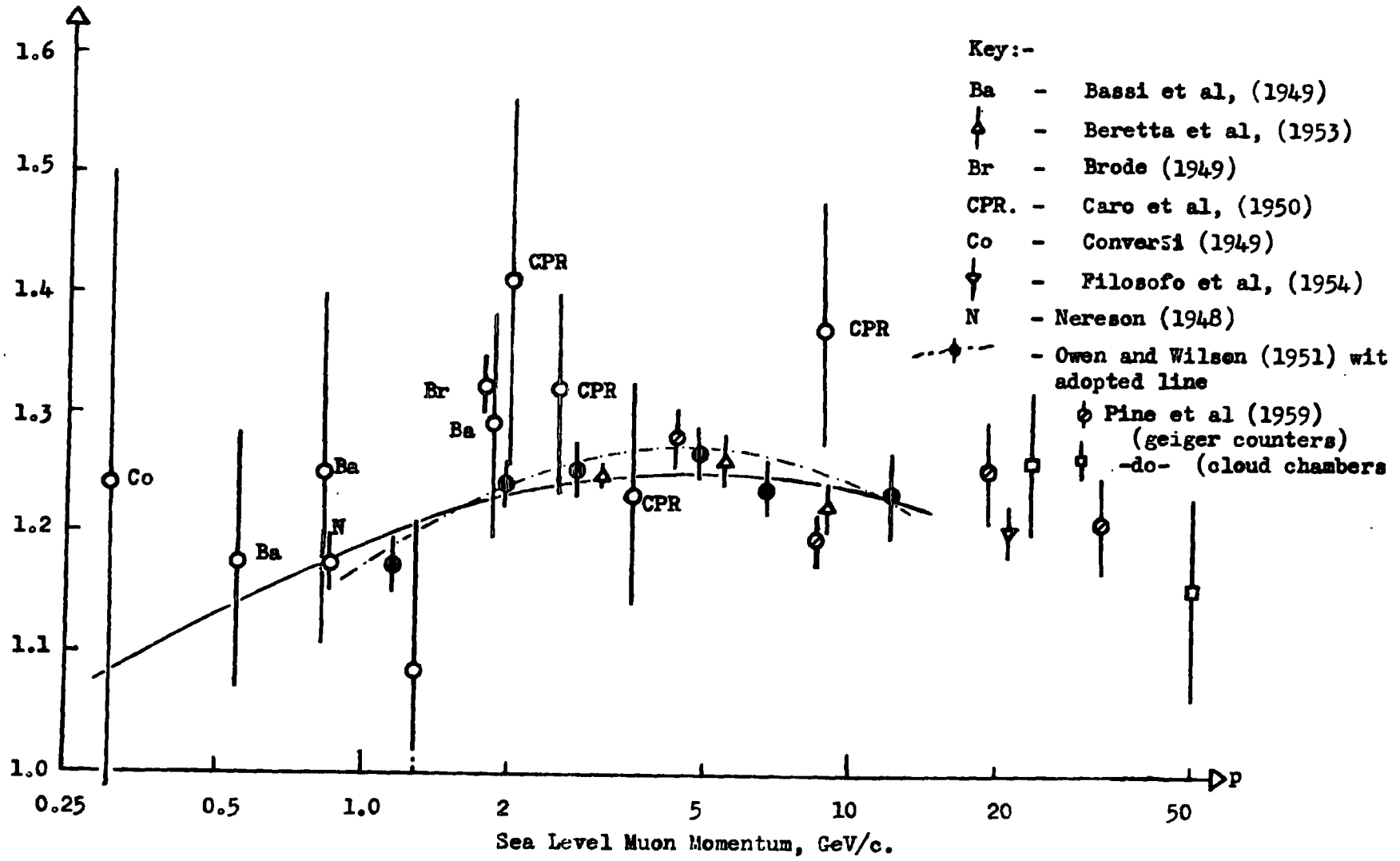

FIG. 8.1.1. Previous measurements of the Positive-Negative Ratio of Muons, with the adopted line of the present work for comparison. (Full line).

excess' co-ordinates to positive-negative ratio points.

8.1.(iii) The Positive-Negative Ratio from the Present Work

In analysis of the data described in Chapter 4, particles with deflection of differing sign were recorded separately. In each case the sign of the field is known, hence the relative numbers of positive and negative particles were determined. Table 8-1-1 below gives the correlation between field, deflection and charge of recorded particles.

Deflection	Field, H	
	Positive	Negative
+	+	-
-	-	+

Charge of particle for deflection stated

Table 8-1-1.

From relative numbers of particles of either charge in each category the relation between category and positive-negative ratio was defined. Category values were converted to momentum values using the method described in section 4.4, and were corrected for momentum loss in the upper half of the spectrograph as described in section 4.8.

8.1. (iv) Correction for Proton Component

It may be shown that the correction to the positive-negative ratio for a known fraction of protons, f, in the sea-level flux, is given by:-

$$\sigma_{muons} = \sigma_{observed} \cdot (1-f) - f \qquad (iv)$$

Appropriate values of f for the various series were obtained from Fig. 4.6.3. (Based on Mylroi and Wilson's results).

8.1.(v) Final Experimental Results

A plot of corrected positive-negative ratio against momentum was then drawn. The fractional error in each point was taken to be:-

$$\sqrt{n_+^{-1} + n_-^{-1}} \simeq 2N^{-\frac{1}{2}}$$

where N is the total no. of particles. This is the result of combining $n_+^{-\frac{1}{2}}$, $n_-^{-\frac{1}{2}}$, the fractional statistical error in each of the two basic quantities used. The curve obtained is shown in Fig. 8.1.2., with the curve of Owen and Wilson (1951) for reference.

8.2. Interpretation of the Positive-Negative Ratio

8.2.(i) Terminology

Let p_μ be the sea level momentum of muons of any given momentum

p_π be the corresponding pion momentum at depth t in the atmosphere

p_π' be the generation momentum of first generation pions having momentum p_π at t.

p_π'' be the generation momentum of second generation pions, interacting once before yielding pions of momentum p_π at t.

$E_{p'}$ be the energy of primary cosmic rays generating pions of momentum p_π' (1st generation)

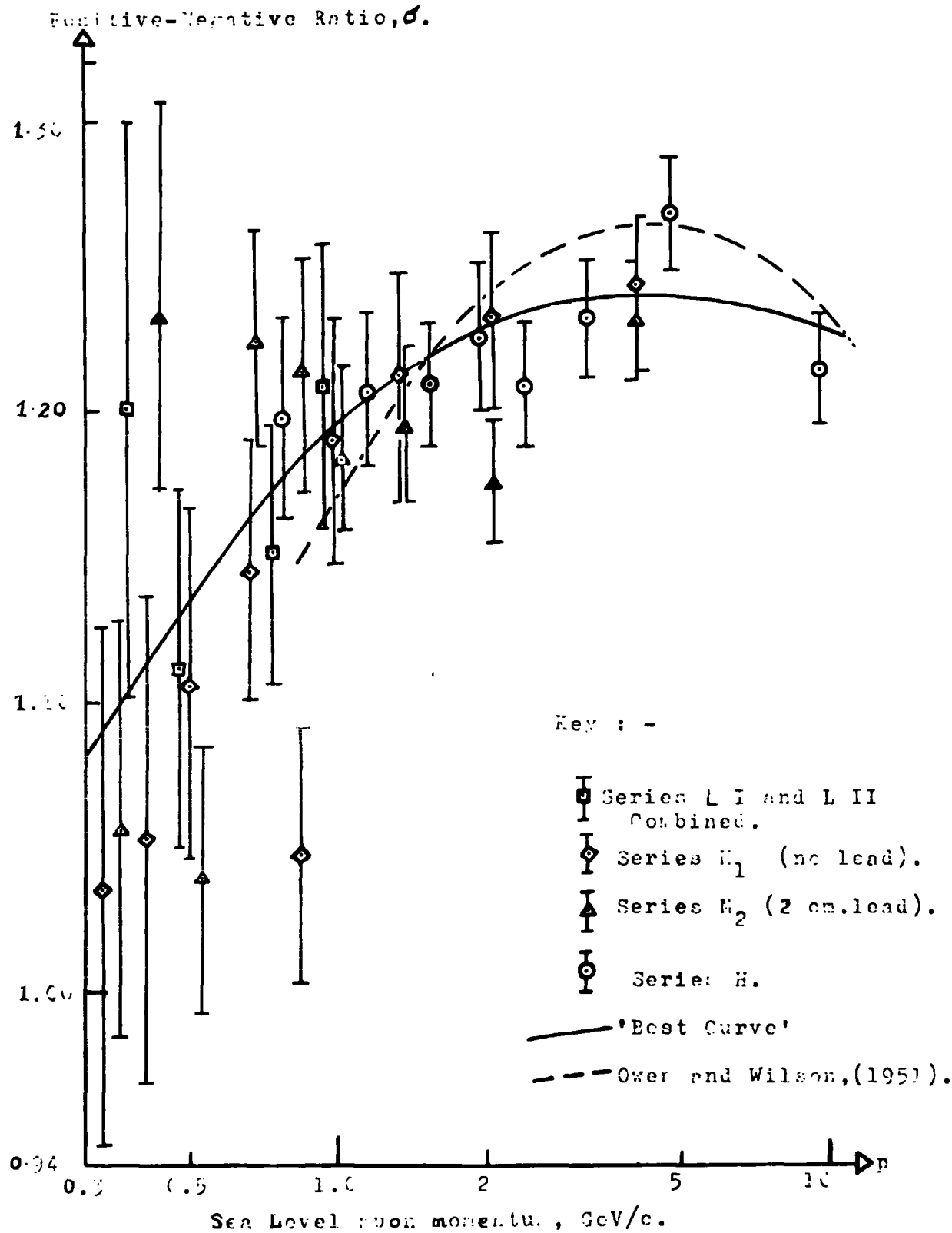

FIG.3.1.2. Experimental Observations of the Positive-Negative Ratio of Muons at Sea level, corrected for momentum loss and Proton Component.

E_p" be the energy of primary cosmic rays generating pions of momentum p " (2nd generation)

σ ' Ratio of numbers of positive and negative

σ " muons reaching sea-level, coming from 1st and 2nd generation collisions of primaries respectively.

σ_t Ratio of number of positive to negative muons at any depth t.

I_p ' Intensities of primary cosmic rays at

I_p " production levels of pions of first and second generations respectively.

e - Average inelasticity of primary cosmic ray collisions, i.e. fraction of energy in each collision not carried off by the colliding particle, usually generating secondary particles.

K - Constant in Fermi's multiplicity law for inelastic collision.

(Ke) Complex constant in Fermi's multiplicity law, used generally in computation since K and e are not initially easily separated.

8.2.(ii) General

The positive - negative ratio of cosmic ray muons is not easy to interpret theoretically. Previous attempts have been made by Yefvin (1955) whose work

shows that, if Fermi's multiplicity law

$$\bar{m} = K E^{\frac{1}{4}} \qquad \text{(Fermi 1951)} \qquad \text{(i)}$$

is true, then the slope of the primary spectrum is 2.15, alternatively if the slope of the differential primary spectrum is taken to be 2.44 (a reasonable mean value in the primary range $10 < E_p < 100$ GeV) then the multiplicity is given by a law:-

$$\bar{m} = K E^{0.21}$$

Neither of these two results would appear to be satisfactory. Pine et al used the positive - negative ratio to yield information about the inelasticity, e, of the primary collisions. An alternative numerical approach, following and further to the computations described in Chapter 7 was used here to give similar results concerning multiplicity and inelasticity.

8.2.(iii) Computation of Theoretical Positive - Negative Ratio

The general method was to use the known incremental intensities, ΔI_μ, of muons at sea-level, coming from each layer of the atmosphere, already found in the way described in Chapter 7, to find a weighted mean positive - negative ratio for the particular sea-level momentum p_μ. Known values of p_π were used to compute values of E_p' and E_p''. It is reasonable to assume that some pions at each level come from second generation collisions since re-generation

accounts for the difference in the absorption and interaction lengths of primaries - 130 and 70 $g.cm^{-2}$ respectively. Also, since the differential primary spectrum has a steep negative slope of power 2.44, it is reasonable to neglect the intensity of generations higher than second. The influence of second generation collisions was found to be small in the present computations.

From computed values of E_p' and E_p'', corresponding values of σ at each t were found, σ' and σ'' respectively, and a weighted mean σ at each level, σ_t, found using:-

$$\sigma_t = \frac{\sum_{\text{two generations}} \sigma \times I_{\text{primary}} \times M}{\sum_{\text{two generations}} I_{\text{primary}} \times M} \qquad \text{(ii)}$$

where M is a factor taking into account the number of primaries interacting at each level and multiplication in collision.

A weighted mean value of σ at sea-level over the values of σ_t was found from the relationship:-

$$\sigma_{S.L} = \frac{\sum_{0<t<1033} \sigma_t \times (\Delta I_\mu)_t}{\sum_{0<t<1033} \Delta I_\mu} \qquad \text{(iii)}$$

Fig. 8.2.1. shows the general scheme - the way in which E_p' and E_p'' at appropriate levels were found, and Fig. 8.2.2. a flow-sheet for the mode of computation of $\sigma_{S.L.}$ The following assumptions were used in the computation:-

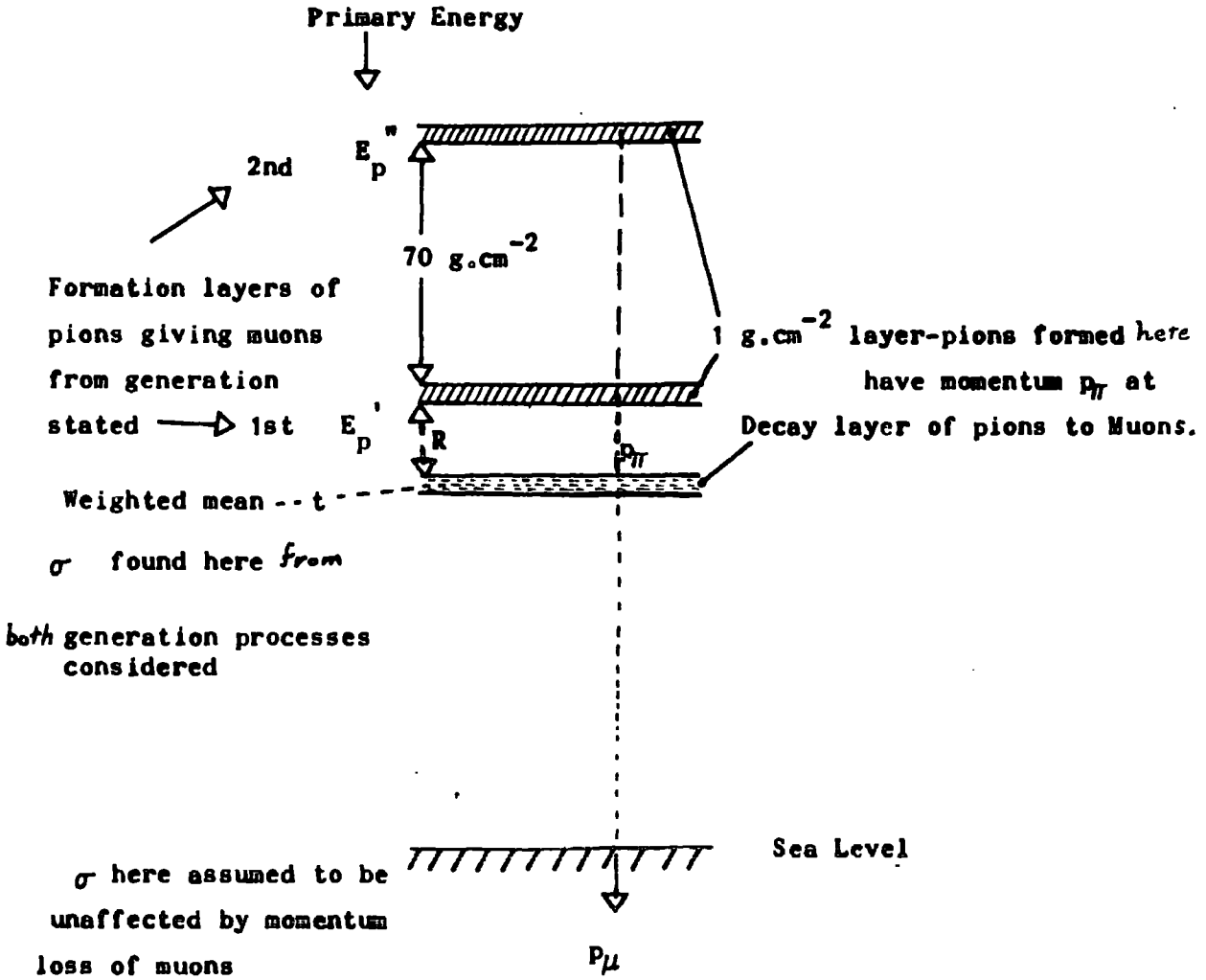

FIG. 8.2.1. General Scheme for Numerical Computation of Sea-Level Positive-Negative Ratio

R is mean pion range between generation and decay

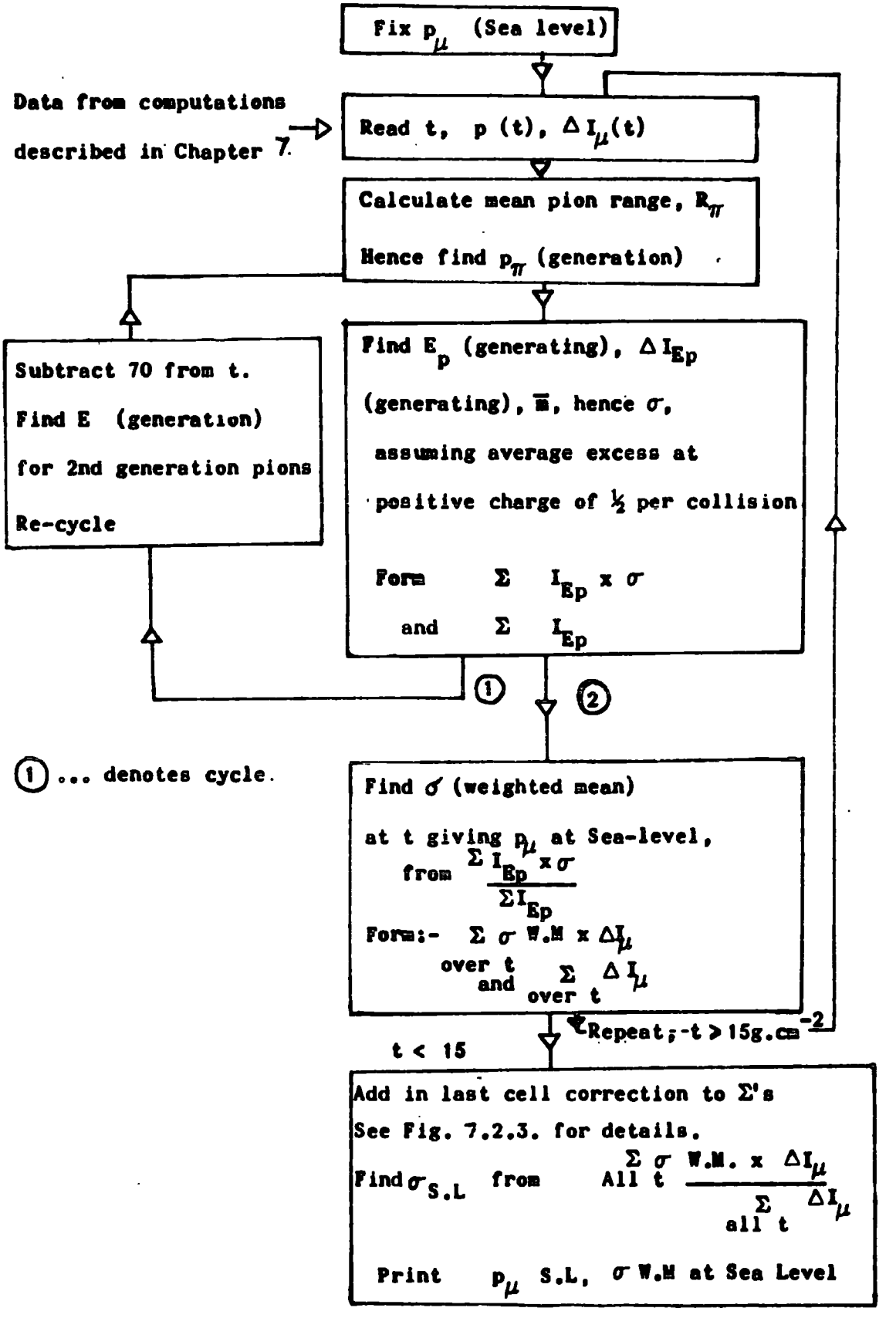

FIG. 8.2.2. Flowsheet for Positive-Negative Ratio Computation.

Charge Excess - it has been assumed that the primary cosmic radiation consists predominantly of protons. When inelastic collisions occur between such protons and atmospheric nuclei it is assumed that a net excess positive charge of $\frac{1}{2}$ (x proton charge) is carried off, the original proton having equal probabilities of emerging as a charged or neutral particle. In second generation collisions it has been assumed that the relative numbers of positively, negatively and uncharged particles remain constant, i.e. the original positive excess of $\frac{1}{2}$ remains but is distributed amongst a larger number of particles, decreasing the overall positive excess. This follows the work of Yeivin and Pine. σ is found as follows - if $\bar{m}$ charged particles are produced in an inelastic collision, of which $\bar{m}/2$ have negative charge, $\bar{m}/2+\frac{1}{2}$ positive charge, then the ratio of positive to negative particles is:-

$$\sigma = \frac{\bar{m}/2+\frac{1}{2}}{\bar{m}/2}$$

$$= 1 + \frac{1}{\bar{m}} \qquad \text{(iv)}$$

Multiplicity - this is assumed to rise as a given power of the inelastic collision energy, following Fermi - see equation 8.2.(i). (Ke) has been regarded as a composite constant having values described later. The particles produced in an inelastic collision are all assumed to have the same energy in the centre of mass

system. This is a reasonable assumption when a large number of collisions are considered. K is then taken to be the constant referring to generation of charged particles only.

Primary Energy - if Fermi's multiplicity law -

$$\bar{m} = (Ke)E^{\frac{1}{4}},$$

holds, then the energy of a primary giving rise to $\bar{m}$ secondaries each of energy E_s is given by:-

$$E_p = \bar{m}E_s$$

or

$$E_p = (KeE_s)^{4/3}, \qquad (v)$$

on substituting for $\bar{m}$.

Second Generation - The energy of primary particles giving second generation muons was found by simply regarding the first generation primary energy E_p' as that of secondary particles from a higher collision at a depth of one interaction length (70 $g.cm^{-2}$) less in the atmosphere.

The primary cosmic ray spectrum was taken to be of the form:-

$$I_p dp = K' E_p^{-2.44}\, dp \qquad (vi)$$

(K' cancelling in the expression for obtaining a weighted mean. The exponent -2.44 is a mean value over the range $1<E_p<10^3$ GeV, after Rossi, (1960)).

Geomagnetic Cut-off of Primaries - following Singer (1958) and Rothwell et al (1958), it was found that cut-off of the primaries occurs at an energy of 1.3 GeV for the

geographic latitude of Durham (55^{o}N). This cut-off was included in the computation - when a primary energy of less than 1.3 GeV was encountered the next generation was considered as giving rise to the muons observed. This is not strictly true, since some low energy muons come from high energy collisions (non-equipartition of energy amongst the secondaries), but is considered sufficiently accurate for this treatment. The highest generation of collisions considered because of this criterion was the fourth.

The <u>interaction length</u> of the primary and interacting secondary cosmic rays was taken to be 70 $g.cm^{-2}$.

<u>Correction for Pion Path</u> - between generation and decay the pions traverse a small thickness of atmosphere. The pions are assumed to have a mean range $\gamma c\tau$ cm. (see Appendix A.7.1.3) before decay. If an isothermal atmosphere is assumed (Appendix A.7.1.2) then the density of air, ρ, is given by:-

$$\rho = \frac{t}{h_o}\text{, where } h_o = 7.02 \text{ Km, an average value over the whole atmosphere}$$

or
$$\rho = \frac{t}{7.02 \times 10^5} \quad g.cm^{-3} \qquad \text{(vii)}$$

Hence the mean depth traversed by the pion between generation and decay will be:-

$$\Delta \bar{t} = s\rho$$

$$= \left(\frac{\gamma . \tau . c . t}{7.02 \times 10^5} \right) \quad g.cm^{-2} \qquad \text{(viii)}$$

Values of Ke chosen - an approximate value of (Ke) was found from the work of Barrett et al, (1952) in which 800 GeV muons at sea-level are associated with primaries of 4×10^4 GeV. giving a value of (Ke) = 2.8.

The computations were then carried out using these assumptions with the result that a curve of σ versus p was obtained below the observed curve. The computations were then repeated for values of (Ke) of 1.2 and 2.0. Actual values of (Ke) consistent with the observed curve were then obtained graphically by interpolation between the known values.

8.2.(iv) Comparison Between Experiment and Theory

Figure 8.2.3. shows the theoretical curves and experimental curves plotted on the same scale. It is clear that (Ke) is not constant with variation of sea-level muon momentum. Values of (Ke) and p_μ have been tabulated in table 8-2-1 together with values of the median E_p corresponding to p_μ. Median values of t and p_π were obtained from the results of the computations described in Chapter 7 (Fig. 7.2.7), and p_π converted to corresponding E_p, considering interaction at the median depth. This is only approximate but gives a guide to the variation of (Ke) and $\bar{m}$ with E_p. These are shown graphically in Fig. 8.2.4.

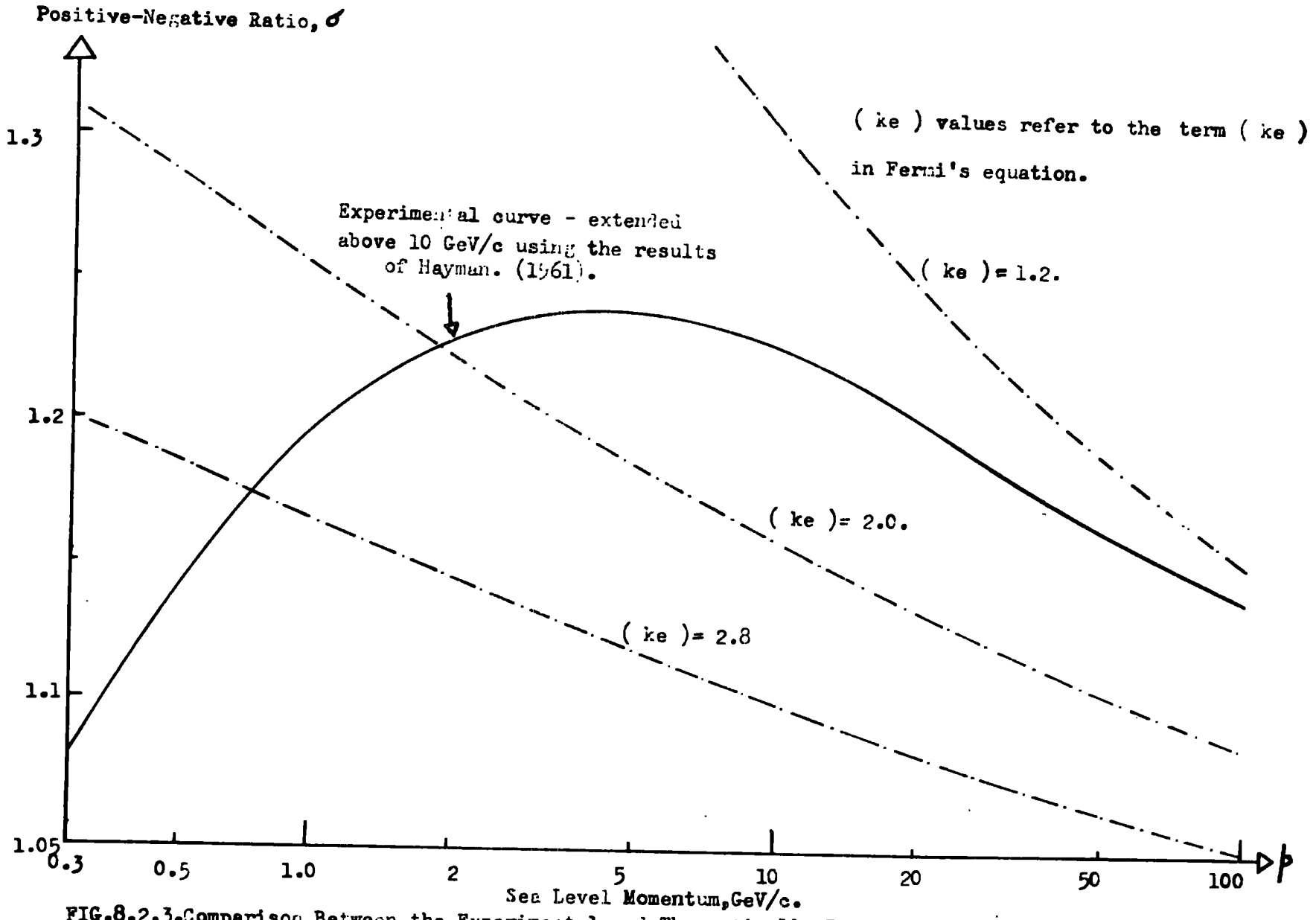

FIG.8.2.3.Comparison Between the Experimental and Theoretically Predicted Positive-Negative Ratio Curves.

p_{μ} (S.L) GeV/c	(Ke), ± 0.1 Mean value (from Experiment)	t MEDIAN g. cm^{-2}	$E_{\pi}(t)$ GeV	$E_p = (Ke)E_{\pi}^{\frac{4}{3}}$ GeV	$\bar{m} = (Ke)\, E_p^{1/4}$	K	e
0.8	2.7	159	3.22	17.8±0.7	5.62±.21	9	
1.0	2.5	154	3.70	19.4±0.8	5.37±.22	8.3	0.3
2	1.95	137	5.83	25.7±1.3	4.38±.22	6.5	
5	1.7	117	9.23	39.3±2.3	4.25±.25	6.1	0.28
10	1.6	101	15.9	74.6±4.7	4.70±.29	6.4	
20	1.5	83	28.9	152.8±10.2	5.29±.35	6.0	0.25
50	1.5	62	67.4	470 ±31	6.89±.46	6.0	
100	1.5	44	131.2	1138 ± 76	8.71±.58	6.0	

Table 8-2-1. Derivation of Mean multiplicity, $\bar{m}$, as a function of primary cosmic Ray Energy, E_p.

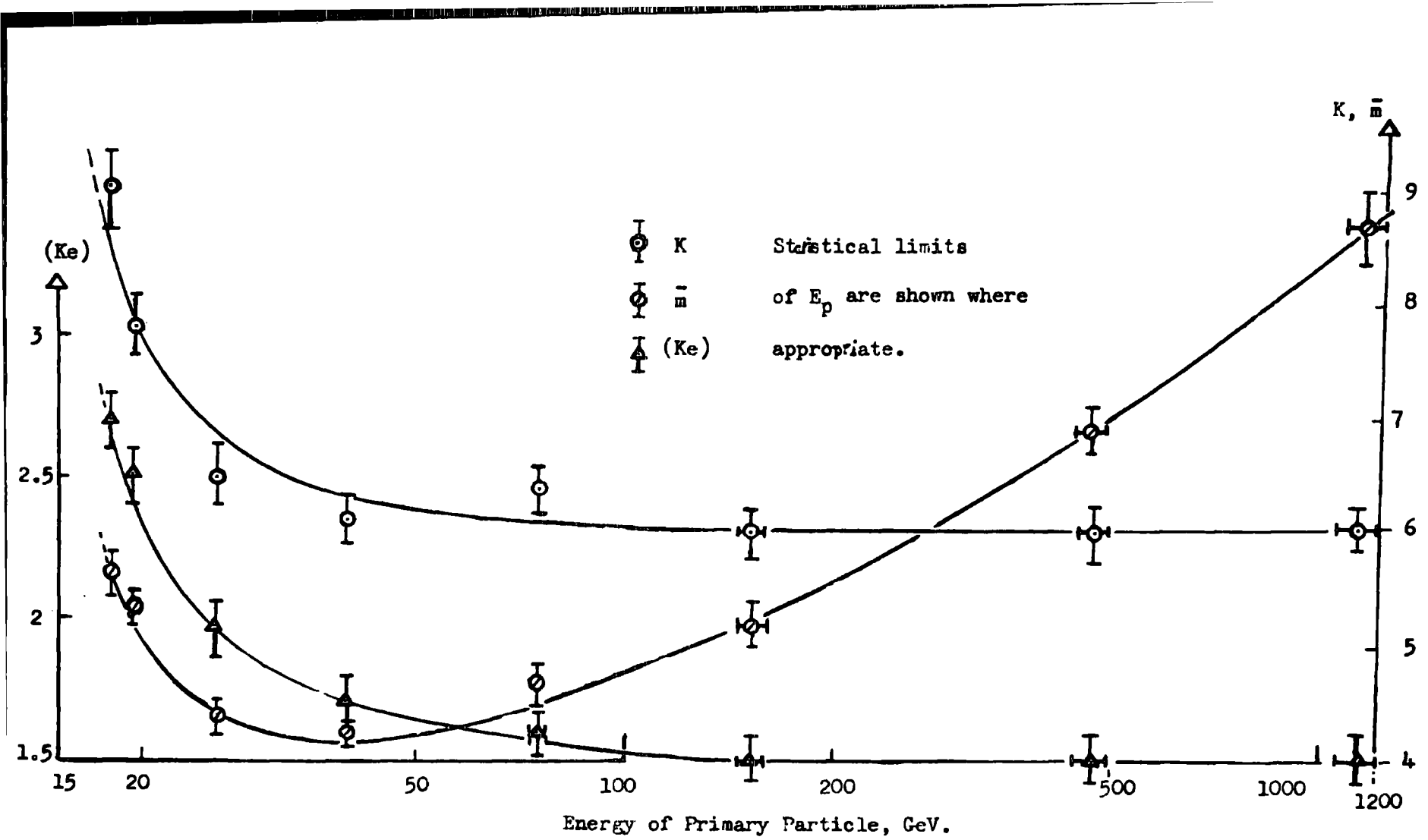

FIG. 8.2.4. The parameters (Ke), $\bar{m}$, and K, derived from the Comparison between theoretical and experimental positive-negative ratios, plotted versus primary energy.

Comparison of $\bar{m}$ with the work of Ishikawa and Maeda (1958) leads one to conclude that the inelasticity is of the order of 0.3 at 20 GeV, falling to an approximately constant value of 0.25 above 50 GeV. The observed fall in inelasticity with energy is also as would be expected from work published by Fretter, (1960). Further support to these conclusions is given by:-

(1) the work of Edwards et al (1958) and Paradzei et al (1958), which combined suggest a mean multiplicity of about 10 at 100 GeV, and

(2) Pine et al, who state that e is ≤ 0.3.

Values of K, in Fermi's equation, separated from e assuming the form for e given by Ishikawa and Maeda, are also shown in Fig. 8.2.4.

Chapter 9.

Correlation with Underground Measurements

9.1. Nature of Correlation

A further check on the accuracy of the results is given by a comparison between the integral spectrum already described (Section 4.13) (converted to a plot of intensity versus depth in rock) and the actual experimental depth intensity curve. Such a check has been performed by many previous workers, e.g. Pine et al.

In order to convert the integral intensity/momentum spectrum to an intensity/range curve in rock the relation between momentum and range in rock must be known. Ashton (1961) has used a comparison between the integral range (rock) spectrum and the depth/intensity curve to check the range/momentum relationship predicted by theory, and found reasonable agreement. The basic theory reviewed by Ashton has been taken to be correct as it stands, and a slight addition made.

9.2. The Range-Momentum Relationship for Muons in Rock Rock

It is convenient to work in terms of a range-energy relationship, then convert energy to momentum where necessary. (At momenta ≥ 1 GeV/c, $E \cong pc$ to better than 0.2%). The range energy relationship is obtained by integrating the rate of energy loss of muons in rock,

i.e.

$$R_E = \int_0^E \frac{1}{(dE/dx)} \cdot dE$$

It is thus necessary to define dE/dx. The rate of energy loss has been considered by many previous workers - notably by Bethe (1930, 1932, 1937) and Bloch (1933), Bhaba (1938), Massey and Corben (1939) (Ionisation loss formula), Halpern and Hall (1940, 1948) (density effect correction), Sternheimer (1956 and 1959) (improved ionisation loss calculations), George (1952) (review of modes of energy loss) and Ashton. The rate of energy loss is the sum of the components due to:-

(i) Ionisation

(ii) Bremstrahlung

(iii) Pair Production

(iv) Nuclear Interaction

(v) Cerenkov Radiation.

With the exception of the nuclear interaction component, the figures quoted follow Ashton (1961).

(i) <u>Ionisation</u>

Following Bethe and Bloch, and Halpern and Hall

$$(dE/dx)_{ion} = \frac{2\mu_e \cdot \pi NZ \cdot r_o^2}{\beta^2 \cdot A} \ln\left\{E_m' + \tfrac{1}{4}\cdot\left(\frac{E_m'}{E+\mu}\right)^2 - 1\right\}$$

$$= 1.51 + 0.0766 \ln\left\{E_m' + \tfrac{1}{4}\left(\frac{E_m'}{E+\mu}\right)^2 - 1\right\} \quad \text{MeV/g.cm}^2\text{, for rock.} \quad \text{(i)}$$

where $E_m' = \left(\frac{E^2}{E^2 + \frac{\mu^2 c^2}{2\mu_e}}\right)$, the maximum transferable energy.

(ii) Bremstrahlung

$$(dE/dx)_{brem.} = 1.5 \times 10^{-7}.E\left\{\ln\left(\frac{E}{\mu c^2}\right) - 0.23\right\} \quad \text{MeV/g.cm}^{-2} \qquad \text{(ii)}$$

(iii) Pair Production

$$(dE/dx)_{p.p.} = 1.6.10^{-6}.E. \quad \text{MeV/g.cm}^{-2} \qquad \text{(iii)}$$

(iv) Nuclear Interaction

Previous workers have assumed a constant fraction of E, viz. $0.5 \times 10^{-6}.E$, for this. However, recent work by Murdoch et al (1960) has shown this not to be accurate, and they give for the following, for rock:-

$$(dE/dx)_{nuclear} = \frac{2\alpha}{\pi}.\sigma.N.\left(\frac{2}{3}\ln\frac{E}{\mu} - \frac{29}{36}\right).E. \quad \text{MeV/g.cm}^{-2} \qquad \text{(iv)}$$

where α is the fine structure constant, i.e. 1/136.7,

N is Avagadro's number, 6.023×10^{23},

and σ is the photonuclear cross-section, 10^{-28}cm^2, according to Fowler and Wolfendale, (1958).

(v) Cerenkov Radiation

The nature of this, and the mode in which polarisation is effected has been described by Jelley (1958). George included a separate term in (dE/dx) to account for the energy loss due to this type of radiation, actually 0.1 ln E MeV/g.cm^{-2} with E in GeV, but several workers, (e.g. Sternheimer) believe that this has already been accounted for in the term for ionisation loss. If the collisions at high energy are regarded as indirect rather than direct, producing momentary polarisation rather than

ionisation, this may be seen to be the case (the impact parameters are relatively much smaller). No separate term for Cerenkov radiation has been included in the present work. The final equation for $(dE/dx)_{total}$ is seen to be the sum of the separate components above. (i)-(iv).

Following Ashton, the integration was performed by dividing it into two parts:-

$$R = \int_0^1 \left(\frac{1}{dE/dx}\right).dE + \int_1^E \left(\frac{1}{dE/dx}\right).dE \qquad \text{(vi)}$$

The range of 1 GeV particle in rock, i.e. $\int_0^1 \left(\frac{1}{dE/dx}\right).dE$, is taken to be 545 $g.cm^{-2}$ following Sternheimer. Sternheimer's figure only takes into account ionisation loss, but is quite accurate since the other modes of energy loss are insignificant below and at 1 GeV.

The terms of (dE/dx) and integration over the range 1 to 10^4 GeV were evaluated using the electronic computer (trapezoidal rule for integration). The result is shown in Fig. 9.2.1.

9.3. The Integral Range Spectrum and the Depth-Intensity Curve

The integral range spectrum was obtained by converting the integral momentum spectrum (Section 4.13), converting momentum to corresponding range using the relationship described. Intensity versus momentum is shown in Fig. 9.3.1. and intensity as a percentage of that above 199 $g.cm^{-2}$

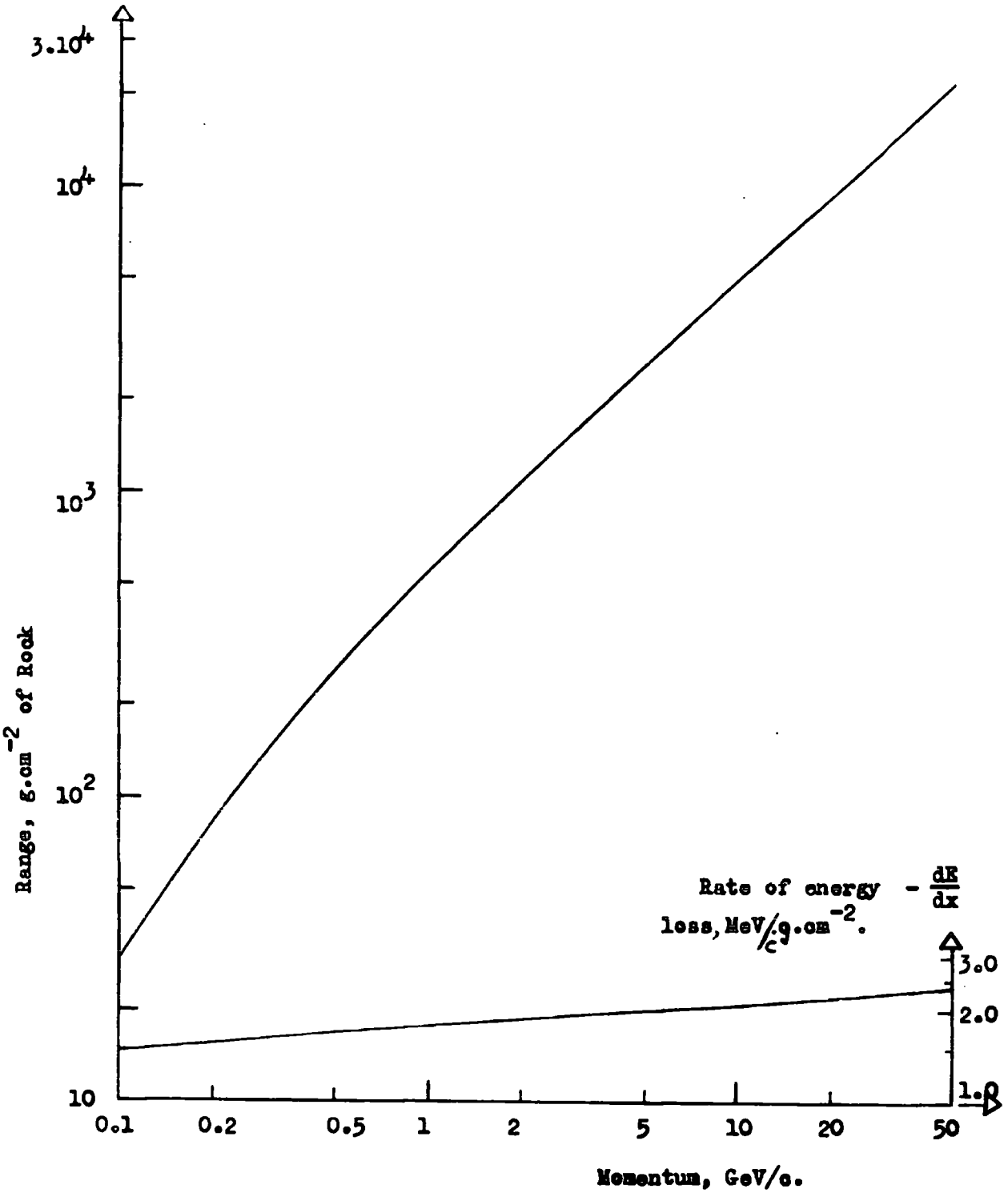

FIG. 9.2.1. Range-Momentum Relationship for Muons in Rock. The lower curve shows the rate of energy loss on which the upper curve is based. Part I

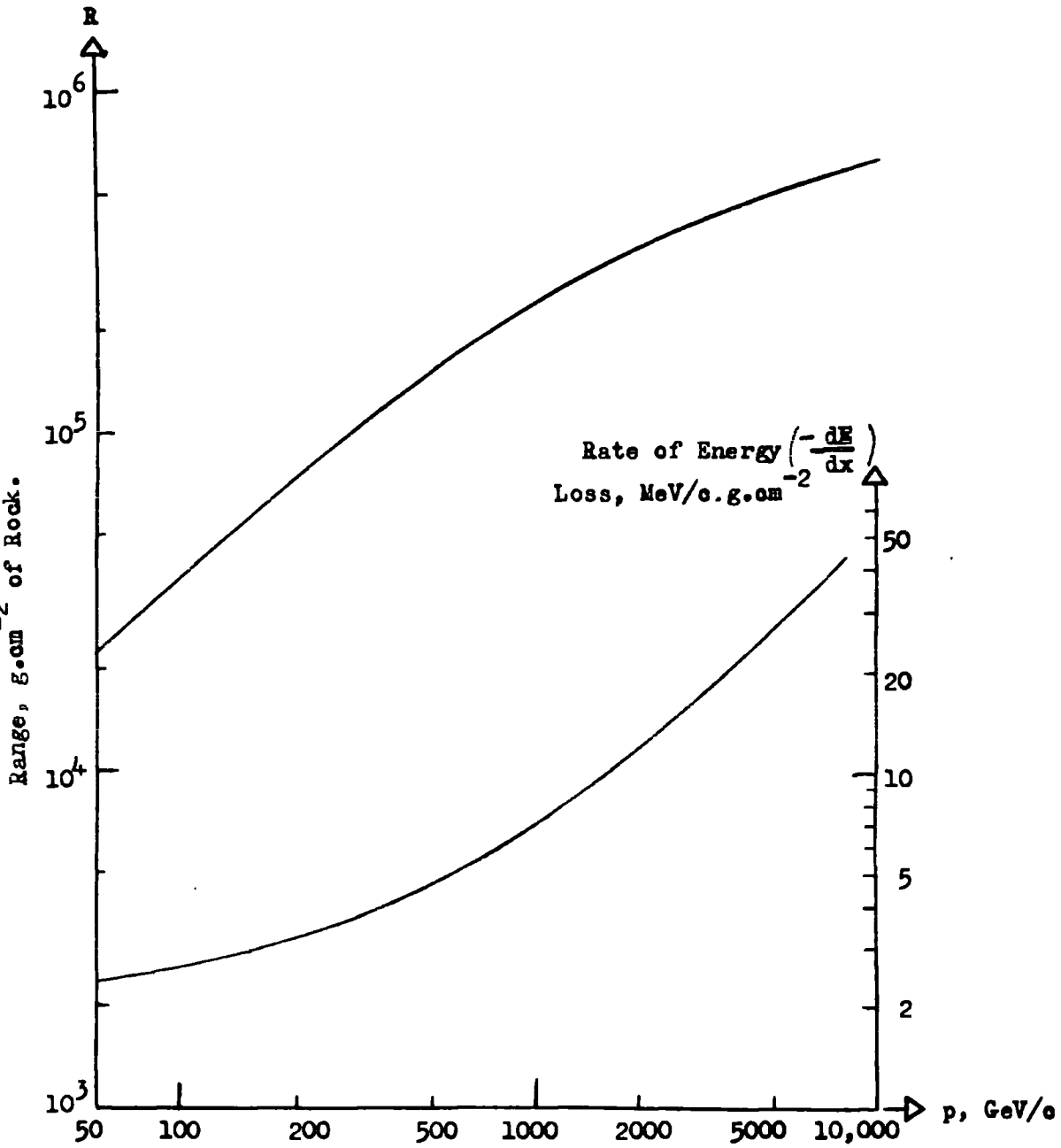

FIG. 9.2.1. Range-Momentum Relationship for Muons in Rock. The lower curve shows the rate of loss on which the upper is based. Part II

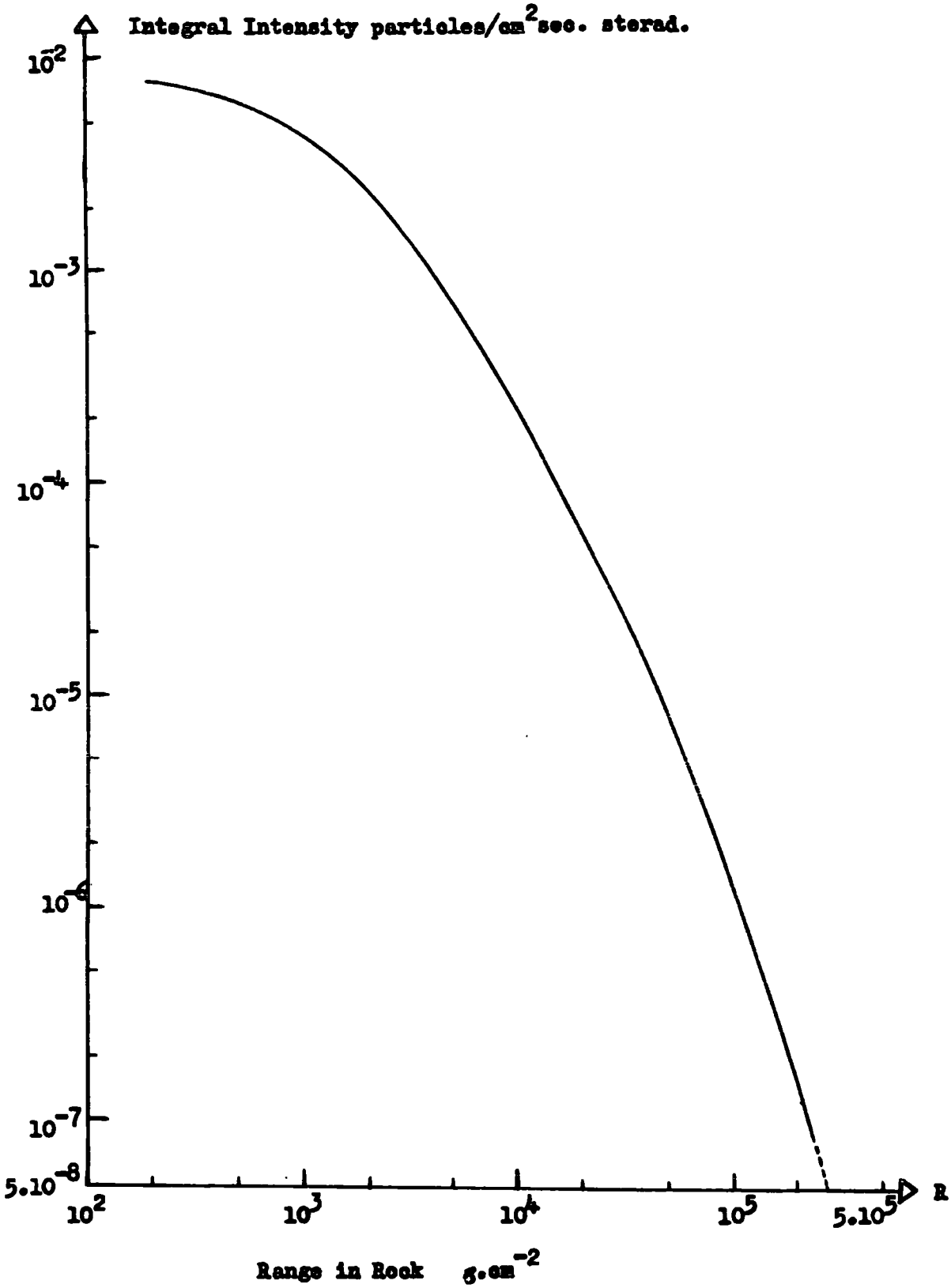

FIG. 9. 3. 1 Integral Range Spectrum of Muons at Sea-Level.

in Fig. 9.3.2. The depth-intensity curve and integral range spectrum were plotted as a series of points on the same graph (Fig. 9.3.3.). No normalisation was found to be necessary - the curves effectively being coincident at zero depth. Pine et al found normalisation at 10^4 g.cm^{-2} necessary. Depth was measured throughout in units of g.cm^{-2} of rock: the much used ambiguous term 'metres of water equivalent' was avoided, since the mean atomic number, Z, and mean atomic weight, A, of rock or other absorber is not the same as that of water - slight correction to the components of (dE/dx) is necessary in conversion. (For the differing Z/A values entering into certain constant terms for dE/dx, e.g. see equation 9.2(i), also Pine et al).

The data of Ehmert (1937) were actually measured under water and were converted to equivalent depth in rock by multiplying the depth in water in g.cm^{-2} by 1.19, a factor consistent with the work of Clay (1939). The data due to other workers, notably Pine et al; Barrett et al (1952); Bollinger (1951); Randall and Hazen (1951); Wilson (1933) and Avan and Avan (1955) was used to define the depth intensity relation, as shown.

The plot shows good agreement between the depth-intensity curve and integral range spectrum, this leading to a conclusion that the sea-level spectrum, momentum-range relationship, and depth-intensity curve are con-

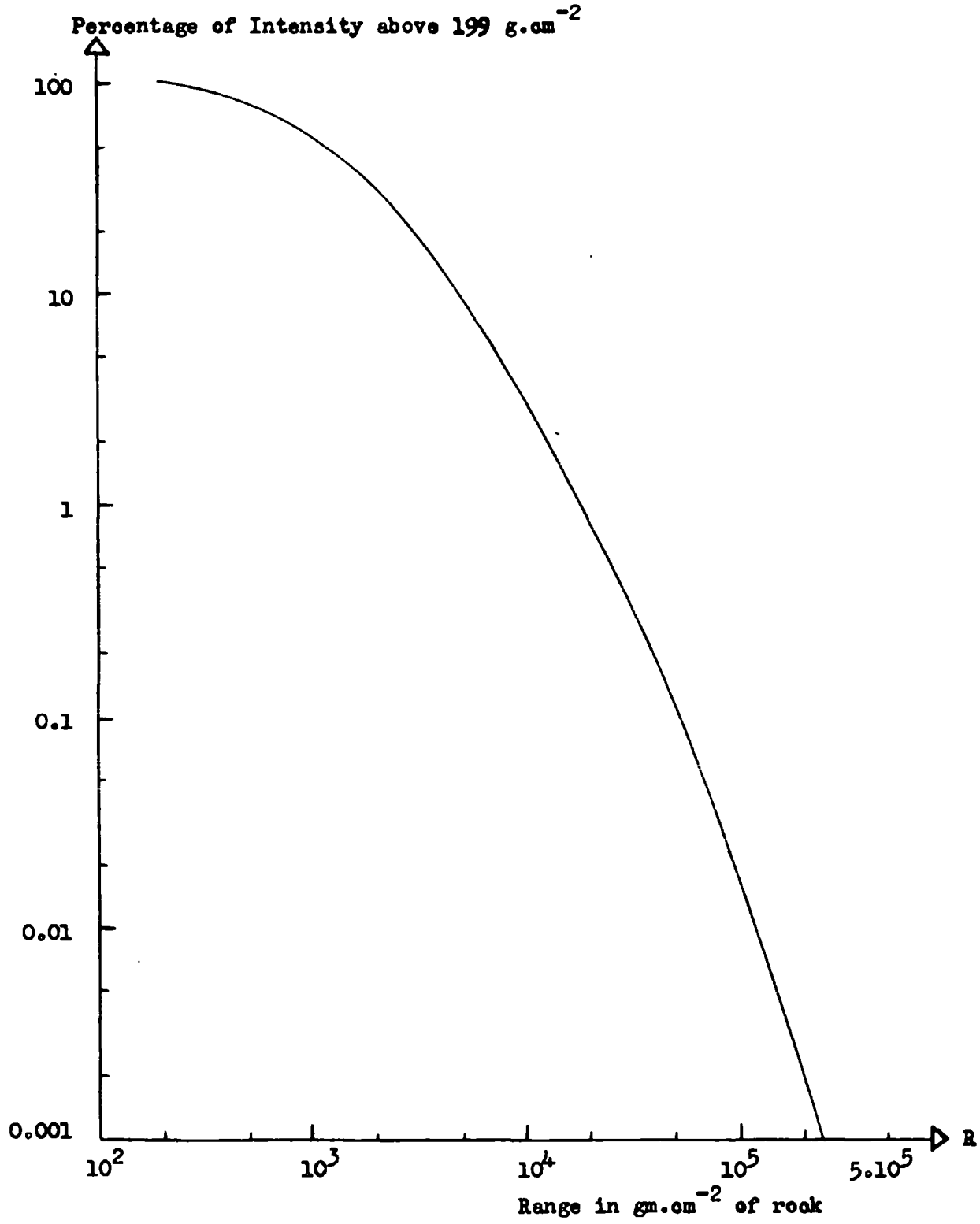

FIG. 9.3.2. Integral Range Spectrum of Muons at Sea-Level Expressed as a percentage of the Intensity above 199 g. cm^{-2}.

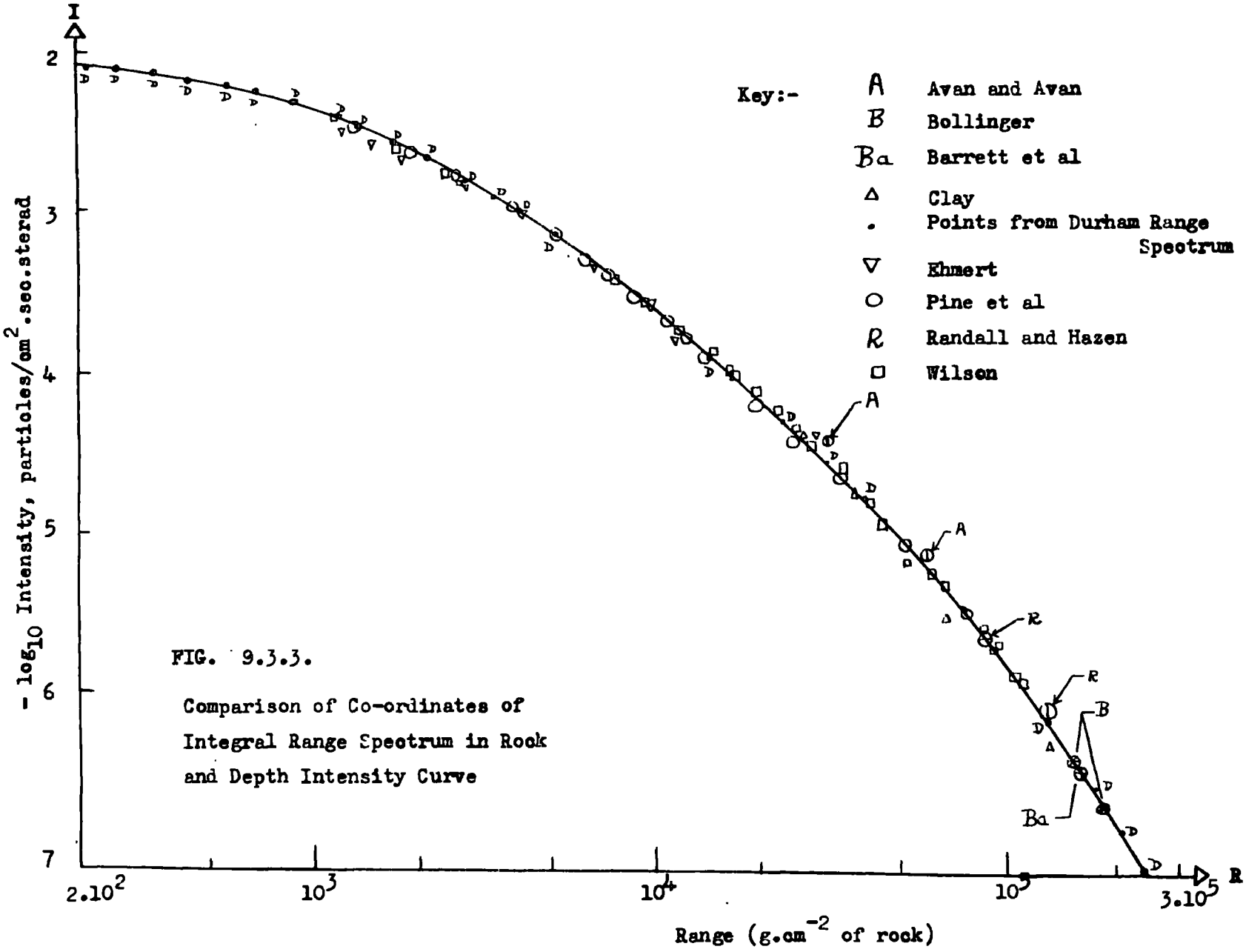

FIG. 9.3.3.

Comparison of Co-ordinates of Integral Range Spectrum in Rock and Depth Intensity Curve

sistent. Ashton (1959 and 1961) found similar agreement using (i) a slightly simpler treatment for energy loss (simpler nuclear interaction term) and hence range-momentum relationship, and (ii) the momentum spectrum as published in 'Nature' (1960), i.e. neglecting many of the corrections at low momentum described in the present work.

One further factor connected with this work is worthy of mention. Fluctuations in momentum loss and therefore in range occur for particles of any given momentum at sea-level, when penetrating the earth. Bollinger (1950, 1951) has considered this problem and applied Monte-Carlo methods for such fluctuations to find the net effect on the shape of the depth-intensity curve. These were found to be of negligible magnitude, as verified by the good agreement between the observations already described. Such fluctuations have increased effect at high ranges when the number of underground particles is relatively lower, and may possibly just be becoming significant in the upper region of the ranges considered here. (Their importance increases with the statistical accuracy of the sea-level range spectrum).

Chapter 10

Conclusions.

10.1. Present Work

The sea-level spectra of the hard component of cosmic rays are the important initial data required in order to consider interactions and other properties of the radiation. The results presented give accurate measurements of the ground level spectra of the hard component at Durham, 198 feet above sea-level, to an accuracy better than 1.5%, in the momentum range 0.4 to 10 GeV/c.

The differential momentum spectrum in the momentum range 1 to 1000 GeV/c has been published by the group (Ashton et al 1960) and is shown in Fig. 10.1.1. That section above 10 GeV/c is complementary to the present work.

The investigation of bias due to rejected multiple events has shown that the bias due to knock-on electron events and low density accompanied muon events is small - appropriate corrections for the former have been made. It seems likely that those events giving rise to a dense shower in the apparatus are associated with very high primary energies, and hence secondary muons (or pions) of momentum above 10 GeV/c - hence they will contribute no bias within the range considered. It is therefore

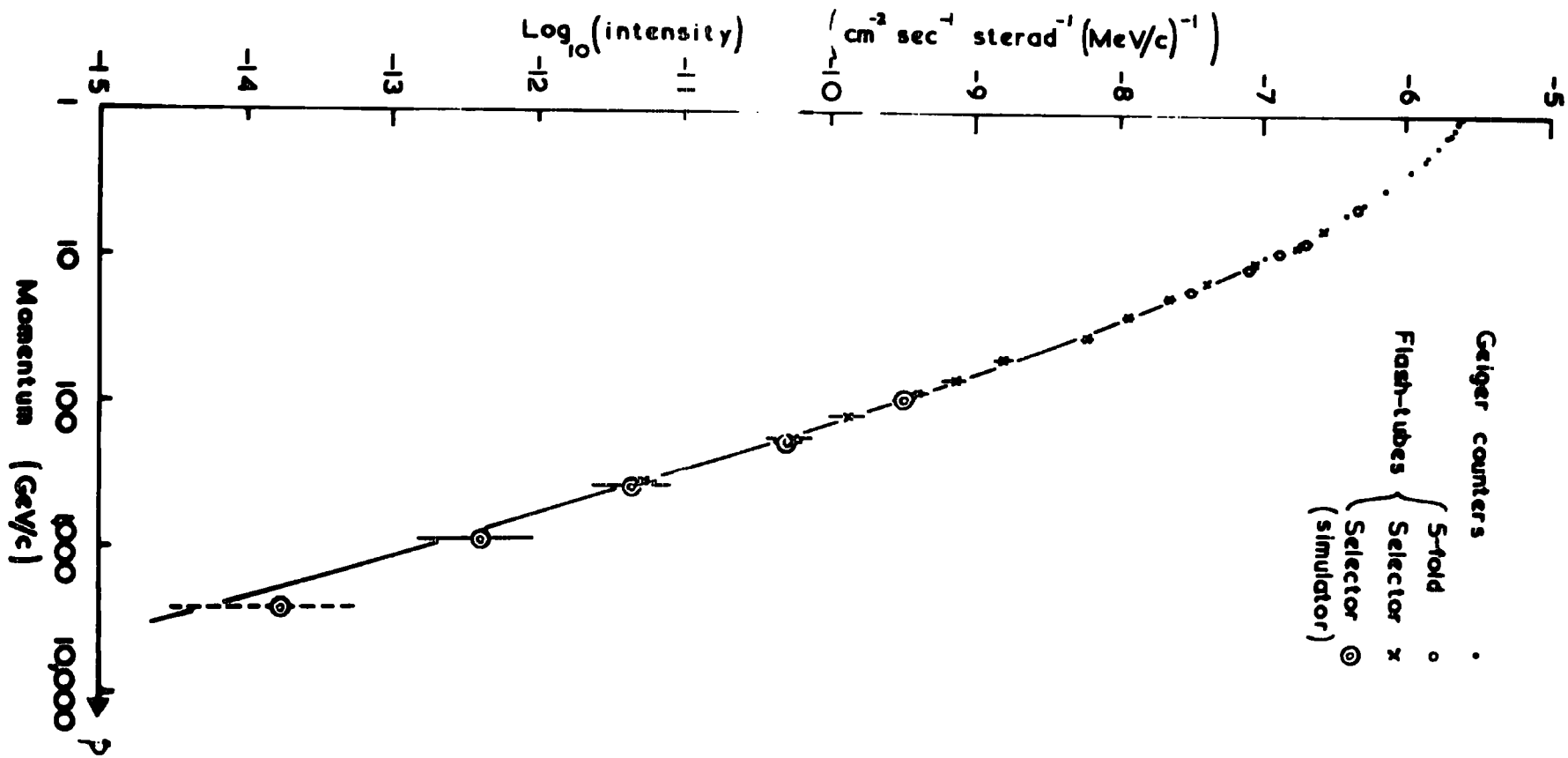

FIG. 10.1.1. The Differential Momentum Spectrum of Single Mesons in the range 1 - 100... GeV/c observed using the Complete Durham spectrograph. The counter results (at low momenta) are not corrected for ionisation loss or scattering.

concluded that this work presents the most accurately known differential spectrum of the hard component of cosmic radiation at sea-level in the momentum range 0.4 to 10 GeV/c. (Fig. 5.7.1.).

Assuming that the sea-level hard component consists, to all practical purposes, of only muons, resulting from decay of cosmic ray pions, a generation spectrum for cosmic ray pions has been found. This follows a propagation model considering distributed pion production through the atmosphere - accurate to the accuracy of the parameters used in computation - to better than 10% in all. The final pion generation spectrum is shown in Fig. 7.3.6., and may be closely represented by a law of the form:-

$$I(p_\pi).dp_\pi = A.p_\pi^{-\gamma}.dp_\pi$$

where A, γ are given by:-

$$A = 1.82.10^{-4}\left(\frac{p_\pi}{4}\right)^{0.712} \text{ for } 0.6<p_\pi<4.0 \text{ GeV/c}$$

$$A = 1.82.10^{-4} \text{ for } p_\pi>4.0 \text{ GeV/c}$$

and $\gamma = 2.64$ (constant)

This generation spectrum has been used to compute the sea-level spectrum of pions, for varying absorption lengths, a best fit to the experimentally observed spectrum being obtained for

$$\lambda_{\text{absorption}} = (135 \pm 3)\text{g.cm}^{-2}.$$

This value, an 'average' value over the momentum range $0.6<p_{\pi}<15$ GeV/c, is not inconsistent with other published values.

The muon positive-negative ratio has been interpreted to give the multiplicity of high energy primary component collisions, $\bar{m}$, as a function of primary energy, E_p, also to give values of the constant (Ke) in Fermi's multiplicity equation:

$$\bar{m} = (Ke)E_p^{\frac{1}{4}}$$

(Ke) is shown as a function of momentum in Fig. 8.2.4. By comparison of $\bar{m}$ with that given by the work of Ishikawa and Maeda (1958), one finds that the inelasticity in such collisions decreases from 0.30 at 20 GeV primary energy to a value of 0.25 at 50 GeV. Corresponding values of K from (Ke), separated from e, are also given in Fig. 8.2.4.

Finally, another independent check on the correctness of the spectrum is given by the good agreement between the observed depth intensity curve, and the integral range spectrum, deduced from the integral momentum spectrum using the range-energy relationship (Fig. 9.3.3.). Alternatively, this implies that the assumed rate of energy loss is correct.

Acknowledgments

The author wishes to thank Professor G.D. Rochester, F.R.S., for provision of the facilities which have made this work possible, and Dr. A.W. Wolfendale for his invaluable detailed direction.

Thanks are also due to Drs. A.J. Apostolakis, F. Ashton and H. Coxell, and Mr. R.H. West, for help given through discussions on various aspects of this work; Messrs. M. Gardener and D.G. Jones for making available the data obtained in the earlier experiments, Mr. G. Brooke and Dr. M.A. Meyer for their part in making available the sea-level pion spectrum measurements.

Extensive use has been made of the Durham University Pegasus computer (50 hours) and members of Staff of the Computing Laboratory are thanked for help willingly given. Many other colleagues and members of the technical staff have given help in numerous small ways and sincere thanks are extended to them.

This work has been performed during tenure of a DSIR research assistantship - the author wishes to thank that body both for financial support and authority to present this work for a higher degree.

References

Allkofer, O.C. 1959 Atomkernenergie, 10, 389

1960 Zeits.f.Phys. 158, 274.

Apostolakis, A.J. and Allen, J.E.

1961 'The Spectra of Muons at Large Zenith Angles'. To be published.

Ascoli, G. 1950 Phys. Rev. 79, 812.

Ashton, F., Kisdnasamy, S., and Wolfendale, A.W.,

1958 Nuovo Cim. Ser. X, 8, 615.

Ashton, F, 1959 Ph.D. Thesis (Durham).

Ashton, F., Brooke, G., Gardener, M., Hayman, P.J., Jones, D.G., Kisdnasamy, S., Lloyd, J.L., Taylor, F.E., West, R.H., and Wolfendale, A.W.

1960 Nature 185, 364.

Ashton, F. 1961 Proc. Phys. Soc. 77, 587.

Avan, L., and Avan, M.,

1955 Comptes Rendus 241, 1122.

Baradzei, L.T., Rubtsov, V.I., Smoroden, V.A., Solovien, M.V., and Talinova, B.V.,

1958 J.E.T.P. 6, 12.

Barkas, W., and Rosenfeld, A.H.,

1958 University of California Radiation Laboratory Report UCRL 8030.

Barrett, P.H., Bollinger, L.M., Cocconi, G., Eisenberg, Y., and Greisen, K.

1952 Rev. Mod. Phys. 24, 133.

Bassi, P., Clemental, E., Filosofo, I., and Puppi, G.,
1949 Nuovo Cim. Ser. IX, 6, 484.

Beretta, E., Filosofo, I., Sommacal, B., and Puppi, G.,
1953 Nuovo Cim. Ser. IX, 10, 1354.

Bethe, H.A., 1930 Ann. d. Physik, 5, 325.
1932 Zeits. f. Phys. 76, 293.
1937 Rev. Mod. Phys. 9, 245.

Bhaba, H.J., and Corben, H.C.,
1935 Proc. Roy. Soc. A152, 559.
1938 Proc. Roy. Soc. A164, 257.

Bloch, F., 1933 Zeits. f. Phys. 81, 363.

Bollinger, L.M. 1950 Phys. Rev. 79, 207
1951 Ph.D. Thesis (Cornell, U.S.A.)

Braddick, H.J.J. 1955 'The Physics of Experimental Method', Chapman and Hall, p.28.

Brode, R.B. 1949 Nuovo Cim. Ser. IX. 6, 565.

Brooke, G., Meyer, M.A., and Wolfendale, A.W.
1961 'The Sea-Level Spectrum of Cosmic Ray Pions' - to be published.

Caro, D.E., Parry, J.K., and Rathgeber, H.D.
1951 Australian J. Sci. Res. A4, 16.

Caro, D.E., Parry, J.K., and Rathgeber, H.D.
1950 Nature 165, 689.

Clay, J. 1939 Rev. Mod. Phys. 11, 128.

Conversi, M. 1949 Phys. Rev. 76, 311

Conversi, M., Focardi, S., Franzinetti, C., Gozzini, A., and Murtas, P. 1955 Proc. Pisa Conference on Elementary Particles.

Coxell, H. 1961 Ph.D. Thesis (Durham)

Duperier, A. 1951 Nature, 167, 312

Duthie, J.G.M., Fisher, C., Fowler, P.H., Kaddoura, A., Perkins, D.H. and Pinkau, K.
1960. Proc. Moscow Conference 1, 35.

Duthie, J.G.M. 1961 Ph.D. Thesis (Bristol)

Edwards, B., Losty, J., Perkins, D.H., Pinkau, K., and Reynolds, J. 1958 Phil. Mag. 3, 237.

Ehmert, A. 1937 Zeits. f. Phys. 106, 751.

Fan, C.Y. 1955 Phys. Rev. 101, 314.

Fermi, E. 1949 Phys. Rev. 75, 1169.
1951 Phys. Rev. 81, 683.
1954 Astrophys. Journal 119, 1.

Filosofo, I., Pohl, E., and Pohl-Rueling, J.
1954 Nuovo Cim. Ser. IX, 12, 809.

Fowler, G.N. and Wolfendale, A.W.
1958 P.C.R.P., 4, 107.

French, B.J. 1959 Ph.D. Thesis, (Imperial College, London)

Fretter, W.F., and Hansen, L.F.
1960 Proc. Moscow Conf. 1, 136.

Fujimoto, Y., Hasegawa, S., Kazuno, M., Nishimura, K., Nui, K., and Ogita, M.

1960 Proc. Moscow Conf. 1, 41.

Gardener, M., Kisdnasamy, S., Roessle, E., and Wolfendale, A.W.

1957 Proc. Phys. Soc., B70, 687.

George, E.P. 1952 P.C.R.P., 1, 409.

Glaser, D.A., Hamermesh, B., and Safanov, G.

1950 Phys. Rev. 80, 625.

Haber-Schaim, U., and Yekutieli, G.

1954 Nuovo Cim. Ser. X, 11, 172.

Halpern, O., and Hall, W.

1948 Phys. Rev. 73, 477.

Hayman, P.J. 1961 Ph.D. Thesis (Durham).

Hazlehurst, J., and Sargent, W.L.W.

1958 Ph.D. Theses (Manchester).

Hyams, B.D., Mylroi, M.G., Owen, B.G., and Wilson, J.G.,

1950 Proc. Phys. Soc. A63, 1053.

Ishikawa, G., and Maeda, K.

1958 Nuovo Cim. Ser. X, 7, 53.

Jakeman, D. 1956 Canad. J. Phys. 34, 432.

Jelley, J.V. 1958 'Cerenkov Radiation', Pergamon Press, P.21.

Jones, D.G. 1961 Ph.D. Thesis (Durham).

Kisdnasamy, S. 1958 Ph.D. Thesis (Durham).

Kocharyan, N.M., Kirakosyan, Z.A., Sharoyan, E.G., and Pickalov, A.P. 1960 J.E.T.P. 11, 12.

Lloyd, J.L. and Wolfendale, A.W.

1955 Proc. Conference on Cloud Chamber and Associated Techniques, P.51.

1955 Proc. Phys. Soc. A68, 1061.

1959 Proc. Phys. Soc. 73, 178.

Maeda, K. 1960 J. Atmos. Terr. Phys. 19, 184.

Massey, H.S.W., and Corben, H.C.

1939 Proc. Camb. Phil. Soc. 35, 463.

Moroney, J.R., and Parry, J.K.

1954 Australian J. Phys. 7, 423.

Morrison, P., Olbert, S., and Rossi, B.

1954 Phys. Rev. 94, 440.

Morrison, P. 1957 Rev. Mod. Phys. 29, 235.

Murdoch, H.S., Oglivie, K.W. and Rathgeber, H.D.

1960 Proc. Moscow Conf. 1, 304.

Mylroi,, M.G. and Wilson, J.G.

1951 Proc. Phys. Soc. A64, 404.

Nash, W.F., and Pointon, A.J.

1956 Proc. Phys. Soc. A69, 725.

Nereson, N. 1948 Phys. Rev. 73, 565.

Olbert, S. 1954 Phys. Rev. 96, 1400.

1954 "An Analysis of the Meson Component of Cosmic Rays in the Atmosphere". Office of Naval Research (U.S.A.), Report No. NR-026-001.

Owen, B.G., and Wilson, J.G.

1951 Proc. Phys. Soc. A64, 417.

1955 Proc. Phys. Soc. A68, 409.

Parker, E.N. 1957 Phys. Rev. 107, 830.

1958 Phys. Rev. 109, 1328.

Pine, J., Davisson, R.J., and Greisen, K.

1959 Nuovo Cim. Ser. X. 14, 1181.

Powell, C.F. 1960 Proc. I.E.E. 107B, 389.

Puppi, G. 1956 P.C.R.P. 3, 352.

Randall, C.A., and Hazen, W.E.

1951 Phys. Rev. 81, 144.

Rathgeber, H. 1960 Private Communication.

Regener, H.V. 1951 Phys. Rev. 84, 161.

Rodgers, A.L. 1957 Ph.D. Thesis (Manchester).

Rossi, B. 1948 Rev. Mod. Phys. 20, 537.

1952(a), 1952(b), 1952(c) "High Energy Particles" Prentice-Hall, U.S.A. P.70, P.68, P.544.

1960 Proc. Moscow Conf. 2, 18.

Rothwell, P., and Quenby, J.H.

1958 Suppl. Nuovo Cim. Ser.X 8, 249.

Sands, M. 1950 Phys. Rev. 77, 180.

Singer, S.F. 1958 P.C.R.P. 4, 213.

Sternheimer, R.M. 1956 Phys. Rev. 103, 511.

1959 Phys. Rev. 115, 137.

West, R.H. 1961 M.Sc. Thesis (Durham)

Wilson, J.G. 1946 Nature 158, 415.

Wilson, V.C. 1938 Phys. Rev. 53, 337.

Yeivin, Y. 1955 Nuovo Cim. Ser. X, 2, 658.

Appendix A.3.8.1.

For terminology and a typical trajectory please refer to Fig. 3.8.9. The trajectory is not straight for low momentum, but an arc of a circle. It can be seen that:-

$$RKS = (l_A / \sin \phi/2) \times \phi$$

and $$RTS = 2l_A$$

Hence the fractional correction,

$$\frac{RKS - RTS}{RKS} = \left(\frac{\phi}{2 \sin \phi/2} - 1 \right) \cong \frac{\phi^2}{24}$$

Typical values of this are as follows:-

ϕ	$\phi^2/24$, %
0.1	0.04
0.2	0.16
0.3	0.37

The maximum correction for a curved trajectory, within the range of angular deflection used, is thus 0.37%, which may be neglected.

Appendix A.4.3.1.

Statistical Formula for Correction of Photographic Records for Superimposed Pulses.

For any given category:-

Let observed rate of particles be r per frame

" true " " " " R " "

Assume R, r both $\ll 1$, and N, the number of frames, large, $\gg 1$.

If two particles of the same category occur, they are observed as one. Thus r is equal to the sum of the probabilities of each possible number of superimposed particles being observed (Each case of superimposed particles being read as one event). Thus r = sum of probabilities of observing 1, 2, 3 .... particles.

From theory of a Poisson distribution (Braddick, 1955) the probability P_n of observing n particles if the actual rate is R/unit time is:-

$$P_n = \frac{R^n}{n!} \cdot e^{-R}$$

Taking a sum from n=0 to $n=\infty$ to find r, one has:-

$$r = \sum_{n=1}^{n=\infty} \frac{R^n}{n!} \cdot e^{-R}$$

$$= 1 - e^{-R}$$ by expansion of the series for e^{-R}.

or $R = \ln\left(\frac{1}{1-r}\right)$

where ln signifies log to base 'e'.

APPENDIX A. 5. 1. 1

Electronic Circuit Added to Trigger the Flash-Tubes for Multiple events.

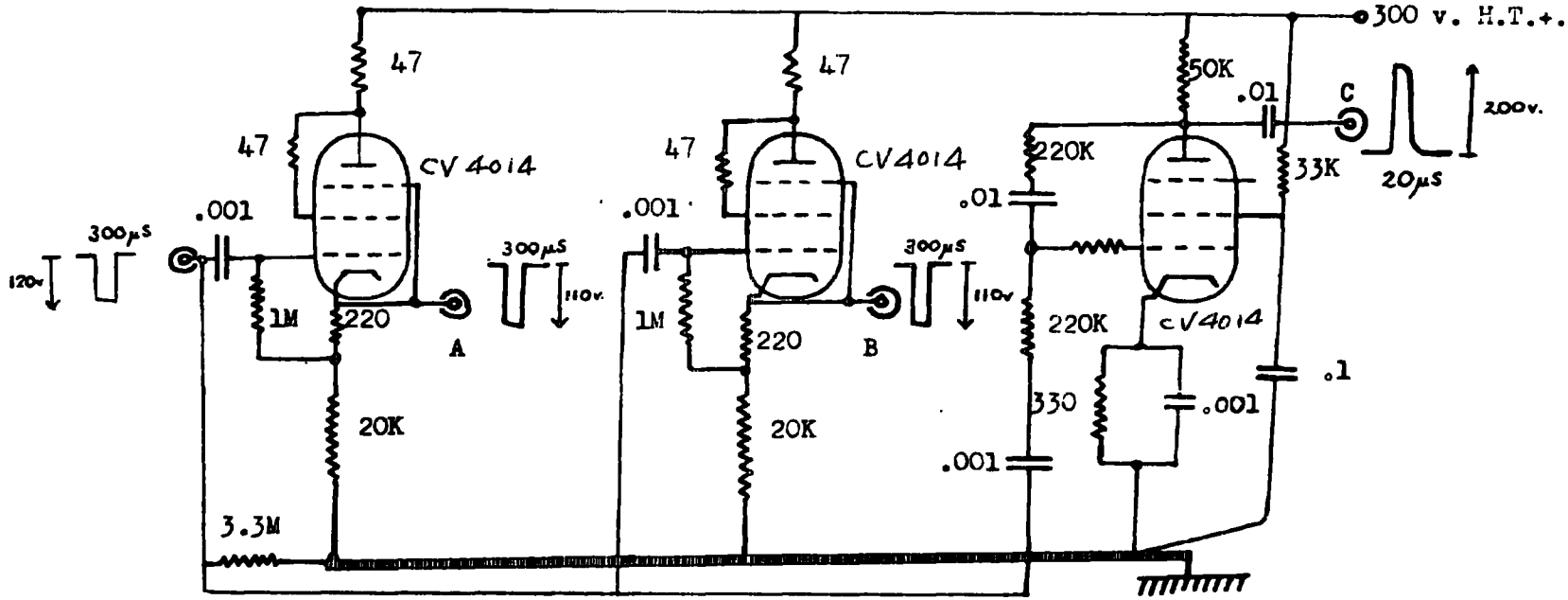

Output A operates a message register

Output B operates blanking of the C.R.O. beam

Output C operates the flash-tube trigger circuits

All resistor values in ohms, capacities in microfarads, unless otherwise stated.

Appendix A.7.1.1.

Mean Range of Pions before Decay as a function of Momentum

If one lets the distance travelled by a pion of given momentum p be S cm., the mean value of S over a large number of such pions will be:-

$$\bar{S} = \frac{\int_{N_o}^{0} S \, dN}{\int_{N_o}^{0} dN} \qquad \text{(i)}$$

It is known from elementary considerations of pion decay that the number decaying in any time dt is given by:-

$$dN = -\frac{N_o}{\tau} e^{-t/\tau} . \, dt \qquad \text{(ii)}$$

Now, t in the particle's frame of reference = $\gamma . t_o$ in the laboratory system. Also, if the pion has a velocity $(\beta.c)$ it will cover S in time γt_o hence $S = \gamma t_o (\beta c)$.

Substituting for S and dN in (i) and changing limits, one obtains

$$\bar{S} = \frac{\int_{o}^{\infty} - \beta c . t \; \frac{N_o}{\tau} \; e^{-t/\tau} . dt}{\int_{o}^{\infty} - \frac{N_o}{\tau} e^{-t/\tau} . \, dt} \qquad \text{(iii)}$$

Integrating the numerator of (iii) by parts and evaluating limits, one has

$$\bar{S} = \beta \gamma c \tau .$$

Replacing β by $(1 - \frac{1}{2\gamma^2})$, it follows that:-

$$\bar{S} = (1 - \frac{1}{2\gamma^2}) \gamma . c . \tau . \qquad \text{(iv)}$$

Substituting $\gamma = p_\pi / m_\pi c$, and values $m_\pi c = 0.1396$ GeV/c, $c = 2.998 \times 10^{10}$ cm/sec., $\tau = 2.56 \times 10^{-8}$ sec, from Barkas et al, into (iv), one obtains:-

$$\bar{S} = 772\left\{\frac{p_\pi}{m_\pi c} - \left(\frac{m_\pi c}{2p_\pi}\right)\right\} \quad \text{cm.}$$

where p_π is measured in GeV/c.

Typical values of $\bar{S}$ and $\Delta\bar{t}$ (see equation 8.2(viii) are:-

p, GeV/c	$\bar{S}$, cm	Mean range at 100 g.cm^{-2} layer, g.cm^{-2}
0.14	3.86×10^{2}	5.36×10^{-2}
1	5.46×10^{3}	7.79×10^{-1}
10	5.51×10^{4}	7.86

Appendix A.7.1.2.

Verification of Owen and Wilson's Equation for Survival Probability

Let the rest mass of the particle considered be μ momentum units.

Let the mean lifetime of the particle considered be τ.

Let the sea-level momentum of the particle considered be p and let its instantaneous momentum at any given height t be p', a variable.

Let the momentum loss in traversing the whole atmosphere be p_o.

Let { time / distance } measured in the laboratory system be { T / x }

Let { time / distance } measured in the particle's frame of reference be { T' / x' }

Let the Lorentz transformation factor be γ, $= p'/\mu\beta$

Let the density of the atmosphere at any given depth be ρ and its scale height be h_o

Let the depth measured from the top of the atmosphere be t, sea-level being t_o.

By definition of mean lifetime one can show that the fractional number of particles decaying in time dT' will be

$$dN/N = -dT'/\tau$$

$$= -dT/\gamma \cdot 1/\tau \qquad \text{(i)}$$

$$= -dT/p' \cdot \mu/\tau \qquad \text{(ii)}$$

Now, $p' = p + p_o\,(1 - t'/t_o)$ See Fig. A.7.1.2.

hence $dN/N = -\mu/\tau\left\{\dfrac{1}{p+p_o\left(1-\dfrac{t'}{t_o}\right)}\right\}dT$ (iii)

If the particle travels a distance dx in corresponding time dT, then:-

$$dx = c.dT.$$

But for the atmosphere -

$$\rho . x = t$$

$$\text{and } dx = dt/\rho$$

$$\text{or } dT = dt/\rho c \qquad \text{(iv)}$$

For an isothermal atmosphere (e.g. Rossi 1952c)

$$h_o = t/\rho = RT \text{ (constant)}$$

$$\text{or } 1/\rho = h_o/t$$

hence from (iv) $dT = h_o/c \;.\; dt/t$ (v)

Substituting for dT in (iii), one has

$$\frac{dN}{N} = -\frac{\mu}{\tau} \cdot \frac{h_o}{c} \cdot \frac{1}{\left\{p+p_o\left(1-\dfrac{t}{t_o}\right)\right\}} .dt/t$$

Integrating over the limits N_o (produced) to N (arriving at sea-level) and corresponding values t to t_o to find the survival probability P, the ratio N/N_o, one finds

$$\int_{N_o}^{N}\frac{dN}{N} = -\frac{\mu}{\tau}\cdot\frac{h_o}{c}\cdot\int_{t}^{t_o}\frac{dt}{t\left\{p+p_o\left(1-\dfrac{t}{t_o}\right)\right\}} \qquad \text{(vi)}$$

This may be integrated by separation into partial fractions. The result is:-

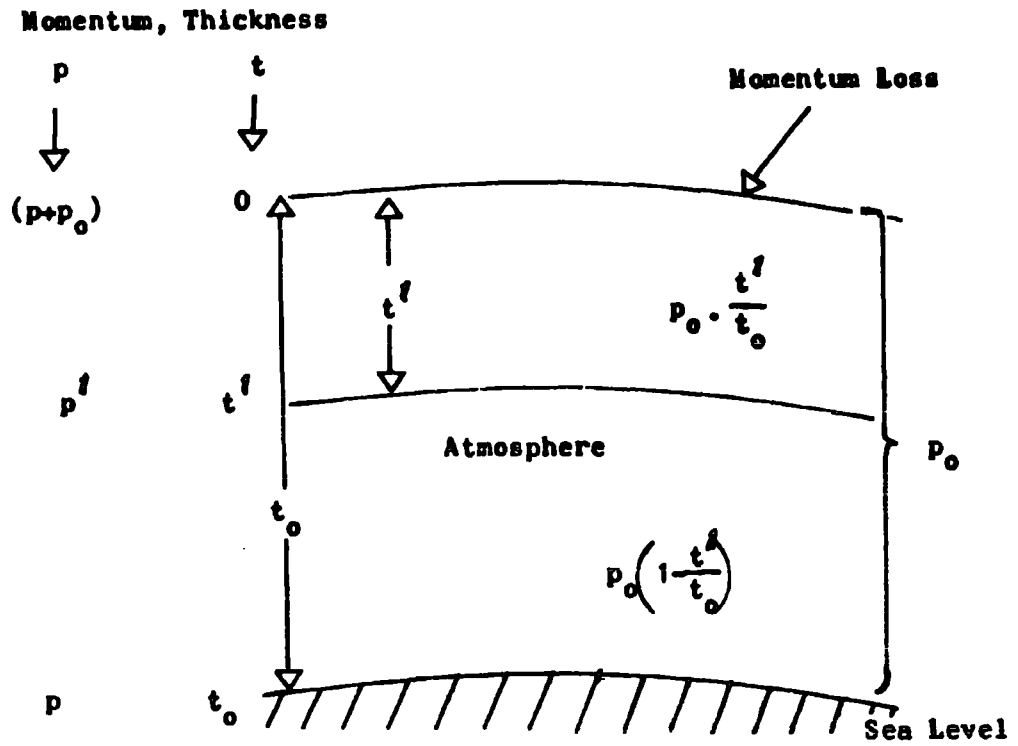

FIG. A.7.1.2. Corresponding momenta and levels of muons traversing the Atmosphere (Used in verification of Owen and Wilson's equation)

$$\ln P = \ln\left(\frac{N}{N_o}\right) = -\frac{h_o \mu}{c\tau(p+p_o)} \cdot \ln\left[\frac{t_o}{t}\left\{1+\frac{p_o}{p}\cdot\left(1-\frac{t}{t_o}\right)\right\}\right]$$

Appendix A.7.1.3.

The Relation Between the Energy of a Pion and the Subsequent Mean Energy of its Decay Muon

This follows from accurate considerations of the kinematics of $\pi-\mu$ decay given by Ascoli, (1950), who states the following:-

$$U_{\mu_0} = \tfrac{1}{2}\left(\frac{m_\pi}{m_\mu} + \frac{m_\mu}{m_\pi}\right) \qquad 1(a)$$

$$U_\mu = U_{\mu_0}\, U_\pi + p_{\mu_0}\, p_\pi \cos\theta \qquad 2(a)$$

where $U_{..}$ etc is the total energy in units of m_0c^2 and $p_{..}$ etc is the momentum in units of m_0c.

Suffix 'o' refers to centre of mass system, and θ is the angle between the trajectory of a pion and that of its decay muon.

The mean value of U_μ in (2a) is given when θ in the Centre of Mass system is $\pi/2$, i.e. $\cos\theta = 0$. Denoting the mean value of U_μ from a unique U_π by $\bar{U}_\mu$, one has:-

$$\bar{U}_\mu = U_{\mu_0} \cdot U_\pi$$

Substituting for U_{μ_0} from (1a) above,

$$\frac{\bar{E}_\mu}{m_\mu c^2} = \tfrac{1}{2}\left(\frac{m_\pi}{m_\mu} + \frac{m_\mu}{m_\pi}\right)\frac{E_\pi}{m_\pi c^2}$$

$$\text{or} \quad \bar{E}_\mu = \frac{E_\pi}{2} \cdot \frac{m_\mu}{m_\pi}\left(\frac{m_\pi}{m_\mu} + \frac{m_\mu}{m_\pi}\right).$$

If, following Pine et al, one writes:-

$$\bar{E}_\mu = r \cdot E_\pi \qquad 3$$

and $r' = m_\pi/m_\mu$, $= 0.76$ (assuming $m_\mu c^2 = 105.7$ GeV, $m_\pi c^2 = 139.6$ GeV, after Barkas et al) then

$$\bar{E}_{\mu} = \frac{r'}{2} \cdot E_{\pi}\left(\frac{1}{r'} + r'\right)$$

or $\bar{E}_{\mu} = 0.787\ E_{\pi}$

or $E_{\pi} = 1.2706\ \bar{E}_{\mu}$

Hence r in the equation 3 above is effectively 0.787, as compared with the value of 0.76 taken by Pine from simpler considerations - the latter value is shown to be 3.9% in error when accurate kinematics are considered.

Appendix A.8.1.1.

Correction of Positive-Negative Ratio for Proton Component

Let the positive-negative ratio observed be σ_o

" " " " " for muons only be σ_M

" " fraction of protons be f

" " no. of all positive particles be n_+

" " " " positive muons be n_{M+}

" " " " protons be n_p

" " " " negative muons be n_-

Then $\sigma_o = \frac{n_{M+} + n_p}{n_-}$

$$= \sigma_M + \frac{n_p}{n_-} \qquad \text{(i)}$$

Now, $f = \frac{n_p}{(n_- + n_M + n_p)}$

$$= \frac{n_p}{n_-(1 + n_+/n_-)}.$$

or $$\frac{n_p}{n_-} = f\,(1 + \sigma_o) \qquad \text{(ii)}$$

Substituting (ii) into (i) above,

$$\sigma_M = \sigma_o - f\,(1+\sigma_o)$$

or $$\sigma_M = \sigma_o\,(1 - f) - f.$$